Electronic structure and defect chemistry in iron perovskites

Maximilian Felix Hoedl

Stuttgart · 2021

ELECTRONIC STRUCTURE AND DEFECT CHEMISTRY IN IRON PEROVSKITES

Von der Fakultät Chemie der Universität Stuttgart
zur Erlangung der Würde eines Doktors der
Naturwissenschaften (Dr. rer. nat.)
genehmigte Abhandlung

vorgelegt von
Maximilian Felix Hoedl
aus Stuttgart, Deutschland

Hauptberichter:	Prof. Dr. J. Maier
Mitberichter:	Prof. Dr. J. Kästner
Prüfungsvorsitzender:	Prof. Dr. R. Niewa
Tag der Einreichung:	21. Juni 2021
Tag der mündlichen Prüfung:	29. Juli 2021

Physikalische Festkörperchemie
Max-Planck Institut für Festkörperforschung
Stuttgart, 2021

Erklärung über die Eigenständigkeit der Dissertation

Ich versichere, dass ich die vorliegende Arbeit mit dem Titel ”Electronic structure and defect chemistry in iron perovskites” selbständig verfasst und keine anderen als die angegebenen Quellen und Hilfsmittel benutzt habe; aus fremden Quellen entnommene Passagen und Gedanken sind als solche kenntlich gemacht.

Stuttgart, 21. Juni 2021 Maximilian Felix Hoedl

Declaration of Authorship

I hereby certify that the dissertation entitled ”Electronic structure and defect chemistry in iron perovskites” is entirely my own work except where otherwise indicated. Passages and ideas from other sources have been clearly indicated.

Stuttgart, 21. Juni 2021 Maximilian Felix Hoedl

Acknowledgements

I would like to express my sincere gratitude to all the people that have helped me during the time of this dissertation. First and foremost, I would like to thank Prof. Dr. Joachim Maier for the opportunity to work on my PhD at the Max Planck Institute for Solid State Research. I truly enjoyed the working environment in the department and was very pleased with the scientific direction. I would also like to thank Prof. Dr. Kästner and Prof. Dr. Niewa for taking the time and effort for reviewing my thesis and taking part in the examination committee. A special thanks goes to Sofia Weiglein and Madeleine Burkhardt for their great administrative support. I am especially grateful to Dr. Rotraut Merkle, for the supervision of this work. Her scientific advise, proof-readings and general direction of the research has tremendously helped me. I also thank Prof. Dr. Eugene Kotomin for his support, discussions and proof-reading. During my time at the MPI, I had many opportunities to travel to conferences and visit international collaborators which had a very positive impact on my work. I would like to express special thanks to Dr. Tor Bjorheim of the University of Oslo, who actually taught me how to perform DFT calculations. Here, I want to mention also Dr. Sarmad Saeed and Dr. Tarjei Bondevik, PhD students at the University of Oslo at the time, who both supported me scientifically and made me part of their research group. I want to thank Dr. Denis Gryaznov from the University of Latvia for his help and valuable scientific advise, Chrstina Ertural from the RWTH Aachen for her technical support regarding the calculations, and Andreas Leonhardt from the MPI for patiently explaining group theory to me.

I enjoyed a lot working at the MPI together with my colleagues and fellow PhD students, and I am very happy to have become close friends with some of them. Thank you all for this wonderful time, and thank you, Torben and Andreas, that the work was so much fun. Working largely on my own for more than four years has taught me how incredibly important it is to have a healthy work-life balance - as cliché as that may sound. I express my deepest gratitude to my girlfriend, roommates and friends - some of whom I have been around for most of my life, others I have met more recently during my studies and the time at the MPI. Finally, I would like to thank my parents, who have placed tremendous faith in my scientific abilities and who have always encouraged me to follow my path. This path has led me from geosciences to materials science to theoretical chemistry, setting the very foundation for the success of this work.

Max

Abstract

Iron-containing perovskites comprise a wide range of compositions exhibiting mixed electronic-ionic conductivity by virtue of electron holes, oxygen vacancies and hydrogen ion (proton) interstitials. The presence of three charge carriers imparts unique functional properties to these materials, but often entails complex defect chemical behavior involving mutual defect interactions. This thesis systematically investigates these aspects by studying the electronic structure and defect chemistry of $Ba_xSr_{1-x}FeO_{3-\delta}$ through first-principles density functional theory (DFT) calculations.

First, the electronic structure of defect-free, cubic $BaFeO_3$ was calculated using DFT and analyzed in terms of local atomic orbitals. The calculations revealed $BaFeO_3$ to be a negative charge transfer material with a dominating $d^5\underline{L}$ ($\underline{L}$ = ligand hole) configuration, confirming previous experimental[1–3] and theoretical[4] studies. A detailed chemical bonding analysis further showed that the Fe-O bond has a mixed ionic-covalent character, and that the frontier orbitals at the Fermi level (and ligand holes) have an anti-bonding $pd\sigma^*$ character. To ease chemical interpretation, the symmetry-adapted linear combinations of these orbitals were generated using group theory and visualized schematically in terms of orbital icons.

The susceptibility of the ideal cubic perovskite structure towards phase transformations was evaluated on the basis of first-principles phonon calculations. The phonon dispersion revealed distinct dynamically unstable modes which are isostructural to Jahn-Teller type distortions. In a series of static DFT calculations, the cubic structure was subsequently distorted along the unstable modes, leading to a moderately Jahn-Teller distorted ground state. The distortion is able to lift the orbital degeneracy of O $2p$ dominated ligand holes inherent to the cubic phase, thereby alleviating stresses in the electronic structure. The difference in total energy between distorted and cubic structures is nevertheless small, potentially explaining why such a distortion has not been observed in experiments.

The defect chemistry of $Ba_xSr_{1-x}FeO_{3-\delta}$ was explored with respect to two different types of point defects: oxygen vacancies and protonic defects. Using DFT calculations of defective neutral supercells, the thermodynamic parameters governing the defect formation were calculated and correlated to electronic structure descriptors. The results of this study demonstrate that many of previously unresolved issues, particularly concerning defect interactions, can be explained by taking into account the complex electronic structure.

The energy of oxygen vacancy formation, i.e. the release of neutral oxygen at the expense of electron holes, increases with increasing Sr-content and increasing oxygen vacancy concentration. Both compositional variations correlate with an increasing Fermi level at which electrons from the removed oxygen have to be accommodated. Such a dependence had qualitatively been inferred previous. Here, a quantified analysis was carried out, taking into account Fermi level position and Fe-O bond strength as a function of oxygen non-stoichiometry (and thus electron hole concentration). With increasing δ, the Fe-O bond is weakened which facilitates oxygen excorporation and should decrease the vacancy formation energy. However, this contribution is effectively outweighed by the concomitant increase in Fermi level, rendering the vacancy formation energy to experience a net increase.

In solid oxides containing oxygen vacancies, protons can be incorporated via the hydration reaction, i.e. the absorption of water vapor in dissociated form (H^+, OH^-), with the proton being attached to a regular oxygen ion and the hydroxide ion filling an oxygen vacancy. The reaction yields mobile protonic defects (hydroxide ions on oxygen ion sites) that impart a protonic conductivity to the materials. In this work, a thermodynamic formalism was developed that allows quantifying the energy changes during the two partial reactions - the proton- and hydroxide affinities - from first-principles DFT calculations. In a comprehensive approach, the new formalism was applied to a wide range of solid oxides, ranging from binary oxides such as MgO to various perovskite oxides, including $BaZrO_3$ and $BaFeO_3$. The study revealed an intriguing correlation between proton- and hydroxide affinities and the ionization potential (IP, position of O $2p$ band relative to the vacuum level) of the materials across the various structure families investigated. Oxygen $2p$ and $2s$ orbitals are stabilized more strongly upon O-H bond formation when they have a higher absolute band position in the unprotonated state (i.e. smaller IP), causing a more negative proton affinity. On the other hand, a higher absolute position of the O $2p$ and $2s$ orbitals makes the hydroxide affinity less negative. These relations have so far not been recognized in the literature, and constitute an important step in understanding the phenomena of proton uptake in solid oxides.

In the series of compositions $Ba_xSr_{1-x}FeO_{3-\delta}$, the hydration energy becomes more negative with increasing Ba-content and increasing concentration of oxygen vacancies. Evaluation of the proton and hydroxide affinities in oxygen non-stoichiometric $BaFeO_{3-\delta}$ showed that the trend with δ largely reflects an underlying trend of increasingly more negative hydroxide affinities. This is suggested to stem from the annihilation of delocalized ligand holes during oxygen vacancy formation; lattice oxygen ions (and incorporated OH^-) become subsequently more negatively charged, and thus experience a stronger electrostatic interaction with their ionic environment. Eventually, the defect in-

teractions for the formation of both oxygen vacancies and protonic defects are related to a common cause - the presence of delocalized ligand holes. This comprehensive understanding of the complex defect chemistry of iron containing perovskites is important for a targeted optimization of materials for applications in electrochemical cells.

Zusammenfassung

Eisenhaltige Perowskite umfassen ein breites Spektrum an Zusammensetzungen, die aufgrund von Elektronenlöchern, Sauerstoffleerstellen und Wasserstoffionen (Protonen) auf Zwischengitterplätzen, eine gemischt elektronisch-ionische Leitfähigkeit aufweisen. Das Vorhandensein von drei unterschiedlichen Ladungsträgern verleiht diesen Materialien einzigartige funktionelle Eigenschaften, bedingt jedoch eine komplexe Defektchemie, die häufig von gegenseitigen Defektwechselwirkungen geprägt ist. Die vorliegende Arbeit befasst sich mit dieser Thematik und untersucht systematisch die elektronische Struktur und Defektchemie von $Ba_xSr_{1-x}FeO_{3-\delta}$ mit Hilfe von Berechnungen auf Basis der Dichtefunktionaltheorie (DFT).

Im ersten Schritt wurde die elektronische Struktur von kubischem $BaFeO_3$ mittels DFT berechnet und auf Basis lokaler Atomorbitale analysiert. Die Berechnungen zeigten, dass $BaFeO_3$ ein Material mit negativem Ladungstransfer und einer dominierenden $d^5\underline{L}$ ($\underline{L}$ = Loch am Liganden) Konfiguration ist. Damit wurden frühere experimentelle[1–3] sowie theoretische[4] Studien bestätigt. Eine detaillierte chemische Bindungsanalyse zeigte weiterhin, dass die Fe-O Bindung einen gemischt ionisch-kovalenten Charakter aufweist, und dass die chemisch aktiven Orbitale am Fermi-Niveau (und die Ligandenlöcher) einen anti-bindenden $pd\sigma^*$-Charakter haben. Um die chemische Interpretation der Ergebnisse zu erleichtern, wurden die Symmetrie-adaptierten Linearkombinationen dieser Orbitale mit Hilfe der Gruppentheorie generiert und grafisch als Orbitalsymbole dargestellt.

Die Neigung der idealen kubischen Perowskit-Struktur zu Phasenumwandlungen wurde auf der Basis von Phononenrechnungen evaluiert. Die Phononendispersion weist dynamisch instabile Phononenmoden auf, die den klassischen Jahn-Teller-Verzerrungen entsprechen. In einer Reihe von statischen DFT-Rechnungen wurde die kubische Struktur schrittweise entlang der instabilen Moden verzerrt, was schließlich zu einem moderat Jahn-Teller verzerrten Grundzustand führte. Ein Vergleich der elektronischen Strukturen zeigte, dass die Jahn-Teller Verzerrung die Orbitalentartung in den O $2p$-dominierten Ligandenlöchern aufhebt und dadurch Stress in der elektronischen Struktur der kubischen Phase abbaut. Der Unterschied in der Gesamtenergie zwischen verzerrter und kubischer Struktur ist hingegen relativ gering, was möglicherweise erklärt, warum eine solche Verzerrung in Experimenten nicht beobachtet wurde.

Im Hinblick auf die Defektchemie in $Ba_xSr_{1-x}FeO_{3-\delta}$ wurden zwei Arten von Punktdefekten betrachtet: Sauerstoffleerstellen und Protonen auf Zwischengitterplätzen. Die thermodynamischen Parameter ihrer Bildungsreaktionen wurden mit Hilfe von DFT-

Berechnungen defekthaltiger neutraler Superzellen berechnet, und anschließend mit der elektronischen Struktur korreliert. Dabei hat sich gezeigt, dass viele der bisher offenen Fragen, insbesondere hinsichtlich der Defektwechselwirkungen, durch die Berücksichtigung der komplexen elektronischen Struktur erklärt werden können.

Die Bildung einer Sauerstoffleerstelle erfolgt durch den Ausbau eines neutralen Sauerstoffatoms auf Kosten von zwei Elektronenlöchern. Die entsprechende Reaktionsenergie nimmt mit steigendem Sr-Gehalt und steigender Sauerstoffleerstellenkonzentration zu. In beiden Fällen korreliert die Veränderung in der Zusammensetzung mit einem steigendem Fermi-Niveau, auf dem die Elektronen des ausgebauten Sauerstoffs untergebracht werden müssen. Eine derartige Korrelation wurde in vorherigen Arbeiten bereits auf qualitativer Ebene erörtert. In der vorliegenden Arbeit wurde indes eine quantitative Analyse durchgeführt, in der neben der Position des Fermi-Niveaus auch explizit die Entwicklung der Fe-O Bindungsstärke mit δ (und damit der Löcherkonzentration) berücksichtigt wurde. Tatsächlich wird die Fe-O Bindung mit steigendem δ zunehmend schwächer, was den Ausbau von Sauerstoff erleichtert und eigentlich zu einer Abnahme der Leerstellenbildungsenergie führen müsste. Dieser Effekt wird jedoch durch den simultanen Anstieg des Fermi-Niveaus deutlich überkompensiert, sodass die die Leerstellbildungsenergie letztlich mit δ zunimmt.

In Festoxiden, die Sauerstoffleerstellen enthalten, können Protonen über die Hydratationsreaktion eingebaut werden. Hierbei wird Wasserdampf in dissoziierter Form (H^+, OH^-) vom Festoxid absorbiert, wobei das Proton an ein reguläres Oxidion im Festkörper gebunden wird, und das Hydroxidion eine Sauerstoffleerstelle füllt. Durch die Reaktion entstehen mobile protonische Defekte (Hydroxidionen auf Oxidionenplätzen), die dem Festoxid eine protonische Leitfähigkeit verleihen. Im Rahmen dieser Arbeit wurde ein thermodynamischer Formalismus entwickelt, der es ermöglicht, die Reaktionsenergie der beiden Teilreaktionen - die Protonen- und Hydroxidionenaffinitäten - mit Hilfe von DFT Berechnungen zu bestimmen.

Der neu entwickelte Formalismus wurde auf eine Reihe von Festoxiden angewendet, zu denen sowohl binäre Oxide wie MgO, als auch verschiedene Perowskite wie $BaZrO_3$ oder $BaFeO_3$ zählen. Es wurde dabei eine interessante Korrelation zwischen den Affinitäten und dem Ionisierungspotential (IP, Position des O $2p$ Bandes relativ zum Vakuum) festgestellt, die über verschiedene Materialklassen hinweg gilt. Sauerstoff $2p$ und $2s$ Orbitale werden durch das Ausbilden einer O-H Bindung stärker stabilisiert, wenn ihr ursprüngliches Niveau im unprotonierten Zustand höher war (d.h. kleineres IP), was letztlich zu einer negativeren Protonenaffinität führt. Andererseits wird die Hydroxidionenaffinität weniger negativ, wenn die O $2p$ und $2s$ Zustände auf einer absoluten Skala höher liegen. Diese Zusammenhänge wurden so in der Literatur noch nicht disku-

tiert, und stellen einen wichtigen Schritt zu einem besseren Verständnis der Protonenaufnahme in Festoxide dar.

Innerhalb der Serie $Ba_xSr_{1-x}FeO_{3-\delta}$ wird die Energie der Hydratationsreaktion mit zunehmendem Ba-Gehalt und zunehmender Konzentration an Sauerstoffleerstellen negativer. Eine Analyse der Protonen- und Hydroxidionenaffinitäten in Sauerstoffdefizitärem $BaFeO_{3-\delta}$ zeigte, dass dies dem Trend negativer werdender Hydroxidionenaffinitäten folgt. Es wird vorgeschlagen, dass dies durch die Vernichtung von Elektronenlöchern während des Sauerstoffausbaus hervorgerufen wird; die Oxidionen im Festoxid (und eingebaute OH^-) haben dadurch eine negativere Ionenladung, die die elektrostatische Wechselwirkung mit der ionischen Umgebung verstärkt.

Damit werden die Defektwechselwirkungen für die Bildung von Sauerstoffleerstellen und protonischen Defekten auf eine gemeinsame Ursache zurückgeführt - das Vorhandensein delokalisierter Ligandenlöcher. Dieses umfassende Verständnis der komplexen Defektchemie von eisenhaltigen Perowskiten ist wichtig für eine zielgerichtete Optimierung solcher Materialien für den Einsatz in elektrochemischen Zellen.

Contents

Introduction

1 Introductory Remarks

1.1 Motivation

The study of solid ion conductors is key to both fundamental research and the corresponding technologies such as fuel- or electrolyzer cells. These are required to compensate for the intermittent availability of renewable electricity - inherent to solar and wind power - through electrochemical conversion into hydrogen or synthetic fuels and on-demand recuperation into electrical energy. Ceramic fuel- and electrolyzer cells offer particularly high efficiencies without requiring the use of noble metal catalysts. While significant strides have already been made in advancing this technology, many of the underlying atomic processes are still poorly understood.

The class of materials investigated in this thesis is known as mixed ionic-electronic conductors, in which the ionic conductivity is mediated by the transport of oxygen or hydrogen ions. These functional properties make them superior candidates as cathode materials in ceramic fuel cells, allowing further performance enhancement. It was only recently, however, that electronic and ionic conductivities were found to be often highly correlated, with potentially adverse consequences for the applications. The underlying physical mechanism is still unclear, but is believed to involve interactions between electronic and ionic charge carriers.

This thesis addresses this question by studying the electronic structure and defect chemistry in iron perovskites - a well-known category of mixed conductors. Using quantum chemical calculations, the delocalized nature of the electrons in these materials is properly described and their interactions with the ionic charge carriers are elucidated. The results of this work contribute to a deeper understanding of the observed phenomena which helps to design novel cathode materials for fuel- and electrolyzer cells.

1.2 Mixed-conducting oxides as cathode materials in PCFCs

Ceramic fuel cells are typically based on solid oxides as electrolyte material (SOFC: Solid Oxide Fuel Cell) that exhibit high oxygen or hydrogen ion (proton) conductivities. The conventional approach relies upon oxygen ion-conducting electrolytes, in which the negatively charged oxygen ions are conducted from the cathode to the anode, where they react with the supplied fuel (e.g. H_2) to water. However, the notoriously high activation barrier of oxygen ion transport requires high operating temperatures and makes the em-

ployed materials prone to long-term chemical stability issues. More recently, ceramic fuel cells are being developed that operate with proton conducting electrolytes (PCFC: Protonic Ceramic Fuel Cell), in which the positively charged hydrogen ions (protons) are conducted from the anode to the cathode where they are consumed in the reaction with ambient oxygen to water. The use of proton-conducting electrolytes offers a number of potential benefits over conventional SOFCs. Since the water is produced at the cathode, it can easily be removed by the oxygen (air) flow, whereas in conventional SOFCs, the water is produced at the anode and dilutes the fuel. In addition, the generally lower activation barrier of proton transport allows for operating temperatures well below those of SOFCs which slows down degradation processes and increases the long-term chemical stability. PCFCs moreover have the ability to operate in reversible electrolysis mode;[5] by applying a voltage with water vapor supplied to the cathode, dry pressurized hydrogen can be produced. This allows PCFCs to be integrated into flexible energy storage systems that produce hydrogen from excess renewable electricity. An important factor limiting PCFC performances is the slow reaction of protons, electrons and ambient oxygen to water at so-called triple phase boundaries where electrolyte, cathode and air are in contact (figure 1.1a).

(a) Reaction at triple phase boundaries **(b)** Bulk path: Reaction on cathode surface

Figure 1.1: Schematic illustration of a PCFC cathode operation.

However, the spatial confinement of this reaction to triple phase boundaries can be lifted by using cathode materials that are both electron and proton conducting (figure 1.1b). Protons passing through the electrolyte can proceed into the cathode via the ”bulk path” and react to water on the entire surface of the porous cathode - a much larger reactive zone that can heavily increase the rate of the reaction. Since most of the currently available mixed proton and electron conducting materials also exhibit oxygen ion conductivity, they are often referred to as triple conducting oxides. Research into PCFCs is quickly evolving and recent developments regarding their performance are astounding; several studies have demonstrated PCFCs to operate reliably on flexible fuels (e.g. H_2 or

CH_4) with power densities higher than in conventional SOFC systems under intermediate temperature conditions (e.g. 500 °C).[6–10] This progress can largely be attributed to an increased proton conductivity in the electrolyte in combination with a mixed proton and electron conducting cathode.[11] Meanwhile, PCFCs were shown to be cost competitive with the more mature SOFC technology,[12] and efforts to scale-up PCFCs into commercially viable products are in progress.[13]

Mixed proton and electron conductivity has been observed in perovskite oxides, ABO_3, in which the A-site is occupied by large alkali earth elements (Sr, Ba) and the B-site by redox active transition metals (Mn, Fe, Co, Ni). Their ability to incorporate protons is generally found to be lower than in proton-conducting electrolyte materials and varies greatly with the cation composition.[14,15] In fact, substituting the B-site with redox-inactive cations such as Zn, Y, and Zr can drastically increase the proton uptake at the cost of a decreased electronic conductivity; the reasons for this detrimental correlation, however, are still largely unknown. In addition, the electrons in these materials are believed to be strongly correlated, with implications for red-ox defect chemical reactions that have rarely been studied in detail. This work explores these fundamental phenomena in the $Ba_xSr_{1-x}FeO_{3-\delta}$ family of materials by studying their electronic structure and defect chemistry. In particular, it is shown how many defect chemical properties, which might naively be attributed to a mixed valence state of the iron, actually involve changes of oxygen states.

1.3 Thesis Outline

The present thesis constitutes a purely theoretical investigation about the interplay between electronic structure and defect chemistry in iron containing perovskites, particularly in the system $Ba_xSr_{1-x}FeO_{3-\delta}$. A theoretical framework is laid out first, covering relevant aspects of the first-principles calculations (§ 2) and defect chemical concepts (§ 3). Based on this, it is described how defect chemical quantities become amenable to DFT calculations by invoking the concepts of first-principles thermodynamics (§ 4). The results of the thesis are divided into four consecutive chapters:

- **The electronic structure of cubic $BaFeO_3$. § 5**

  Starting with a defect-free and non-distorted cubic perovskite lattice, the electronic structure of $BaFeO_3$ is calculated and analyzed in terms of local atomic orbitals. While previous studies have been devoted to the electronic structure of $BaFeO_3$, here the focus is on a chemically intuitive description, adding to the existing literature a detailed analysis of the Fe-O chemical bond. It is shown that the Fe-O bond

has a mixed ionic-covalent character, and that the chemically active frontier orbitals are anti-bonding combinations of Fe $3d$ and O $2p$ orbitals. The conclusions drawn in this chapter lay the foundation for the discussion in the subsequent chapters.

- **Jahn-Teller distortion in $BaFeO_3$. § 6**

  In this chapter, the artificial assumption of an ideal cubic perovskite lattice is relaxed and potential structural distortions are investigated. For this purpose, the phonon dispersion is calculated which reveals dynamically unstable displacement modes that are isostructural to Jahn-Teller distortions. The electronic structure of the distorted ground state of $BaFeO_3$ is explored and compared to the ideal cubic structure; this allowed tracing the structural instability inherent to the parent cubic phase to degenerate O $2p$ dominated electronic states at the Fermi level.

- **Oxygen non-stoichiometry in $Ba_xSr_{1-x}FeO_{3-\delta}$. § 7**

  Here, the oxygen non-stoichiometry in the $Ba_xSr_{1-x}FeO_{3-\delta}$ system is investigated through a combination of electronic structure analysis and first-principles thermodynamics. The space of potential configurations of multiple oxygen vacancies per supercell is extensively screened to identify structures close to the global energy minimum. It is shown how the vacancy formation energy is dependent on A-site composition of the perovskite and on the concentration of previously introduced oxygen vacancies - a typical hallmark of defect interactions.

- **Proton uptake in $Ba_xSr_{1-x}FeO_{3-\delta}$. § 8**

  Based on the presence of oxygen vacancies, this chapter explores the thermodynamics of proton uptake in the $Ba_xSr_{1-x}FeO_{3-\delta}$ system via the hydration reaction - a dissociative absorption of H_2O into oxygen vacancies. It is shown how A-site composition and the concentration of oxygen vacancies systematically affect the energetics of the hydration reaction. A new thermodynamic formalism is developed that allows decomposition of the overall hydration reaction into individual reaction steps. A wide range of materials is sampled with the developed formalism, revealing intriguing correlations between hydration thermodynamics and the electronic structure of the materials.

In the course of these chapters, the structural and compositional degrees of freedom in the $Ba_xSr_{1-x}FeO_{3-\delta}$ system are successively increased; the final composition being characterized by a complex interplay between electronic structure, Jahn-Teller distortions, and two types of point defects. The disentanglement of these phenomena - possible only in the field of simulation - facilitates their understanding and ensures a comprehensible presentation of the work.

Theoretical Framework

2 First-Principles Calculations

The theoretical investigations in this work are based on a so-called first-principles (or *ab initio*) approach - i.e. they rely entirely on fundamental physical laws without requiring empirical models or assumptions. In particular, the density functional theory (DFT) as implemented in the Vienna *Ab initio* Simulation Package (VASP) was used to calculate the electronic structures and total energies of the $Ba_xSr_{1-x}FeO_{3-\delta}$ family of materials. This chapter provides a brief introduction to DFT and its implementation in VASP, and presents the analytical tools necessary for a chemical interpretation of the calculated data. More detailed treatments of this subject can be found in many other sources, e.g.,[16,17].

2.1 Density functional theory

In its original form, the DFT establishes an exact relationship between the total energy of a system and its electron density distribution.[17,18] Specifically, the DFT states that the system's ground state total energy can be found by minimizing the energy functional $E[n(r)]$ with respect to the electron density $n(r)$.[i] In order to determine $n(r)$, modern implementations of DFT (such as VASP) use the Kohn-Sham equations[19] that allow calculating the electron density from a set of one-electron wave functions through

$$n(r) = \sum_j |\psi_j|^2 \tag{2.1}$$

The central idea of the Kohn-Sham approach is to introduce a fictitious reference system of non-interacting electrons which capture major parts of the true electron energies and which can be solved very accurately. The residual electron-electron interactions - exchange and correlation - are approximated by letting the non-interacting electrons feel an exchange-correlation potential that accounts for all the differences between the reference and the real system. The exact form of this potential is, however, unknown and various approximations have been developed over time. In the present thesis, the so-called generalized gradient approximation (GGA) is used in which the exchange-correlation potential is derived from the gradient of the electron density distribution. A good description of the GGA and other exchange-correlation potentials is given in[20]. Within Kohn-Sham DFT, the one-electron wave functions are optimized by solving a set of Kohn-Sham equa-

[i] A functional takes as variable another function, in this case, E is a function of n which is a function of r.

tions - the equivalent form of the time-independent Schrödinger equation adapted to a set of non-interacting one-electron wave functions,

$$\left\{-\frac{\hbar^2\nabla^2}{2m} + V_{\text{eff}}(\mathrm{r})\right\}\psi_j(\mathrm{r}) = \epsilon_j\psi_j(\mathrm{r}) \tag{2.2}$$

with an effective potential of the form

$$V_{\text{eff}}(\mathrm{r}) = V_{\text{en}}(\mathrm{r}) + V_{\text{H}}(\mathrm{r}) + V_{\text{XC}}(\mathrm{r}) \tag{2.3}$$

which consists of the potential for the interactions between electrons and nuclei, V_{en}, the Hartree potential, V_{H}, describing the electrostatic interaction of the electrons, and the potential for exchange and correlation, V_{XC}, accounting for all differences between the non-interacting reference system and the true one-electron wave functions.[20] The potential from the nuclei is thereby assumed to be fixed as a result of the Born-Oppenheimer approximation.[21] The rationale behind this approximation is that electrons are considered to move so much faster than the nuclei they instantaneously adapt to any given atomic arrangement. Solving the Kohn-Sham equations yields the electron density, $n(r)$ via equation 2.1, with respect to which, the energy functional $E[n(r)]$ is minimized. As a consequence of the Born-Oppenheimer approximation, the energy contribution from the electrostatic interaction between the nuclei, E_{nn}, becomes a simple additive constant to the total energy. Eventually, the total energy of a system may be expressed in terms of its individual contributions

$$E^{\text{tot}} = T_{\text{e}} + E_{\text{ee}} + E_{\text{en}} + E_{\text{XC}} + E_{\text{nn}} \tag{2.4}$$

where T_{e} is the kinetic energy of the electrons, E_{ee} the energy from electrostatic interactions among the electrons (Hartree energy), E_{en} the energy from the electrostatic interaction between electrons and nuclei, E_{XC} the energy from exchange and correlation effects and E_{nn} the energy from the electrostatic interaction among the nuclei. Equation 2.4 describes the total energy of a system as calculated with VASP and forms the basis for the first-principles thermodynamic modelling in this work.

The Kohn-Sham DFT approach provides an efficient and accurate means to solving the one-electron wave functions and calculating a system's total energy. The optimized wave functions thereby serve as basis for analyzing the electronic structure of the system. However, the Kohn-Sham equations rely on an expression for the exchange-correlation

potential, the exact form of which is unknown. Research into ever more accurate expressions for it, is still evolving and there exists nowadays a plethora of different available functionals to choose from - even within the GGA. When studying a material, the type of exchange correlation functional must be chosen carefully to match key experimental data. Hence, although formally being addressed as a "first-principles" method, in practice, the necessity of empirical approximations usually remains.

2.2 Practical implementation of DFT

The DFT calculations in this work were performed with VASP[22–24] and follow a certain procedure as shown schematically in figure 2.1. The computational details of each step are discussed below; numerical input parameters are given in appendix A.1. The input atomic structure is specified by the lattice parameters and atomic coordinates in the unit cell, upon which periodic boundary conditions are imposed. As a consequence of the periodic boundary conditions, changes made in the unit cell regarding composition or structure are repeated into all unit cells of the crystal. Hence, to study point defects at low concentrations while using periodic boundary conditions, it is necessary to increase the size of the unit cell, for otherwise defect concentrations would be unreasonably high. This can be achieved by forming so-called supercells - several adjacent unit cells joined together to form a new, larger unit cell. The size of such a supercell inherently determines the lowest possible concentration of the introduced defect, and, if dilute conditions are to be modelled, should be sufficiently large to preclude noticeable interactions between the defect and its periodic images. The point defect calculations of chapter § 7 and § 8 are based on supercell expansions.

The Kohn-Sham equations are solved in an iterative, self-consistent manner as the effective potential itself depends on the electron density. An initial guess for the electron density to generate the initial effective potential is consequently required. VASP provides several options in this regard: the initial electron density can be generated from a superposition of atomic densities, or from random initial wave functions, the latter of which was used in the present work. The exchange-correlation potential in this work is described with the GGA and is further corrected with an additional on-site Hubbard-U interaction term[26] for the $3d$ electrons of the Fe atoms. DFT calculations involving such additional Hubbard-U correction schemes are frequently referred to as DFT+U, this term distinction is, however, omitted in the present work. Self-consistency of the electronic cycle is reached when the total energy between two subsequent steps falls below a previously specified threshold. Note that VASP hereby calculates the total energy including the energy term, E_{nn}, from the electrostatic interaction among the nuclei. Finally, the

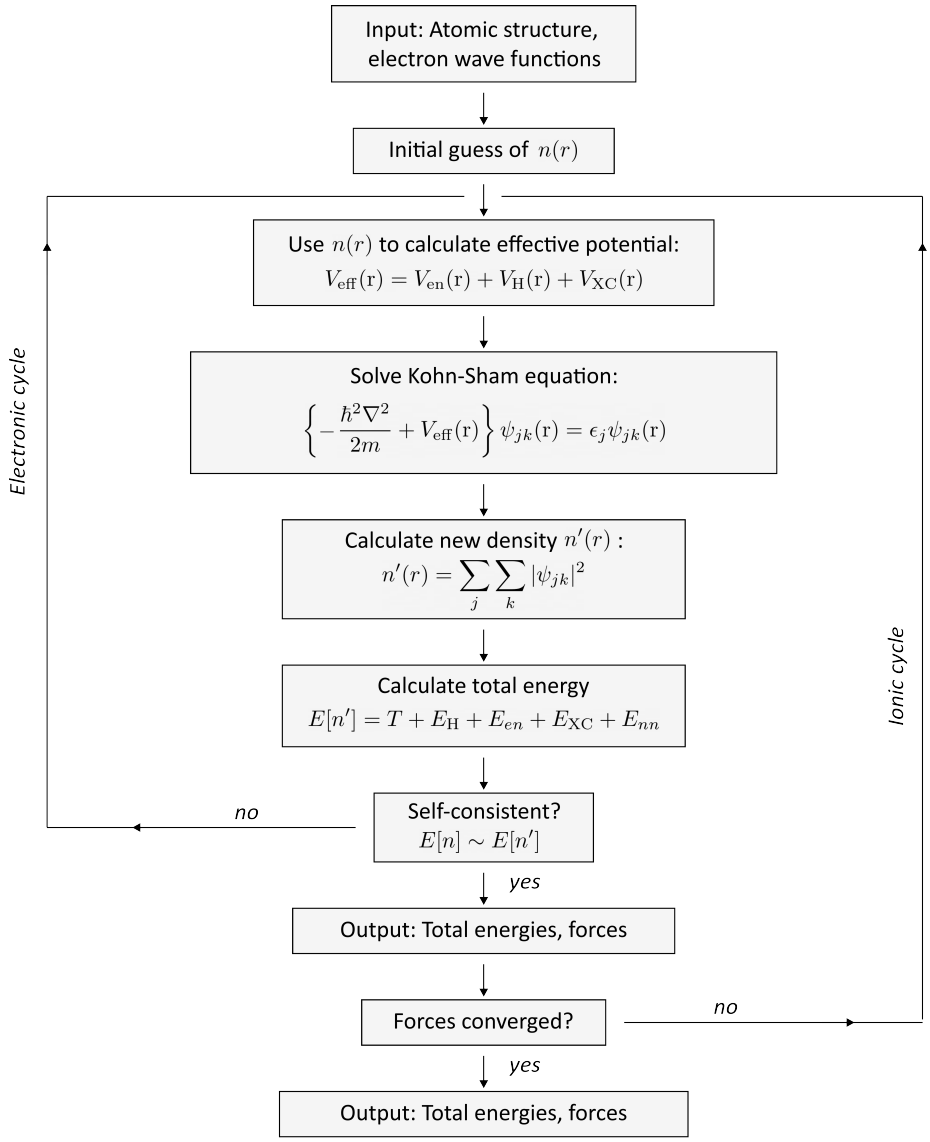

Figure 2.1: Steps of a DFT calculation, adapted from[25].

electronic cycle yields a set of refined one-electron wave functions (and electron density) for a fixed potential of the nuclei. Since the provided atomic structure is not necessarily the most stable one, an ionic cycle can be initiated in which the total energy is minimized with respect to the atomic positions. After finishing the electronic cycle, the atoms are moved according to the forces acting on them and the generated atomic structure serves as a new input structure. The ionic cycle is converged when the residual forces fall below a specified threshold. In general, the total energy as a function of the atomic positions is known as the potential energy surface, $E_{\mathrm{PES}}(R_1, ...R_n)$, and the global minimum of this function corresponds to the most stable structure. In order for VASP to find the global minimum, the input structure needs to be sufficiently close to the most stable structure for otherwise the algorithm runs into local, meta-stable minima on the potential energy

surface. Ultimately, when both electronic and ionic cycles are converged (ideally to the ground state), the output comprises a rich data set including the optimized electronic and ionic structures, along with a corresponding total energy that can be used for thermodynamic modelling.

2.3 Linear combination of atomic orbitals

The one-electron wave functions, ψ_j, are commonly described in terms of a basis set, i.e., a linear combination of mathematical functions called basis functions,

$$\psi_j = \sum_{\mu} c_{\mu j} \phi_{\mu}^{\text{basis}} \tag{2.5}$$

where the expansion coefficients, $c_{\mu j}$, are the quantities to be refined in the electronic cycle and by which the optimized wave functions are characterized. The basis set can either be composed of atomic orbitals (yielding a linear combination of atomic orbitals, LCAO), or delocalized plane waves. In VASP, the wave functions are expressed using a plane wave basis set, which generally ensures a high accuracy together with a high efficiency in terms of computational cost. Indeed, this was crucial in the present work as it allowed a very large number of point defect calculations to be processed. However, the delocalized nature of plane waves makes a chemical interpretation of the electronic structure extremely cumbersome and precludes a chemical bonding analysis in terms of bonding and anti-bonding orbital interactions. To ensure both high efficiency *and* viable chemical interpretation, the optimized wave functions were projected onto an auxiliary LCAO basis set in a post-process using the recently developed code LOBSTER.[27–31]

In the solid state, atomic orbitals (AOs) are represented as Bloch functions of the form

$$\phi_{\mu}(k) = \frac{1}{\sqrt{N}} \sum_{n=1}^{N} e^{(ikR_n)} \, \chi(r - R_n) \tag{2.6}$$

where $\chi(r - R_n)$ are localized atomic orbital that rest on some atom in the n-th unit cell. The periodic array of N localized atomic orbitals is modulated by a plane wave function with the wave number $k = \frac{2\pi}{\lambda}$. The shape of such an AO and the effect of k are illustrated in figure 2.2 featuring the real-part of a p-type Bloch function on a one-dimensional chain of alternating Fe and O atoms. At $k = 0$, the Bloch function reduces to a periodic array of atomic orbitals. As $k \neq 0$, the phase factor starts to modulate the amplitude of the AOs and determines their spatial extent and sign. As such, the wave number counts the

number of nodal planes between atomic orbitals centered in different unit cells. Since the p-orbital is odd with respect to the constituent oxygen site, changing the sign of every other p-orbital at $k = \frac{\pi}{a}$ leads to the complete disappearance of nodal planes between the unit cells.

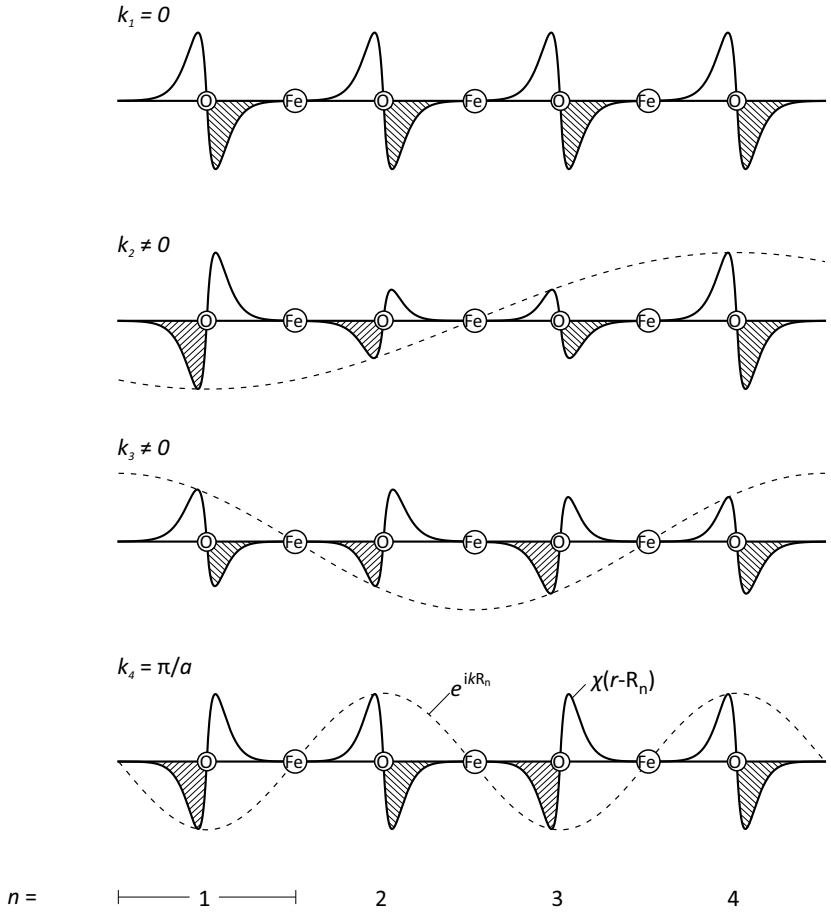

Figure 2.2: Real part of a Bloch function derived from the p orbital of an oxygen atom along an Fe-O linear chain, for different values of k.

In figure 2.2 only the real part of the Bloch wave is shown. The imaginary part has a modulating envelope function that is displaced along the axis such that the total charge density distribution is the same in every unit cell. This ensures that the Bloch wave fulfills the translational invariance of the crystal and only the phase is changed by k. However, the phase determines the number of nodes between the unit cells and thus the extent of inter-unit cell interactions. The one-electron wave functions, ψ_j, may consequently be expressed as a linear combination of the periodic AOs

$$\psi_j(k) = \sum_{\mu=1}^{n} c_{\mu j}(k)\phi_\mu(k) \tag{2.7}$$

where the coefficients, $c_{\mu j}$, may be complex-valued due to the complex nature of the periodic AOs (the complex part is omitted here and in subsequent formulas in this section). In reminiscence of molecular orbital theory, the one-electron wave functions expressed in this form have been termed crystal orbitals (COs).[27] The COs must be evaluated for each value of k individually. To be more specific, two AOs can involve in covalent bonding at one value of k while being mutually orthogonal at another k. For instance, the p-orbital in figure 2.2 is point symmetric with respect to the Fe sites at $k = 0$, hence orthogonal to, e.g., a d-orbital centered on the Fe atoms. Meanwhile, at $k = \frac{\pi}{a}$, the p-orbital is modulated by the phase factor in such a way that it becomes *gerade* with respect to the Fe atoms, allowing covalent mixing with the respective d-orbital. This also naturally explains why one particular crystal orbital, ψ_j, spans a band of energies rather than one discrete energy level, since it has different degrees of chemical bonding at different values of k. The values of k that need to be considered in a calculation lie in the range $-\frac{\pi}{a} \leq k \leq \frac{\pi}{a}$; values for k exceeding this range only yield repetitions of linear combinations already generated. In three dimensions, k becomes a vector and the range of k values is confined to the Brillouin zone (figure 2.3). For practical reasons, the continuous function of k is usually discretized into a grid of equally spaced k-points at which the COs are evaluated.

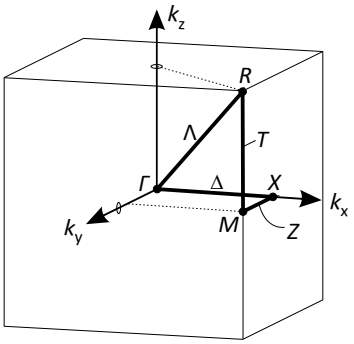

Figure 2.3: Brillouin zone of the simple cubic perovskite lattice.

Having projected the refined wave functions to an auxiliary basis set of LCAO wave functions, the electronic structure of a crystalline material becomes amenable to classical concepts of chemical bonding. To retrieve this kind of chemical information, there exists a number of analytical tools to process the projected set of wave functions. These are provided within the LOBSTER code and shall be defined briefly, following refs.[16,29].

One of the most widely used analytical tools in this regard is the projected density of states (PDOS) function

$$\mathrm{PDOS}_\mu(E) \sim \sum_{jk} c_{\mu j}\, dE \tag{2.8}$$

where $c_{\mu j}$ are the coefficients of AO μ in CO j. The term μ is thereby short hand notation and can refer to both the type of orbital and the constituent atom in the unit cell. What the PDOS essentially does is summing up the coefficients of a given AO in every CO at every k-point within infinitesimal energy intervals. Integrating the PDOS of a given orbital type from $E = -\infty$ to the Fermi level, E_F, yields the gross orbital population (GP)

$$\mathrm{GP}_\mu = \int_{-\infty}^{\epsilon_\mathrm{F}} \mathrm{PDOS}_\mu \tag{2.9}$$

On this basis, the Mulliken charges[32] may be defined as

$$\mathrm{Q}_A = Z_A - \sum_\mu \mathrm{GP}_\mu \tag{2.10}$$

where Z_A is the atomic number of a particular atom type in the unit cell, from which the sum of GP_μ over all atomic orbitals belonging to that atom is subtracted. Another widely used method to calculate atomic charges is based on a space partitioning into atomic domains and integrating the electron density in these domains, according to Bader.[33] However, Bader atomic charges were tested and found to be very sensitive toward structural distortions in the vicinity of point defects (especially vacancies) and are therefore not used in this work.

As the different COs (an their constituting AOs) typically span a broad band of energies, it is often useful for the discussion to calculate the average energy of a given type of orbital, known as the center of mass (ϵ_μ) of a band, according to

$$\epsilon_\mu = \frac{\sum_{jk} c_{\mu j}\epsilon_j}{\sum_{jk} c_{\mu j}} \tag{2.11}$$

Another important tool that is essential for a chemical bonding analysis is the crystal orbital Hamilton population (COHP) by which the orbital overlap of some chosen combination of AOs can be classified as bonding, non-bonding or anti-bonding. The COHP

can be written as

$$\mathrm{COHP}_{\mu\nu}(E) \sim H_{\mu\nu} \sum_{jk} c_{\mu j} c_{\nu j} \, dE \tag{2.12}$$

where $H_{\mu\nu}$ are the off-diagonal elements of the Hamiltonian matrix H, which yield the bonding energy contribution to an energy level ϵ_j (in contrast to the diagonal elements $H_{\mu\mu}$, which yield the net atomic energies). A more detailed derivation of this quantity can be found in[16]; here it suffices to discuss how the COHP can be used to evaluate the character of an orbital interaction. In practice, the COHP is plotted as a function of the energy and is placed next to the PDOS curve or band structure diagram, serving as a bonding indicator. It essentially weighs the PDOS of a pair of AOs by their corresponding off-site Hamiltonian matrix element. Three different cases can be distinguished,

- $\mathrm{COHP}_{\mu\nu}(E) < 0$: Negative values mean that the orbital interaction between a pair of AOs has a stabilizing effect on the energy of the CO and that, consequently, the orbital interaction has a bonding character.
- $\mathrm{COHP}_{\mu\nu}(E) = 0$: This means that the interaction of the AOs under consideration has no impact on the energy level of the CO, i.e. they are non-bonding.
- $\mathrm{COHP}_{\mu\nu}(E) > 0$: Positive values indicate a destabilizing effect of the orbital interaction and thus an anti-bonding interaction.

For practical reasons, the negative COHP is usually plotted such that peaks to the right (negative values) indicate bonding interactions and peaks to the left (positive values) indicate anti-bonding interactions. Finally, the integrated COHP up to the Fermi level of a given pair of AOs yields the electronic energy associated with their interaction

$$\mathrm{iCOHP}_{\mu\nu} = \int_{-\infty}^{\epsilon_\mathrm{F}} \mathrm{COHP}_{\mu\nu} \tag{2.13}$$

which can be used as a quantitative measure of bond covalency.

The combination of the presented tools - PDOS, GP, Q_A, ϵ_j, and COHP - provides valuable insight into the electronic structure of crystalline solids and allows one to perceive it in a chemically intuitive way. Therefore, the importance of projecting the optimized plane-wave basis set to an auxiliary LCAO basis set cannot be stressed enough. It should be mentioned that a similar projection scheme is implemented directly in VASP. However, in this scheme, key quantities such as the COHP are not computed, and the quality of the projection is often poor, rendering the chemical interpretation of the data questionable.

3 Defect Chemistry

The defect chemistry of a material deals with the compositional or positional disorder in the atomic structure of a crystal - so called defects - which can either span extended areas, e.g. dislocations or grain boundaries, or be confined to single lattice sites, e.g. point defects. This thesis deals exclusively with point defects in bulk crystals. Unlike the term "defect" might suggest, their presence in the crystal, especially in the case of point defects, often imparts exceptional functional properties to a material that are vital to a number of technologies. In particular, this work focuses on the $Ba_xSr_{1-x}FeO_{3-\delta}$ family of materials and explores the nature two different types of point defects: oxygen vacancies and proton interstitials. This chapter briefly reviews some of the fundamental aspects of point defect chemistry relevant to this work. For a more detailed treatment, the reader is referred to[34].

3.1 Equilibrium thermodynamics of point defects

Point defects are deviations from the perfect crystal structure confined to a single lattice site, such as a missing atom (a vacancy) or interstitial atom. They can be classified as intrinsic, i.e. they result from internal reactions within the crystal, or extrinsic, i.e. their formation involves the exchange of ions with the surroundings. A typical example of an intrinsic defect is the Frenkel disorder where an ion is displaced from its regular lattice site into an interstitial site leaving behind a vacancy. This thesis deals with the formation of extrinsic point defects in $Ba_xSr_{1-x}FeO_{3-\delta}$, and in particular, with oxygen vacancies and protonic defects. Oxygen vacancies are formed by release of neutral oxygen at the expense of electron holes, according to

$$O_O^x + 2h^\bullet \rightleftharpoons v_O^{\bullet\bullet} + \frac{1}{2}O_2 \tag{3.1}$$

In equation 3.1 the Kröger-Vink notation[35] is used in which lattice ions and point defects are treated as chemical entities characterized by the atomic or electronic species (O = oxygen, v = vacancy, h = electron hole), a subscript sign indicating the occupied lattice site, and a superscript sign indicating the relative charge with respect to the perfect crystal ($\bullet$ = positive charge, $\prime$ = negative charge). In this context, $v_O^{\bullet\bullet}$ describes a vacancy at an oxygen lattice site with an absolute charge of zero, i.e. doubly positively charged

relative to a regular O^{2-} ion in the perfect crystal.

A protonic defect formally refers to a hydrogen ion on an interstitial lattice site. However, since protons usually form a short bond of approximately 1 Å to one of the oxygen ions, these defects are more realistically described as hydroxide ions on oxide ion sites, $OH_O^{\bullet}$. They can form at the expense of electron holes according to

$$O_O^x + \frac{1}{2}H_2 + h^{\bullet} \rightleftharpoons OH_O^{\bullet} \tag{3.2}$$

or via the hydration reaction

$$O_O^x + v_O^{\bullet\bullet} + H_2O \rightleftharpoons 2OH_O^{\bullet} \tag{3.3}$$

where a water molecule dissociates into a proton (H^+) and a hydroxide ion (OH^-), with the proton being attached to a regular oxygen ion, and the hydroxide ion filling an oxygen vacancy, yielding two protonic defects per incorporated H_2O molecule. While reaction 3.2 involves electron transfer and thus constitutes a redox-reaction, reaction 3.3 is a pure acid-base reaction.

The fundamental quantity that determines the extent of such disorder reactions is the Gibbs energy of the crystal, which strives for a minimum at a given pressure and temperature. The total Gibbs energy of a real crystal can be broken down into the contribution of the perfect crystal, and the Gibbs energy of formation of a single defect, $\Delta_f G_d$, multiplied by the number of defects.

$$G_{\text{real}} = G_{\text{perf}} + \Delta_f G_d \, N_d \tag{3.4}$$

From here on, the subscript "f" stands for "formation", and "d" for "defect". The introduction of point defects in the crystal is associated with a significant increase in possible site configurations because each point defect, e.g. $v_O^{\bullet\bullet}$, can occupy any of the O_O^x available lattice sites. For a given concentration of point defects, there exists a finite number Ω of distinguishable ways to arrange all defects over the regular lattice sites. The configurational entropy associated with Ω is given by

$$S_{\text{conf}} = k_B \, \ln \Omega \tag{3.5}$$

The change in Gibbs energy associated with the formation of a point defect, $\Delta_f G_d$, can be further divided into two parts. A concentration-dependent term stemming from the

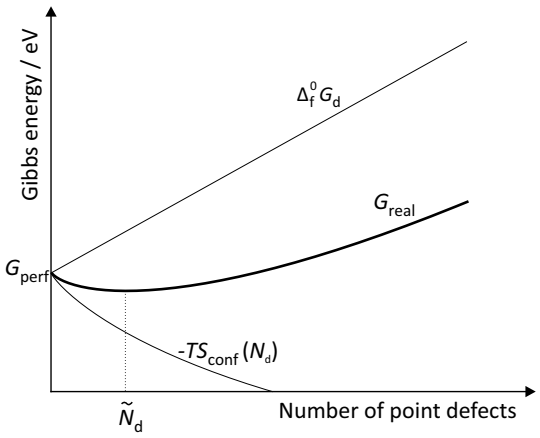

Figure 3.1: Gibbs energy contributions in a real crystal. The minimum in G_{real} determines the equilibrium number of point defects, $\tilde{N}_{\mathrm{d}}$.

change in configurational entropy, and a term, $\Delta_{\mathrm{f}}^{0} G_{\mathrm{d}}$, representing the energy required to form an individual defect. $\Delta_{\mathrm{f}}^{0} G_{\mathrm{d}}$ is assumed to be unaffected by any previously introduced defects, hence independent on N_{d}. This assumption holds for small concentrations of point defects, but eventually becomes invalid at higher concentrations when defects begin to interact with each other (see § 3.2).

$$G_{\mathrm{real}}(N_{\mathrm{d}}) = G_{\mathrm{perf}} + \Delta_{\mathrm{f}}^{0} G_{\mathrm{d}}\, N_{\mathrm{d}} - T\, S_{\mathrm{conf}}(N_{\mathrm{d}}) \tag{3.6}$$

The term $\Delta_{\mathrm{f}}^{0} G_{\mathrm{d}}$ is the key quantity to compare the thermodynamic stability of a certain point defect in a given crystal lattice, e.g. $\mathrm{v}_{\mathrm{O}}^{\bullet\bullet}$ in ABO_3 perovskites. It is composed of an enthalpy change, associated with the breaking and formation of chemical bonds, and a change in vibrational entropy.

$$\Delta_{\mathrm{f}}^{0} G_{\mathrm{d}} = \Delta_{\mathrm{f}}^{0} H - T\, \Delta_{\mathrm{f}}^{0} S_{\mathrm{vib}} \tag{3.7}$$

The Gibbs energy change of forming an individual defect, $\Delta_{\mathrm{f}}^{0} G_{\mathrm{d}}$, is always positive, since otherwise regular structure elements would be unstable and the crystal would collapse. On the other hand, the change in configuration entropy is always negative, thus favoring the incorporation of point defects, irrespective of the actual type or atomic species. The equilibrium number of point defects will therefore be determined by a balance between the gain in configuration entropy and the cost of locally breaking the periodicity of the crystal, see figure 3.1.

The slope of G_{real} against the amount of substance of a given point defect n_{d} with pressure and temperature held constant, is defined as the partial Gibbs energy, or the chemical potential μ_{d} of that defect. By separating out Avogadro's constant the chemical potential is defined as the partial Gibbs energy with respect to the number of defects N_{d}, equal to the slope of G_{real} in figure 3.1.

$$\frac{\partial G_{\mathrm{real}}}{\partial n_{\mathrm{d}}} = N_{\mathrm{A}} \frac{\partial G_{\mathrm{real}}}{\partial N_{\mathrm{d}}} = \mu_{\mathrm{d}} \tag{3.8}$$

The chemical potential describes the incremental change of Gibbs energy when adding or removing a point defect to the crystal. In this regard, a high chemical potential of a point defect corresponds to a steep increase in Gibbs energy and therefore indicates how much this defect is "disliked" by the crystal.[34] Or similarly, a defect with a high chemical potential present in the crystal, will have a high tendency to change its chemical environment, for example by diffusion or segregation processes, in order to lower the total Gibbs energy of the crystal. The general form of the chemical potential of a point defect can be obtained by differentiating equation 3.6 with respect to N_{d}, thereby inheriting the assumption of non-interacting defects.

$$\begin{aligned}
\mu_{\mathrm{d}} &= \frac{\partial}{\partial N_{\mathrm{d}}} N_{\mathrm{A}}\, G_{\mathrm{perf}} + \frac{\partial}{\partial N_{\mathrm{d}}} N_{\mathrm{A}}\, \Delta_{\mathrm{f}}^{0} G_{\mathrm{d}}\, N_{\mathrm{d}} - \frac{\partial}{\partial N_{\mathrm{d}}} T\, N_{\mathrm{A}}\, k_{\mathrm{B}}\, \ln \Omega \\
&= N_{\mathrm{A}}\, \Delta_{\mathrm{f}}^{0} G_{\mathrm{d}} - \frac{\partial}{\partial N_{\mathrm{d}}} RT\, \ln \Omega \\
&= \mu_{\mathrm{d}}^{0} - \frac{\partial}{\partial N_{\mathrm{d}}} RT\, \ln \Omega
\end{aligned} \tag{3.9}$$

with $N_{\mathrm{A}}\, \Delta_{\mathrm{f}}^{0} G_{\mathrm{d}} = G_{\mathrm{m}}^{0} = \mu_{\mathrm{d}}^{0}$. The number Ω of distinguishable combinations for the defects in the crystal, is given by the binomial coefficient with N_{d} defects distributed on N regular lattice sites.

$$\Omega = \binom{\text{number of lattice sites}}{\text{number of point defects}} = \binom{N}{N_{\mathrm{d}}} = \frac{N!}{N_{\mathrm{d}}!(N - N_{\mathrm{d}})!} \tag{3.10}$$

Using the Stirling's approximation $\ln x! = x \ln (x) - x$ to eliminate the factorials in equation 3.10 and inserting into equation 3.9 then leads to the general form of the chemical potential for point defects.

$$\mu_{\mathrm{d}} = \mu_{\mathrm{d}}^{0} + RT\, \ln \frac{N_{\mathrm{d}}}{N - N_{\mathrm{d}}} \tag{3.11}$$

An important conclusion of the above derivation is that the enthalpy and vibrational entropy change required to form a single defect are embedded in the standard, concentration-independent term of the chemical potential, μ_{d}^{0}. Equation 3.11 can be further simplified by assuming that the number of defects is very small compared to that of regular lattice sites $N_{\mathrm{d}} << N$, and by using defect concentrations $c_{\mathrm{d}} = \frac{N_{\mathrm{d}}}{N}$, giving

$$\mu_d = \mu_d^0 + RT\ \ln c_d \tag{3.12}$$

The thermodynamic treatment of point defects in crystals outlined above is to a large extent analogous to the description of ideal dilute solutions. For example, the chemical potential of a substance in an ideal dilute solution is composed of a standard term representing the chemical potential of the pure substance and a term which depends on the concentration of the substance. This formalism is equivalent to equation 3.12 and holds for small concentrations of the substance in the solution. Following this terminology, point defects are commonly referred to as *ideal dilute* when the Gibbs energy of forming a single defect is independent on the concentration of defects already present in the crystal.

3.2 Point defect interactions

At concentrations exceeding the limit of ideal dilution, point defects begin to experience interactions between them, requiring a correction of their thermodynamic description. For example, the Gibbs energy of a crystal will increase more steeply upon introducing a defect than would be expected from ideal dilute behavior, when there is a repulsive interaction acting on the introduced species. The formal procedure for describing such deviations is to replace the concentration c_{d} of a defect by an effective concentration, termed activity. The activity of a defect is given by the product of the concentration and an activity coefficient γ_{d}.

$$\mu_{\mathrm{d}} = \mu_{\mathrm{d}}^{0} + RT\ \ln \gamma_{\mathrm{d}}\, c_{\mathrm{d}} = \mu_{\mathrm{d}}^{0} + RT\ \ln \gamma_{\mathrm{d}} + RT\ \ln c_{\mathrm{d}} \tag{3.13}$$

In the case of a repulsive interaction acting on the defects, the activity coefficient would take a value $\gamma_{\mathrm{d}} > 1$. This results in a lower gain in configuration entropy with N_{d}, pushing the minimum in G_{real} to lower defects concentrations (figure 3.2a). Using equation 3.13 means that all deviations from ideal behaviour resulting from defect interactions must be captured by the activity coefficients, whereby the standard chemical potential

μ_{d}^{0} remains unchanged. Activity coefficients are therefore often difficult to find, but can be described, for example, with the Debye-Hückel theory or empirical power laws.[34] In addition to the energetic defect interactions, the number of available lattice sites N eventually becomes exhaustible, so that the constraint $N_{\mathrm{d}} << N$ loses its validity and the concentration-dependent term must be described by the explicit form given in equation 3.11. Provided that correct activity coefficients are available, the equilibrium concentration of interacting point defects can be obtained with this approach, as shown in figure 3.2a.

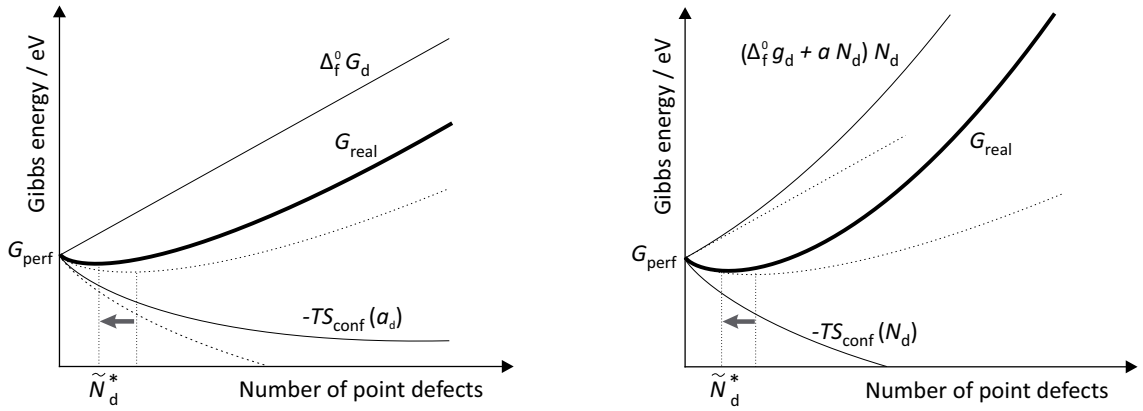

(a) Activity approach

(b) First order correction

Figure 3.2: Thermodynamic treatments of point defect interactions. Dashed lines represent ideally dilute behavior. The equilibrium number of interacting point defects is given by $\tilde{N}_{\mathrm{d}}^{*}$.

In the present work, the activity coefficient term ($RT \ln \gamma_{\mathrm{d}}$) is approximated using an approach referred to as "first-order correction". This approach is based on expanding the Gibbs energy required to form a single defect as a power series, according to

$$\Delta_{\mathrm{f}}^{0} G_{\mathrm{d}} = \Delta_{\mathrm{f}}^{0} g_{\mathrm{d}} + a_{\mathrm{d}}\, c_{\mathrm{d}} + b_{\mathrm{d}}\, c_{\mathrm{d}}^{2} + c_{\mathrm{d}}\, c_{\mathrm{d}}^{3} + ..., \tag{3.14}$$

where the coefficients a_{d}, b_{d}, c_{d} represent the concentration-dependent deviations from ideal behaviour. The concentration c_{d} on which $\Delta_{\mathrm{f}}^{0} G_{\mathrm{d}}$ depends does not necessarily have to be the concentration of the defect to be formed, but can also be that of another species. In cases in which the entropy follows the ideal behavior and enthalpy deviations depend approximately linear on the concentration, the power series can be truncated after the first order, and the defect interactions are described by a "first-order-correction" of the formation enthalpy

$$\Delta_{\mathrm{f}}^{0} H = \Delta_{\mathrm{f}}^{0} h + a_{\mathrm{d}}\, c_{\mathrm{d}} \tag{3.15}$$

where the coefficient a_{d} introduced in this way can be considered an interaction parameter, according to which positive values indicate repulsive interactions and negative values indicate attractive interactions. The chemical potential of the interacting defect reads accordingly,

$$\mu_{\mathrm{d}} = \mu_{\mathrm{d}}^{0} + a_{\mathrm{d}}\, c_{\mathrm{d}} + RT\ \ln c_{\mathrm{d}} \tag{3.16}$$

where the term $a_{\mathrm{d}} c_{\mathrm{d}}$ has replaced the activity coefficient term of equation 3.13. The modified dependence of the Gibbs energy of defect formation is shown in figure 3.2b. The first-order correction is used in the present thesis to describe defect interactions with respect to the formation of oxygen vacancies and protonic defects. This approach is used for several reasons: (i) the interaction parameter a_{d} can be calculated with DFT, (ii) the interaction parameter can, in certain cases, be compared to experimentally determined values, and (iii) this method allows a detailed understanding of defect interactions and can help to extract the major determinants that govern defect concentrations beyond dilute conditions. Comparing the two figures 3.2a and 3.2b shows that both approaches may yield the same equilibrium concentration of interacting point defects, if the activity coefficient γ and the interaction parameter a correctly capture the defect interactions. In addition to the formalisms mentioned here for describing defect interactions, there are several other approaches. In cases, when defect interactions are subtle, the deviation from ideal dilute behavior can be described in terms of the Debye-Hückel theory[36] in which the defect formation enthalpy scales with $c_{\mathrm{d}}^{\frac{1}{2}}$ rather than having a linear dependence. At higher defect concentrations, the Debye-Hückel theory eventually loses its validity and deviations from ideal behavior are often better described by the so-called cube-root-law[37], according to which the defect formation enthalpy scales with $c_{\mathrm{d}}^{\frac{1}{3}}$. Despite the physical justifications of both the Debye-Hückel and the cube-root-law, it has been observed that in many materials, including iron-containing perovskites, the defect interactions are well described by a first-order correction according to equation 3.15.[14,38] A specific case of defect interaction occurs when point defects pair up to so-called defect associates. The defect associates themselves may then behave as dilute particles and can be assigned a new set of chemical potentials, see[34] for further information.

4 First-Principles Approaches to Point Defects

The study of defect chemistry at the atomic level is extremely cumbersome with experimental techniques. Meanwhile, with modern computational resources and developments in electronic structure methods, it has become increasingly fruitful to study the defect chemistry of a material from first-principles, e.g., using DFT. This chapter provides the conceptual link between first-principles DFT calculations (described in § 2) and the defect chemistry of a material (described in § 3).

4.1 First-principles thermodynamics

The macroscopic thermodynamic properties of crystals that were introduced in the previous chapters (e.g. G_{real}) can be identified with microscopic, physical quantities calculated by means of DFT for a periodically repeated unit cell. The thermodynamic state function describing a system under conditions that are accessible by DFT is the Helmholtz free energy as a function of volume and temperature $F(V,T)$, because DFT calculations are carried out for a fixed volume, typically at zero Kelvin. Within the adiabatic approximation it is argued that electronic excitations and lattice vibrations occur on different time scales, allowing to separate the Helmholtz free energy into an electronic and a vibrational part.[39]

$$F(V,T) = F^{\mathrm{el}}(V,T) + F^{\mathrm{vib}}(V,T) \tag{4.1}$$

The electronic part of the Helmholtz free energy is given by

$$F^{\mathrm{el}} = U^{\mathrm{el}} - TS^{\mathrm{el}} \tag{4.2}$$

where U^{el} is the internal electronic energy of the system and S^{el} the electronic entropy. At zero Kelvin, the internal energy corresponds to the DFT total energy, E^{tot}, defined in equation 2.4 and F^{el} is directly obtained with a DFT calculation. At temperatures above absolute zero, electrons can be thermally excited to unoccupied crystal orbitals following a Fermi-Dirac distribution. The number of occupied states at a given temperature is then obtained by the product of the Fermi-Dirac distribution and the density of available

states. [i] With increasing temperature, F^{el} consequently changes due to the occupied crystal orbitals of higher energy (U^{el}) and the increase in configurational entropy associated with the occupation of the various electronic states (S^{el}). The effect of temperature on the electronic free energy at conditions that are relevant for electrochemical applications is, however, usually small for systems having a bandgap or a rather low density of states at the Fermi level. For instance, F^{el} of $BaFeO_3$ changes by only 0.05 eV at $T = 1500\ K$, with a negligible contribution of the electronic configurational entropy.[ii] The vibrational part of the Helmholtz free energy is given by

$$F^{\mathrm{vib}} = U^{\mathrm{vib}} - TS^{\mathrm{vib}} \tag{4.3}$$

where U^{vib} is the vibrational internal energy and S^{vib} the vibrational entropy. At elevated temperatures, the ions in the crystal begin to oscillate around their equilibrium positions resulting in collective vibrational motions. These are generally treated as quantized elastic waves, called phonons, that propagate along certain directions in the crystal with an energy that is related to the frequency of the wave. The excitation of different phonon modes in thermal equilibrium follows a Bose-Einstein distribution. A detailed description on the calculation of vibrational frequencies in crystals can be found in ref.[41]. With rising temperature, lattice vibrations increase and more phonons become excited. Their contribution to the Helmholtz free energy, F^{vib}, is given by the sum over the phonon energies (U^{vib}) and the change in vibrational entropy S^{vib}. The latter is associated with the increase in configurational disorder when lattice vibrations are distributed over the thermally accessible phonon modes governed by the Bose-Einstein distribution. Vibrational excitations can make up a significant part of the total Helmholtz free energy at conditions relevant for electrochemical applications. In case of $BaFeO_3$, F^{vib} changes by 3.05 eV at $T = 1500$ K, where the vibrational internal energy U^{vib} contributes +1.93 eV and the vibrational entropy TS^{vib} contributes -4.98 eV. [iii] However, *changes* in F^{vib} caused by the presence of point defects are much smaller as they typically occur in small concentrations without substantially altering the crystalline host.

Having deduced the Helmholtz free energy in terms of physical quantities, which can

[i] Formally the DOS is temperature dependent and should be calculated with finite temperature DFT. It was found, however, that the variation of the DOS with temperature is generally small, which justifies the use of the zero Kelvin DOS in conjunction with a Fermi-Dirac distribution.[40]

[ii] Computational details are given in appendix § A.1. The change in U^{el} is estimated by imposing a Fermi-Dirac distribution on the calculated density of states, and integrating the area of the excited states. The electronic entropy is calculated with $S^{\mathrm{el}} = -k_{\mathrm{B}} \int n(E)[f \ln(f) + (1-f)\ln(1-f)]dE$

[iii] Computational details are given in appendix § A.1. Vibrational frequencies were calculated within the harmonic approximation using the Phonopy code[42], see § A.3.

be calculated from first-principles, provides access to other thermodynamic state functions. The Gibbs energy, previously introduced as a measure for determining the stability of point defects (§ 3), describes a system's state at constant pressure and temperature. In order to transform the Helmholtz free energy into the Gibbs energy, the relationship between pressure and volume needs to be considered, which yields

$$G(p,T) = F + pV \tag{4.4}$$

When dealing with changes in Gibbs energy, equation 4.4 becomes $\Delta G = \Delta F + p\Delta V + V\Delta p$. During structure optimization of a DFT calculation, the cell volume is either fixed ($\Delta V = 0$) or allowed to change, under the condition of constant pressure ($\Delta p = 0$). In this thesis, constant pressure conditions are used exclusively, and finite changes in Gibbs energy reduce to

$$\begin{aligned} \Delta G &= \Delta F + p\Delta V \\ &= \Delta U - T\Delta S + p\Delta V \\ &= \Delta H - T\Delta S \\ &\approx \Delta E^{\mathrm{tot}} - T\Delta S + p\Delta V \end{aligned} \tag{4.5}$$

assuming that changes in the internal energy are largely represented by changes in the total energies. The present work focuses on the calculation of ΔE^{tot} for defect chemical reactions at absolute zero temperature, where $\Delta U = \Delta E^{\mathrm{tot}}$.

4.2 Defect formation energy

The defect formation energy, $\Delta_{\mathrm{f}} E_{\mathrm{d}}$, is defined as the energy required to form a single defect in the crystal and can be calculated by DFT through

$$\Delta_{\mathrm{f}} E_{\mathrm{d}} = \sum_{\text{products } i} \nu_i E^{\mathrm{tot}} - \sum_{\text{reactants } j} \nu_j E^{\mathrm{tot}} \tag{4.6}$$

where ν are the stoichiometric coefficients of the products and reactants in a defect reaction, and E^{tot} are their total energies which are calculated with DFT. The total energies of the defect containing and the complementary defect free crystals are thereby obtained

from supercell calculations. To be more specific, $2 \times 2 \times 2$ neutral supercells are used in the present work in which oxygen vacancies or protonic defects are accommodated. Total energies of gas phase molecular species are calculated by placing the molecule in a large vacuum box that precludes interactions with the periodic images of the molecule. For the formation of an oxygen vacancy according to reaction 3.1, this results in the following expression

$$\Delta_{\mathrm{f}} E_{\mathrm{v}_{\mathrm{O}}^{\bullet\bullet}} = \left(E^{\mathrm{tot}}(\mathrm{v}_{\mathrm{O}}^{\bullet\bullet}) + \frac{1}{2} E^{\mathrm{tot}}(\mathrm{O}_2) \right) - E^{\mathrm{tot}}(\mathrm{perf}) \tag{4.7}$$

where $E^{\mathrm{tot}}(\mathrm{v}_{\mathrm{O}}^{\bullet\bullet})$ corresponds to a supercell containing an oxygen vacancy, and $E^{\mathrm{tot}}(\mathrm{perf})$ to the defect-free (perfect) supercell containing electron holes. A graphical representation of equation 4.7 is given in figure 4.1 for the formation of an oxygen vacancy in $BaFeO_3$.

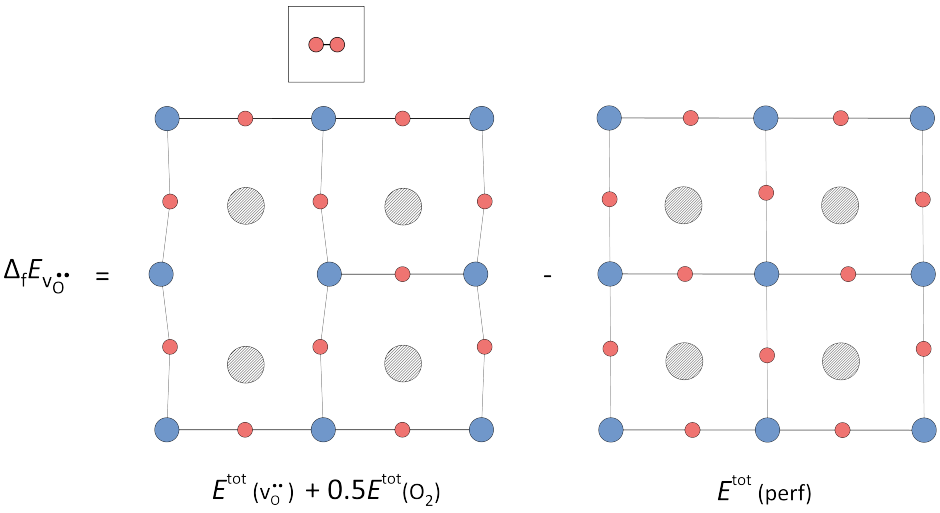

Figure 4.1: Graphical representation of equation 4.7 with oxygen shown as red, iron as blue, and Ba as hatched balls.

The defect formation energy of a protonic defects reads accordingly,

$$\Delta_{\mathrm{f}} E_{\mathrm{OH}_{\mathrm{O}}^{\bullet}} = E^{\mathrm{tot}}(\mathrm{OH}_{\mathrm{O}}^{\bullet}) - \left(E^{\mathrm{tot}}(\mathrm{perf}) + \frac{1}{2} E^{\mathrm{tot}}(\mathrm{H}_2) \right) \tag{4.8}$$

From the formation energies of individual defects, the *reaction* energies of more complex defects can be obtained. This applies, for instance, to the hydration reaction describing the dissociative incorporation of an H_2O according to reaction 3.3. The hydration energy is given by,

$$\Delta_\mathrm{r} E_{\mathrm{H_2O}} = 2\Delta_\mathrm{f} E_{\mathrm{OH}^\bullet_\mathrm{O}} - \Delta_\mathrm{f} E_{\mathrm{v}^{\bullet\bullet}_\mathrm{O}} \tag{4.9}$$

where the hydration energy is decomposed into the filling of an oxygen vacancy, $-\Delta_\mathrm{f} E_{\mathrm{v}^{\bullet\bullet}_\mathrm{O}}$, and twice the formation of a proton interstitial, $2\Delta_\mathrm{f} E_{\mathrm{OH}^\bullet_\mathrm{O}}$.

4.3 Calculation of defect interactions

In an ideal dilute system, defect formation energies are assumed to be independent of the concentration of defects already present in the crystal. This means that defects are too far apart from each other to experience any noticeable interaction. However, if the limit of ideal dilution is exceeded, the defect formation energies differ by an amount representing the defect interaction. Within a first-order correction, the defect formation energy becomes,

$$\Delta_\mathrm{f} E_\mathrm{d} = \Delta_\mathrm{f} e_\mathrm{d} + a_\mathrm{d}\, c_\mathrm{d} \tag{4.10}$$

where a_d is the defect interaction parameter. To study potential defect interactions, the defect formation energy is calculated as a function of defect concentration by subsequently increasing the number of defects in the supercell. If defect interactions are negligible, the defect formation energy remains constant. If the defect formation energy increases approximately linearly as a function of c_d, the first-order correction can be applied and the quantities $\Delta_\mathrm{f} e_\mathrm{d}$ and a_d are obtained from linear fitting. With respect to the oxygen vacancy formation in $BaFeO_{3-\delta}$ in the present work, supercells with the stoichiometry $Ba_8Fe_8O_{24}$ are used in which up to four vacancies are accommodated. On this basis, the oxygen vacancy formation energies are calculated for the first, second, third and fourth oxygen vacancy, e.g. according to

$$\mathrm{Ba_8Fe_8O_{23}} \rightleftharpoons \mathrm{Ba_8Fe_8O_{22}} + \frac{1}{2}\mathrm{O_2} \tag{4.11}$$

for which the reaction energy, expressed using abbreviated sum formulae, reads

$$\Delta_\mathrm{f} E_{\mathrm{v}^{\bullet\bullet}_\mathrm{O},\mathrm{O_{22}}} = \left(E^\mathrm{tot}(\mathrm{O_{22}}) + \frac{1}{2}E^\mathrm{tot}(\mathrm{O_2})\right) - E^\mathrm{tot}(\mathrm{O_{23}}) \tag{4.12}$$

In practice, the presence of multiple vacancies per supercell requires their distribution over the available oxygen sites, which can lead to a large number of different configurations. These configurations can be found "by hand" only in the most simple cases, i.e. for one or two vacancies distributed over 24 possible sites. For more than two vacancies, the *supercell* code[43] was used, which can detect all distinguishable configurations in a supercell of given stoichiometry. Similarly, the present work investigates the energy of hydration (reaction 3.3) as a function of oxygen vacancy concentration. For example, equation 4.13 describes the hydration of an oxygen-deficient system

$$\mathrm{Ba_8Fe_8O_{23}} + \mathrm{Ba_8Fe_8O_{22}} + \mathrm{H_2O} \rightleftharpoons 2\mathrm{Ba_8Fe_8O_{23}H} \tag{4.13}$$

The corresponding reaction energy represents the hydration energy, $\Delta_{\mathrm{r}}E_{\mathrm{H_2O,O_{22.5}}}$, in an oxygen non-stoichiometric system. In terms of a unit cell sum formula, this becomes $\mathrm{BaFeO_{3-\delta}}$, with $\delta = \frac{1.5}{8} = 0.19$.

4.4 Thermochemical cycles of defect reactions

The formation of a point defect from an external reservoir comprises several partial reactions, which together form the overall reaction. These typically involve the transfer of the atomic species into the crystalline host, and the redistribution of electrons to or away from the introduced species, rendering the point defect effectively charged. By reason of energy conservation, the energy change of the overall defect reaction can be re-formulated as the sum of the energy changes of the partial reactions into which the overall reaction can be divided. Quantifying the energy changes of the partial reactions, and constructing a complete thermochemical cycle of the defect reaction, is imperative to understand the physical origins of the overall reaction energy. A good example to study the energetics of partial reactions, and to outline the technical difficulties in their determination, is the formation of a proton interstitial, $\mathrm{OH_O^\bullet}$, in a solid oxide according to

$$\mathrm{O_O^x} + \frac{1}{2}\mathrm{H_2} + \mathrm{h^\bullet} \rightleftharpoons \mathrm{OH_O^\bullet} \tag{4.14}$$

During structural and electronic relaxation, the electron of the incorporated neutral hydrogen atom redistributes into the valence band, thereby annihilating an electron hole. As a result, the energy change of reaction 4.14 contains the energy difference in E_{HOMO} of the molecular hydrogen and E_{VBM} of the solid. In addition to this *electronic* contribution,

the energy change of reaction 4.14 comprises the incorporation of the charged species into the crystal and the associated electrostatic interactions in the vicinity of the defect. This, purely ionic partial reaction is usually referred to as the ion affinity of the solid, or, in this particular case, the proton affinity (PA). In other words, the formation of an $OH_O^\bullet$ with respect to neutral molecular hydrogen consists of an electronic (red-ox) and an ionic (acid-base) component.

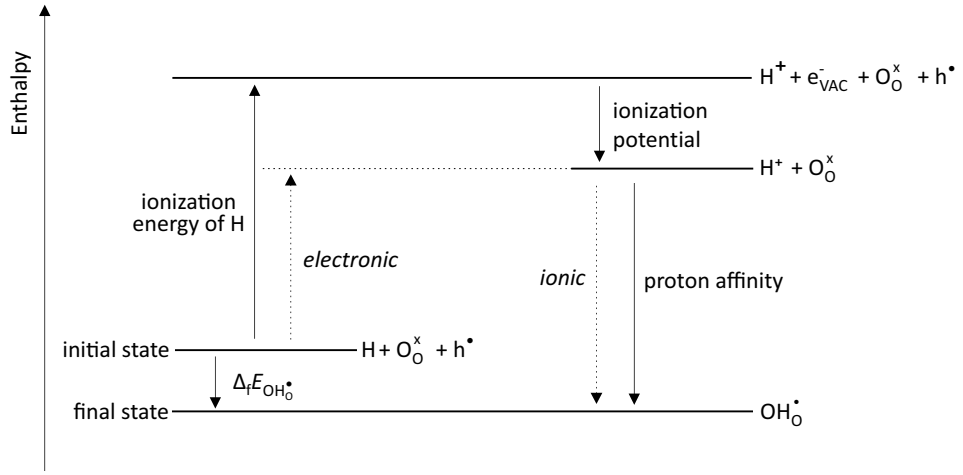

Figure 4.2: Thermochemical cycle showing electronic and ionic contributions to the defect formation energy. The ionization energy of hydrogen is taken as tabulated value.

The **electronic contribution** to the defect formation energy of reaction 4.14 cannot directly be calculated from the difference in E_{HOMO} and E_{VBM}. As described in more detail in appendix § B.2, the energy zero-points for the energy levels (e.g. band edges) of a calculation based on periodic boundary conditions is system-dependent. This means that band edges of different materials can not be compared to each other unless the energy zero-points of the materials are aligned to a common reference point. One possibility to achieve this, is to align them to the electrostatic potential at vacuum through separate surface slab calculations of the respective materials (see appendix § B.2 for details of surface slab calculations). When the energy zero-point is aligned to vacuum, the E_{VBM} of a solid is given by the ionization potential (IP), i.e., the energy difference between vacuum and the valence band maximum. Finally, the difference in E_{HOMO} and aligned E_{VBM} is obtained as the difference in ionization energies of molecular hydrogen and the solid under consideration, and can be embedded in a thermochemical cycle (figure 4.2).

Having separated the electronic contribution, the **ionic contribution**, in this case the proton affinity (PA), can indirectly be determined via a combination of all other terms in the thermochemical cycle (figure 4.2).

$$-\,\mathrm{PA} = \Delta_\mathrm{f} E_{\mathrm{OH}^\bullet_\mathrm{O}} + E_{\mathrm{Ion,H}} - E_\mathrm{IP} \tag{4.15}$$

where a negative sign stands for energy gain and a positive sign for energy costs. In fact, a direct determination of ion affinities by DFT in a "products-minus-reactants" fashion is inhibited by the fact that total energies of charged molecular species in vacuum boxes cannot be calculated. For instance, the total energy of an $H_2{}^+$ molecule in a vacuum box increases with respect to the volume of the vacuum box, without converging to a constant energy value at large volumes. The charged molecule is so poorly screened by the "empty" box that electrostatic interactions with its periodic images cannot be excluded in boxes of achievable volumes. However, embedding a particular ion affinity in a thermochemical cycle, e.g. the one in figure 4.2, allows the energy change of such a reaction to be quantified indirectly. This procedure for determining ion affinities using DFT can be found in[44] and was developed as part of this work in collaboration with the University of Oslo.

Combining both electronic and ionic partial reactions naturally yields the defect formation energy. It should be noted that defect formation energies are commonly calculated without decomposition into the individual partial reactions, and without aligning the valence band maximum of the solid under consideration to the vacuum potential. The unaligned valence band maximum of the solid does, however, not affect the overall energy change of a reaction in which charged defects are formed with respect to neutral atoms or molecules. It merely leads to a different weighting of electronic and ionic contributions. This becomes evident by considering the thermochemical cycle in figure 4.2, where a shift in the position of the valence band maximum would only change the proportions of the arrows "ionization potential" and "proton affinity". In conclusion, defect formation energies of charged species by exchange of neutral atoms can be readily calculated with unaligned valence band maxima. A decomposition into electronic and ionic contributions, on the other hand, requires the alignment of E_VBM to a universal reference.

4.5 Energy level diagrams

A calculated electronic structure can be visualized in various ways, among them the well known band structure diagram or the density of states curve. However, it is sometimes useful to display only the most salient features of the electronic structure in the condensed form of an energy level diagram. Figure 4.3 shows, e.g., the energy level diagram of an intrinsic semiconductor aligned with respect to the vacuum potential. In

such a diagram, only the energy levels of frontier crystal orbitals (VBM, CBM), and other common characteristics of band structures like band widths of the ionization potential are shown. As some of the terminologies used in connection with energy level diagrams are often used in a somewhat ambiguous manner, they will be briefly defined here.

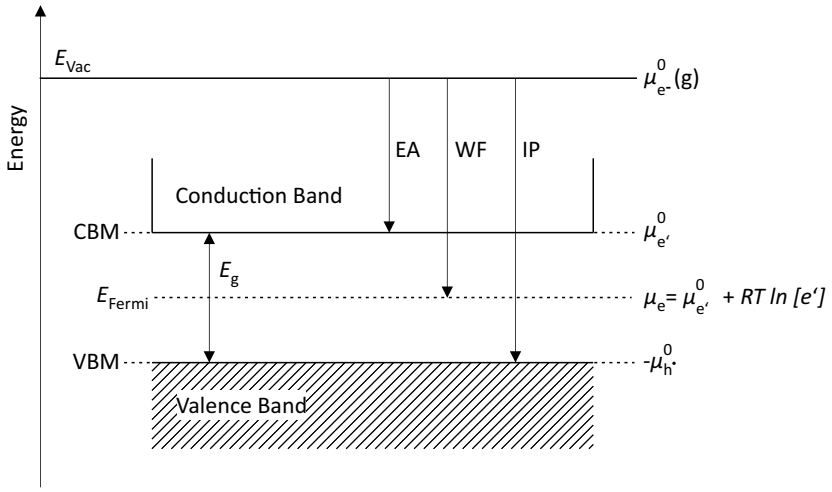

Figure 4.3: Electronic energy level diagram

The **Fermi level**, E_{Fermi}, and the **chemical potential of the electron**, $\mu_{\mathrm{e}'}$, can be used interchangeably and describe an energy level with a 50% probability of occupation, serving as inflection point of the Fermi-Dirac distribution function. In the context of semiconductors, the position of the Fermi level is somewhere in the band gap to ensure that the number of excited electrons in the conduction band equals the number of electron holes in the valence band. In that case, the Fermi level is merely a hypothetical energy level since there are no actual energy levels in the band gap. The Fermi level is temperature dependent and approaches a value precisely in the middle of the band gap at $T \rightarrow 0$.[41,45,46] In the case of metals, E_{Fermi} or $\mu_{\mathrm{e}'}$ lies at the top of a partially filled band and thus coincides with an actual energy level. The zero Kelvin extrapolate of that value is called the Fermi energy. It represents the highest occupied state in a metal in the ground state and separates the filled from the empty states.[41,45] The term "Fermi energy" is sometimes used as a synonym for Fermi level, in the context of semiconductors. In a thermodynamically strict sense, the chemical potential of the electron represents the (free) energy change of the system with respect to adding or removing an electron and is composed of a standard term and a concentration dependent term. For semiconductors, the standard chemical potential of the electron can be identified with the bottom of the conduction band, E_{CBM}, provided that standard conditions refer to the ground state at 0 K.[34,46]

$$\mu_{\mathrm{e}'} = E_{\mathrm{CBM}} + RT \ln \frac{N_{e'}}{\bar{N}_{CB}} = \mu^0_{\mathrm{e}'} + RT \ln [e'] \tag{4.16}$$

where the number of electrons in the conduction band, $\frac{N_{e'}}{\bar{N}_{CB}}$, is given by Fermi-Dirac statistics.

The **vacuum level** is defined as the energy of an electron at the electrostatic potential of vacuum with zero kinetic energy. From a thermodynamic point of view, the vacuum level can be considered as the standard chemical potential of an electron in vacuum. It is often customary to draw the vacuum level in energy level diagrams of heterointerfaces (e.g. Schottky barriers) parallel to the band bending at the interface. This should be understood only as an auxiliary level describing the electric potential across the interface. An offset in the vacuum potential between two adjacent materials simply visualizes that charge was redistributed in order to equalize the Fermi levels, which led to a uniform shift of the bulk levels. The energy required to excite an electron to vacuum far away from the interface is still equal to the ionization energy of the bulk crystal. However, if the electron at vacuum were hypothetically moved across the interface, an additional amount of work would have to be performed to overcome the interface dipole.[41,46] The **work function** is defined as the energy difference between E_{Vac} and E_{Fermi}. While for semiconductors the Fermi level is a purely statistical concept, for metals the work function represents the minimum energy required to remove an electron from the bulk to vacuum.[41] The **ionization potential** (IP) is defined as the energy difference between E_{Vac} and E_{VBM}. It represents the minimum energy to remove an electron from a semiconductor.[47] In metals, work function and ionization potential are the same.

The concept of displaying chemical potentials in the form of an energy level diagram can be generalized to ionic defects.[34] The process of exciting an electron to the conduction band and leaving behind a hole in the valence band can be considered an electronic disorder reaction, in which the standard Gibbs reaction energy is given by the band gap, or equivalently, the difference in standard chemical potentials of the electron and the hole. The Fermi level then governs the extent of that disorder reaction at a given temperature, granting equal concentrations of excited electrons in the conduction band and holes in the valence band. In analogy to the energy levels of an electronic disorder reaction, the respective energy levels of an ionic (Frenkel) disorder reaction can be drawn (figure 4.4). For example, the standard Gibbs reaction energy of forming an oxygen interstitial by displacing a regular oxide ion, and creating a vacancy at the original site, is given by the difference in standard chemical potentials of the oxygen interstitial and the oxygen vacancy. The *ionic* Fermi level then governs the extent of this disorder reaction ac-

cording to a Fermi-Dirac distribution. The difference to the electronic Fermi level is that the densities of states for interstitials and vacancies are given by the number of available interstitial and regular sites, thus obeying a "site exclusion" instead of a Pauli exclusion as for electrons.[34]

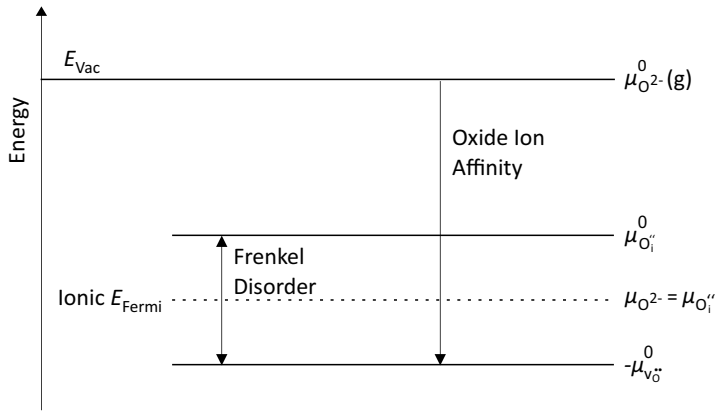

Figure 4.4: Ionic energy level diagram

The chemical potentials of the ions can be aligned to a universal reference by using the solid's affinity to in- or excorporate a particular ion with respect to vacuum. For example, the standard chemical potential of an oxygen vacancy, aligned to vacuum, is given by the oxide ion affinity (OA), defined as: $\mathrm{v}_\mathrm{O}^{\bullet\bullet} + \mathrm{O}^{2-} \rightarrow \mathrm{O}_\mathrm{O}^\mathrm{x} \mid \Delta E = \mathrm{OA}$. Aligned ionic Fermi levels allow the study of a variety of fundamental (electro)chemical problems. In[48], the difference in the standard chemical potentials of a particular defect between two individual materials was used to predict the segregation energy at a potential interface. Furthermore, the chemical potential of an exchangeable ion, or the standard chemical potentials of the respective defects, has been suggested to reflect the ion acidity or basicity of the solid.[49,50] Materials of a different particular ion acidity will naturally react in an acid-base reaction to equalize their ionic Fermi-levels through a flow of ions from one material to the other.

The electronic and ionic energy level diagrams can also be merged into a single representation - a coupled electronic-ionic energy level diagram (figure 4.5). The standard chemical potentials of the electron and the oxide ion at vacuum need not necessarily coincide; they are linked via the relation $\mu^0_\mathrm{O} = \mu^0_{\mathrm{O}^{2-}} - 2\,\mu^0_{\mathrm{e}^-}$. The general concept of such coupled electronic-ionic energy level diagrams was derived in[51]. In the present work, the oxide ion affinities of different materials were calculated using first-principles DFT calculations and the concept of thermochemical cycles. Figure 4.5 is a schematic, but is intended to visualize that oxide ion affinities are typically much larger (-17.4 eV in $BaFeO_3$) than electron affinities (-6.2 eV in $BaFeO_3$).

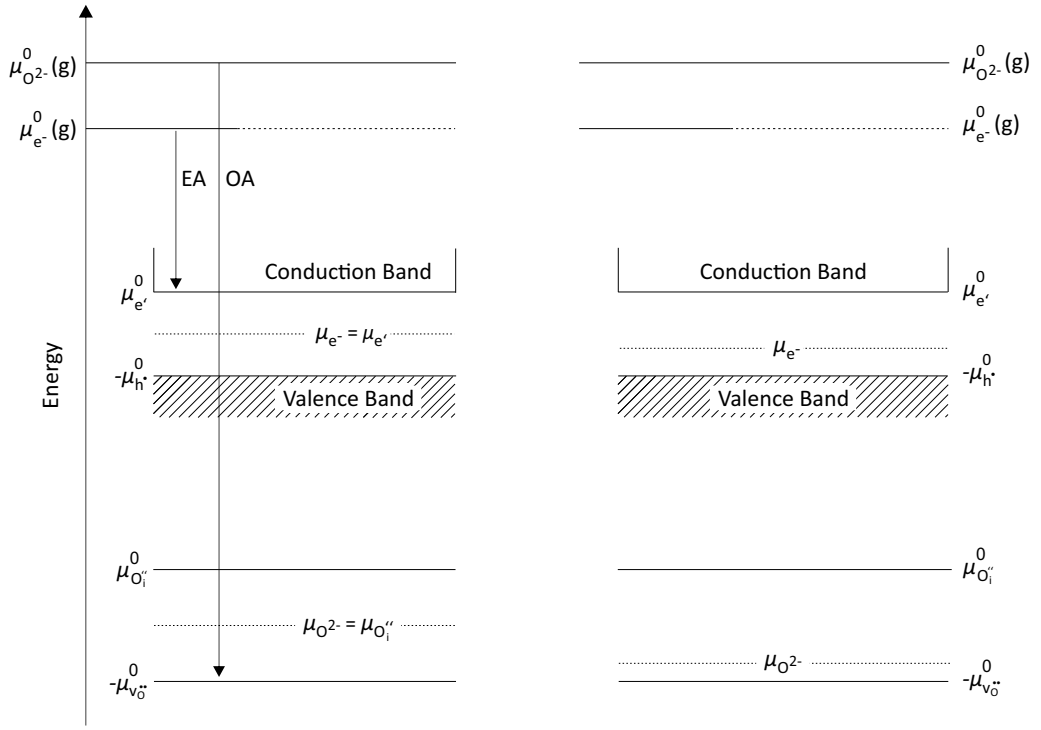

(a) Intrinsic **(b)** Acceptor doped

Figure 4.5: Coupled electronic-ionic energy level diagrams of an undoped and acceptor-doped semiconductor without contact. Both materials are equilibrated to the same oxygen partial pressure. Coupled electronic-ionic energy level diagrams without vacuum as a common energy reference were derived in [51].

In the case of an intrinsic semiconductor, both electronic and ionic Fermi levels are exactly in the middle of the respective band gaps. As temperature increases, electrons are excited into the conduction band and oxide ions are lifted into interstitial lattice sites, leaving behind vacancies at the original sites. The concentrations of electronic and ionic defects are governed by Fermi-Dirac distribution functions, and are high in situations where the distance between the chemical potential and the band edge is small. The individual distribution functions are thereby coupled to meet the condition of charge neutrality (figure 4.5a). In an acceptor-doped semiconductor, the electronic and ionic Fermi levels shift to compensate for the introduced dopants. These shifts are coupled through the condition $\mu_{\mathrm{O}} = \mu_{\mathrm{O}^{2-}} - 2\mu_{\mathrm{e}^-}$, where μ_{O} must remain constant due to the external partial pressure of oxygen. This condition causes $\mu_{\mathrm{O}^{2-}}$ to shift twice as much as μ_{e^-} due to the different charges of O^{2-} and e^-. Whether the acceptor doping is compensated for by ionic or electronic defects then depends on the distance between Fermi levels and band edges, i.e. the electronic and ionic band gaps (figure 4.5b).

When the two materials of figure 4.5 are contacted, an equilibrium is established by redistributing electronic and ionic defects until $\mu_{O^{2-}}$ and μ_{e^-} are equalized. In this particular case, electrons and oxygen interstitials flow from the undoped to the acceptor-doped site, resulting in the formation of an electric field across the interface. This local electric field causes the band edges to bend in the interface region. Far away from the interface, the band edges relative to the Fermi level are the same as in the bulk and are therefore uniformly shifted. The standard chemical potentials of the electron and the oxygen ion in vacuum follow the band bending across the interface. This illustrates how an O^{2-} and an e^- at vacuum (right above the solid) would have to perform different amounts of work upon crossing the interface.

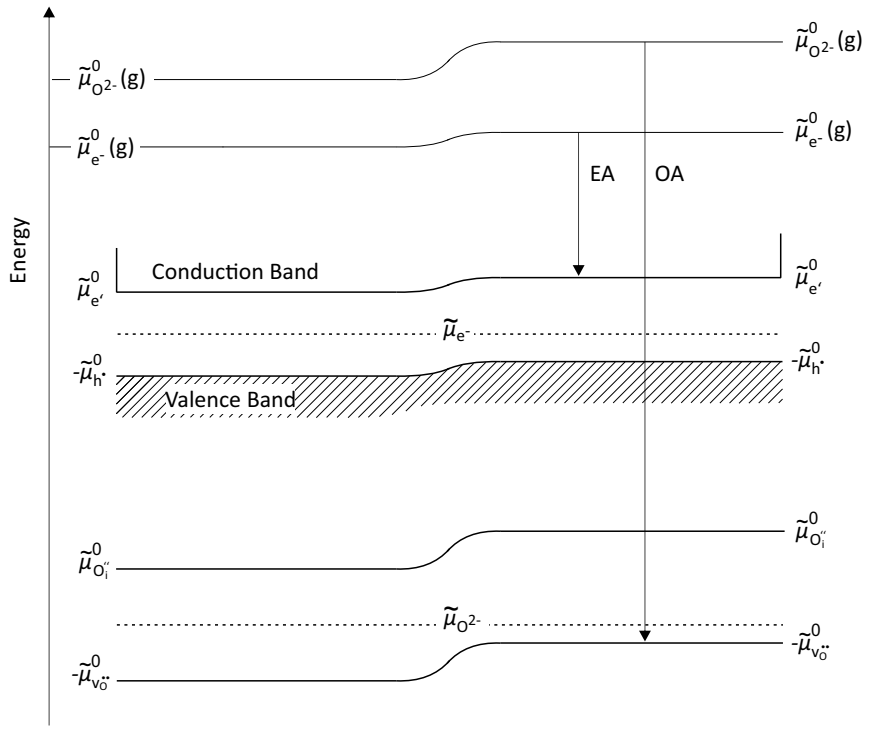

Figure 4.6: Coupled electronic-ionic energy level diagrams across the interface of an undoped and acceptor-doped semiconductor. The formation of electric fields at the interface requires the use of *electro*-chemical potentials, $\tilde{\mu}_i$.

Results and discussion

5 Electronic Structure of Cubic $BaFeO_3$

5.1 Introduction

In this chapter, the electronic structure of cubic $BaFeO_3$ is explored through DFT calculations using local atomic orbitals and a symmetry-based chemical bonding analysis.

In a simple ionic model, the oxidation states in $BaFeO_3$ are Ba^{2+}, Fe^{4+} and O^{2-}, giving local electron configurations of d^4 for the Fe ion and p^6 for the O ion. The ionic model suggests that the O ions have a closed-shell configuration and that the partially filled d-band renders the material electronically conducting. Assuming a high spin configuration - typical for Fe in octahedral coordination with oxygen ligands - the d^4 ions become Jahn-Teller active and a cooperative lattice distortion is expected.

X-ray spectroscopic studies on thin films and first principles calculations, however, have shown that the electronic ground state of cubic $BaFeO_3$ consists of a mixed d^4 and $d^5\underline{L}$ ($\underline{L}$ = ligand hole) configuration, with a dominating $d^5\underline{L}$ character.[1–3] In other words, charge is moved from the oxygen ligands to the Fe, leaving behind electron holes on the oxygen ligands and causing the oxidation state of Fe to approach 3+. A $d^5\underline{L}$ configuration could also naturally explain why, in $BaFeO_3$, no Jahn-Teller distortion has been observed as would be typical for d^4 configurations. Attempts to directly observe the Fe oxidation state via comparing the x-ray spectra of $BaFeO_3$ to Fe^{3+} benchmark materials led to controversial results.[3,52] Since peaks characteristic of Fe^{3+}, which are present in e.g. $LaFeO_3$, are absent in $BaFeO_3$, a Fe valence of 4+ was concluded. The presence of a dominant $d^5\underline{L}$ configuration is, in turn, strongly supported by studies on oxygen deficient $BaFeO_{3-\delta}$. In a density functional study[4], it was found that the occupation of the Fe $3d$ band hardly changes with increasing oxygen deficiency and that mainly O $2p$ holes are populated. A similar, albeit less rigorous conclusion was obtained by comparing x-ray spectra between oxidized and reduced $BaFeO_{3-\delta}$ in a recent study.[53] Both Fe and O states were found to change significantly with oxygen non-stoichiometry reflecting a situation of heavily mixed d^4 and $d^5\underline{L}$ states. The local electron configuration of Fe is also directly linked to the magnetic properties of $BaFeO_3$. In[54], it was found that the magnetic moment of Fe is fairly independent of the oxygen non-stoichiometry, which suggests that mainly oxygen ligand holes are populated upon reduction, in line with a $d^5\underline{L}$ dominated configuration.

Overall, the plethora of both theoretical[4] and experimental[1–3,53,54] studies has produced a consistent picture of the electronic structure of cubic $BaFeO_3$. However, the results are often poorly expressed in chemical terms (orbitals) and lack a systematic bond-

ing analysis of the Fe-O bond. The present study aims to contribute in this direction using DFT calculations of cubic $BaFeO_3$ and analysis in terms of local atomic orbitals. A quantified analysis of the Fe-O chemical bond is carried out using the COHP, supported by group theoretical considerations.

5.2 Crystal Structure

The cubic perovskite structure can be regarded as a network of corner-sharing $[FeO_6]$ octahedra, with linear Fe-O-Fe arrangements (figure 5.1a). The interstices between the octahedra are occupied by the larger barium cations. The primitive unit cell (dashed lines in figure 5.1a) can be defined by the Fe centers of eight octahedral units, with oxygen located on the edges of the cube. Each oxygen is in an axial coordination with two Fe as nearest neighbours.

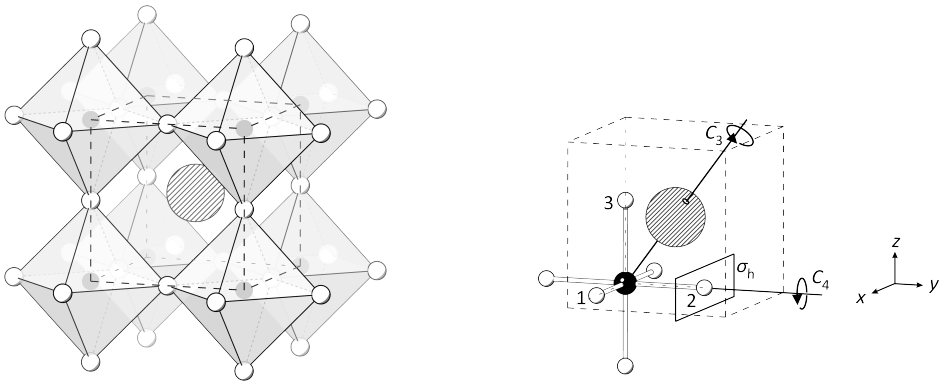

(a) Polyhedral representation **(b)** Unit cell

Figure 5.1: Cubic perovskite crystal structure of $BaFeO_3$. White spheres = O, dark spheres = Fe, hatched sphere = Ba. The oxygen ions are labelled as 1,2 and 3.

Figure 5.1b shows the primitive unit cell containing one formula unit of $BaFeO_3$. The five ions are labeled Ba, Fe, and 1, 2, 3, with the numbers representing the three oxygen ions. The individual ions occupy crystallographic sites of different point symmetry. Oxygen ions reside at sites with the point group D_{4h}, which is characterized by a fourfold rotation axis along the Fe-O-Fe axis and a mirror plane perpendicular to this rotation axis. All symmetry operations of D_{4h} which have an oxygen site as fix point, map all other ions in the crystal to themselves or symmetry-equivalent positions. Since the three oxygen ions are transformed into each other by the threefold rotation axis, they are symmetry-equivalent and belong to a Wyckoff position with a multiplicity of three. Fe

and Ba occupy sites with point group O_h, characterized by threefold rotation axes that the leave the crystal invariant. Since they have no symmetry equivalent positions in the unit cell, they belong to a Wyckoff position with a multiplicity of one. The space group of the simple cubic crystal structure is $\mathrm{Pm\bar{3}m}$ (221). It contains the symmetry operations of the point group O_h (and thus also D_{4h}), as well as translational symmetry operations. The latter reflect the invariance of the crystal under the action of lattice translations and form a subgroup of the space group. The lattice constant of the cubic unit cell was optimized with VASP yielding a value of $a = 4.015$ Å which is in good agreement with the experimental value of 3.97 Å, reported in refs.[3,52,55].

5.3 General characteristics of the electronic structure

The electronic properties of $BaFeO_3$ are largely determined by the Fe $3d$ and O $2p$ orbitals which will form the basis for the analysis of the electronic structure. Orbitals belonging to a particular ion are subject to the local ionic environment at the constituent crystallographic site, which can be described in group-theoretical terms by the site symmetry group. The Fe ion is subject to an octahedral crystal field described by the site symmetry group O_h. Consequently, the Fe d-orbitals will transform under the symmetry operations of that group according to some irreducible representation of the group. An irreducible representation (irrep) bears the information on how an object or orbital behaves under each symmetry operation of a group, i.e. invariant, change sign or mapped to a symmetry equivalent position, see[56–58] for more information. For the d orbitals, these are the twofold degenerate irrep e_g for the d_{z^2} and $d_{x^2-y^2}$ orbitals, and the threefold degenerate irrep t_{2g} for the d_{xy}, d_{xz} and d_{yz} orbitals. The three oxygen ions are subject to an axial crystal field with two nearest Fe neighbors, described by the site symmetry group D_{4h}. At each O ion, there is one p-orbital oriented parallel to Fe-O axis which transforms according to the irrep a_{2u}, and two p-orbitals perpendicular to that axis which transform as e_u. The three a_{2u} orbitals in the unit cell are grouped into $p_{\parallel}$, the six e_u orbitals into $p_{\perp}$.

Figure 5.2 shows the d- and p-orbitals together with their respective symmetry species (i.e. the label of the irrep they transform as). The energies are estimated from crystal field theory, according to which orbitals whose lobes point directly at the neighboring ions lead to stronger electrostatic interactions. Electrons in the e_g orbitals thus experience a stronger repulsion by the negatively charged oxygen ions, leading to a higher energy than that of the t_{2g} orbitals. On the other hand, electrons in the $p_{\parallel}$ orbitals experience a stronger attraction by the positively charged Fe ions than electrons in the $p_{\perp}$ orbitals, resulting in a lower energy of the $p_{\parallel}$ orbitals.

The degree of crystal field splitting depends on the strength of the metal-ligand interac-

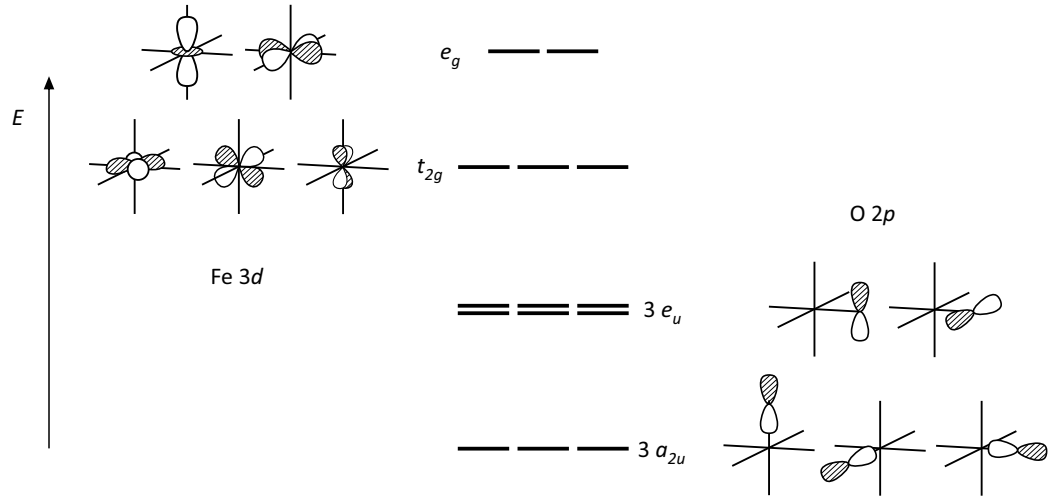

Figure 5.2: Crystal field splitting of O $2p$ and Fe $3d$ orbitals. The orbital sets are labeled according to the irreps of the respective site symmetry group. The e_u orbitals are shown only for the O2 ion.

tions and co-determines the spin configuration in $BaFeO_3$. If the interaction is weak, the splitting between the e_g and t_{2g} states is small, and the system adopts the high spin configuration $e_g^1\ t_{2g}^3$, so as to avoid the electrostatic repulsion between electrons occupying the same orbital. On the other hand, if the metal-ligand interaction is strong, the splitting between the e_g and t_{2g} states is large, so it ultimately becomes energetically more favorable to have doubly occupied t_{2g} orbitals and leave the high-energy e_g orbitals empty; the result is the low-spin configuration $e_g^0\ t_{2g}^4$. To demonstrate that a situation in which the t_{2g} orbitals are doubly occupied is energetically unfavorable, the electronic structure of a hypothetical phase of $BaFeO_3$ is calculated first in which each orbital is forced to be doubly occupied with paired spins only. This is called performing a non spin-polarized calculation; the system is deprived of a majority spin species and the magnetism of the phase is effectively quenched. The approach is inspired by ref.[59].

Figure 5.3 shows the calculated density of states (DOS) and crystal orbital Hamilton population (COHP) curve of non spin-polarized $BaFeO_3$. The COHP is used as a bonding indicator that shows whether the overlap between some chosen atomic orbitals (AOs) is of bonding (peaks to the right), non-bonding (no peak) or anti-bonding (peaks to the left) character (see § 2.3). The integrated COHP (iCOHP) yields the binding energy associated with the overlap of the chosen AOs and can be considered a quantitative measure of covalency. Comparison of the pDOS in figure 5.3 with the crystal field diagram in figure 5.2 illustrates how Fe $3d$ and O $2p$ orbitals have engaged in covalent interactions. The discrete energy levels of figure 5.2 have effectively broadened into bands of energy by virtue of orbital overlap. This overlap can be classified as $pd\sigma$ when the constituting

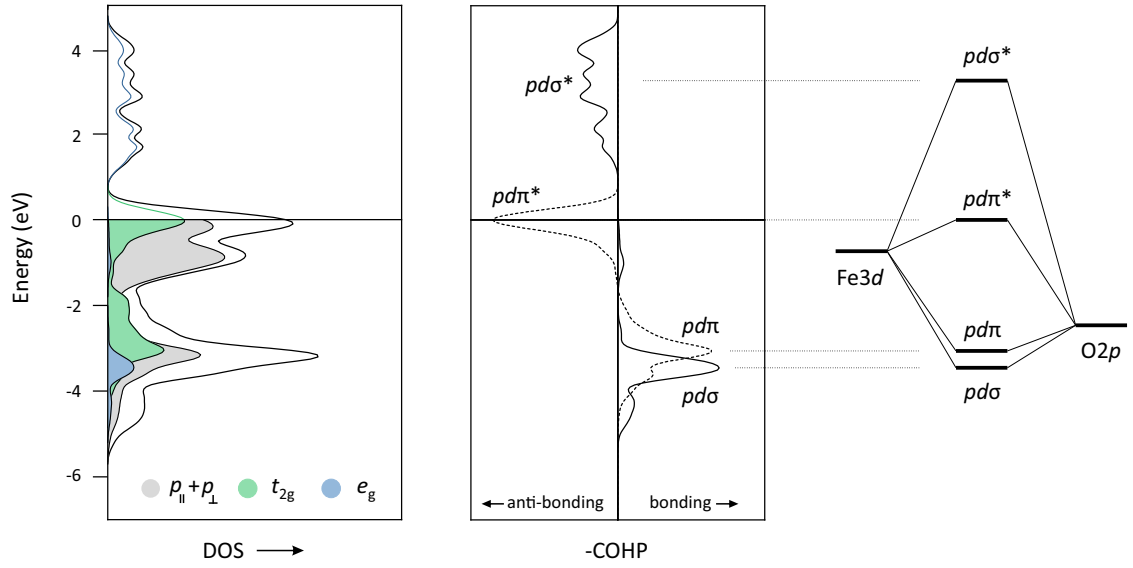

Figure 5.3: DOS (left) and COHP (right) curves of non-magnetic, cubic $BaFeO_3$.

AOs are the e_g and $p_{\parallel}$ orbitals, and as $pd\pi$ when the constituting AOs are the t_{2g} and $p_{\perp}$ orbitals. In particular, the pDOS shows that the e_g and t_{2g} AOs contribute almost equally to some occupied COs at -4 to -2 eV and some partially occupied COs at -1 to 4 eV. As the COHP curve reveals, the occupied COs are bonding $pd\sigma$ and $pd\pi$ interactions. The partially occupied COs, on the other hand, are anti-bonding $pd\sigma^*$ and $pd\pi^*$ interactions. As a result of the covalent binding, the characteristic pattern of the octahedral crystal field splitting of the d-orbitals is preserved only for the partially occupied COs at -1 to 4 eV. Here, the e_g AOs lie on top of the t_{2g} AOs. However, this clearly is the combination of crystal field splitting and a stronger destabilization of the e_g dominated COs due to the $pd\sigma^*$ bonds than the destabilization of the t_{2g} dominated COs due to the $pd\pi^*$ bonds. Consequently, the crystal field pattern in the bonding COs at -4 to -2 eV has disappeared.

The Fermi level at $E = 0$ eV falls in the realm of the t_{2g} dominated COs that have $pd\pi^*$ anti-bonding character. This is a crucial feature of the electronic structure for it means that the occupied states at and right below the Fermi level weaken the Fe-O bonds and thus represent a structural instability of the system. The integrated COHP yields -0.54 eV per $pd\sigma$-bond and -0.27 eV per $pd\pi$-bond, making up 37% of the total iCOHP of -2.19 eV per Fe-O bond. The remaining 63% stem from orbital overlap involving the Fe $3p$, Fe $4s$ and O $2s$ orbitals. The values of the integrated COHP, together with several other electronic properties for the different phases of $BaFeO_3$ are summarized in table 5.1.

By switching on spin-polarization, the constraint of having only doubly occupied orbitals is lifted and the system can relax into a high-spin configuration. In one-electron theory, this is modelled using singly occupied spin-orbitals, such that a high-spin config-

uration is better described as $e_{g\uparrow}^1\ t_{2g\uparrow}^3\ e_{g\downarrow}^0\ t_{2g\downarrow}^0$, where $t_{2g\uparrow}^3$ is completely filled. The energy levels between the spin-up and spin-down spin orbitals can be significantly separated by virtue of so-called exchange interactions. The physical origin of this type of interaction can be explained in terms of an effective nuclear charge felt by the electrons.[16] It follows from Pauli's principle that two electrons of like-spin cannot occupy the same position in space and thus experience a repulsion (*exchange repulsion*) between them. This translates into a reduced probability of finding like-spin electrons near each other. As a result, they do not shield the nuclear charge as effectively as electrons of opposite spin. It is therefore often energetically favorable for a system to maximize the total spin so as to reduce the shielding of the nuclear charge and thus to increase the electron-nucleus attraction of the

Table 5.1: Electronic properties of different cubic phases of $BaFeO_3$.

	NON SPIN-POLARIZED	SPIN-POLARIZED
a / Å	4.015	4.015
Δ_{CFS} eV	0.32	0.85
U / eV	-	6.85
Δ_{CT} / eV	not determined	-3.52
$d^{\uparrow}$	3.12	4.82
$d^{\downarrow}$	3.12	1.00
μ_{eff} / μ_{B}	0.00	4.7
Q_{Ba}	1.77	1.75
Q_{Fe}	1.28	1.64
Q_{O}	-1.02	-1.13
IP	not determined	6.1
iCOHP $pd\sigma$	-0.54	-0.40
iCOHP $pd\pi$	-0.27	-0.29
iCOHP Fe-O	-2.19	-1.93

Δ_{CFS}: crystal field splitting; U: energy cost for transferring an electron from the spin-up $3d$ band to the spin-down $3d$ band (with respect to band centers of mass), after[60,61]; Δ_{CT}: charge transfer energy, energy cost for transferring an electron from the O $2p$ band to the Fe $3d$ band, after[60,61]; $d^{\uparrow}$, $d^{\downarrow}$: d-band population; μ_{eff}: effective magnetic moment given by $\mu_{\mathrm{eff}} = g\sqrt{S(S+1)}$, where $g \approx 2$ and $S = (d^{\uparrow} - d^{\downarrow})/2$[62] ; Q_{i}: Mulliken atomic charges; iCOHP: crystal orbital Hamilton population integrated up to the Fermi level. The Fe-O iCOHP includes $pd\sigma$, $pd\pi$, and orbital overlap between O 2s and Fe 3p orbitals.

majority spin electrons. This increase in electron-nucleus attraction is associated with a contraction of the respective spin-orbitals, which goes at the cost of a stronger electrostatic electron-electron repulsion within the contracted spin-orbitals. The spin state of a system thus represents a compromise between electron-nuclear attraction (stronger in high spin states) and electron-electron repulsion (weaker in low spin states). Regarding $BaFeO_3$, there are five spin-up Fe d-orbitals and five spin-down d-orbitals. The exchange interaction leads to a contraction and lower energy of the spin-up orbitals. This leads, in principle, to two possible scenarios with respect to the local spin configuration of the Fe ions. Assuming a nominal d^4 electron configuration, the electrons can be distributed in a high-spin or low-spin configuration, as depicted in figure 5.4.

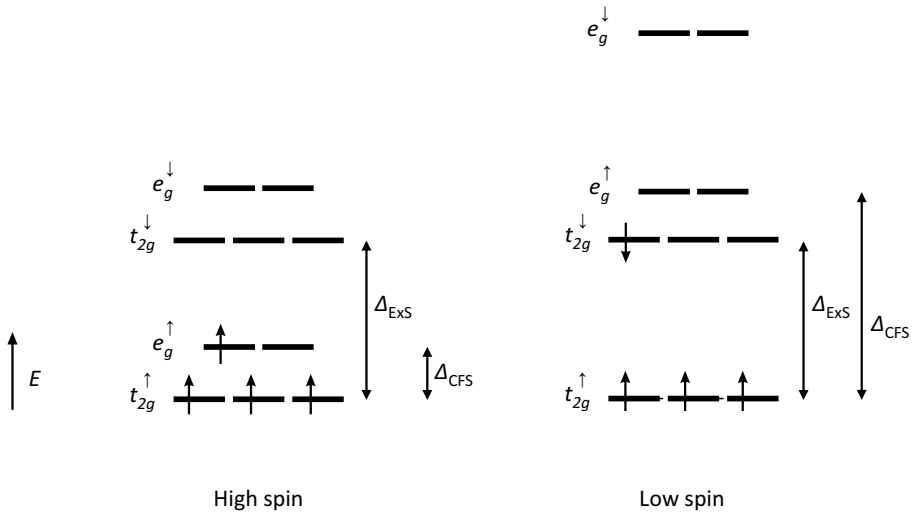

Figure 5.4: Possible ground state spin configurations of Fe d^4 in $BaFeO_3$. Δ_{CFS} stands for the octahedral crystal field splitting, Δ_{ExS} for the exchange splitting.

Which configuration is more stable also depends on the strength of the octahedral crystal field. In case of a weak crystal field - typical for Fe in oxides - the electrons adopt a high-spin configuration so as to increase their electron-nuclear attraction. When the crystal field is sufficiently strong, the electrons are forced to adopt a low-spin configuration at the cost of an increased shielding from the nucleus. Both spin-configurations result in an unequal number of spin-up and spin-down electrons and therefore render the system magnetic.

Figure 5.5 shows the DOS and COHP curves of the $BaFeO_3$ magnetic phase. The DOS is now composed of two spin-components, each of which is equipped with a COHP curve. Regarding the DOS, one can clearly see that the Fe ion has adopted a high spin configuration. The spin-down $e_g^\downarrow$ and $t_{2g}^\downarrow$ bands are considerably separated from the spin-up $e_g^\uparrow$ and $t_{2g}^\uparrow$ bands by 6.9 eV. The Fermi level falls in the upper region of the O $2p$ bands which thus

remain partially unoccupied. The COHP diagrams show the formation of $pd\pi$ and $pd\sigma$ bonds, similar to the non-magnetic case. As for the spin-down COHP, the anti-bonding states are formed by crystal orbitals having d-character which remain unoccupied. The bonding states are formed by crystal orbitals with p-character which are occupied. This reflects a relatively stable configuration because the Fe-O binding is not destabilized by populated $pd\sigma^*$ and $pd\pi^*$ states. In the case of the spin-up COHP, the situation is reversed. The bonding states are now formed by crystal orbitals of d-character whereas the anti-bonding states are formed by crystal orbitals of p-character. The Fermi level thus falls in a $pd\sigma^*$ anti-bonding region with crystal orbitals of predominant p-character.

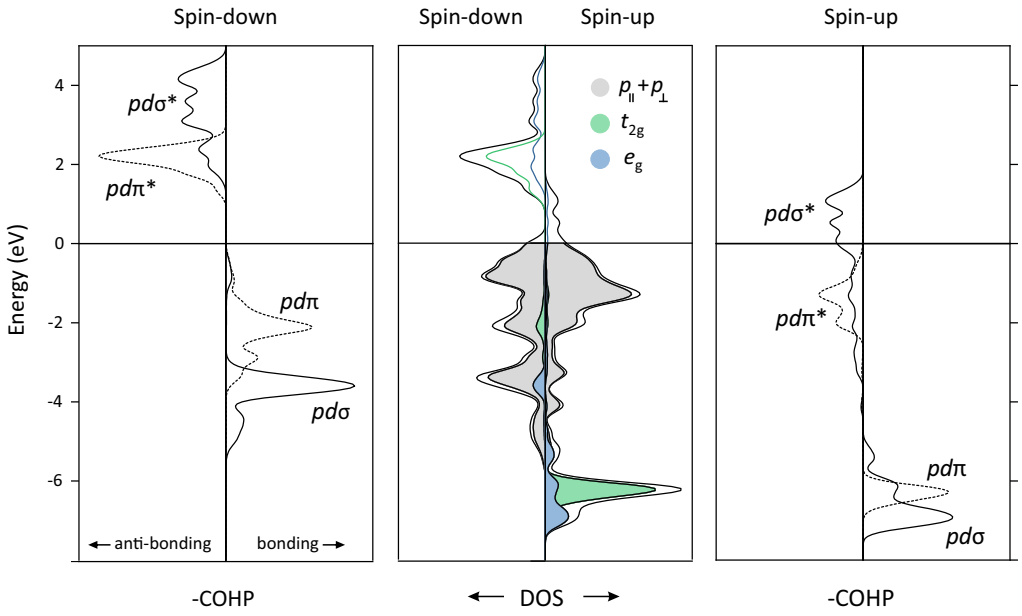

Figure 5.5: DOS (middle) and COHP curves (left: spin down, right: spin-up) of magnetic, cubic $BaFeO_3$.

The characteristic pattern of the octahedral crystal field splitting is preserved only in the unoccupied spin-down DOS where the e_g-band is more destabilized through the formation of $pd\sigma^*$ bonds than the t_{2g} band through the formation of $pd\pi^*$ bonds. This pattern disappears in the spin-up DOS, where the d orbitals involve in strong bonding interactions. Moreover, the peaks in the spin-up COHP are less pronounced than the peaks in the spin-down COHP with the same scale on the x-axis. This can be explained by the fact that the spin-up orbitals are more contracted than the spin-down orbitals. As explained previously, in a high spin configuration the shielding of the nuclear charge in the majority spin orbitals is reduced and the electrons experience a stronger electron-nuclear attraction. As a result, the respective spin-orbitals contract. This, in turn, reduces the pd overlap and results in less pronounced peaks in the spin-up COHP. The integrated COHP

up to the Fermi level yields -1.93 eV per Fe-O bond for both spin components together. The energy associated with Fe-O bonding has thus decreased by 12% compared to the nonmagnetic phase (-2.19 eV). This is a clear indication that the exchange interactions and the splitting of the d-orbitals resulted in a stronger ionic bonding as compared to the nonmagnetic counterpart. The pd-binding in the magnetic phase is composed of -0.40 eV (58%) per $pd\sigma$ bond and -0.29 eV (42%) per $pd\pi$ bond (see table 5.1).

The gross orbital populations are $d^{5.82}$ and $p^{5.23}$ and thus deviate significantly from the nominal electron configurations of d^4 and p^6. This is, to some extent, due to the mixed ionic-covalent character of the Fe-O bond, as evidenced by the COHP curves in figure 5.5. On the other hand, these orbital populations are the fingerprint of a so-called negative charge transfer from the O ions to the Fe ion. The charge transfer energy is defined as the energy cost of transferring an electron from the O $2p$ valence band to the Fe $3d$ band (with respect to band centers of mass), i.e. charge fluctuations of type $d^n \rightarrow d^{n+1}\underline{L}$.[60,61] Negative charge transfer energies consequently indicate that the ground state is shifted to the right hand side of this reaction. This charge transfer is enabled by the spin-up d-bands lying **below** the O $2p$ band. Figure 5.6 illustrates this process using local electron configurations of the ions. The resulting electron configuration of $d^{5.82}$ is thus strongly reminiscent of a $d^5\underline{L}$ configuration ($\underline{L}$: O 2p ligand hole). A value greater than 5 stems from the combination of negative charge transfer and a covalent Fe-O bond. The calculated Mulliken charges are $Ba^{1.75}Fe^{1.64}O_3{}^{-1.13}$.

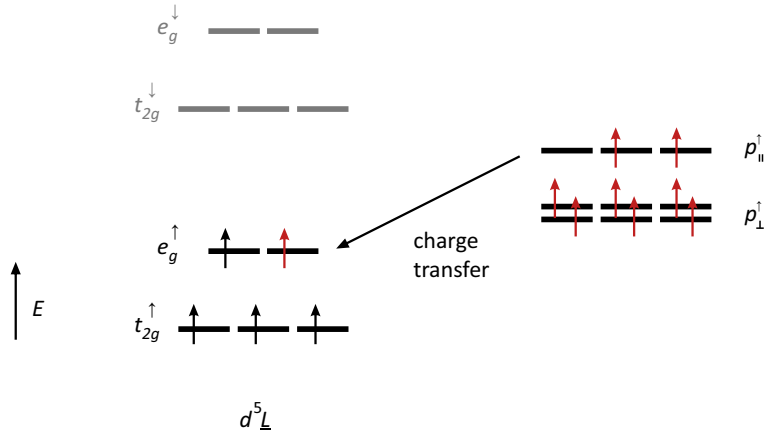

Figure 5.6: Negative charge transfer in $BaFeO_3$.

In conclusion, the electronic structure instability identified in the nonmagnetic phase is alleviated by an electronic phase transformation upon which the d-orbitals split and a negative charge transfer is induced. This significantly decreases the total energy by -2.73 eV. The electronic structure of the magnetic phase is characterized by electron holes in

the $p_{\|}$ valence band. The COHP at the Fermi level reveals that these holes are partially delocalized in anti-bonding $pd\sigma^*$ crystal orbitals. What remains in the magnetic phase is a residual structural instability due to these populated $pd\sigma^*$ anti-bonding states at and below the Fermi level.

5.4 Band structure analysis

Having established the general characteristics of the electronic structure through the analysis of the DOS and COHP curves in the preceding section, the underlying orbital interactions are further explored using group theory and band structure analyses. Recall that the crystal orbitals are k-dependent and are described, in the formalism employed here, as linear combinations of atomic orbitals:

$$\psi_j(k) = \sum_{\mu=1}^{n} c_{\mu j}(k)\phi_\mu(k) \tag{5.1}$$

where $\psi_j(k)$ are the crystal orbitals (COs) - or bands - and $\phi_\mu(k)$ the atomic orbitals (AOs). In the following section, the symmetry properties of the atomic orbitals, $\phi_\mu(k)$, are determined for a set of high-symmetry k-points. These symmetry properties place important constraints on the band structure; they dictate the degeneracy of COs at the different k-points and lines and they dictate whether AOs have the right symmetry to combine into a common CO. After the group-theoretical treatment, the band structure is calculated by DFT for a path through the Brillouin zone connecting the same set of high-symmetry k-points as used in the symmetry analysis. To ease chemical interpretation, the calculated band structure is analyzed using the so-called fat bands technique, where individual bands are plotted with a certain line width that is proportional to the coefficient $c_{\mu j}$ of a given atomic orbital μ.

5.4.1 Symmetry properties of the orbitals

The symmetry properties of local atomic orbitals within the unit cell are determined by the shape of the orbital (s, p, d,...) and the site symmetry of the constituent ion. As a result, the atomic orbitals transform according to some irreducible representations (irrep) of the site symmetry group of that ion. Upon expanding the atomic orbitals into extended Bloch waves, a k-vector is introduced that reflects the translational symmetry of the crystal. Hence, the symmetry properties of the k-dependent atomic orbitals (Bloch waves) are dependent on three factors, listed below, and the AOs transform according to some irreducible representation of the space group.

1. The shape of the orbitals (s, p, d,...)
2. The site symmetry at the constituent atom within the unit cell
3. The translational symmetry between unit cells

Consider for example the p_x-orbital in figure 5.7, left. The twofold rotation axis along the y-axis transforms this orbital into the neighbouring unit cell and changes its sign to $-p_x$. Due to the translational symmetry, the new site can be regarded as being identical as the original site; the twofold rotation effectively changes only the sign of the p_x orbital. This example represents the case for $k = (0, 0, 0)$ where the phase factor reduces to unity and the irreps of the space group become the same as those of the O_h point group. In figure 5.7, right, the same operation is carried out for the case $k = (\frac{\pi}{a}, 0, 0)$. Here, a phase factor of "-1" is multiplied with the transformed p_x orbital. Thus, the twofold rotation carried out at $k = (\frac{\pi}{a}, 0, 0)$ leaves the p_x orbital entirely invariant. Consequently, the atomic Bloch wave constructed from the p_x orbital will transform as two different space group irreps at the two k-points considered here.

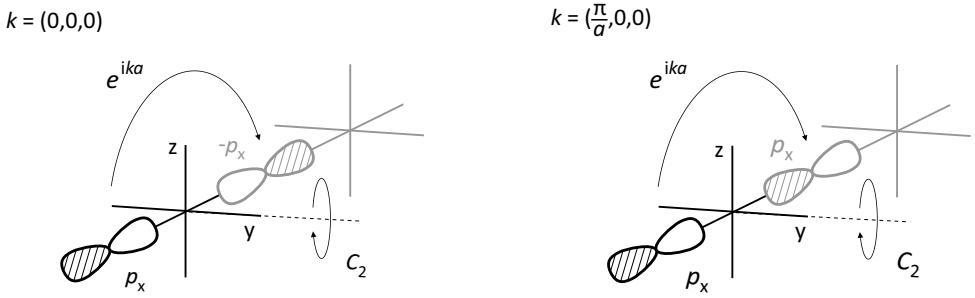

Figure 5.7: Effect of a twofold rotation and translation at $k = (0, 0, 0)$ and $k = (\frac{\pi}{a}, 0, 0)$ acting on the p_x orbital. Modified after[63]

The irreps of the atomic Bloch waves are determined for the following sets of atomic orbitals: the e_g and t_{2g} sets of the Fe ion, and the $p_{\parallel}$ and $p_{\perp}$ sets of the O ion. Since no symmetry operation can transform an orbital of one of these sets into another one, each set forms a separate basis set. At different k-points these basis sets decompose into a finite number of space group irreps, such as the $p_{\parallel}$ basis set decomposes at $k = (\frac{\pi}{a}, 0, 0)$ into a one-dimensional irrep for the p_x as depicted in figure 5.7 on the right, and a two-dimensional irrep for the remaining p orbitals of the basis. The space group irreps of the four basis sets are determined for the k-points $\Gamma = (0, 0, 0)$, $X = (\frac{\pi}{a}, 0, 0)$, $M = (\frac{\pi}{a}, \frac{\pi}{a}, 0)$ and $R = (\frac{\pi}{a}, \frac{\pi}{a}, \frac{\pi}{a})$. These k-points themselves are invariant or transformed into a symmetry equivalent k-point under the action of some point group symmetry operations. For example, $X = (\frac{\pi}{a}, 0, 0)$ remains invariant with respect to a four-fold rotation around

k_x and a mirror plane perpendicular to that axis. The set of operations that leave a k-point invariant form the group of the wave vector. The point groups of the four k-points considered here are listed in table C.1 in the appendix. When a basis set decomposes into some space group irreps at a particular k-point, then these irreps belong to the point group of that k-vector. The k-point $X = (\frac{\pi}{a}, 0, 0)$ has the group D_{4h} and the basis set $p_{\parallel}$ decomposes into the irreps a_{1g} ($X_1^+(1)$) and e_u ($X_5^-(2)$) of that group. The symbols in brackets represent a different notation by[64] which is more common in solid state physics and is consistent with the Bilbao Crystallographic Server[65,66]. In this notation, the information stored in the Mulliken labels (a, e,...) is given up for the position in the Brillouin zone. The superscript "+" or "-" indicates whether the Bloch wave is *gerade* or *ungerade* with respect to the central Fe ion and the roman number in brackets gives the dimension of the irrep. In the present thesis, Mulliken symbols are used only in conjuncture with site-symmetry irreps, whereas space group irreps are given in the solid-state notation. The irreps into which the four basis sets decompose at the four k-points considered here are determined using the program "BANDREP"[67] which is part of the online resources of the Bilbao Crystallographic Server[65,66] and are listed in table 5.2. There are several types of information that can be retrieved from table 5.2.

- Each of the four basis sets decomposes into a set of k-dependent irreps (the entries in each row of table 5.2). The orbitals belonging to a given irrep can be transformed into each other by some symmetry operation of the crystal. Hence, they must be physically indistinguishable and yield the same energy eigenvalues. Indeed, the energy eigenvalue corresponding to an n-dimensional irrep (number in brackets) will be n-fold degenerate.[56] By inspection of table 5.2 it is thus possible to exactly predict the maximum number of different energy eigenvalues that will come out of the calculation. There will only be as many energy eigenvalues as there are irreps per k-point.

- The orbitals that belong to an irrep behave under the symmetry operations of the crystal in the same way as the irrep itself. When the orbitals are located on the central Fe ion, i.e. an ion through which all the symmetry elements pass, the decomposition into the irreps of the space group is simply a splitting of the original basis set into smaller subsets. However, when the orbitals lie on the symmetry equivalent O ions around the central Fe ion, the decomposition into the irreps often goes along with the formation of linear combinations among these orbitals, so that the combinations can actually transform as one of the irreps of the group.[57,68] Although it is possible to derive the irreps into which the O basis sets decompose without knowing the actual form of these linear combinations, it is often helpful to

Table 5.2: Site-symmetry induced space-group irreps of Bloch waves at different k-points.

	Γ	X	M	R
e_{g}	$\Gamma_3^+(2)$	$\mathrm{X}_1^+(1)$, $\mathrm{X}_2^+(1)$	$\mathrm{M}_1^+(1)$, $\mathrm{M}_2^+(1)$	$\mathrm{R}_3^+(2)$
$t_{2\mathrm{g}}$	$\Gamma_5^+(3)$	$\mathrm{X}_4^+(1)$, $\mathrm{X}_5^+(2)$	$\mathrm{M}_4^+(1)$, $\mathrm{M}_5^+(2)$	$\mathrm{R}_5^+(3)$
e_{u} ($p_\perp$)	$\Gamma_4^-(3)$, $\Gamma_5^-(3)$	$\mathrm{X}_3^-(1)$, $\mathrm{X}_4^-(1)$, $\mathrm{X}_5^+(2)$, $\mathrm{X}_5^-(2)$	$\mathrm{M}_3^+(1)$, $\mathrm{M}_4^+(1)$, $\mathrm{M}_5^+(2)$, $\mathrm{M}_5^-(2)$	$\mathrm{R}_4^+(3)$, $\mathrm{R}_5^+(3)$
$a_{2\mathrm{u}}$ ($p_\parallel$)	$\Gamma_4^-(3)$	$\mathrm{X}_1^+(1)$, $\mathrm{X}_5^-(2)$	$\mathrm{M}_1^+(1)$, $\mathrm{M}_2^+(1)$, $\mathrm{M}_3^-(1)$	$\mathrm{R}_1^+(1)$, $\mathrm{R}_3^+(2)$

generate them at a later time for chemical interpretation. The linear combinations of the O $2p$ orbitals have been generated for the present thesis and can be found in appendix C.1, together with additional explanations. They are typically referred to as symmetry-adapted linear combinations (SALC).

- The orbitals and SALCs transforming as the irreps in table 5.2 represent eigenfunctions of the system. Those orbitals that transform as the same irrep at a given k-point can further involve in covalent interactions, i.e. form crystal orbitals of bonding or anti-bonding character. Since only orbitals that transform as the same irrep are compatible to combine in common COs, the irreps in table 5.2 represent so-called compatibility relations.

There are five different irreps at the Γ-point which means that there are at most five different energies in the band structure. The p- and d-type AOs have no irrep in common, so there will be no covalent mixing between them at this k-point. The six $p_\perp$ AOs split into the two threefold degenerate irreps Γ_4^- and Γ_5^-, yielding potentially two different eigenvalues. This splitting can be understood as the formation of $pp\pi$ interactions between adjacent oxygen ions, as depicted in figure 5.8. The bonding and antibonding linear combinations of the $p_\perp$ represent the SALCs that span the irreps Γ_4^- and Γ_5^- and have been generated with the use of a projection operator (see appendix C.1). The antibonding linear combination of the $p_\perp$ can further involve in covalent interaction with the $p_\parallel$ AOs which also span a Γ_4^- irrep.

At the point $X = (\frac{\pi}{a}, 0, 0)$, the Bloch wave derived from the p_x orbital of the O1 ion transforms as $X_1^+(1)$ as opposed to the other $p_\parallel$ Bloch waves which transform as $X_5^-(2)$. This corresponds to the example made in figure 5.7. Due to the alternating sign of the p_x-orbitals in the crystallographic x-direction, the Bloch wave becomes $gerade$ with respect to central Fe as indicated by the "+" superscript. It can then form a $pd\sigma$ bond with the X_1^+ of the e_g AOs. At the same time, the $p_\parallel$ and $p_\perp$ AOs have no more irreps in common and can thus no longer involve in pp bonding. Moreover, the t_{2g} and $p_\perp$ Bloch waves

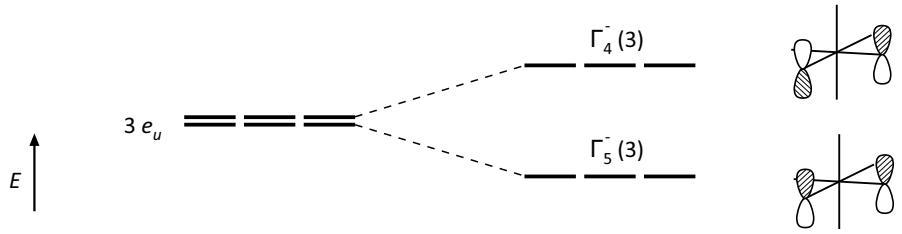

Figure 5.8: Splitting of the $p_\perp$ orbitals into two threefold-degenerate sets at the Γ-point. The SALC of these levels reveal that these are $pp\pi$ bonding and anti-bonding combinations. Modified after[63].

both contain the irrep X_5^+ which enables the formation of $pd\pi$ bonds. Moving forward to the point $M = (\frac{\pi}{a}, \frac{\pi}{a}, 0)$ the irreps decompose further resulting in the largest number of different irreps and thus energy eigenvalues in the band diagram. Both e_g AOs have now common irreps with the $p_\parallel$ AOs which leads to stronger $pd\sigma$ bonding. Similarly, all t_{2g} AOs have common irreps with the $p_\perp$ which leads to stronger $pd\pi$ bonding. Finally, the level of degeneracy is increased again in reaching the point $R = (\frac{\pi}{a}, \frac{\pi}{a}, \frac{\pi}{a})$. There are six different irreps, so there will be at most six different energies. All d-type orbitals are involved in $pd\sigma$ and $pd\pi$ bonds. The $p_\parallel$ and $p_\perp$ AOs have no common irrep, which precludes covalent mixing between them at the R-point.

5.4.2 Spin-down band structure

The calculated spin-down band structure of cubic $BaFeO_3$ is shown in figure 5.9. There are in total 14 COs, made from 5 Fe $3d$ and 9 O $2p$ AOs. The Fermi level separates the unoccupied COs with predominant d-orbital character from the occupied COs with predominant p-orbital character by ≈ 1 eV. A small fraction of the p-type COs remains unoccupied, corresponding to 0.1 hole per unit cell. In line with the symmetry considerations, there are no more than five independent energies at the Γ point. The $p_\perp$ AOs have engaged in $pp\pi$ interactions (see figure 5.8) evidenced by a splitting of 0.7 eV between the two three-fold degenerate sets Γ_4^- at -0.2 eV and Γ_5^- at -0.9 eV. Since there is no covalent mixing between p and d states, or within the d states, the energy difference between Γ_3^+ and Γ_5^+ of the d-orbitals of 0.4 eV represents the purely ionic octahedral crystal field splitting. The axial crystal field splitting of the p-orbitals cannot be determined unambiguously since the $p_\perp$ and $p_\parallel$-orbitals can mix even at the Γ point. However, taking the difference between the average of Γ_4^- at -0.2 and Γ_5^- at -0.9 for the $p_\perp$ orbitals and Γ_4^- at -3.2 eV for the $p_\parallel$ orbitals yields an estimate of -2.6 eV for the axial crystal field splitting.

The orbital interactions that lead to $pd\sigma$ and $pd\pi$ bonding are analyzed using the so-called fat bands technique; individual COs - or bands - are plotted with a certain color

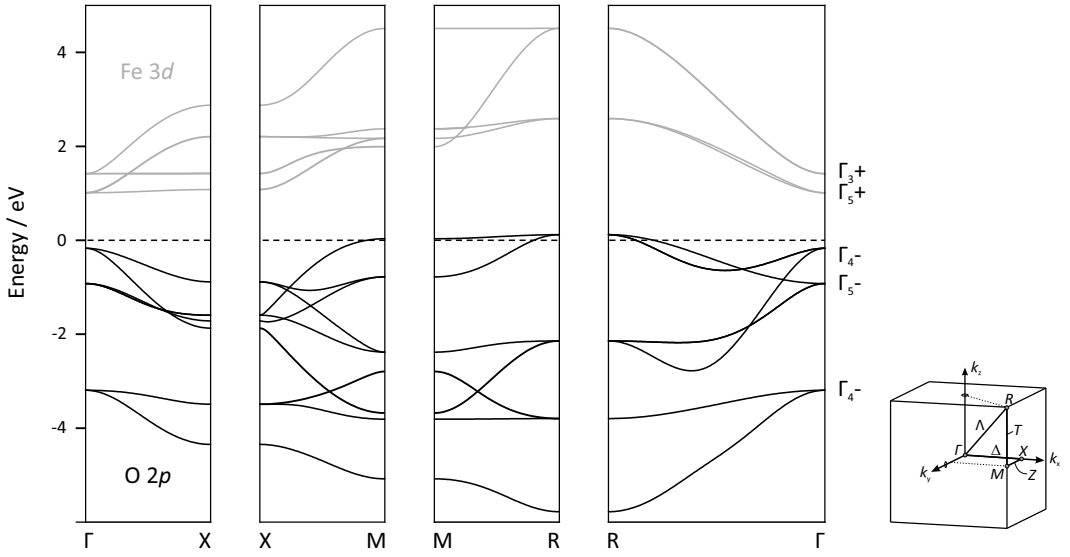

Figure 5.9: Spin-down band structure of cubic $BaFeO_3$ showing d and p bands.

and line width that represent the type and coefficient of some chosen AOs. This allows one to see where in k-space the coefficients of a given AO are distributed among different COs.

- **Formation of $pd\sigma$-bonds**: The fat bands of the p_x AO of the O1 ion and $d_{x^2-y^2}$ AO are shown in figure 5.10, top. The O1 ion refers to the oxygen ion in the Fe-O axis oriented in x-direction, see figure 5.1. The chosen AOs contribute mainly to three COs, one unoccupied anti-bonding CO at 1.5 to 4 eV and two occupied bonding COs at -3 to -6 eV. Due to the anti-bonding nature, the unoccupied CO runs up, reaching a band width of 3.1 eV. The occupied COs having bonding character run down in energy, together reaching a band width of 2.6 eV. To understand the mixing of the p_x orbital into *two* occupied COs, it is helpful to construct the symmetry adapted linear combinations (SALC) projected from the p_x orbital. The p_x AO combines with the p_y of the O2 ion, e.g., at the M point in the SALCs $p_x + p_y$ and $p_x - p_y$. The latter combination, $p_x - p_y$, transforms as the irrep M_2^+ and can thus form $pd\sigma$-bonds with the $d_{x^2-y^2}$ AO. At the M point, the $pd\sigma$-binding reaches coefficients of 30% p_x (60% $p_x - p_y$) and 40% $d_{x^2-y^2}$ in the occupied CO M_2^+ at $\approx$ -3 eV. Similar coefficients are obtained for the R-point.

- **Formation of $pd\pi$-bonds**: The orbital overlap associated with $pd\pi$ bonds is generally smaller compared to $pd\sigma$ bonds. This is reflected by a less covalent mixing of the involved AOs. The fat bands plot featuring the p_y of the O1 ion and d_{xy} AOs and the corresponding COHP curve are shown in figure 5.10, bottom. The strongest

mixing occurs at the X-point where coefficients reach 80% d_{xy} and 20% p_y in the unoccupied CO $X_5^+(2)$ at 2 eV. The formation of $pd\pi$-bonds is also evidenced by the dispersion of the t_{2g} bands, reaching a band width of 1.6 eV.

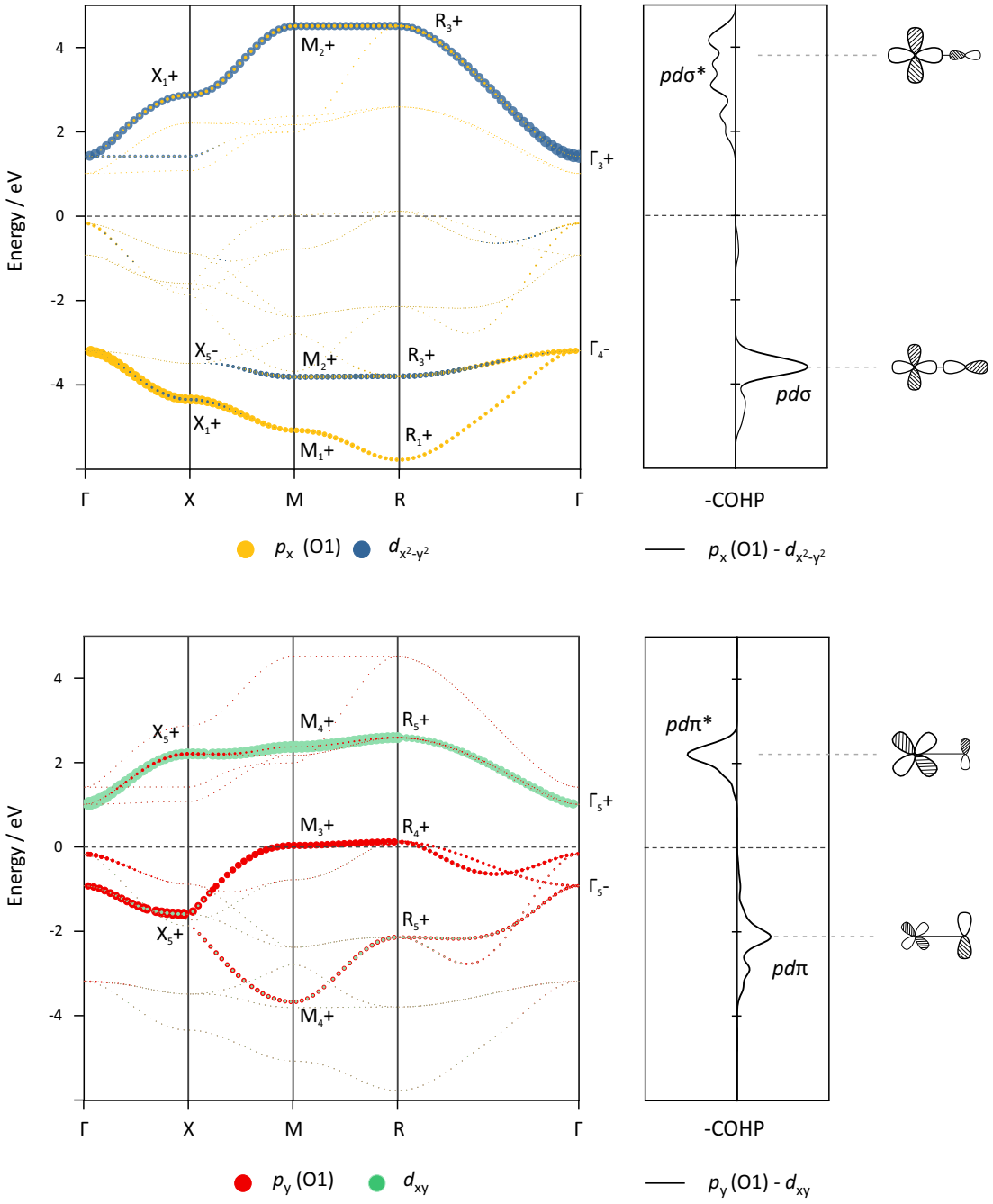

Figure 5.10: Fat bands plot of the spin-down band structure. The line width of the bands is proportional to the coefficient of the AO in the respective CO. The O1 ion refers to the oxygen ion in the Fe-O axis oriented in x-direction, see figure 5.1.

5.4.3 SPIN-UP BAND STRUCTURE

The calculated spin-up band structure of cubic $BaFeO_3$ is shown in figure 5.11. The d dominated COs at -5 to -7 eV lie **below** the p dominated COs at -4 to 1 eV. There are two COs crossing the Fermi level. The unoccupied states of these COs correspond to an electron hole concentration of 0.9 hole per unit cell, i.e. 90% of the total hole concentration. Notably, only two COs are responsible for the vast majority of electron holes and, as such, the electronic conductivity in $BaFeO_3$. The octahedral crystal field splitting between Γ_3^+ (e_g) and Γ_5^+ (t_{2g}) is -1.3 eV. Regarding the axial crystal field splitting of the p-orbitals, a value of 2.6 eV is estimated based on the difference between the average of Γ_4^- at -0.3 eV and Γ_5^- at -1.2 eV for the $p_\perp$ orbitals and Γ_4^- at -3.3 eV for the $p_\parallel$ orbitals. The orbital interactions that lead to $pd\sigma$ and $pd\pi$ bonding are analyzed using the fat bands technique.

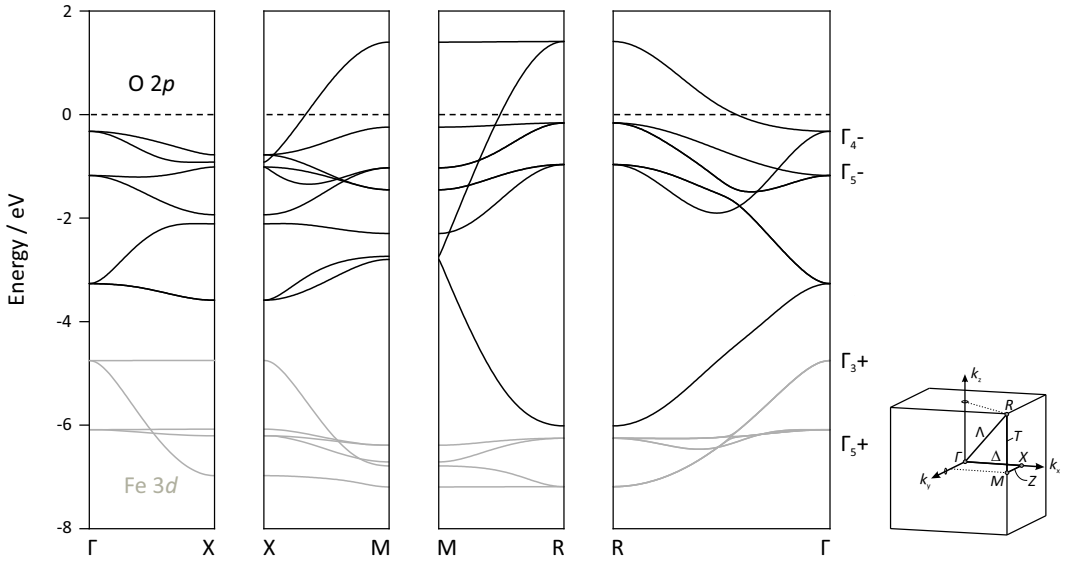

Figure 5.11: Spin-up band structure of cubic $BaFeO_3$ showing d and p bands.

- **Formation of $pd\sigma$-bonds**: The fat bands plot featuring the p_x of the O1 ion and $d_{x^2-y^2}$ AOs together with the corresponding COHP curve is shown in figure 5.12, top. Considering first the COHP curve, the $pd\sigma$ bonding interaction at -7 to -5 eV lies in the realm of the $d_{x^2-y^2}$ dominated CO. On the other hand, the anti-bonding interaction at -4 to 2 eV is associated with COs having p_x-character including the states at the Fermi level. The fact that the $p_\parallel$ AOs, such as the p_x of the O1 ion, involve in anti-bonding interactions leads to two competing effects: (i) The axial crystal field at the oxygen lattice sites stabilizes the $p_\parallel$ orbitals more than the $p_\perp$ orbitals. In the absence of covalent interactions between p and d orbitals (i.e. at the Γ point) the $p_\parallel$ COs will therefore lie below the $p_\perp$ COs, (ii) The formation of $pd\sigma^*$

bonds destabilizes the $p_{\parallel}$ COs more than the formation of $pd\pi^*$ bonds destabilizes the $p_{\perp}$ bonds. In the case of strong covalency, the $p_{\parallel}$ dominated COs will therefore be at higher energy than the $p_{\perp}$ COs.

Indeed, at the Γ-point the p_x AO contributes mostly to the lower lying Γ_4^+ CO at ≈-3 eV. On leaving the Γ-point, a $pd\sigma^*$ bond is established as indicated by the mixing of p_x and $d_{x^2-y^2}$ AOs between the Γ and X points. The system tries to counteract the destabilizing effect of the populated $pd\sigma^*$ states at -3 to -2 eV by shifting the p_x contribution to a CO of higher energy at ≈-1 eV, and, eventually to an unoccupied CO. This is an important result for it means that the COs crossing the Fermi level are mixtures of $p_{\parallel}$ and e_g AOs which have an anti-bonding character. The SALC of the M_1^+ irrep projected from the p_x AO is $p_x + p_y$. The unoccupied CO M_1^+ at ≈ 1 eV is composed of 80% $p_x + p_y$ and 20% $d_{x^2-y^2}$. Similar coefficients are obtained for the unoccupied COs at the R-point. The $pd\sigma$ bonding leads to a significant dispersion of the respective bands reaching a band width of 2.5 eV for the e_g dominated bands. The band width for the $p_{\parallel}$ dominated bands is 4.7 eV due to the strong mixing with the $p_{\perp}$ bands.

- **Formation of $pd\pi$ bonds**: The $pd\pi$-binding in the spin-up band structure is even weaker than in the spin-down band structure. The fat bands plot with the p_y of the O1 ion and d_{xy} AOs and the corresponding COHP curve are shown in figure 5.12, bottom. The covalent mixing between these AOs is virtually absent in the fat bands plot but revealed in the corresponding COHP curve. The weak $pd\pi$ bond also manifests in narrow t_{2g}-bands with a band width of only 0.7 eV, see figure 5.11.

The spin-up COs that cross the Fermi level account for 90% of the electron holes in the system and therefore play a special role in the electronic conductivity and redox activity of $BaFeO_3$. These COs are anti-bonding combinations of $p_{\parallel}$ and e_g AOs. The coefficients in these orbitals can be identified with the often discussed term of hole delocalization in $BaFeO_3$. As can be seen from the fat bands in figure 5.12, top (region above $E = 0$ eV), the coefficients in the unoccupied part change very little. Thus, 90% of the holes in $BaFeO_3$ are delocalized in crystal orbitals composed of ≈ 80% O $2p$ AOs and 20% Fe $3d$ AOs.

5.5 Summary and discussion

The analysis in this chapter showed that cubic $BaFeO_3$ is characterized by a negative charge transfer with a low DOS at the Fermi level. The charge transfer energy, Δ_{CT}, for charge fluctuations of type $d^n \rightarrow d^{n+1}\underline{L}$, is considerably large with $\Delta_{\mathrm{ct}} = -3.52$ eV which means that a lot of electron density is transferred from the O $2p$ to the metal Fe $3d$ bands.

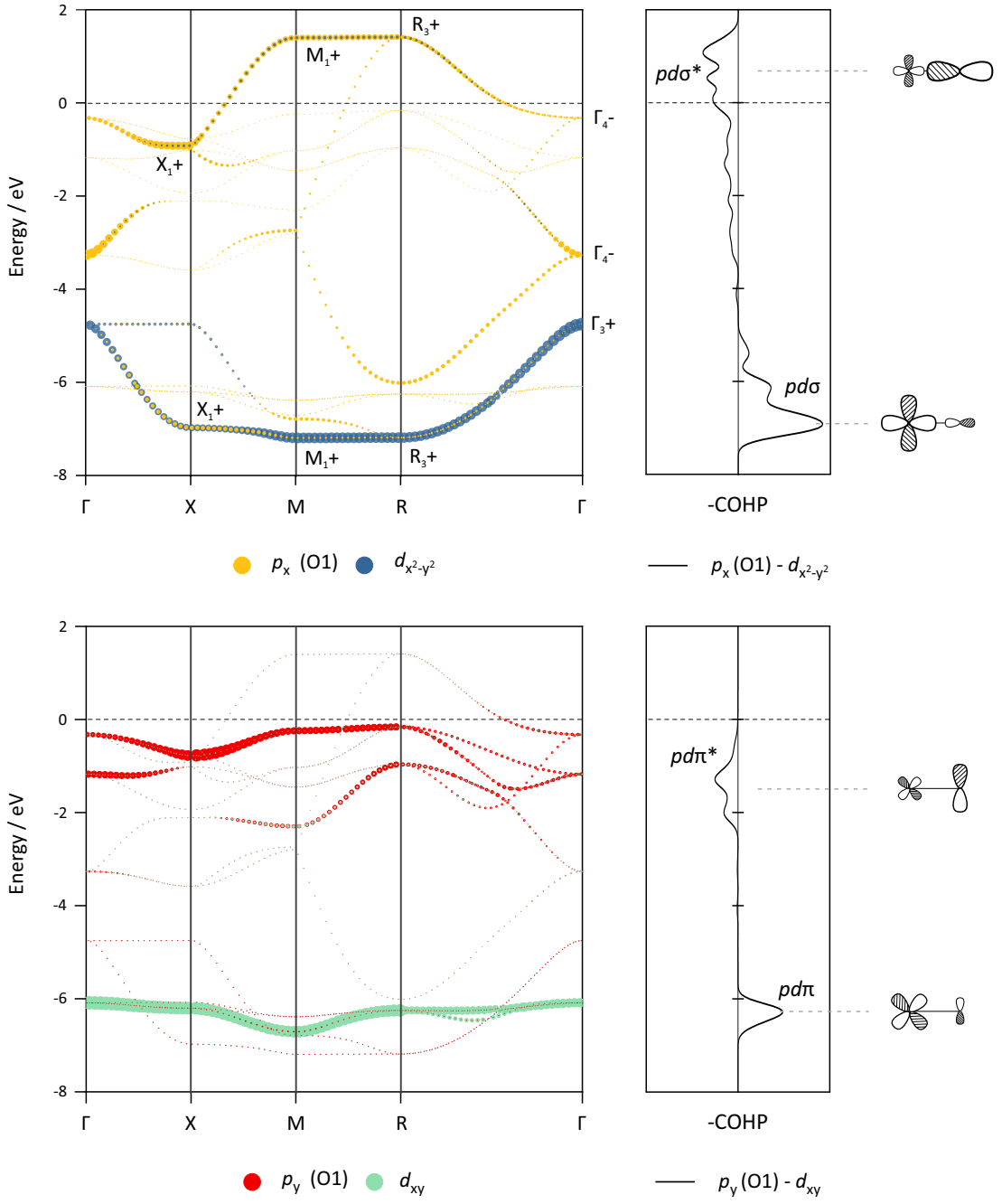

Figure 5.12: Fat bands plot of the spin-up band structure. The line width of the bands is proportional to the coefficient of the AO in the respective CO. The O1 ion refers to the oxygen ion in the Fe-O axis oriented in x-direction, see figure 5.1.

The calculations are thus strongly indicative of a $d^5\underline{L}$ dominated configuration and are in line with x-ray spectroscopic studies by[1–3] where charge transfer energies of -3.0 eV[2] and -0.7 eV[3] are reported. According to the definition of[60,61], this characterizes $BaFeO_3$ as a negative charge transfer material. The differential occupation of $d^{\uparrow}$ and $d^{\downarrow}$ bands leads to an effective magnetic moment of $4.4\ \mu_B$ per Fe which is in very good agreement

with the majority of experimentally determined values of 4.4[55], 4.1[52] and 4.3[54] μ_B, with the exception of 2.5 μ_B measured by[3]. The strong agreement with the reported data, in turn, supports the choice of calculation parameters used in this work. In addition to the reported studies, this chapter provides a chemically intuitive description of the electronic structure in terms of local atomic orbitals. A quantified Fe-O bond analysis has been carried out, showing that the Fe-O bond has significant covalent contribution. The electron holes at the Fermi level were shown to be largely delocalized in anti-bonding $pd\sigma^*$ bonds with an $\approx 80\%$ share at the oxygen ions; they represent the chemically active frontier orbitals in the system. The connection between the calculated electronic structure and experimentally accessible electronic features can be made by aligning the energy levels to the electrostatic potential at vacuum (figure 5.13).

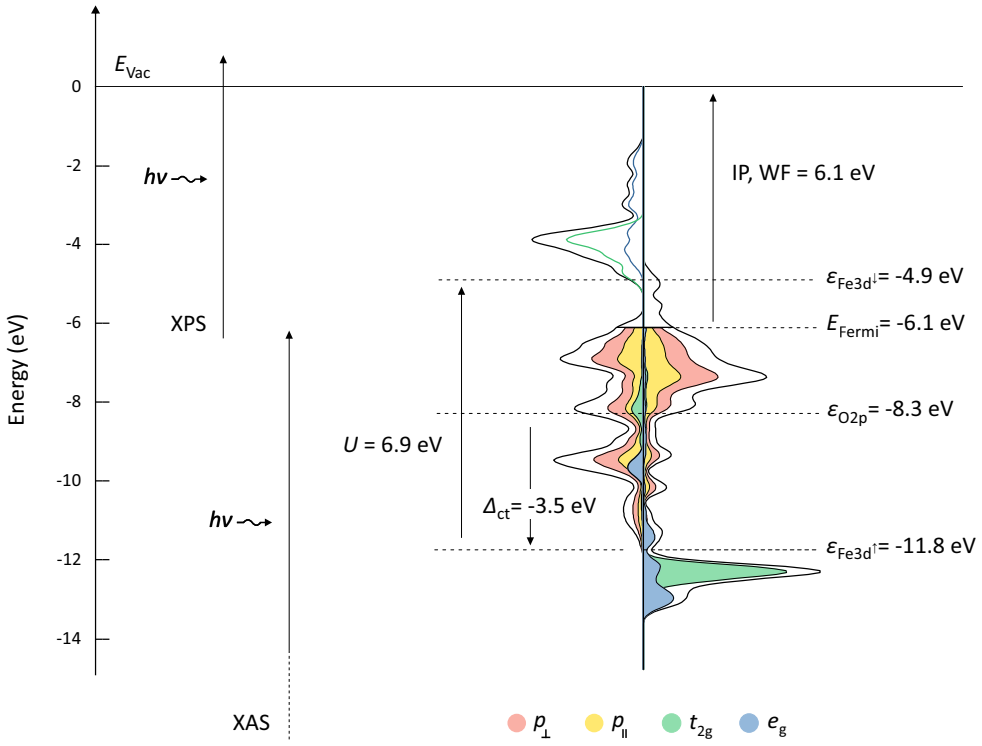

Figure 5.13: DOS of cubic $BaFeO_3$ aligned with respect to vacuum. XAS = X-ray absorption spectroscopy, XPS = X-ray photoelectron spectroscopy.

This is achieved by performing a surface slab calculation (see appendix B.2 for details). As shown in figure 5.13, in x-ray photoelectron spectroscopy (XPS), electrons are excited from anti-bonding $pd\sigma^*$ and non-bonding $p_\perp$ orbitals into the vacuum where their kinetic energy provides information about the nature of the bond in the solid. In x-ray absorption spectroscopy, electrons are excited from core orbitals into unoccupied $pd\sigma^*$ and $p_\perp$ valence orbitals leaving behind core holes. The photon emitted during the recombination

process is detected and contains information about the states at the Fermi level.

It is important to note that a negative charge transfer does not necessarily imply a strong covalency of the Fe-O bond. In fact, a $d^5\underline{L}$ scenario can, in principle, be purely ionic if the respective ligand and metal bands are energetically sufficiently far apart. However, a main statement of this thesis is that the Fe-O bond actually has a significant covalent character. The iCOHP of the Fe-O bond, a quantitative measure of covalency, is -1.93 eV in $BaFeO_3$, taking into account not only the $pd\sigma$ and $pd\pi$ overlap but also the overlap associated with O 2s and Fe 3p orbitals. For comparison, the iCOHP of the Fe-O bond in $SrFeO_3$ - a compound generally considered more covalent - is indeed more negative with a value of -2.23 eV. [i] On a last note, a key aspect of the Fe-O bond is that anti-bonding $pd\sigma^*$ and $pd\pi^*$ states fall in the upper valence band and are largely occupied. In terms of a structure-bonding relationship, these populated states weaken the Fe-O bond strength and pose a structural instability in the system. This raises the possibility of lattice distortions or charge ordering effects to reduce orbital overlap and alleviate these stresses. These effects are discussed in the following chapter.

[i] $SrFeO_3$ calculated in space group $\mathrm{Pm\bar{3}m}$ with $a = 3.89$ Å using VASP, DFT+U with $U = 4$ eV for Fe, Energy cutoff of 500 eV, k-point grid $8 \times 8 \times 8$, break condition for the SCF of 10^{-8} eV.

6 Jahn-Teller distortion in $BaFeO_3$

6.1 Introduction

In this chapter, the structural stability of cubic $BaFeO_3$ towards cooperative lattice distortions is studied by means of first-principles phonon calculations and a symmetry-mode displacement approach.

$BaFeO_3$ adopts different crystal structures depending on the synthesis conditions. The most stable structure is hexagonal, which can be transformed into a metastable cubic perovskite structure under certain conditions. The two phases of $BaFeO_3$ are closely related; both are characterized by a network of connected [FeO_6] octahedra. However, in the cubic phase these octahedra are corner-sharing only whereas in the hexagonal phase, there are layers of corner- and face-sharing octahedra. The cubic crystal structure of $BaFeO_3$ was shown to be retained down to at least 8 K without signs of a Jahn-Teller distortion in the x-ray or neutron diffractograms.[55] However, at temperatures between 111 and 97 K, the formation of an anti-ferromagnetic order and sudden decrease in electrical resistivity were observed indicating that cubic $BaFeO_3$ is subject to a magnetic phase transition.[55,69] Interestingly, a similar behavior was observed in the hexagonal phase of $BaFeO_3$, albeit here accompanied by structural distortions.[70] Highly oxidized hexagonal $BaFeO_{3-\delta}$ is a paramagnetic semiconductor at room temperature, with uniform [FeO_6] octahedra that undergoes two phase transitions as the temperature is decreased. Below $T_\mathrm{t} = 170$ K, a charge disproportionation of type $2\mathrm{Fe}^{4+} \rightleftharpoons \mathrm{Fe}^{4+\delta} + \mathrm{Fe}^{4-\delta}$ takes place, where the differently charged Fe ions are associated with distorted [FeO_6] octahedra.[70] The transition is marked by a maximum in the magnetic susceptibility[54,71–74], a peak splitting in the Mössbauer spectra[72,75–77], and an abrupt decrease in the electrical resistivity[71,73]. The second phase transition features the formation of a long-range anti-ferromagnetic state at a Néel temperature of $T_\mathrm{N} = 130$ K, which is sustained down to at least 4 K.[74,76]

Although both phases - hexagonal and cubic - develop an anti-ferromagnetic order below T_N associated with lower electrical resistivity, the hexagonal phase, in addition, develops a charge disproportionate state with distorted [FeO_6]-octahedra below T_t. The purely corner-sharing network of octahedra in the cubic phase, on the other hand, seems to be more resilient to this type of lattice distortions than the hexagonal phase. This chapter explores potential structural instabilities in the cubic phase using first-principles phonon calculations. It will be shown that the partially occupied $pd\sigma^*$ band in the cubic structure produces stresses on the Fe-O bonds that strive for a deformation of the ideal

[FeO_6] octahedra. These stresses appear to be on the brink of causing a Jahn-Teller distortion. Here, the total energy is slightly reduced upon distortion, suggesting a Jahn-Teller distorted ground state of $BaFeO_3$ at low T.

6.2 Dynamical Instability in Cubic $BaFeO_3$

When a cubic $BaFeO_3$ cell is subjected to a geometry optimization in VASP, the cubic symmetry is preserved and a lattice constant of $a = 4.015$ Å is obtained. The optimization algorithms in VASP are designed to find local extreme points on the potential energy surface, for which the forces acting on the ions, i.e. the first derivative of the energy with respect to atomic displacements, vanish, or fall below previously specified thresholds. However, extreme points can be both local minima or maxima on the potential energy surface, between which the algorithm cannot distinguish. Thus, a converged structure is not necessarily stable under the thermodynamic conditions specified in the calculation, i.e. at absolute zero and constant pressure. To assess the stability of a structure, the phonon modes can be analyzed, which describe the behavior of the ions under oscillation around their original position.

The *dynamical* stability of a structure requires that any displacement of an ion away from its equilibrium position leads to an increase in the total energy of the crystal. In the case of a dynamical instability, the total energy is reduced against certain atomic displacements, such that the distorted structure is more stable. The change in total energy with respect to finite atomic displacements can be calculated with DFT by performing multiple static calculations of displaced structures. This allows one to obtain the force constant matrix $C_{ij}^{\alpha\beta}$,

$$C_{ij}^{\alpha\beta} = \frac{\partial^2 E}{\partial u_{i\alpha} \partial u_{j\beta}} \tag{6.1}$$

where an ion i (j) is displaced by $u_{i\alpha}$ in the direction α (β). The condition for a stable structure requires all elements of the force constant matrix to be positive, while instabilities result in negative elements. When treating the vibrational motion of ions in periodic structures, the displacement of an ion in the unit cell and its periodic images are commonly described in terms of a plane wave,

$$u_{i,\alpha} = \epsilon_{i,\alpha,q}\, e^{i(qR_{i,\alpha} - \omega_{i,q}t)} \tag{6.2}$$

where the collective displacement of the ions of type i are characterized by a wave vector $q = \frac{2\pi}{\lambda}$, with λ being the wave length. For a given wave vector q, the ions move in a direction specified by the polarization vector $\epsilon_{i,\alpha}$ with the frequency ω_i. Since each of the N ions in the unit cell has three degrees of freedom ($\alpha = 1, 2, 3$), there are $3N$ plane waves at a given q-vector that describe the motion of the ions in a crystal. The polarization vectors and frequencies of the $3N$ plane waves for a given q-vector are obtained by solving the eigenvalue problem,

$$D_{ij}^{\alpha\beta}(q)\epsilon_{i,\alpha,q} = M\omega_{i,q}^2\epsilon_{i,\alpha,q} \tag{6.3}$$

where $D(q)$ is the dynamical matrix, defined as the force constant matrix transformed into reciprocal space,

$$D_{ij}^{\alpha\beta}(q) = \frac{1}{\sqrt{M_i M_j}} \sum_{\alpha} C_{ij}^{\alpha\beta} e^{(-iq\ R_\alpha)} \tag{6.4}$$

with M_i (M_j) being the mass of ion i (j).[41,42] The solutions of equation 6.3 yield $3N$-phonon modes, or normal modes, for every given q-vector, where each mode is characterized by its eigenvector (polarization vector) and eigenvalue (frequency squared). In the case of a dynamical instability, the eigenvalues of certain phonon modes are negative and structural distortions in the direction of the associated polarization vector decrease the total energy of the crystal. The decrease in total energy of such a distortion is greater the more negative the respective eigenvalue is. In the present study, the forces entering the dynamical matrix were calculated using VASP. Phonon modes were calculated in a harmonic approximation using the code phonopy[42].

Figure 6.1 shows the dispersion of the frequencies, $\omega_{i,q}$, as a function of q on a path through the Brillouin zone for cubic $BaFeO_3$. There are five atoms in the unit cell, resulting in 15 phonon modes for a given q-point. The frequencies of these modes are partly degenerate, which reduces the number of different frequencies at certain q-points, e.g. to only five values at the Γ-point. Upon leaving the Γ point, the collective displacement of ion i and its periodic images is enveloped by smaller wavelengths, which may have different frequencies and thus result in a dispersion of the phonon mode. In addition, the dispersion may be the result of the phonon mode being the combination of displacements of ions i and j, provided that both displacements have the same symmetry properties for a given q-point. Inspection of figure 6.1 shows a pronounced structural instability at the R-point ($\omega = -4.25i$ THz), which corresponds to a doubly degenerate phonon mode.

The negative frequency of this modes shows that structural distortions in the direction of the polarization vectors must reduce the total energy of the crystal, rendering the cubic structure of $BaFeO_3$, as such, dynamically unstable.

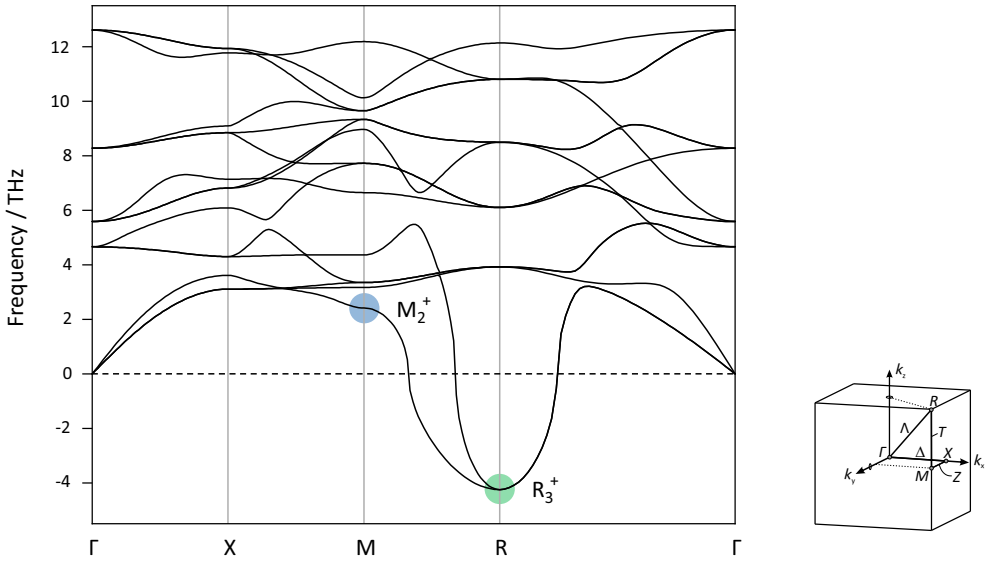

Figure 6.1: Phonon dispersion of cubic $BaFeO_3$ with negative imaginary frequencies at the R-point.

As the dynamical matrix $D(q)$ contains information about the physical properties of the crystal, it must be totally invariant with respect to the symmetry operations of the crystal. This means that the eigenvectors (polarization vectors) must behave under the symmetry operations of the crystal according to some irreducible representations (irreps) of the space group. In this regard, the displacements that produce the negative frequency in 6.1 are found to transform as the two dimensional irrep R_3^+ (2). This irrep belongs to the group O_h of the q-vector $R = (\frac{\pi}{a}, \frac{\pi}{a}, \frac{\pi}{a})$. The atomic displacements associated with the phonon mode R_3^+ fall in the class of Jahn-Teller distortions, which produce different bond lengths in the $[FeO_6]$ octahedra and thus lift the orbital degeneracy of the Fe $3d$-orbitals. The polarization vectors associated with these modes are depicted in figure 6.2.

Since in $BaFeO_3$ the ground state is dominated by a $d^5\underline{L}$ configuration that leaves the Fe ion Jahn-Teller inactive, the origin of the R_3^+ instability is not immediately evident and will be further investigated in § 6.4. Apart from the R_3^+ mode, a Jahn-Teller distortion can also be induced by displacements associated with the mode M_2^+. This mode induces the same pattern of octahedral deformation as in figure 6.2b, but yields a different cooperative ordering of distorted $[FeO_6]$-octahedra than the R_3^+ mode (discussed further in § 6.3). From the phonon dispersion in figure 6.1 it can be seen that the frequency of the M_2^+ mode is positive ($\omega = 2.41$ THz). This means that displacements associated with M_2^+

lead to an increase in the total energy of the crystal, and that the material is dynamically stable with respect to these displacements. Both Jahn-Teller distortions, R_3^+ and M_2^+, are typically coupled with the strain mode Γ_3^+ that leads to a stretching or contraction of the cubic lattice parameters without further symmetry reduction than already caused by the Jahn-Teller distortion. As a result, the distorted structures not only contain different bond lengths in the [FeO_6] octahedra, but also different lattice parameters.

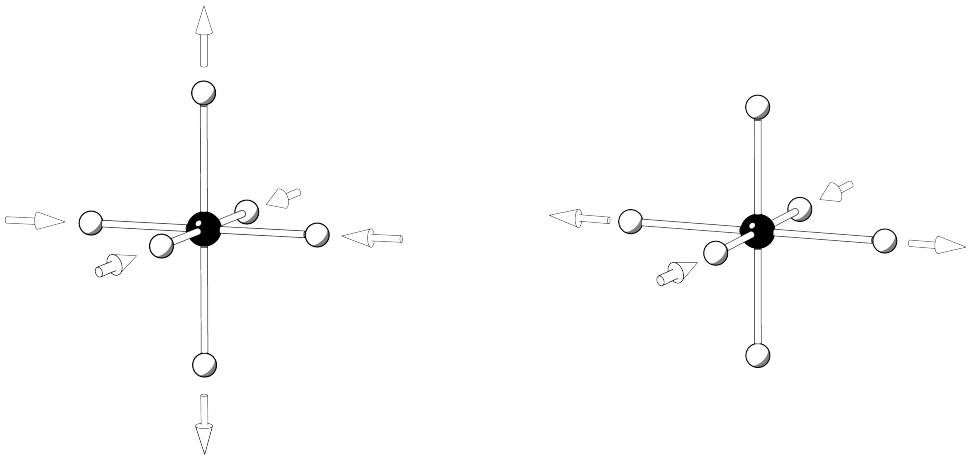

(a) R_3^+ **(b)** R_3^+, M_2^+

Figure 6.2: Octahedral deformation, or, polarization vectors associated with the phonon modes R_3+ and M_2^+.

It is important to note that negative frequencies in figure 6.1 indicate dynamical instabilities only in the cubic phase. Structural distortions in the direction of a given phonon mode can, however, readily destabilize additional modes, see e.g.[78,79]. It may therefore be that some phonon modes - although initially stable in the cubic phase - are unstable in a distorted structure, i.e. in combination with other modes. For the present study, only distortions associated with the R_3^+ and M_2^+ modes, combined with the strain mode Γ_3^+ are considered, since the phonon dispersion clearly indicates that $BaFeO_3$ is susceptible to such a Jahn-Teller distortion. Whether additional phonon modes, e.g. those associated with octahedral rotations or breathing type distortions, become destabilized in the Jahn-Teller distorted structures is not further investigated here.

6.3 Phase transition

Having identified the dynamical instability associated with the R_3^+ mode, a series of static DFT calculations was performed, in which the structure is successively distorted

along one of its polarization vectors. The total energy as a function of mode amplitude along this series should eventually reach a minimum by which the correct magnitude of Jahn-Teller distortion in $BaFeO_3$ can be determined. The amplitude, Q_i, of a given mode i is defined as,

$$Q_i = \sqrt{\sum_j \zeta_{i\alpha}^2} \tag{6.5}$$

where $\zeta_{j\alpha}^2$ is the displacement of ion j in the direction α.[80] In the case of multidimensional irreps, such as R_3^+, an order parameter has to be chosen to specify along which of the polarization vectors the structure is to be distorted. The order parameters that correspond to figures 6.2a and 6.2b are $(a, 0)$ and $(0, a)$ for the R_3^+ mode, respectively (see appendix C.2 for more information). The distorted structures are generated with the program ISODISTORT[81,82], as part of the ISOTROPY suite[83], in conjuncture with tools from the Bilbao Crystallographic Server[65,66]. The total energy as a function of amplitude of the R_3^+ mode with order parameter $(a, 0)$ is shown in figure 6.3.

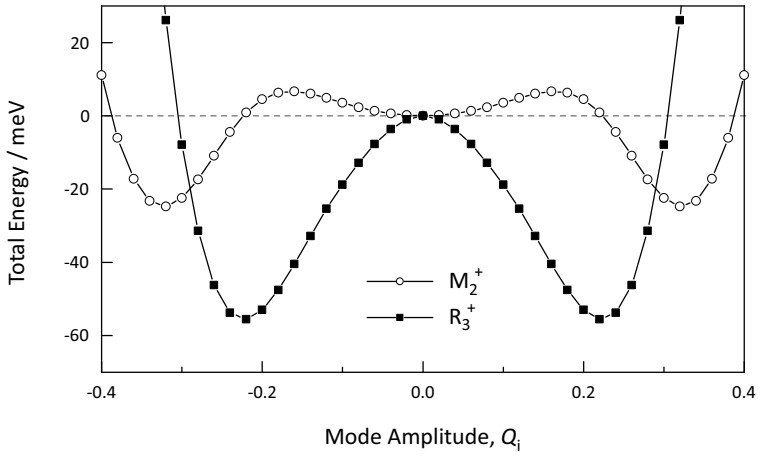

Figure 6.3: Total energy evolution for distortions associated with the phonon modes R_3^+ and M_2^+, starting from the parent cubic structure of $BaFeO_3$ at fixed cell volume.

As expected from the phonon dispersion, the total energy is minimized along the R_3^+ distortion and eventually reaches a minimum at $Q_{R_3^+} = 0.22$. In addition, figure 6.3 shows how the energy evolves along the other Jahn-Teller displacement mode, M_2^+. Here, the total energy increases for small displacements of $Q_{M_2^+} < 0.16$, which causes the respective frequency in the phonon dispersion to be positive. For larger displacements, however, the energy begins to decrease again and reaches a minimum at $Q_{M_2^+} = 0.32$. The undistorted cubic structure therefore represents a local energy minimum with re-

spect to the M_2^+ phonon mode, and the system must overcome an activation barrier of 6.65 meV in order to transition to the more stable, Jahn-Teller distorted phase. The curves in figure 6.3 represent a particular choice of order parameter for which the largest energy gain upon distortion was found. A comparison with other order parameters and their combinations can be found in appendix C.2.

The Fe-O bond lengths within the distorted [FeO_6] octahedra are point-symmetric, reflecting the *gerade* symmetry of the underlying irreps. For example, when one Fe-O bond is elongated, the opposite Fe-O bond is elongated in the same way. The irrep R_3^+ with order parameter $(a, 0)$ induces a bond length distribution with four Fe-O bonds being elongated (shortened) and two Fe-O bonds shortened (elongated), depending on the sign of the amplitude. This corresponds to the displacement depicted in figure 6.2a. The irrep M_2^+ leaves two Fe-O bond lengths unchanged with respect to the cubic phase and leads to an elongation (contraction) of two and contraction (elongation) of another two Fe-O bonds. This corresponds to the displacement depicted in figure 6.2b. For both irreps, the Jahn-Teller distorted structures become tetragonal with the space groups $\mathrm{I4/mmm}$ and $\mathrm{P4/mbm}$ for the R_3+ and M_2^+ modes, respectively. The main difference between the Jahn-Teller distortion patterns, R_3^+ and M_2^+, is related to the cooperative ordering of distorted [FeO_6] octahedra within a given structure. The two Jahn-Teller distorted structures, corresponding to the energy minima in figure 6.3, are depicted in figure 6.4.

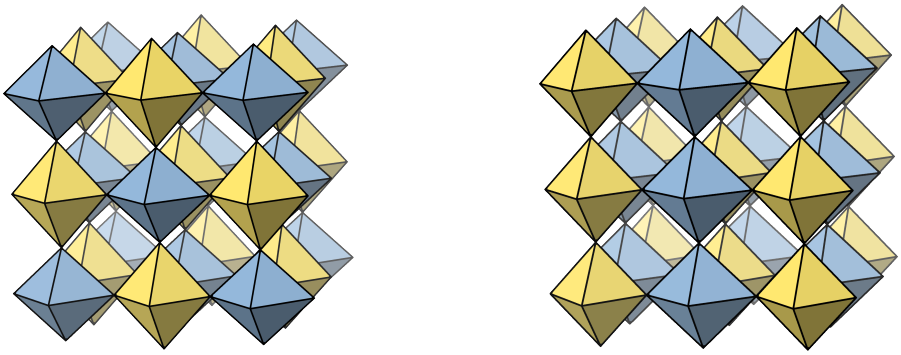

(a) Rock-salt ordering

(b) Columnar ordering

Figure 6.4: Jahn-Teller distorted structures of $BaFeO_3$ with alternating tetragonal elongation (yellow) and tetragonal compression (blue) of [FeO_6] octahedra. Distortion patterns induced by the phonon modes R_3^+ (a) and M_2^+ (b).

A distortion associated with the R_3^+ mode produces a three-dimensional arrangement of alternating elongated and contracted octahedra, resulting in a so-called rock-salt ordering[84], as shown in figure 6.4a. On the other hand, a distortion associated with the M_2^+ mode produces a columnar ordering of the octahedra along one of the crystallographic

axes, also referred to as checkerboard ordering[84], as shown in figure 6.4b. The different ordering patterns reflect the symmetry of the underlying wave vectors to which the irreps R_3^+ and M_2^+ belong. The q-vector $R = (\frac{\pi}{a}, \frac{\pi}{a}, \frac{\pi}{a})$ is left invariant by symmetry operations of the group O_h, while the q-vector $M = (\frac{\pi}{a}, \frac{\pi}{a}, 0)$ has a lower symmetry described by the group D_{4h}. The latter contains a four-fold rotation axis along q_z, which leads to a columnar arrangement of the octahedra in the corresponding real space direction z and a checkerboard arrangement in the planes normal to that direction. In the O_h group there is no single high-symmetry axis, hence, the resulting distortion pattern is isotropic.

Jahn-Teller distortions are typically coupled to different strain modes that result in a stretching or contraction of the cubic lattice constants without further symmetry reduction. These are, in particular, the strain modes Γ_3^+, a uniform stretching (contraction) of two of the lattice constants and a contraction (stretching) of the third lattice constant compatible with the Jahn-Teller bond length distribution, and Γ_1^+, a uniform volume expansion (contraction) of the cell. The strained cells, in turn, allow for larger Jahn-Teller mode amplitudes, so that ultimately the distorted structure with the lowest energy results from a fine balance between the different modes. In order to find the correct balance of strain and Jahn-Teller mode amplitudes, the two structures of figure 6.4 are relaxed in a standard geometry optimization in VASP. The resulting lattice parameter, bond lengths

Table 6.1: Structural properties of different phases of $BaFeO_3$.

	Cubic	R_3^+	M_2^+	defect approach
Space group	$Pm\bar{3}m$	$I4/mmm$	$P4/mbm$	$P4/mbm$
Crystal system	cubic	tetragonal	tetragonal	tetragonal
ΔE_{tot} / eV per f.u.	0.0	-0.020	-0.016	-0.016
a / Å	8.028	7.991	8.130	8.130
b / Å	-	7.991	8.130	8.130
c / Å	-	8.244	7.952	7.952
$a^{\mathrm{pseudo-cubic}}$ / Å	4.014	4.038	4.035	4.035
Fe^1 - O^1 / Å	2.007	2.082	2.174	2.173
Fe^1 - O^2 / Å	-	2.082	1.891	1.891
Fe^1 - O^3 / Å	-	1.857	1.988	1.988
Fe^2 - O^1 / Å	-	1.913	-	-
Fe^2 - O^2 / Å	-	1.913	-	-
Fe^2 - O^3 / Å	-	2.265	-	-

and total energy with respect to the cubic phase are summarized in table 6.1.

Although the geometry optimization in VASP is generally aimed at finding the ground state structure, the algorithm often ends up at local minima associated with metastable phases of higher symmetry. While this has practical implications in the present case, allowing the determination of the strain and Jahn-Teller mode amplitudes of the R_3^+ and M_2^+ distorted structures, it makes it difficult to asses whether one of the obtained structures is, in fact, the true ground state structure. The distortion along specific irreps that are identified on the basis of dynamical instabilities in the phonon dispersion - as has been done here - represents only one of many possible techniques to search for the ground state structure. Another technique is to break the symmetry of the structure by incorporating a point defect and perform a geometry optimization of the defective structure. Depending on the type of point defect, this can lead to a substantial deformation of the lattice, often well beyond the immediate ionic environment of the defect. In a second step, the point defect is removed and the distorted structure is relaxed again. This technique was used here by inserting a protonic defect in $BaFeO_3$ and relaxing the distorted structure with the proton removed. The results of this calculation are appended in table 6.1 under the point "defect approach".

The incorporation of a proton and subsequent relaxation of the structure has led to the same distortion pattern as obtained by the M_2^+ mode - a columnar ordering of distorted [FeO_6] octahedra with three different Fe-O bond lengths per octahedron. The distortion lowers the total energy per formula unit by 16 meV and is accompanied by a volume increase of 1.6%. What is found to be energetically most favorable is a distortion along the R_3^+ mode, in line with the initial observation that this mode produces a negative frequency in the phonon dispersion. It is therefore concluded that $BaFeO_3$ undergoes a displacive phase transformation of $\mathrm{Pm\bar{3}m} \rightarrow \mathrm{I4/mmm}$ type, where the total energy is reduced by 20 meV per formula unit. This phase transformation is accompanied by a volume increase of 1.8%. In the distorted structure, there are two different types of Fe ions, one having four short and two long Fe-O bonds representing a so-called tetragonal elongation of the ideal octahedron, and one having four long and two short Fe-O bond, representing a tetragonal compression of the ideal octahedron.

6.4 Electronic Structure of distorted $BaFeO_3$

The ideal octahedral geometry represents the optimal arrangement of six negatively charged anions around a central cation in terms of minimizing both steric interactions as well as electrostatic repulsion between the electron density in the $M-L$ bonds (M =metal, L =ligand).[57] However, when the degenerate t_{2g} or e_g orbitals of the central transition

metal cation are partially occupied, the electrostatic repulsion between these d-electrons and the ligands can be reduced by distorting the ideal octahedral geometry. For example, in a high-spin d^4 system with ideal octahedral geometry, the d_{z^2} and $d_{x^2-y^2}$ orbitals forming the e_g band must have identical dispersion and both be half occupied. A tetragonal elongation of the octahedra in z-direction reduces the electrostatic repulsion between electrons occupying the d_{z^2} orbital and the ligands, in exchange for an increased repulsion between electrons occupying the $d_{x^2-y^2}$ orbital and the ligands. This effectively lowers the energy of the d_{z^2} orbital which becomes occupied, while increasing the energy of the now unoccupied $d_{x^2-y^2}$ orbital. Such a distortion of the ideal octahedra, known as a Jahn-Teller distortion, is realized when the decrease in electrostatic repulsion between occupied d-orbitals and ligands overcompensates for the energetic losses associated with the deformation of the ideal octahedral geometry. The atomic displacement patterns of a Jahn-Teller distortion have either M_2^+- or R_3^+-symmetry, the latter of which has been identified in $BaFeO_3$ in the preceding section.

Although the distortion pattern found in $BaFeO_3$ is isostructural to a Jahn-Teller distortion, the underlying physical origin for such a distortion is not immediately clear. As a consequence of the $d^5\underline{L}$-dominated configuration in $BaFeO_3$, the spin-up d-band ends up being largely occupied and the Jahn-Teller activity of the Fe ion is effectively quenched. The few e_g states visible in the Fermi level region reveal a mixed $d^5\underline{L} - d^4$ configuration, which in principle could be weakly Jahn-Teller active, but these states are strongly delocalized in pd bonds such that an octahedral distortion is unlikely to reduce the electrostatic repulsion between e_g- and p-orbital electrons.

Figure 6.5, left, shows the DOS curve for Jahn-Teller distorted $BaFeO_3$ compared to the original cubic phase. Despite a high overall similarity between the distorted and undistorted structures, there are significant differences in the DOS curves, in particular in the Fermi level region of the spin-up DOS. What can be observed here is an increase in the spin-up DOS below the Fermi level (highlighted in green), a depletion at and right above the Fermi level (highlighted in red) and, again, an increase in the top most states of the spin-up DOS. These changes can be brought out even more clearly by focusing on the group of orbitals that most strongly contributes to the DOS in this region - the $p_\parallel$-orbitals - and by calculating a DOS difference curve according to equation 6.6.

$$\Delta_{\mathrm{PDOS}} = \sum p_\parallel\,(R_3^+) - \sum p_\parallel\,(\mathrm{cubic}) \tag{6.6}$$

The corresponding Δ_{PDOS} curve is shown in figure 6.5 in the middle. The increase and depletion observed in the total spin-up DOS are seemingly mirrored in the Δ_{PDOS} curve

of the $p_{||}$ orbitals. Integrating the green shaded areas below the Fermi level in figure 6.5, left and middle, shows that the $p_{||}$ orbitals account for 85% of the increase in total spin-up DOS. As for the depleted red shaded region at and above the Fermi level, the $p_{||}$ orbitals account for 107% of the total spin-up DOS, implying that there must be a slight increase in some other type of orbital. And finally, the green shaded area in the topmost region of the total spin-up DOS comes from $p_{||}$ orbitals to 43%. For comparison, the Δ_{PDOS} curve for the e_g orbitals (not shown here, see figure B.5 in the appendix) does exhibit the same pattern as the $p_{||}$ orbitals, but constitute only 3% to the increase below the Fermi level, 15% to the depletion at and above the Fermi level, and 27% to the increase in the top-most part of the spin-up DOS. In conclusion, the $p_{||}$ orbitals alone cannot explain the changes in the overall spin-up DOS but they constitute the largest portion of the changes.

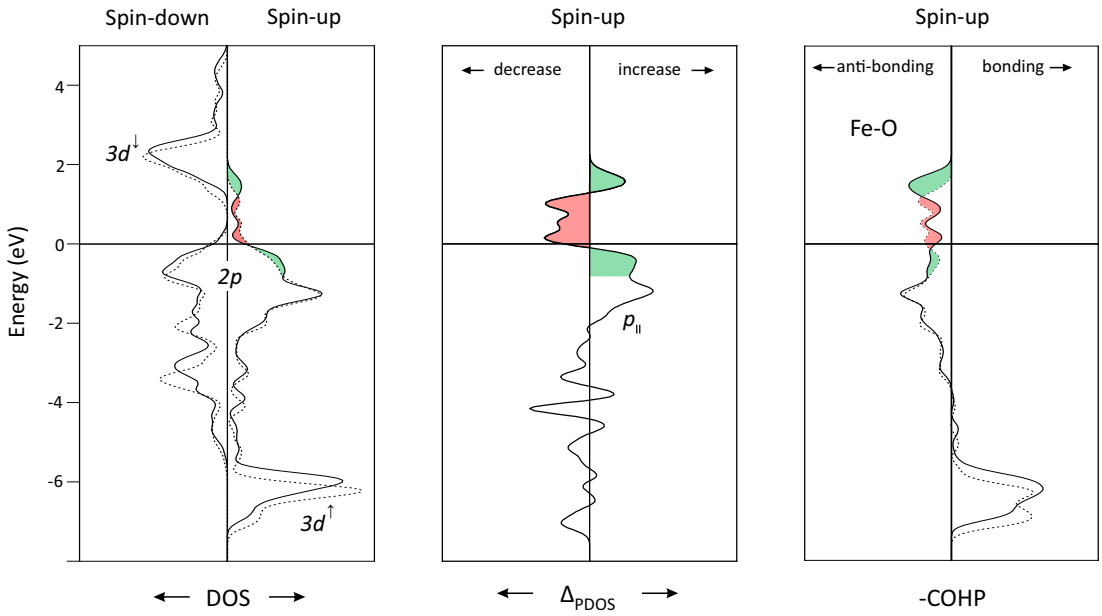

Figure 6.5: Total DOS (left), pDOS ($p_{||}$) difference curve (middle) and COHP curve (right) of Jahn-Teller distorted $BaFeO_3$. The dashed line corresponds to the undistorted cubic phase.

The spin-up COHP curve for the average Fe-O bond in figure 6.5, right, further shows that the increase in the total spin-up DOS and Δ_{PDOS} below and above the Fermi level (green shaded regions) is associated with a stronger antibonding character of the pd bond. On the other hand, states in the depleted red shaded area become less anti-bonding, as evidenced by the COHP curve. This is an important piece of information because it shows that the octahedra are distorted at the cost of an increased Fe-O antibonding character and that the distortion is not aimed at alleviating the stresses caused by the occupied $pd\sigma^*$ bonds, as had been hypothesized previously. Therefore, it must be the electrostatic

interaction between the electrons in the $p_{\|}$ orbitals and the axially coordinated Fe ions that drives the distortion and overcompensates for the increased antibonding character. How an octahedral distortion can help to enhance the electrostatic interaction between electrons in $p_{\|}$ orbitals and axially coordinated Fe ions can be readily explained in terms of a localized orbital picture. Figure 6.6 shows how the orbital degeneracy of the three $p_{\|}$ orbitals in the unit cell of $BaFeO_3$ is lifted upon tetragonal elongation and tetragonal compression of an ideal octahedron, respectively. When Fe and O ions approach each other, the electrons in the $p_{\|}$ orbital whose lobe is pointing along the Fe-O axis experience a stronger electrostatic attraction by the positively charged Fe ions which effectively lowers the energy of the respective p-orbital. Thus, the changes observed in figure 6.5 concerning the total spin-up DOS and the Δ_{PDOS} curve can be regarded as a de-facto splitting of the $p_{\|}$-frontier orbitals with a non-vanishing DOS in the formed band gap and an increased DOS directly above and below it.

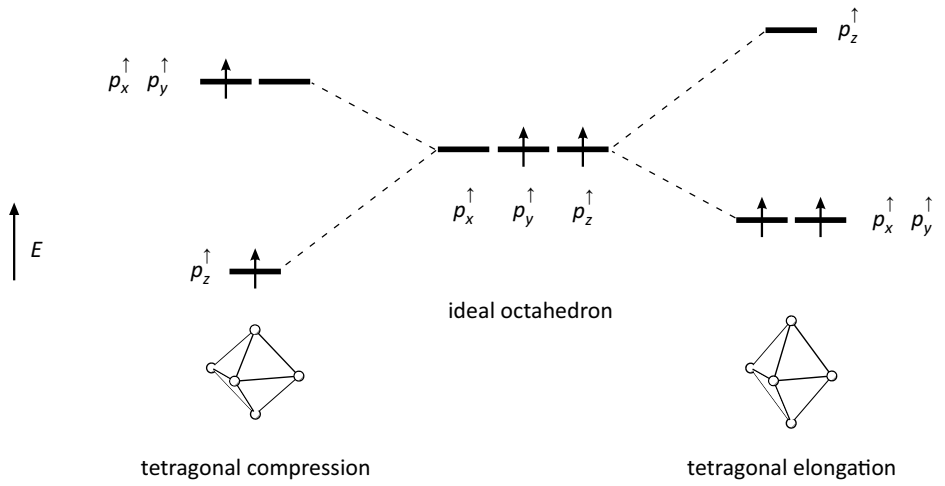

Figure 6.6: Set of $p_{\|}$ orbitals under the effect of a tetragonal elongation and tetragonal compression. The degeneracy of the p_x and p_y orbitals in the distorted octahedra is most likely to be lifted by $p_x + p_y$ and $p_x - p_y$ linear combinations (see § 5.4). The orbital in the direction of elongation (compression), p_z, is more strongly destabilized (stabilized) due to a greater change in bond lengths.

Ultimately, the above analysis shows that due to the negative charge transfer in $BaFeO_3$, the Jahn-Teller activity of the Fe ion is indeed largely quenched. But the introduced ligand hole must be distributed over the degenerate $p_{\|}$ orbitals, which, in turn leads to a Jahn-Teller activity of the oxygen ions that eventually induces a distortion from the ideal cubic perovskite structure. The electronic properties of the Jahn-Teller distorted phase are summarized in table 6.2, along with the corresponding data of undistorted

cubic $BaFeO_3$. The plethora of other subtle differences in electronic structure between distorted and undistorted phases will not be discussed further here.

Table 6.2: Electronic properties of different phases of $BaFeO_3$.

	NON SPIN-POL.	SPIN-POL.	JT DISTORTED
a / Å	4.015	4.015	4.038
Δ_{CFS} / eV	0.32	0.85	not determined
U / eV	-	6.85	6.73
Δ_{CT} / eV	not determined	-3.52	-3.26
$d^{\uparrow}$	3.12	4.82	4.78
$d^{\downarrow}$	3.12	1.00	1.07
μ_{eff} / μ_{B}	0.00	4.7	4.6
Q_{Ba}	1.77	1.75	1.73
Q_{Fe}	1.28	1.64	1.65
Q_{O}	-1.02	-1.13	-1.12
IP	not determined	6.1	6.1*
iCOHP $pd\sigma$	-0.54	-0.40	-0.47
iCOHP $pd\pi$	-0.27	-0.29	-0.32
iCOHP FE-O	-2.19	-1.93	-2.01

The non spin-polarized and polarized cubic phases are discussed in chapter 5.

Δ_{CFS}: crystal field splitting; U: energy cost for transferring an electron from the spin-up $3d$ band to the spin-down $3d$ band (with respect to band centers of mass), after[60,61]; Δ_{CT}: charge transfer energy, energy cost for transferring an electron from the O $2p$ band to the Fe $3d$ band, after[60,61]; $d^{\uparrow}$, $d^{\downarrow}$: d-band population; μ_{eff}: effective magnetic moment given by $\mu_{\mathrm{eff}} = g\sqrt{S(S+1)}$, where $g \approx 2$ and $S = (d^{\uparrow} - d^{\downarrow})/2$[62]; Q_{i}: Mulliken atomic charges; iCOHP: crystal orbital Hamilton population integrated up to the Fermi level. The Fe-O iCOHP includes $pd\sigma$, $pd\pi$, and orbital overlap between O 2s and Fe 3p orbitals.

* The IP of the JT-distorted phase is estimated from a slab calculation using the ideal cubic structure fixed to the pseudo-cubic lattice constant of the JT-distorted phase, see[85] for details.

6.5 Summary and discussion

By analysis of the phonon spectrum, the cubic perovskite structure of $BaFeO_3$ has proven to be dynamically unstable with respect to the phonon mode R_3^+ - a Jahn-Teller type of distortion of the ideal octahedral geometry. A distortion of the cubic perovskite structure along the R_3^+ mode and subsequent relaxation of the lattice dimensions in VASP led to a new distorted ground state whose total energy is 0.02 eV per formula unit lower than that of the original cubic phase. These results indicate that $BaFeO_3$ undergoes a displacive phase transformation of type $\mathrm{Pm\bar{3}m} \rightarrow \mathrm{I4/mmm}$ at low temperature. Despite a lower total energy, the Jahn-Teller distorted phase has not been observed experimentally. This may be rationalized by the very small differences in total energy that the distortion entails. Table 6.3 summarizes the relative total energies of different phases of $BaFeO_3$, highlighting the flat potential energy surface between the distorted Jahn-Teller and undistorted cubic phases. Energy differences as small as these are easily outweighed by external factors, be it experimentally by the presence of point defects, or theoretically by the choice of calculation parameters. For example, a slight oxygen non-stoichiometry implies a higher occupation of the $p_{\|}$ dominated valence band and, as such, would weaken the Jahn-Teller activity of the oxygen ligands.

Table 6.3: Relative stabilities of different phases of $BaFeO_3$ with respect to the ideal cubic phase.

	Cubic	Jahn-Teller	Hexagonal*
E_{tot} / f.u. (eV)	0.00	-0.02	-0.07

* Hexagonal structure taken from [86] with space group $\mathrm{P6_3/mmc}$ and optimized lattice parameter of $a = 5.716$ Å and $c = 14.060$ Å.

A global energy minimum can, according to table 6.3, only be arrived at by allowing the structure to give up its corner-sharing network of [FeO_6] octahedra and transition into a phase of alternating corner- and edge sharing octahedra with an overall hexagonal crystal symmetry. The energy barrier of this transition is expected to be large, since it involves the breaking of Fe-O bonds and the tilting of [FeO_6] octahedra. The higher total energy of the cubic, or Jahn-Teller, phase explains why it is generally easier to synthesize the hexagonal phase of $BaFeO_3$.

The origin of the distortion could be traced to an unusual Jahn-Teller activity of the ligands, as a consequence of the negative charge transfer and the associated $d^5\underline{L}$ configuration. A distortion of the ideal octahedral geometry is able to lift the degeneracy of

the $p_{\|}$ orbitals between which the ligand hole is distributed. Although it had previously been hypothesized in this work that the occupied $pd\sigma^*$ states in the cubic phase might cause a deformation of the octahedra to reduce the orbital overlap, it is the increase in electrostatic attraction between electrons in the $p_{\|}$ orbitals and the Fe ions that causes the deformation. By analogy to the classical Jahn-Teller effect where partially occupied degenerate d-orbitals cause a distortion of R_3^+ symmetry, the term Jahn-Teller distortion is used here as well.

7 Oxygen Non-Stoichiometry in $Ba_xSr_{1-x}FeO_{3-\delta}$

7.1 Introduction

This chapter explores the oxygen non-stoichiometry in the system $Ba_xSr_{1-x}FeO_{3-\delta}$ using DFT calculations of defective supercells and first-principles thermodynamics.

The $Ba_xSr_{1-x}FeO_{3-\delta}$ system is known to exhibit a wide range of oxygen stoichiometries without loosing its structural integrity in terms of corner-sharing octahedra , see e.g.[87]. The associated high concentrations of oxygen vacancies combined with a relatively high mobility give rise to appreciable oxygen ion conductivities[88] - in addition to the prevailing electronic conductivity. From a defect-chemical perspective, oxygen vacancies are formed according to reaction 7.1 where neutral oxygen is released into the surrounding atmosphere, with electrons of the former oxygen ion annihilating electron holes.

$$\mathrm{O_O^x} + 2\mathrm{h}^{\bullet} \rightleftharpoons \mathrm{v_O^{\bullet\bullet}} + \frac{1}{2}\,\mathrm{O_2(g)} \tag{7.1}$$

The enthalpy change during reaction 7.1 varies significantly with A-site composition of the perovskite host. For instance, thermogravimetry experiments in the $Ba_xSr_{1-x}FeO_{3-\delta}$ system revealed that the enthalpy increases from 0.60 eV in $Ba_{0.95}La_{0.05}FeO_3$[89] to 1.06 eV in $SrFeO_3$[90]. Moreover, in various compositions of the $(La, Ba, Sr)FeO_{3-\delta}$ system, the enthalpy shows pronounced deviations from ideal dilute behavior with increasing vacancy concentration - a typical hallmark of defect interactions.[38,89,91] For example, in $Ba_{0.5}Sr_{0.5}FeO_3$, thermogravimetry experiments show that the oxygen vacancy formation enthalpy increases from 0.63 to 0.87 eV with increasing vacancy concentration from $\delta = 0$ to 0.5.[89] The variations in oxygen vacancy formation enthalpy with composition and stoichiometry of the perovskite have been proposed to correlate with several electronic structure descriptors such as the position of the d-band[92], or the position of the Fermi level relative to O $2p$ band center[93,94]. More specifically, in[91,95], the so-called itinerant electron model was introduced to explain the variations with oxygen vacancy concentration. In this model, the enthalpy variation is related to an increasing Fermi level at which electrons from the removed oxygen ions are subsequently accommodated in the course of reaction 7.1.

Notwithstanding the physical significance of the proposed correlations, they have rarely been quantified by DFT calculations of defective systems (i.e. calculated Fermi level po-

sitions). This may stem from technical problems in distributing several vacancies in a confined supercell and the associated computational cost of calculating different defect arrangements. Here, these problems are tackled by a systematic screening of possible defect arrangements and a large number of DFT calculations. The energy change of reaction 7.1 is calculated for $Ba_xSr_{1-x}FeO_{3-\delta}$ ($x = 0.0,\ 0.5,\ 1.0$) as a function of vacancy concentration in the range $0 \leq \delta \leq 0.5$. The calculations reveal systematic trends in the vacancy formation energy, with both x and δ correlated to changes in the electronic structures of the defective supercells. This study has been published in[85], together with additional data on Fe-O bond lengths distributions and chemical expansion, which are not fully discussed here.

7.2 The nature of oxygen vacancies in $BaFeO_{3-\delta}$

The formation of an oxygen vacancy in the lattice of $BaFeO_3$ induces a distortion of the local ionic environment near the vacancy in response to the missing Fe-O bonds. Figure 7.1 shows this local lattice distortion in the $\{100\}$ and $\{010\}$ lattice planes sliced from a $Ba_8Fe_8O_{23}$ supercell. In addition to the ionic structure, contour lines of the electron density distribution are shown which are discussed further below. Focusing on the ionic structure in figure 7.1, top, it can be noticed that the missing Fe-O bonds around the vacancy cause the adjacent Fe ions to move away from the vacant site, inducing bent Fe-O-Fe arrangements perpendicular to the direction of the vacancy. The square pyramidal [FeO_5] polyhedra surrounding the oxygen vacancy contract with bond lengths of about 1.9 Å, compared to $2.0 - 2.2$ Å in the [FeO_6] octahedra.

Local lattice distortions generally tend to localize the redistributed electron density near the defective site, thereby effectively screening the electrostatic field emanating from the defect.[41] This effect can be analyzed by plotting the electron density difference between a neutral supercell with an oxygen vacancy and doubly positively charged supercell of the same geometry in which no redistributed electron density is present. As such, the electron density difference reveals where the two electrons highest in energy, originating from the removed O^{2-} ion, have been redistributed to. The result is shown in figure 7.1 in the form of a contour map, where each line represents a constant value of electron density difference. High values indicate that a lot of electron density of the removed oxygen ion has been taken up.

As can be seen in figure 7.1, top, there is no electron density remaining within the vacancy itself, effectively making it a doubly positively charged vacancy, $v_O^{\bullet\bullet}$. Instead, the electron density of the removed oxygen is redistributed among the Fe and O ions adjacent to the vacancy. The shape of the contour lines in the extension of the Fe-$v_O^{\bullet\bullet}$-Fe axis

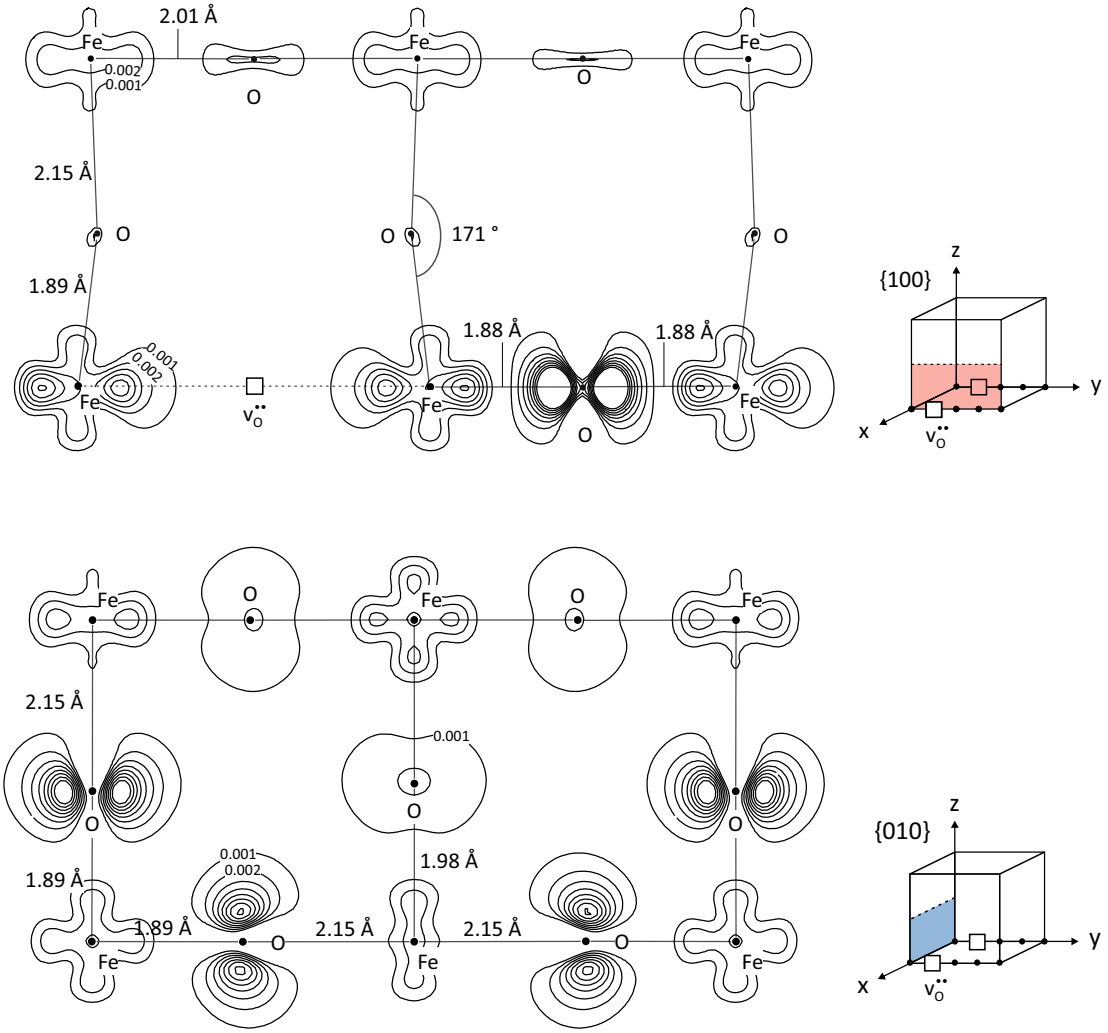

Figure 7.1: Ionic structure and electron density difference in the {100} (top) and {010} (bottom) lattice planes sliced from a $Ba_8Fe_8O_{23}$ supercell.

thereby resembles the $p_{\parallel}$ and $d_{x^2-y^2}$ orbitals, indicating that the electron holes annihilated during reaction 7.1 correspond to the previously discussed $pd\sigma^*$ states at the Fermi level (see § 5). The contour lines in figure 7.1, top, should, however, not obscure the fact the oxygen ions perpendicular to the Fe-$v_O^{\bullet\bullet}$-Fe axis, too, take up electron density by populating $p_{\perp}$ orbitals whose nodal plane coincides with the {100} lattice plane depicted in figure 7.1. This can be revealed by looking at the lattice plane {010}, shown in in figure 7.1, bottom. The shape of the contour lines seemingly resembles $p_{\perp}$ orbitals which are populated during reaction 7.1. This is an unexpected result considering that in fully stoichiometric cubic $BaFeO_3$ the electron holes were identified predominantly as unoccupied $p_{\parallel}$ and, to a minor extent, as unoccupied Fe e_g orbitals. Evidently, the presence of an oxygen vacancy destabilizes the $p_{\perp}$ orbitals of vicinal oxygen ions in the [FeO_5] octa-

hedra from deep within the O $2p$ band to the Fermi level, rendering them partially unoccupied. Upon redistributing the electron density from the removed oxygen ion, these states are populated and consequently appear in the electron density difference plot, figure 7.1. Although the overall degree of delocalization is difficult to quantify, figure 7.1 provides clear evidence that the electron density of the removed oxygen is redistributed beyond the Fe ions closest to the vacancy in the [FeO_5] octahedra. In fact, most of the redistributed electron density is taken up by oxygen ions in the [FeO_5] octahedra and, to a lesser extent, in the neighboring [FeO_6] octahedra. This is consistent with the ligand character of the electron holes in $BaFeO_3$ as discussed in § 5, and demonstrates that, from a chemical point of view, both Fe and O ions have a mixed valence character that give rise to the red-ox activity of $BaFeO_{3-\delta}$.

7.3 General considerations on the $BaFeO_{3-\delta}$ crystal structure

It has already been shown in connection with figure 7.1 that the formation of an oxygen vacancy leads to a substantial distortion of its local ionic environment. As the vacancy concentration rises, these lattice distortions become more severe and can affect large parts of the crystalline host, eventually leading to phase transformations and several different phases of $BaFeO_{3-\delta}$ as a function of δ. In general, $BaFeO_{3-\delta}$ adopts two different crystal structures - hexagonal and cubic - depending on external conditions. Using, for instance, the oxidized hexagonal crystal structure as a starting point, an increasing concentration of oxygen vacancies leads first to a phase transformation into a pseudo-cubic perovskite phase with corner-sharing [FeO_6] octahedra [96,97] and, ultimately, into a vacancy ordered monoclinic perovskite phase with Fe in octahedral and tetrahedral coordination [98,99]. Notably, the monoclinic phase is not isostructural with the Brownmillerite phase found for $Sr_2Fe_2O_5$ but has a more complex structure. [98,100]

The phase transformation with increasing δ from a hexagonal to a pseudocubic crystal structure can be well explained in terms of the Goldschmidt tolerance factor [101], defined as

$$t = \frac{r_A + r_O}{\sqrt{2}(r_B + r_O)} \tag{7.2}$$

where r refers to the ionic radii in ABO_3 perovskites. With a Goldschmidt tolerance factor exceeding 1, $BaFeO_{3-\delta}$ crystallizes in a hexagonal perovskite structure with face-sharing [FeO_6] octahedra. However, as more O $2p$ and Fe $3d$ orbitals become occupied in the course of reaction 7.1, the ionic radii of these ions increase allowing the Gold-

schmidt tolerance factor to approach 1 and thus making a purely corner-sharing network of [FeO_6] octahedra more favorable. This not only explains the phase transformation from a hexagonal into a pseudo-cubic structure but, in fact, opens up a synthesis route to obtain metastable cubic $BaFeO_3$ by low-temperature oxidation of the pseudocubic $BaFeO_{3-\delta}$ phase. A relaxation into the ground state hexagonal structure is thereby prevented by large energy barriers associated with the breaking of Fe-O bonds. As a result, fully oxidized cubic $BaFeO_3$ could be stabilized.[55] Alternatively, the cubic perovskite phase can be stabilized by slight doping with, e.g., 0.05 La or Ce on the Ba site,[102,103] bringing the Goldschmidt tolerance factor closer to 1. Using the fully oxidized cubic phase as the starting point, an increasing concentration of oxygen vacancies leads naturally to the pseudo-cubic crystal structure and, at even higher vacancy concentrations, to the vacancy-ordered monoclinic phase.

In the present work, the oxygen non-stoichiometry is explored for a wide range of δ that covers both the pseudo-cubic and the vacancy-ordered monoclinic phase. However, the investigated phase space is restricted to the pseudo-cubic phase because the experimental data available for comparison are obtained for cubic $Ba_{0.95}La_{0.05}FeO_{3-\delta}$. Oxygen non-stoichiometric phases are modelled by distributing up to 4 oxygen vacancies over the 24 oxygen sites of a $2 \times 2 \times 2$ supercell, corresponding to concentrations of $\delta = 0.125,\ 0.25,\ 0.375,\ 0.5$. The different $v_O^{\bullet\bullet}$ arrangements in supercells containing more than one vacancy yield over 100 distinguishable configurations. Some of these configurations containing Fe in 4-fold coordination yielded lower total energies after structural optimization than the lowest-energy configuration with only 5- or 6-fold coordination. This can be rationalized by $BaFeO_{3-\delta}$ favoring the vacancy-ordered monoclinic phase, leading to 4- and 6-fold-coordinated Fe. To separate the cubic and pseudocubic phases from the phase space, only configurations with Fe in 5- or 6-fold coordination are used for the analysis, while configurations with Fe in 4-fold coordination are deliberately omitted. This is justified for several reasons: (*i*), vacancy ordered superstructures are not found experimentally for doped $BaFeO_{3-\delta}$ perovskites at elevated temperatures where $v_O^{\bullet\bullet}$ concentrations are measured, (*ii*), a comparison can be made to $Ba_xSr_{1-x}FeO_{3-\delta}$ and $SrFeO_{3-\delta}$ which generally crystallize in cubic or pseudo-cubic crystal structures, and (*iii*), including configurations containing 4-fold coordinated Fe would lead to a spurious energy contribution from the phase transformation into the reaction enthalpies. The $v_O^{\bullet\bullet}$ arrangements found for the $BaFeO_{3-\delta}$ system, leaving Fe in 5- or 6-fold coordination, are assumed to be the same for the $Ba_xSr_{1-x}FeO_{3-\delta}$ and $SrFeO_{3-\delta}$ compositions. For a given oxygen stoichiometry, the three configurations with the lowest total energy are used for the calculation of the thermodynamic parameters. The oxygen vacancy positions and optimized lattice parameter of these configurations are given in appendix B.4.

7.4 THERMODYNAMICS OF OXYGEN NON-STOICHIOMETRY

Oxygen vacancy formation energies were calculated for $Ba_xSr_{1-x}FeO_{3-\delta}$ (x=0.0, 0.5, 1.0) through

$$\Delta_f E_{v_O^{\bullet\bullet}} = \left(E^{tot}(v_O^{\bullet\bullet}) + \frac{1}{2} E^{tot}(O_2) \right) - E^{tot}(perf) \tag{7.3}$$

where E^{tot} of the defective and perfect crystals are obtained from supercell calculations, and $\frac{1}{2} E^{tot}(O_2)$ by placing an O_2 molecule in a vacuum box. To be precise, the reaction describes the excorporation of neutral O with the former electrons of the O^{2-} remaining in the vacancy containing supercell, thereby reducing the ions surrounding the vacancy. Moreover, oxygen vacancy formation energies were calculated as a function of oxygen vacancy concentration in the range $0 \leq \delta \leq 0.5$, by accommodating various oxygen vacancies in one supercell. The results of these calculations are shown in figure 7.2; with increasing Sr content, the vacancy formation energy increases and, for a given composition, the formation energy exhibits an approximately linear increase with increasing oxygen vacancy concentration.

In an ideal dilute system, defect interactions are negligible and the defect formation energy is expected to be independent of the defect concentration. As shown in figure 7.2, however, the formation energy increases strongly across all compositions indicating non-ideal behavior and the presence of profound defect interactions. The approximately linear dependence of the formation energy on the concentration of vacancies justifies the use of a phenomenological first-order correction, as described in § 3.2,

$$\Delta_f E_d = \Delta_f e_d + a_d \, c_d \tag{7.4}$$

with a constant molar formation energy at dilute conditions, $\Delta_f e$, and an interaction parameter, a_d, describing the deviation from dilute behavior at higher defect concentrations. With respect to the data in figure 7.2, a linear fit yields the molar vacancy formation energy, $\Delta_f e_{v_O^{\bullet\bullet}}$, and an interaction parameter $a_{v_O^{\bullet\bullet}}$.

Focusing first on the variation of $\Delta_f e_{v_O^{\bullet\bullet}}$ with A-site composition of the perovskite host. The molar vacancy formation energy is found to increase with increasing Sr content, ranging from 0.36 eV in $BaFeO_{3-\delta}$ to 0.81 eV in $SrFeO_{3-\delta}$. This trend correlates with a variety of other materials properties that describe the ionic and electronic structure of the materials listed in table 7.1. Specifically, with increasing Sr-content the pseudocu-

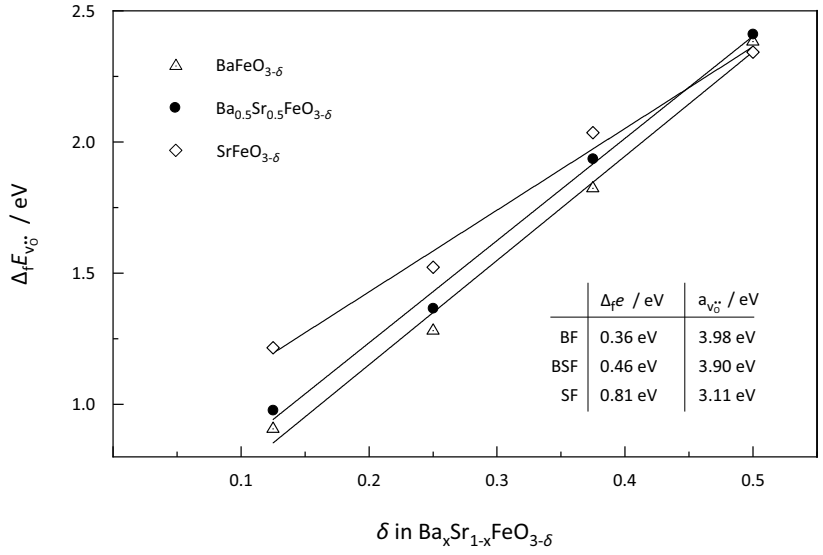

Figure 7.2: Oxygen vacancy formation energies for the system $Ba_xSr_{1-x}FeO_{3-\delta}$ ($x = 0.0,\ 0.5,\ 1.0$) as a function of vacancy concentration, δ. Each data point represents an average of the three configurations with the lowest total energies.

bic lattice constant decreases owing to the smaller ionic radius of Sr compared to Ba, and the Jahn-Teller distortion becomes negligible, as evidenced by the ratio of a/c. The disappearance of the Jahn-Teller distortion is driven by the increase in Fe-O covalency, which suppresses the Jahn-Teller activity of the oxygen ions, and increase in lattice rigidity, which increases the strain energy required to deform the cubic structure. In addition, with increasing Sr content, the iCOHP of the Fe-O bond becomes more negative, indicating that the covalent bond strength increases. Furthermore, the centers of mass of the occupied O $2p$ bands, ϵ_{O2p}, shift downward in energy. Notably, the values of ϵ_{O2p} given in table 7.1 are aligned to the Fermi level, which itself lies in the upper region of the O $2p$ band. As such, the centers of mass indirectly measure the width of the O $2p$ band, which is larger the more negative the center of mass is. The Mulliken atomic charges change only mildly across the series and appear to be less sensitive towards structural changes induced by Sr substitution on the A-site. In conclusion, the discussed correlations suggest that the vacancy formation energy is large in materials with a small pseudo-cubic lattice constant, a highly negative average Fe-O iCOHP, and a deep center of mass of the O $2p$ band relative to the Fermi level.

To understand, why these parameters correlate with the vacancy formation energy, it is helpful to take a closer look at the individual energetic contributions to the overall vacancy formation energy. To form an oxygen vacancy, it is necessary to break two Fe-O bonds, which consequently consumes twice the total Fe-O binding energy. The total Fe-

Table 7.1: Thermodynamic parameters along with structural and electronic properties of $Ba_xSr_{1-x}FeO_{3-\delta}$. Pseudo-cubic lattice constants refer to $\delta = 0$.

	$BaFeO_{3-\delta}$	$Ba_{0.5}Sr_{0.5}FeO_{3-\delta}$	$SrFeO_{3-\delta}$
$\Delta_f e_{v_O^{\bullet\bullet}}$ / eV	0.36	0.46	0.81
$a_{v_O^{\bullet\bullet}}$ / eV	3.98	3.90	3.11
$a^{\mathrm{pseudo-cubic}}$ / Å	4.036	3.958	3.893
a/c	0.971	1.000	1.000
iCOHP Fe-O / eV	-2.015	-2.051	-2.142
$Q^{\mathrm{O}}_{\mathrm{Mulliken}}$ / e	-1.125	-1.130	-1.131
ϵ_{O2p} / eV	-2.160	-2.375	-2.572

O iCOHP (-2.015 eV in case of $BaFeO_3$) represents the covalent contribution of the total Fe-O binding energy that must be supplied to the system in order to break the bond, and therefore naturally correlates with the vacancy formation energy. Although the energy required for breaking the Fe-O bond is minimized by the structural relaxation near the vacancy, the total Fe-O iCOHP certainly represents a major contribution to the vacancy formation energy. In fact, it was shown in[104] that for the case of $SrTiO_3$, structural relaxation reduces the energy cost of forming an oxygen vacancy by $\approx$ 1-2 eV. In addition, electrons of the removed oxygen ion remain in the material and must be redistributed to the Fermi level. The energy required for this process can be estimated by multiplying the difference in O $2p$ band center and the Fermi level, -2.16 eV, with the Mulliken charge of the oxygen ion, -1.13 eV, giving 2.44 eV (in case of $BaFeO_3$). Consequently, when the difference in O $2p$ band center and Fermi level becomes greater - as is the case with increasing Sr-content - the vacancy formation energy increases. Note that the O $2p$ band centers in table 7.1 are relative to the Fermi level at $E = 0$ eV, i.e., they represent the difference between band center and Fermi level. These considerations naturally explain why both iCOHP and ϵ_{O2p} correlate with the vacancy formation energy.

7.5 Defect interactions

The defect interaction parameters in the system $Ba_xSr_{1-x}FeO_{3-\delta}$ ($x = 0.0,\ 0.5,\ 1.0$) were found to be positive across the compositional variations (see table 7.1). This means that the presence of oxygen vacancies disfavors further vacancy formation, or, equivalently, that the presence of holes disfavors further oxidation, i.e. hole formation. The underlying defect interactions must have implications either on the Fe-O bond strength,

the position of the O $2p$ band, the oxygen ion charge, or a combination of these properties, for the formation energy to change. The evolution of these properties as a function of oxygen vacancies is therefore imperative for an understanding of the nature of the defect interactions. Figure 7.3 shows a comparison of the densities of states of fully oxidized Jahn-Teller distorted $Ba_8Fe_8O_{24}$ and reduced $Ba_8Fe_8O_{20}$, both referenced to the vacuum potential.

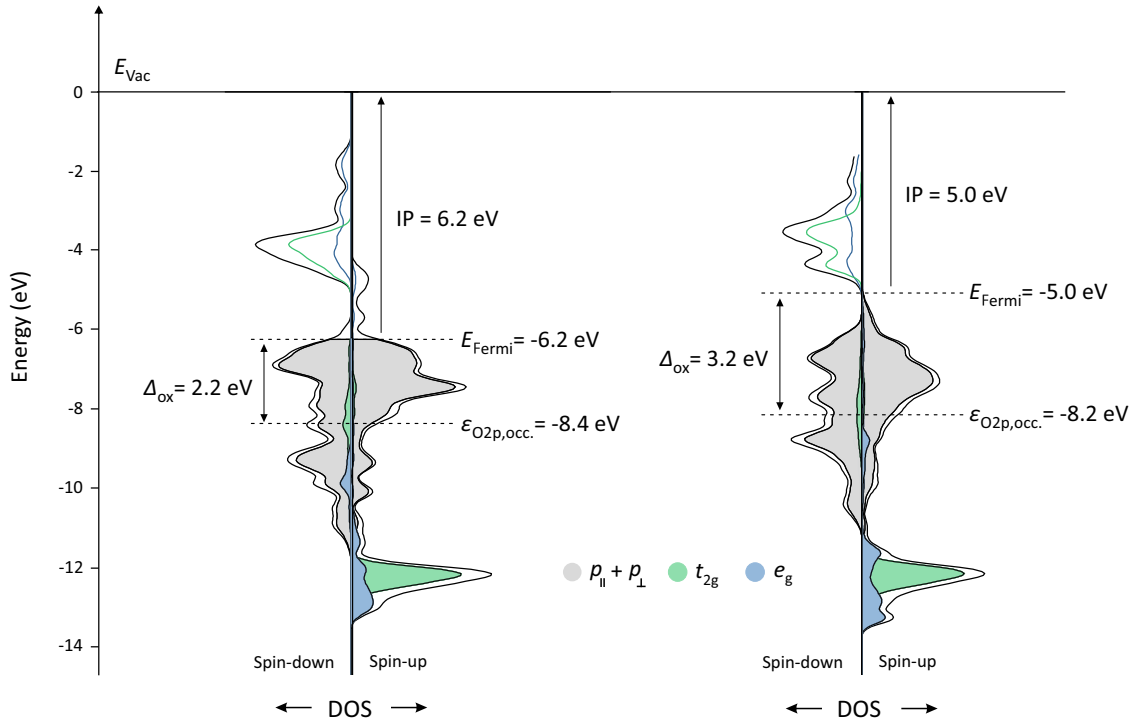

Figure 7.3: Densities of states (DOS) of $Ba_8Fe_8O_{24}$ (left) and $Ba_8Fe_8O_{20}$ (right). The scale on the x-axis is the same, demonstrating how in $Ba_8Fe_8O_{20}$ the O $2p$ DOS is generally smaller.

The center of mass of the O $2p$ band relative to the same vacuum level changes little as the concentration of vacancies increases, but the difference between the center of mass and the Fermi level increases significantly from 2.2 eV in the oxidized to 3.2 eV in the reduced state. This is because electrons remaining in the crystal from the removed oxygen ions are accommodated at the Fermi level, which consequently goes up. The rate at which the Fermi level rises is thereby determined by the DOS at the Fermi level which, in $Ba_xSr_{1-x}FeO_{3-\delta}$, is small and causes the Fermi level to increase rapidly as relatively few electrons are added. If, theoretically, the Fermi level were in the middle of a band rather than in the flat upper end, adding electrons would lead to a much smaller increase in the Fermi level. By subsequent annihilation of the electron holes, the O $2p$ band in the reduced state eventually becomes fully occupied. Consequently, the average Mulliken

atomic charge of the oxygen ions becomes more negative from -1.13 eV in the oxidized to -1.32 eV in the reduced state. With regard to the vacancy formation energy, a greater difference between the center of mass of the O $2p$ band and the Fermi level, in combination with a more negative ionic charge of the oxygen ions, increases the energetic cost of removing an oxygen ion from the crystal.

On the other hand, the increased energy requirements associated with the higher Fermi level are counterbalanced by a decrease in Fe-O bond strength as the concentration of vacancies rises. In particular, the average Fe-O iCOHP becomes less negative from -2.02 eV in the oxidized state to -1.78 eV in the reduced state. This reduces the energetic cost of breaking the Fe-O bonds required to remove an oxygen ion from the crystal. The remaining energy contributions to the overall formation energy are the lattice distortion in the vicinity of the introduced vacancy and the energy gain upon forming an O-O double bond in the oxygen molecule. The latter is expected to change only slightly as a function of oxygen vacancies because the center of mass of the O $2p$ band relative to the vacuum potential in figure 7.3 remains largely unchanged in the oxidized (-8.4 eV) and reduced states (-8.2 eV). Thus, the difference to the center of mass of the O $2p$ band in the oxygen molecule also remains unchanged, hence, the energy gain upon forming an O-O double bond in the oxygen molecule. The local lattice distortion around the vacancy aims to mitigate the energy increase associated with the breaking of the Fe-O bonds. It is hard to estimate whether the energy gain from local distortions depends on vacancy concentration. On a qualitative basis, lattice distortions would be expected to become stronger at higher vacancy concentrations because the pseudocubic lattice constant increases and the overall lattice becomes softer. On the other hand, lattice distortions from previously introduced vacancies could dampen the structural flexibility and reduce the extent of further lattice distortions. It is therefore assumed as first approximation that the extent to which the energetic losses associated with the Fe-O bond breaking are mitigated by local lattice distortions is independent of the concentration of oxygen vacancies.

To obtain a net increase of the vacancy formation energy as a function of vacancy concentration, those energy contributions that increase must outweigh those that decrease as a function of vacancy concentration. Indeed, as shown in figure 7.4, the slopes of twice the average Fe-O iCOHP (because *two* Fe-O bonds must be broken to remove one oxygen ion) and the center of mass of the O $2p$ band multiplied by the average oxygen ion Mulliken charge are different. The decrease in Fe-O bond strength is overcompensated by the increased energy requirements to move the electrons of the former oxygen ion from the center of the O $2p$ band to the Fermi level. When combined, this translates into a net increase in the energy required to form an oxygen vacancy, and could explain the deviation from ideal dilute behavior. In conclusion, the observed non-ideality in figure 7.2 can

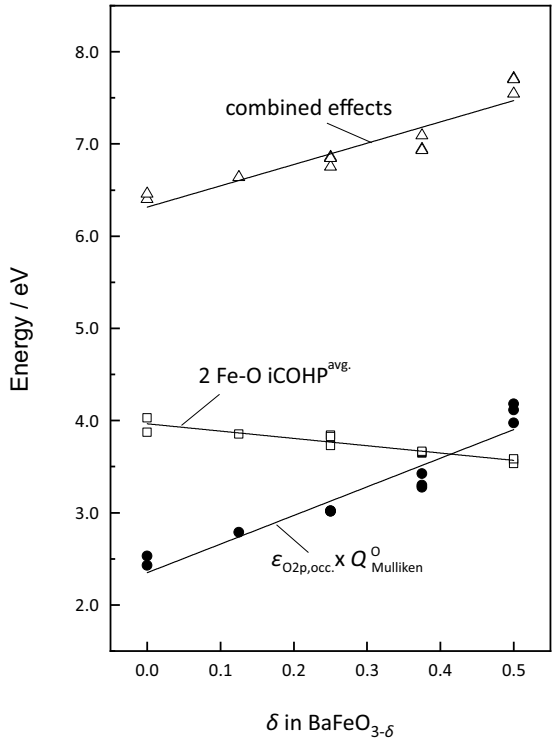

Figure 7.4: Different energy contributions to the overall oxygen vacancy formation energy. The Fe-O iCOHP represents the covalent part of the Fe-O binding energy, $\epsilon_{\mathrm{O2p,occ.}}$ is given relative to the Fermi level such that it represents the difference between band center and Fermi level.

be assigned to the annihilation of delocalized ligand holes and the associated increase in Fermi level. These findings also provide quantitative evidence for the itinerant electron model[95], in which the increase in vacancy formation energy was argued to stem from an increasing Fermi level without taking into account the evolution of Fe-O bond strength, oxygen ion charge, or absolute position of the O $2p$ band.

7.6 Summary and discussion

The formation of oxygen vacancies in $Ba_xSr_{1-x}FeO_{3-\delta}$, formed by release of neutral oxygen under the consumption of electron holes, is characterized by substantial perturbations of both ionic and electronic structures. Investigations of oxygen non-stoichiometric supercells by DFT showed that the square pyramidal [FeO_5] polyhedra surrounding the oxygen vacancy contract, with their equatorial oxygen ions relaxing slightly into the vacancy. Analysis of the electron density distribution further showed that the electrons coming from the removed oxygen ion are delocalized beyond the [FeO_5] polyhedra with oxygen ions taking up the majority of the redistributed electron density.

Table 7.2: Comparison of calculated oxygen vacancy formation energies and experimentally measured standard molar formation enthalpies of $(Ba,Sr)FeO_{3-\delta}$.

	$BaFeO_3$	$Ba_{0.5}Sr_{0.5}FeO_3$	$SrFeO_3$
Calculated in this work			
$\Delta_f e_{v_O^{\bullet\bullet}}$ / eV	0.36	0.46	0.81
$a_{v_O^{\bullet\bullet}}$ / eV	3.98	3.90	3.11
Experimental data			
$\Delta_f^0 h_{v_O^{\bullet\bullet}}^{exp.}$ / eV	0.60* [14]	0.63* [14]	1.06** [90]
$a_{v_O^{\bullet\bullet}}^{exp.}$ / eV	0.10 [14]	0.48 [14]	0.00** [90]

* measured enthalpies extrapolated to $\delta = 0$. The experimental value for $BaFeO_3$ was determined for La-stabilized $Ba_{0.95}La_{0.05}FeO_{3-\delta}$.

** average of formation enthalpies in the range $0.28 < \delta < 0.43$; no significant deviation from ideal dilute behavior was observed in this study

Oxygen vacancy formation energies in $Ba_xSr_{1-x}FeO_{3-\delta}$ were found to increase with increasing Sr substitution on the A-site, ranging from 0.36 eV in $BaFeO_{3-\delta}$ to 0.81 eV in $SrFeO_{3-\delta}$. This is caused by the smaller ionic radius of Sr compared to Ba and an associated increase in Fe-O bond strength and a higher Fermi level. The latter increases the energetic cost of redistributing the electrons of the removed oxygen ions from the O $2p$ band to the Fermi level. The calculated formation energies are consistent with experimentally measured standard molar enthalpies of oxidation, see table 7.2. Both theoretical and experimental techniques agree that the vacancy formation energy/enthalpy increases with increasing Sr content, with absolute values differing by merely ≈0.2 eV. The comparability is, nevertheless, impaired by different pressure and temperature conditions: Experimental data refer to standard conditions of $T = 298$ K and $p = 1$ bar, while calculations were performed at 0 K and 0 bar. To estimate the effect of the different conditions, the contribution of lattice vibrations to the oxygen vacancy formation enthalpy was calculated using first-principles phonon calculations for the case of one vacancy in a $2 \times 2 \times 2$ supercell (appendix B.1). Increasing the temperature from 0 to 298 K thereby reduces the energy of oxygen vacancy formation by only $\approx$ 0.1 eV, which justifies the comparison between the experimental and theoretical data in Table 7.2.

For a given composition, the formation energy was found to increase linearly as a function of vacancy concentration, which is interpreted as a hallmark of defect interactions. Unlike classical defect interactions between charged point defects, here, the interactions involve delocalized electron holes at the Fermi level. As vacancy concentration increases,

the Fermi level shifts upward in energy, increasing the energy cost of further vacancy formation. This corresponds to what has been termed the itinerant electron model[91], originally used to model oxygen non-stoichiometry in $La_{0.8}Sr_{0.2}CoO_{3-\delta}$[95]. However, the model is based on generic rigid bands instead of calculated DOS and neglects the evolution with vacancy formation of the B-O bond strength and the oxygen ion charge, both key determinants of the formation energy. As shown in this work, these properties undergo significant changes: The charge of the oxygen ions becomes more negative and the covalency of the Fe-O bond decreases with vacancy formation. The slopes of the vacancy formation energy versus vacancy concentration can be interpreted as materials specific defect interaction parameters. Comparison with experimentally measured interaction parameters in table 7.2, however, reveals pronounced disparities between theoretical and experimental values. The calculated interaction parameters are larger than the experimental ones and show a decreasing trend with Sr content, while no systematic trend is observed in the experimental data. It could not finally be clarified where these inconsistencies come from; the employed DFT functional may overestimate the degree of hole delocalization which translates into larger defect interaction parameters and, the experimental techniques comes with certain error bars. Nevertheless, the trend of increasing oxygen vacancy formation energy and oxygen vacancy concentration is consistent.

8 Proton Uptake in $Ba_xSr_{1-x}FeO_{3-\delta}$

8.1 Introduction

In this chapter, the proton uptake in the system $Ba_xSr_{1-x}FeO_{3-\delta}$ is studied using DFT calculations of defective supercells combined with first-principles thermodynamics.

In equilibrium with ambient water vapor, oxides of the $Ba_xSr_{1-x}FeO_{3-\delta}$ family were found to exhibit a moderate propensity for the dissociative absorption of water in their bulk. The incorporated hydrogen species are present as mobile proton interstitial defects that give rise to proton conductivity at intermediate temperatures, i.e. 300–700 °C.[14] Owing to the presence of now three different types of charge carriers - electron holes, oxygen vacancies and protons - these materials belong to the class of so-called triple conducting oxides.[6] However, measured proton concentrations in this class of materials have been found to be systematically lower than in acceptor doped $Ba(Zr,Ce)O_{3-\delta}$ closed-shell perovskite oxides - despite having the same structure type and similar molar volumes. In addition to this overall trend, the propensity for proton uptake in triple conducting oxides varies greatly with the cation composition on the A- and B-site of the perovskite host.[14] For instance, in the system $Ba_xSr_{1-x}FeO_{3-\delta}$, measured proton concentrations vary between 0.14% per formula unit in $Sr_{0.85}Ba_{0.15}FeO_{3-\delta}$[105] and 3% in $Ba_{0.95}La_{0.05}FeO_{2.53}$[14] at 250 °C and 16 mbar H_2O. Moreover, doping with large, redox-inactive cations such as Zn^{2+} on the B-site can massively increase proton uptake, e.g., from 3% in $Ba_{0.\,95}La_{0.05}FeO_{2.53}$ to 10% in $Ba_{0.95}La_{0.05}Fe_{0.8}Zn_{0.2}O_{2.4}$ under the same conditions.[14] The generally lower propensity of triple conducting oxides towards proton uptake compared to closed-shell oxides is believed to stem from a detrimental interaction between protons and electron holes. Indeed, measurements of $Ba_{1-x}La_xFeO_{3-\delta}$ show that proton uptake is significantly reduced in samples with higher hole concentrations.[106] Following this line of argument, the doping with redox-inactive cations on the B-site increases the proton uptake, since here too, the electron hole concentration is decreased - leaving aside the specifics of the different dopants here.

The interaction between protons and electron holes appears to be of paramount importance in governing the propensity of triple conducting oxides towards proton uptake. Yet, the nature of this interaction is still largely unknown. To clarify this, a concise quantum-chemical treatment is required that correctly captures the properties of the delocalized electron holes. To date, only few theoretical studies have dealt with proton incorporation in triple conducting oxides[107–111], focusing primarily on the calculation of the ther-

modynamic parameters regarding the formation and mobility of protonic defects. The underlying materials parameters favoring high proton uptake have, in turn, rarely been studied by first-principles DFT calculations; the interaction between protons and electron holes practically not at all.

These topics are addressed in this chapter using DFT calculations of $2 \times 2 \times 2$ supercells containing protonic defects and variable amounts of oxygen vacancies (thus also electron holes). The nature of protonic defects in the system $Ba_xSr_{1-x}FeO_{3-\delta}$ ($x = 0.0, 0.5, 1.0$) is analyzed and the thermodynamic parameters governing their formation are calculated. A new thermodynamic formalism is developed based on which proton uptake can be decomposed into individual reaction steps whose reaction energies are traceable by DFT. This helps rationalize the observed trends in proton uptake and unveils an intriguing correlation between proton uptake and the ionization potential of solid oxides. The results of this chapter are published in[44,85].

8.2 The nature of protonic defects in (Ba, Sr)$FeO_{3-\delta}$

The incorporated protons formally occupy an interstitial site. However, the formed protonic defect is more realistically described as a hydroxide ion (short covalent O-H bond) on an oxygen ion site. The proton also leads to the formation of hydrogen bonds to neighboring oxygen ions and can induce considerable local lattice distortions. Here, the equilibrium geometries of protonic defects are determined for the system $Ba_xSr_{1-x}FeO_{3-\delta}$ ($x = 1,\ 0.5,\ 0$) by performing structural optimizations with DFT using $2 \times 2 \times 2$ supercells. As a starting geometry, the proton is placed on one of the idealized proton positions shown in figure 8.1a.

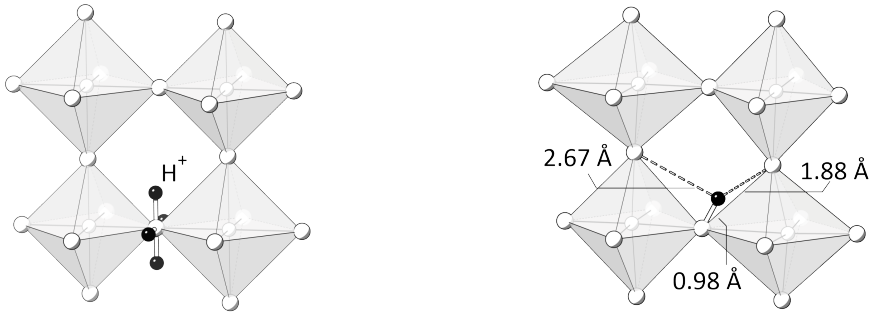

(a) Idealized proton positions **(b)** Optimized geometry

Figure 8.1: Crystal structures of $BaFeO_3$ in polyhedral representation with idealized proton positions (a) and optimized geometry of a protonic defect (b).

Table 8.1: Geometries of protonic defects in $Ba_xSr_{1-x}FeO_{3-\delta}$.

	$BaFeO_{3-\delta}$	$Ba_{0.5}Sr_{0.5}FeO_{3-\delta}$	$SrFeO_{3-\delta}$
d_{O-H} / Å	0.984	0.985	0.985
$d_{O\cdots H}$ / Å	1.877	1.850	1.910
$\angle_{Fe-O-H}$ / °	62.3	74.5	79.1

The choice of the starting geometry is based on previous investigations of protons in perovskite oxides. It has been shown both experimentally by neutron diffraction[112–118], muon-spin relaxation measurements[119] and IR-spectroscopy[120], and theoretically by atomistic modelling[121] and quantum mechanical calculations[108,120,122–126], that protons reside preferably on interstitial lattice sites in close proximity of ≈ 1 Å to an oxygen ion, with which they form hydroxyl groups, $OH_O^{\bullet}$. The O-H axis of these groups is typically oriented perpendicular to the Fe-O-Fe axis along the bisector of two oxygen-oxygen connecting lines, as shown in figure 8.1a. A few studies of $LaScO_3$[115,118,127] have reported a different orientation of the O-H axis with the proton pointing to an *A*-site cation, resulting in O-H bond lengths up to 1.2 Å (not shown here).

Figure 8.1b shows the optimized geometry of a protonic defect in $Ba_8Fe_8O_{24}H$. The proton is located at a typical 0.98 Å distance to an oxygen ion and is tilted significantly toward another intra-octahedral oxygen ion. This results in one shorter O···H bond length of 1.88 Å and a longer one of 2.67 Å. The driving force for the tilt stems from the energy gain upon forming a stronger hydrogen bond, which competes with the strain energy required to distort the lattice in that direction.[128] In $BaFeO_3$, the energy gain from the hydrogen bond formation seems to have significantly outweighed the associated strain energy, resulting in a relatively low Fe-O-H tilt angle of 62.3°. The geometries of protonic defects in $Ba_{0.5}Sr_{0.5}FeO_3$ and $SrFeO_3$ have a similar overall appearance. However, as the crystal lattice contracts and becomes more rigid with increasing Sr content, the strain energy necessary to tilt the O-H axis increases and causes systematically larger tilt angles of 74.5° in $Ba_{0.5}Sr_{0.5}FeO_3$ and 79.1° in $SrFeO_3$, see table 8.1. In contrast to the tilt angles and the associated O···H bond lengths, the O-H bond length appears to be rather insensitive towards changes in *A*-site composition.

Protonic defects also induce a significant perturbation of the local electronic structure. Figure 8.2 shows a contour map of the electron density distribution around a protonic defect in $BaFeO_3$. The proton is largely immersed in the electron cloud of the oxygen ion, leading merely to a bulge in the outer rim of the electron density of the oxygen ion. Between O and H in the hydroxyl group, a slight accumulation of electron density can be noticed, indicating the formation of covalent bond.

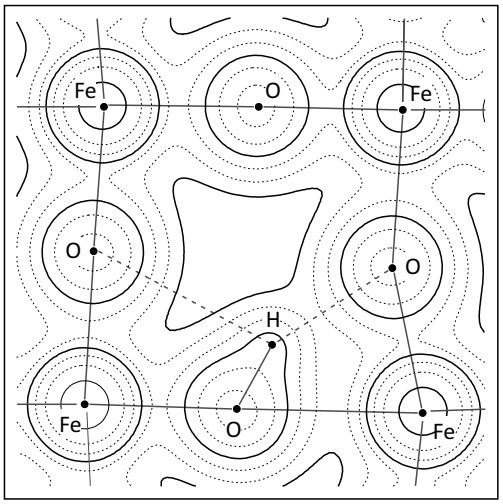

Figure 8.2: Contour map of the electron density distribution in $Ba_8Fe_8O_{24}H$; contour lines are drawn according to $10^{-2+\frac{n}{3}}\ e\ \mathrm{bohr}^{-3}$; bold lines correspond to 2×10^n with $n = -2, -1, 0$.

The chemical bonding in the hydroxyl group is analyzed using the pDOS and COHP of a $Ba_8Fe_8O_{24}H$ supercell; the results are shown in figure 8.3. Inspection of the pDOS curve shows that the H $1s$ orbital contributes to three crystal orbitals: two occupied ones at ≈-19 and ≈-7 eV and one unoccupied at ≈6 eV. The occupied crystal orbitals represent distinct electronic states below the edges of the O $2p$ valence band and the deeper lying O $2s$ band. They are composed - in addition to the H $1s$ orbital - of O $2p$ and O $2s$ orbitals of the oxygen ion in the hydroxyl group, referred to here as O_{OH}. The corresponding COHP curve reveals that the occupied states have a bonding character, where the O $2p$ and O $2s$ orbitals are partially hybridized as illustrated by the orbital icons in figure 8.3. The unoccupied state is largely composed of the H $1s$ orbital which translates into a positive Mulliken charge of 0.23 e and effectively renders the hydrogen atom into a proton. In conclusion, what figure 8.3 reveals is the formation of a covalent O-H bond by which the O $2p$ and O $2s$ energy levels of the O_{OH} ion are shifted downward (stabilized) in energy.

8.3 Proton uptake reactions in triple conducting oxides

In perovskite oxides exhibiting mixed p-type electronic and oxygen vacancy mediated ionic conductivity, such as $Ba_xSr_{1-x}FeO_{3-\delta}$, protons can be incorporated via two different chemical reactions. In the hydration reaction (8.1), protons are incorporated by a dissociative absorption of water into oxygen vacancies.

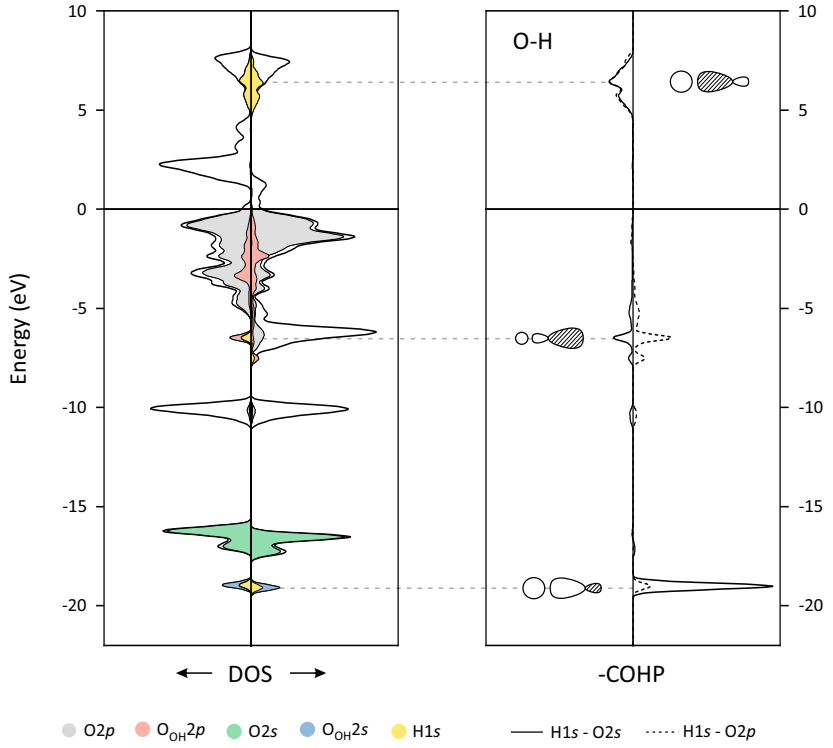

Figure 8.3: DOS (left) and COHP (right) curves of $Ba_8Fe_8O_{24}H$. In the DOS, the H1s states are multiplied by a factor of 10, the O_{OH} states by a factor of 5 for better visibility.

$$H_2O(g) + O_O^x + v_O^{\bullet\bullet} \rightleftharpoons 2OH_O^{\bullet} \tag{8.1}$$

This reaction is a pure acid-base reaction (no electron transfer involved); a water molecule dissociates into a proton and a hydroxide ion, with the proton being transferred to an oxygen ion in the crystal and the hydroxide ion filling an oxygen vacancy. The result are two protonic defects, $OH_O^{\bullet}$, i.e. hydroxide ions on oxygen ion sites. Alternatively, in the hydrogenation reaction (8.2), protons are incorporated at the expense of electron holes with the oxygen from H_2O being left behind in the gas phase.

$$H_2O(g) + 2O_O^x + 2h^{\bullet} \rightleftharpoons 2OH_O^{\bullet} + \frac{1}{2}O_2 \tag{8.2}$$

This reaction is a red-ox reaction; the electron of an incorporated hydrogen atom is transferred to the Fermi level where it annihilates an electron hole. Thus, protons could be incorporated into the material even if it contained no oxygen vacancies, provided that electron holes are present.

In closed-shell oxides, where no electron holes are present at the Fermi level, proton uptake occurs predominantly via the hydration reaction (8.1). In mixed conductors, the predominant reaction could be shown to switch between hydration (8.1) and hydrogenation (8.2) depending on external conditions.[129–131] In a defect-chemical model with ideal dilute defects, the transition point is marked by the condition $2[\mathrm{v}_\mathrm{O}^{\bullet\bullet}] = [\mathrm{h}^\bullet]$, with the hydration reaction prevailing at higher vacancy concentration. In this work, the focus is on the hydration reaction (8.1) because (i) this allows for comparison with proton uptake in closed-shell oxides and (ii) this mode is generally studied by thermogravimetry experiments.

The enthalpy of hydration varies strongly with structure and composition of the solid oxide and has been suggested to correlate with materials specific parameters such as the difference in the electronegativity of the perovskite B- and A-site cations,[132] the tolerance factor,[133] or the partial charge of the oxygen ions.[134,135] In addition, for perovskites, a high molar volume (lattice constant) and a high space group symmetry (close to the ideal perovskite lattice) have also been considered crucial for high proton uptake.[128,135] All suggested correlations are empirical and are often related to the basicity of the material; the rationale being that more basic oxygen ions can stabilize protons more effectively, thereby rendering the hydration energy more negative.

The hydration reaction (8.1) is, however, an amphoteric reaction; the solid behaves simultaneously as a base when lattice oxygen ions are protonated, and as an acid when oxygen vacancies accommodate a hydroxide ion. Hence, the enthalpy of hydration is governed by both the proton affinity of the oxygen ions and the hydroxide affinity of the oxygen vacancies. In this work, a computational scheme has been developed, in collaboration with the University of Oslo, that allows quantifying these affinities using first-principles DFT calculations. Analysis of the affinities could help rationalize the observed trend between the enthalpy of hydration and the "basicity" and unveiled the important role of the electronic structure in hydration thermodynamics.

8.4 Proton- and hydroxide affinities

The proton and hydroxide affinities are defined as the energy changes of reactions 8.3 and 8.4, respectively.

$$\mathrm{H}^+(g) + \mathrm{O}_\mathrm{O}^\mathrm{x} \rightleftharpoons \mathrm{OH}_\mathrm{O}^\bullet \tag{8.3}$$

$$\mathrm{OH}^-(g) + \mathrm{v}_\mathrm{O}^{\bullet\bullet} \rightleftharpoons \mathrm{OH}_\mathrm{O}^\bullet \tag{8.4}$$

As outlined in § 4.4, a direct calculation of the ion affinities in a "products-minus-reactants" fashion is inhibited by the fact that total energies of charged molecular species in vacuum boxes cannot be calculated when using periodic boundary conditions. The energy changes during reactions 8.3 and 8.4 can, however, be calculated indirectly via thermochemical cycles. The formalism is explained in § 4.4 for the case of the proton affinity, exemplary calculations can be found in appendix § B.5.

The proton and hydroxide affinities of various closed-shell oxides ranging from binary oxides e.g. MgO to ternary oxides e.g. $BaZrO_3$ have been calculated. The study revealed an intriguing correlation between the ion affinities and the ionization potential of the solid, across the various structure families investigated, as shown in figure 8.4.

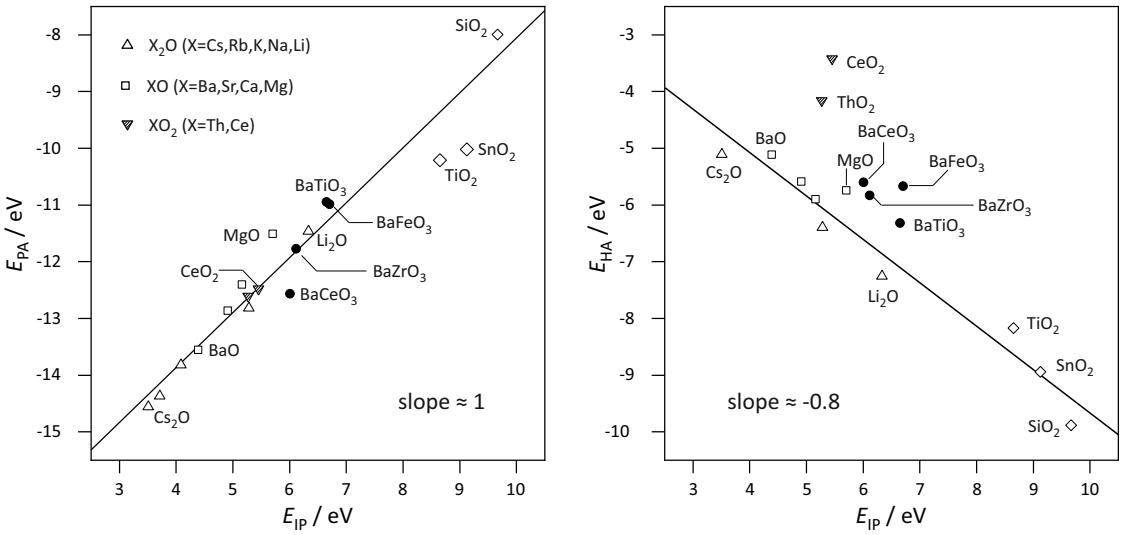

Figure 8.4: Ion affinities as a function of ionization potential (calculated with the HSE functional) for a variety of binary and perovskite oxides.

For the materials in figure 8.4 the valence band is mainly composed of O 2*p* states, i.e. the ionization potential (difference between top of valence band and vacuum) reflects the properties of the oxygen ions which are the proton binding site. The slopes of proton and hydroxide affinity with respect to the ionization energy are of opposite sign, demonstrating the amphoteric nature of the overall hydration reaction. While the proton affinity becomes more favorable with decreasing ionization potential (i.e., higher valence band maximum), the hydroxide affinity exhibits the opposite trend. The correlation is particularly good for the proton affinity, which is related to the fact that the proton is bound with an ≈1 Å short covalent bond to an oxygen ion - shorter than the O^{2-} ion radius of 1.4 Å - such that it is immersed in the oxygen ion's electron cloud and less sensitive to neighboring cations. Figure 8.4 shows that also the hydroxide affinity varies systematically with the ionization potential where the slope has the opposite sign. The somewhat

larger scatter can be related to the larger sensitivity of hydroxide incorporation to the local coordination by cations. For example, in CeO_2, ThO_2 an oxygen/hydroxide ion is coordinated by 4 more distant cations, while in perovskites it has 2 close cation neighbors.

The relation between ion affinities and the ionization potential also partly holds for redox-active oxides such as $BaFeO_3$ since the valence band still mainly consists of O $2p$ states. Here, it is particularly interesting to compare the ion affinities of $BaFeO_3$ with those of cubic $BaTiO_3$ since both have very similar lattice constants with 4.038 Å in $BaFeO_3$ and 4.051 Å in $BaTiO_3$. While the proton affinities of the two materials are very similar (-11.1 eV Å in $BaFeO_3$ and -10.9 eV in $BaTiO_3$) and follow the overall trend with the ionization potential, the hydroxide affinities differ more strongly with -5.7 eV Å in $BaFeO_3$ and -6.5 eV in $BaTiO_3$.

The reasons for the difference in hydroxide affinity - albeit similar ionization potentials - may be complex. Nevertheless, it can largely be explained by different O-site Madelung potentials. As discussed in § 5, the negative charge transfer and associated $d^5\underline{L}$ configuration entails less negative O-ion Mulliken charge, i.e., -1.13 e in $BaFeO_3$ versus -1.24 e in $BaTiO_3$ in combination with a less positive B-site cation Mulliken charge. The smaller difference in cation and anion charge translates into a smaller O-site Madelung potential and, consequently, reduces the energy gain upon transferring an OH^- from the gas phase into the solid. The ionization potential appears to be less affected by the reduced Madelung potential which, in turn, could be explained by a stronger B-O covalency in $BaFeO_3$. A stronger B-O bond leads to an energetic stabilization of the O $2p$ band and counteracts the destabilizing effect of the reduced Madelung potential. The reduced hydroxide affinity ultimately causes $BaFeO_3$ to deviate from the overall trend with ionization potential.

The overall trend observed in figure 8.4 between ion affinities and ionization potential can be understood by examining the electronic structures (DOS) of proton containing systems. Figure 8.5 compares the DOS of protonated $BaZrO_3$ and protonated $BaFeO_3$. As described in the previous section, O-H bond formation leads to a downward shift of the O_{OH} $2p$ and $2s$ energy levels. The extent of this downward shift can be quantified using the centers of mass of protonated and unprotonated oxygen ions in a a given material. In $BaZrO_3$ having an ionization potential of 6.1 eV, the downward shift is 2.3 eV for the O $2p$ states, as shown in figure 8.5. In $BaFeO_3$ having a larger ionization potential of 6.7 eV, on the other hand, the downward shift is significantly smaller with 1.9 eV for the O $2p$ states. This constitutes an important finding: O $2p$ levels are more strongly stabilized upon O-H bond formation when they have a higher energy in the unprotonated state. As a result, the proton affinity is more negative in materials with a smaller ionization potential.

The hydroxide affinity describes the incorporation of an OH^- from the gas phase. Cor-

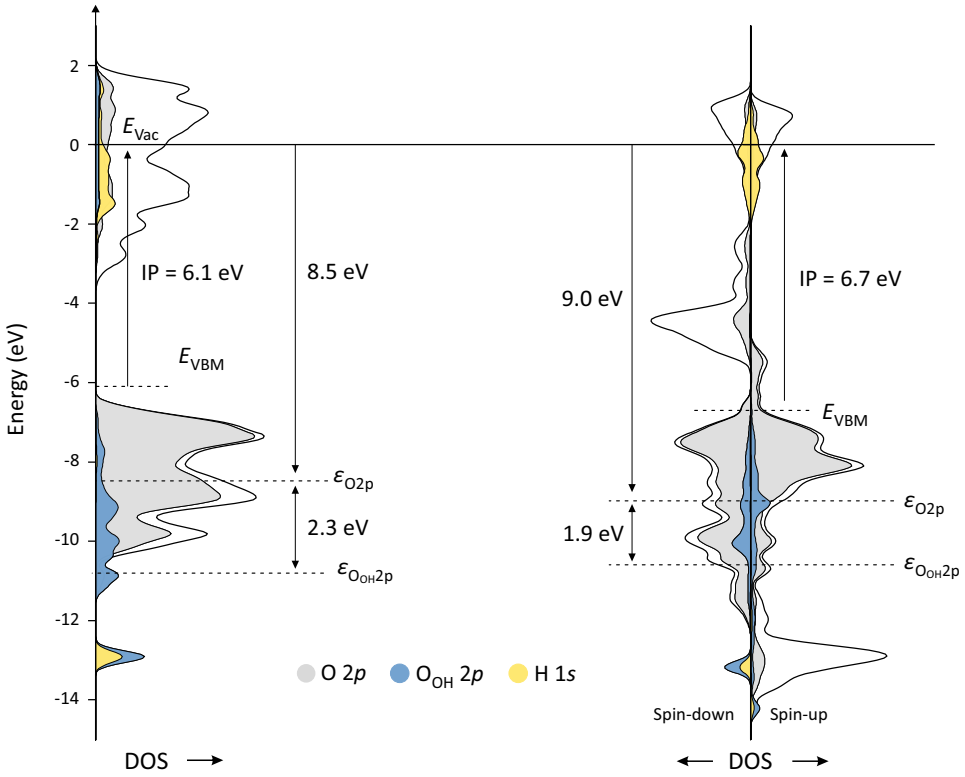

Figure 8.5: DOS of $Ba_8Zr_8O_{24}H$ (left) and $Ba_8Fe_8O_{24}H$ (right). Ionization potentials calculated with the HSE functional for consistency with figure 8.4

respondingly, the lower the newly formed O and O_{OH} states, the more negative the hydroxide affinity is. As indicated in figure 8.5, the O_{OH} states are below the states of unprotonated O and consequently lie deeper for oxides with a larger ionization potential, i.e., in $BaFeO_3$. However, this trend may be violated when the O-ion charge is significantly reduced as is the case for $BaFeO_3$ by virtue of the $d^5\underline{L}$ configuration. A lower O-ion charge may decrease the gain in energy upon incorporating a hydroxide ion from the gas phase albeit a larger ionization potentials.

The hydration energy is the sum of proton and hydroxide affinity plus the invariant gas phase water dissociation energy ($H_2O \rightarrow H^+ + OH^-$ | $\Delta E = 16.9$ eV). Since the proton affinity varies more strongly across the materials (slope of ≈ 1) compared to the hydroxide affinity (slope of ≈ -0.8), the energy of hydration, $\Delta_r E(H_2O)$ is more negative for materials with smaller ionization potential, at least within one structure family such as perovskite or rocksalt-structured oxides (figure 8.6). The observed steeper slope of the proton affinity compared to hydroxide affinity also supports the empirical correlation that materials with higher overall basicity often exhibit a more negative hydration enthalpy. The lower slope of the hydroxide affinity can be explained by envisioning the process as the simultaneous incorporation of an oxygen ion and a proton. The incorpo-

ration of an oxygen ion can be expected to correlate with the ionization potential with a similar slope as the proton affinity. However, the downward shift of the O $2p$ levels upon O-H bond formation is smaller in oxides with large ionization potentials such as $BaFeO_3$, which effectively flattens the slope of the hydroxide affinity with the ionization potential. With respect to $BaFeO_3$, the hydration energy is less negative than $BaTiO_3$ despite similar ionization potentials. This was shown to originate from a less negative hydroxide affinity, which is suggested to stems from a lower O-site Madelung potential by virtue of the $d^5\underline{L}$ configuration.

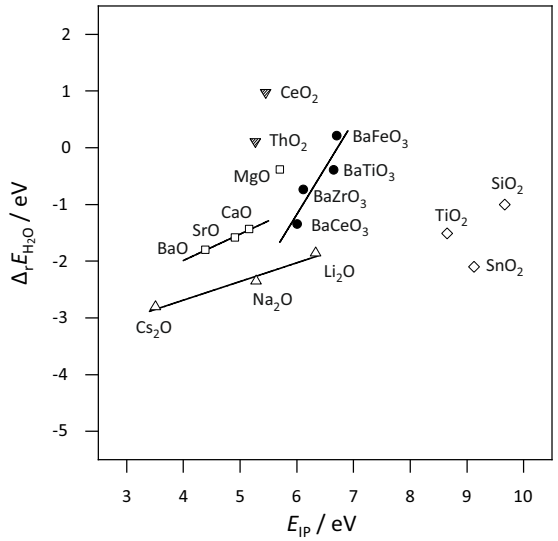

Figure 8.6: Hydration energies for the system $Ba_xSr_{1-x}FeO_{3-\delta}$ ($x = 0.0,\ 0.5,\ 1.0$) as a function of vacancy concentration, δ.

8.5 Hydration thermodynamics in (Ba, Sr)$FeO_{3-\delta}$

The calculation of hydration energies by DFT in stoichiometric compounds in which the oxygen ions occupy only one (e.g. cubic perovskites) or a few crystallographic sites (e.g. orthorhombic perovskites) requires only a small number of different proton positions to be probed to find the configuration with the lowest total energy. This allowed calculating the hydration energies for the large variety of different oxides discussed in the previous section. However, the calculation of hydration energies in oxygen non-stoichiometric systems drastically increases the number of configurations to be probed, since multiple defects (vacancies and protons) must be distributed in a supercell. To narrow the phase space to a manageable level, the protons are distributed here only in the oxygen non-stoichiometric supercells, which had yielded the three lowest total energies in the unprotonated state. Nevertheless, this still resulted in over 180 different config-

urations that had to be calculated with DFT. Out of this pool, the configurations that yielded the three lowest total energies per oxygen non-stoichiometry were used for the calculation of thermodynamic parameters; the defect positions in these configurations are documented in appendix B.4. Based on these configurations, the hydration energies for the system $Ba_xSr_{1-x}FeO_{3-\delta}$ with $x = 0.0,\ 0.5,\ 1.0$ were calculated according to, e.g.,

$$Ba_8Fe_8O_{23} + Ba_8Fe_8O_{22} + H_2O \rightleftharpoons 2\, Ba_8Fe_8O_{23}H \tag{8.5}$$

where the corresponding reaction energy, $\Delta_r E_{H_2O,O_{22.5}}$, is the hydration energy of an oxygen non-stoichiometric system. The total energies of the reaction constituents are obtained from supercell calculations, and $E^{tot}(H_2O)$ by placing an H_2O molecule in a vacuum box. The results are shown in figure 8.7; each data point represents the average of three configurations with different defect arrangements that yielded the lowest total energies after structural optimization. With increasing oxygen vacancy, or equivalently, decreasing electron hole concentration, the hydration energies become significantly more negative. For instance, in $BaFeO_{3-\delta}$, the hydration energy decreases from -0.2 to -1.0 eV; in $SrFeO_{3-\delta}$ the variation is smaller with a change from +0.2 to -0.2 eV.

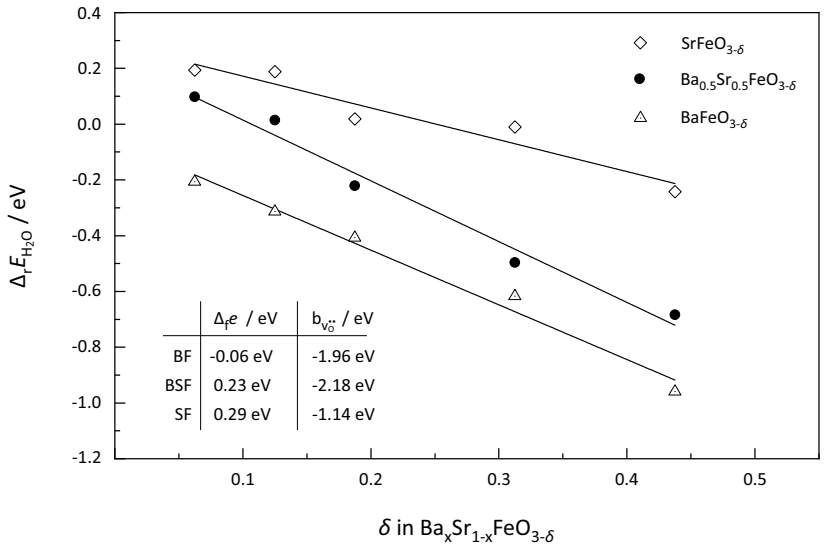

Figure 8.7: Hydration energies for the system $Ba_xSr_{1-x}FeO_{3-\delta}$ ($x = 0.0,\ 0.5,\ 1.0$) as a function of vacancy concentration, δ. Each data point represents an average of the three configurations with the lowest total energies.

The decrease in hydration energy with oxygen vacancy concentration represents non-ideal behavior and signals the presence of defect interactions. The approximately linear dependence of the hydration energy on the concentration of vacancies justifies using a

phenomenological first-order correction, as described in § 3.2,

$$\Delta_r E_d = \Delta_r e_d + b_d \, c_d \tag{8.6}$$

with a constant molar hydration energy at dilute conditions, $\Delta_r e$, and an interaction parameter, b_d, to describe the deviation from dilute behavior at higher defect concentrations. The molar hydration energies, $\Delta_r e_{H_2O}$, in the system $Ba_xSr_{1-x}FeO_{3-\delta}$ obtained from fitting the data in figure 8.7 are found to become more negative with increasing Ba-content, ranging from 0.29 eV in $SrFeO_{3-\delta}$ to -0.06 eV in $BaFeO_{3-\delta}$. Following the arguments of the previous section, it may be inferred that the larger Ba cations lead to smaller ionization potential and, consequently, to more negative proton affinities and less negative hydroxide affinities. Major deviations from this trend are not expected since the the Mulliken atomic charges of O and Fe remain relatively similar along the series with, e.g., -1.13 e for O and +1.64 e for Fe in $BaFeO_3$ versus -1.13 e for O and +1.73 e in $SrFeO_3$. Thus, the more negative hydration energy in system with a higher Ba-content is expected to stem from an increased basicity of the oxygen ions. A direct comparison of ion affinities along the series was not possible due to technical problems in calculating the slabs of $Ba_{0.5}Sr_{0.5}FeO_3$ and $SrFeO_3$. [i]

To understand the trend between hydration energy and hole or oxygen vacancy concentration, the proton and hydroxide affinities of oxygen non-stoichiometric $BaFeO_{3-\delta}$ were calculated and are shown in figure 8.8 as a function of δ. Both proton and hydroxide affinity become more negative for higher oxygen vacancy concentrations, with the slope of the hydroxide affinity being markedly steeper. This indicates that the decrease in hydration energy can be attributed largely to a more negative hydroxide affinity. The slopes in figure 8.8 differ significantly from the trend with ionization potential across different materials families discussed in the previous chapter. Here, the proton affinity varies much less than expected, and the hydroxide affinity even exhibits the opposite trend. The reasons for the different trends are complex. There are indications that the increase in O-ion charge and radius with increasing oxygen vacancy concentration leads to an increase in the O-H bond length.[85] This reduces the orbital overlap in the O-H bond and counteracts the trend between O_{OH} $2p$ and $2s$ downward shifts and ionization potential, leaving the proton affinity rather constant. In addition, a higher O-ion charge in the reduced state increases the energy gain upon incorporating an OH^- from the gas phase via increased electrostatic interactions with the adjacent cations, thereby rendering

[i] Ion affinities of $Ba_{0.5}Sr_{0.5}FeO_3$ and $SrFeO_3$ could not be calculated due to convergence problems in the surface slab calculations; the use of static slabs lead to a severe charge leaking into the vacuum which prevented convergence of the electronic cycle.

the hydroxide affinity more negative.

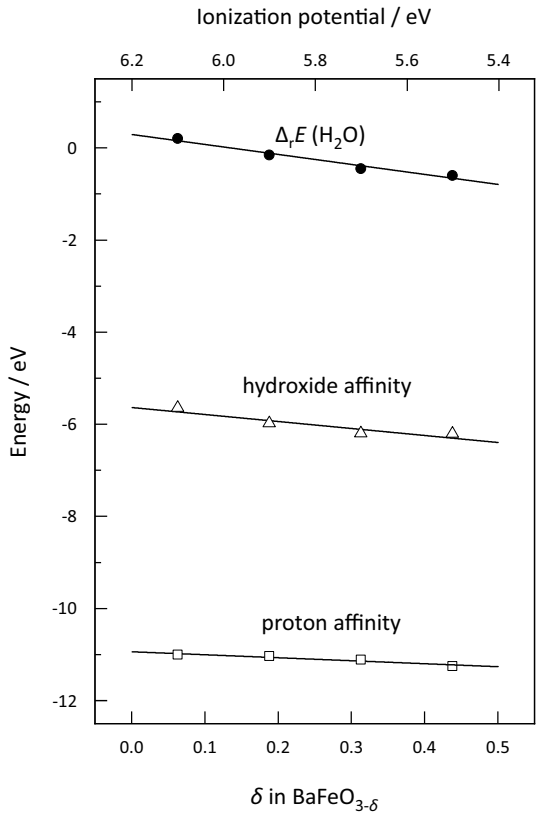

Figure 8.8: Hydration energy, proton and hydroxide affinity in $Ba_8Fe_8O_{24-\delta}H$ as a function of vacancy concentration, δ. Each data point represents an average of the three configurations with the lowest total energies. Small differences in calculated $\Delta_r E_{H_2O}$ stem from different calculation approaches with either charged or neutral cells.

8.6 Electronic-ionic energy level diagrams

The calculation of ion affinities not only helps rationalize trends in the hydration thermodynamics but also allows one to construct quantified electronic-ionic energy level diagrams, see § 4.5. These diagrams provide quick access to the salient features of materials and can be used to model interfaces at which different ion or electron chemical potentials are equalized by diffusion. Here, the electronic-ionic energy level diagrams are constructed for the materials $BaZrO_3$ and $BaFeO_3$, whose interface is also of technological significance as a model for electrolyte-cathode interfaces in protonic ceramic fuel cells.

The oxygen ion affinity (OA) is taken as $E_{OA} = E_{HA} - E_{PA}$ and yields the standard chemical potential of the oxygen vacancy. To obtain the standard chemical potential of an interstitial oxygen ion, the reaction energy of a Frenkel disorder reaction must be cal-

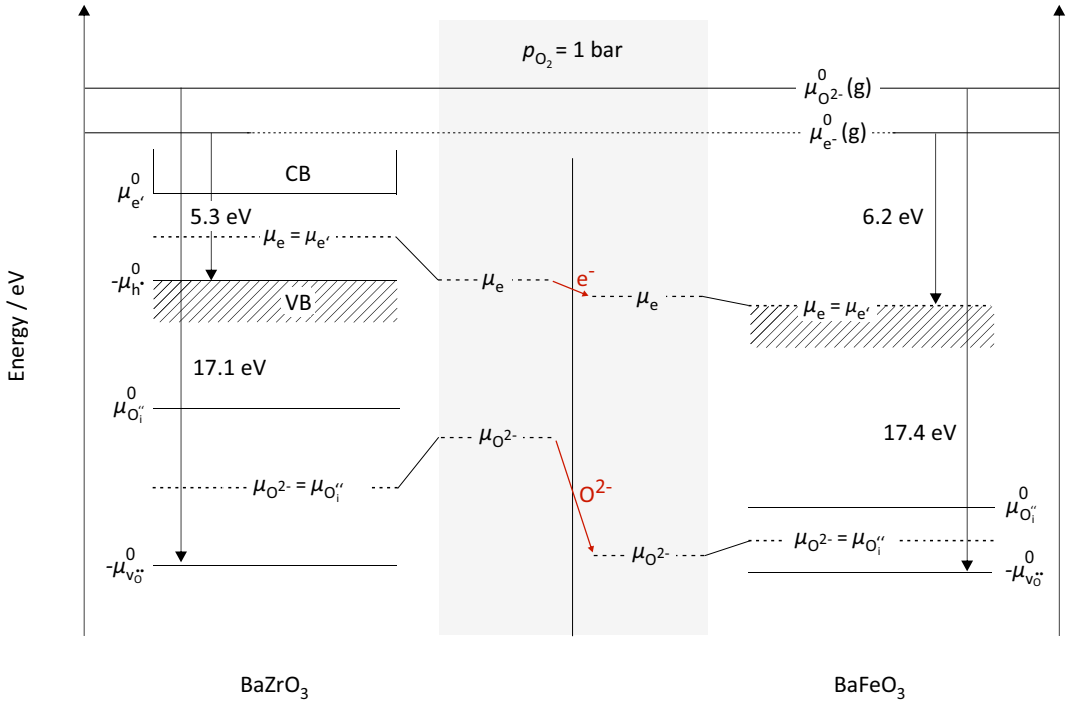

Figure 8.9: Intrinsic electronic-ionic energy level diagrams of $BaZrO_3$ and $BaFeO_3$, i.e. electronic and ionic Fermi levels in the middle of the respective band gaps (for $BaZrO_3$ this is achieved at very low p_{O_2}, for $BaFeO_3$ at high p_{O_2}). Grey-shaded area represents a common p_{O_2} of 1 bar, which for $BaZrO_3$ implies an increase in p_{O_2} and for $BaFeO_3$ a decrease.

culated, where an oxygen ion is transferred from its regular position to a well-separated interstitial site, leaving behind an oxygen vacancy according to reaction 8.7.

$$O_O^x + v_i \rightleftharpoons v_O^{\bullet\bullet} + O_i'' \tag{8.7}$$

There exist different geometric possibilities of oxygen Frenkel defects in perovskites; here the interstitial oxygen ion is placed on the so-called hollow position[136] in the input structure and optimized in $2 \times 2 \times 2$ supercells using VASP. Optimized geometries and details of these calculations are given in appendix B.6. The chemical potential of the oxygen ion is obtained as the difference in standard chemical potentials of the oxygen interstitial and the oxygen vacancy.

The electronic-ionic energy level diagrams are shown in figure 8.9. The standard chemical potentials of the electron and oxygen ion at vacuum are linked via the relation $\mu^0_O = \mu^0_{O^{2-}} - 2\mu^0_{e^-}$. On the left and right hand side of figure 8.9 are the calculated, intrinsic

energy levels diagrams of the two materials. The stoichiometry in the materials is fixed in the calculation which prevents any defect formation that would otherwise be expected in vacuum, i.e. extremely low oxygen partial pressures. The actual conditions (oxygen partial pressure) that would yield Fermi level positions in the middle of the respective band gaps are fairly different in the two materials. In $BaFeO_3$, a situation without large concentration of oxygen vacancies (i.e. an O^{2-} Fermi level close to the standard chemical potential of the vacancy) is achieved only at extremely high oxygen partial pressures.[53] On the other hand, in $BaZrO_3$, relatively small shifts in the O^{2-} Fermi level e.g. through the formation of oxygen interstitials can cause large shifts in the electronic Fermi level in order to compensate these defects. Hence, the ideal position of the electronic Fermi level in the middle of the bandgap is achieved only at extremely low oxygen partial pressures.[137]

What happens when both materials are equilibrated at the same intermediate oxygen partial pressure of, e.g., 1 bar? In $BaZrO_3$, this corresponds to an increase in oxygen partial pressure due to which oxygen interstitial defects, O_i'', will form that cause the O_{2-} Fermi level to shift upwards, or alternatively, ambient oxygen may be incorporated into oxygen vacancies that resulted from Frenkel disorder with the same effect of shifting the O_{2-} Fermi level upwards. The O_i'' defects are compensated by electron holes, rendering the material a p-type electronic conductor. Due to the large band gap, the electronic Fermi level shifts downwards quite strongly in order to achieve the appropriate concentration of electron holes. In $BaFeO_3$, a decrease in oxygen partial pressure would lead to the formation of oxygen vacancies and an associated downward shift of the O_{2-} Fermi level. The vacancies are compensated by the annihilation of electron holes which causes the electronic Fermi level to slightly increase.

As a result, the grey-shaded area in figure 8.9 shows the energy levels as aligned to the same oxygen partial pressure of 1 bar, which is in the range of typical fuel cell conditions. The electronic Fermi level in $BaZrO_3$ is higher than in $BaFeO_3$ causing electrons to diffuse from $BaZrO_3$ to $BaFeO_3$ if the materials were contacted. In addition, the O^{2-} Fermi level in $BaZrO_3$ is much higher which would lead to a diffusion of oxygen ions from $BaZrO_3$ to $BaFeO_3$. It can be concluded that contacting $BaZrO_3$ and $BaFeO_3$ at 1 bar oxygen partial pressure would result in a space charge region, with the $BaZrO_3$ side positively charged. This, in turn, will result in a proton depleted region in $BaZrO_3$ and is expected to have some detrimental effects on the fuel cell performance.

8.7 Summary and discussion

The nature of protonic defects in $Ba_xSr_{1-x}FeO_{3-\delta}$ ($x = 0.0,\ 0.5,\ 1.0$) and the thermodynamic parameter which govern their formation have been investigated by first-principles DFT calculations.

The equilibrium proton geometry in these systems is characterized by typical O-H bond lengths of approximately 1 Å and significant tilts to neighbouring oxygen ions, favoring strong hydrogen bonding. A bonding analysis using the COHP revealed strong covalent interactions within the O-H moiety, involving two bonding states with predominant O $2p$ and O $2s$ character and an antibonding state with H $1s$ character. The tilt to a neighbouring oxygen ion is systematically more pronounced in systems with a higher Ba content, owing to a softer lattice that facilitates the local deformation associated with the tilt. Hydration energies become more negative with increasing Ba-content on the A-site. For a given composition, they moreover decrease strongly with increasing oxygen vacancy concentration indicating the presence of defect interactions. The approximately linear decrease with oxygen vacancy concentration justifies using a first-order correction for the hydration energy by which material-specific defect interaction parameter could be extracted. Table 8.2 compares the calculated hydration energies and defect interactions parameters with values obtained from thermogravimetry experiments. There is a good agreement between calculated and experimental hydration energies, whereas there are pronounced discrepancies concerning the magnitude of the defect interaction parameters (similar to the interaction parameter in the case of oxygen non-stoichiometry, discussed in § 7). It should be noted that the comparability between experiment and theory is impaired by different pressure and temperature conditions: Experimental data refer to standard conditions of $T = 298$ K and $p = 1$ bar, while calculations were performed at 0 K and 0 bar. However, it has been discussed in connection with the vacancy formation energy already that standard temperature and pressure conditions have only a minor effect on the calculated formation energy, see § 7.6. More realistically, the discrepancy between theoretical and experimental values stems from accuracy problems of the employed DFT methodology affecting the degree of hole delocalization and uncertainties in the experiments.

A new thermodynamic formalism was developed based on which the hydration energy is decomposed into the proton affinity of lattice oxygen ions and the hydroxide affinity of oxygen vacancies. The formalism was applied to a large variety of binary and perovskite oxides revealing a systematic trend between the calculated affinities and the oxide's ionization potential: oxides with a small ionization potential exhibit a more favorable proton affinity and less favorable hydroxide affinity. The trend holds for oxides

Table 8.2: Comparison of calculated hydration energies and experimentally measured standard hydration enthalpies of $(Ba,Sr)FeO_{3-\delta}$.

	$BaFeO_{2.5}$	$Ba_{0.5}Sr_{0.5}FeO_{2.5}$	$SrFeO_{2.5}$
Calculated in this work			
$\Delta_r e_{H_2O}$ / eV	-1.04	-0.86	-0.28
b_{H_2O} / eV	-1.96	-2.18	-1.14
Experimental data			
$\Delta_r^0 h_{H_2O}^{exp.}$ / eV	-0.64*[14]	-0.63[14]	-
$b_{H_2O}^{exp.}$ / eV	-0.12*[14]	-	-

* The exp. value for $BaFeO_{3-\delta}$ was determined for La-stabilized $Ba_{0.95}La_{0.05}FeO_{3-\delta}$.

ranging from very acidic (SiO_2) to very basic oxides (Cs_2O, BaO), emphasizing the fundamental nature of this intriguing relation.

In mixed conducting perovskites, the situation is more complex. The proton affinity of $BaFeO_3$ largely follows the global trend with ionization potential, whereas the hydroxide affinity is significantly lower than expected from the trend. It is proposed that this is the result of the negative charge transfer in $BaFeO_3$ and the associated $d^5\underline{L}$ configuration. This leads to reduced anion and cation charges and therefore a lower electrostatic potential at the O-site, rendering the hydroxide affinity less negative. It could also explain the generally less negative hydration energies observed in p-type conducting iron perovskites. Consistent with this argument, the more negative hydration energy with increasing oxygen vacancy concentration in $Ba_xSr_{1-x}FeO_{3-\delta}$ could be attributed primarily to a more negative hydroxide affinity. With increasing oxygen vacancy concentration, ligand holes are progressively annihilated and lead to an increase in oxygen ion charge. As a result, the electrostatic potential at the O-site becomes stronger, the hydroxide affinity more negative.

Overall, the results presented herein emphasize that the hydration reaction is strongly influenced by the concentration of ligand holes in $BaFeO_{3-\delta}$. Consequently, a description based on the formal oxidation states of Fe is oversimplified, since the properties of oxygen ions and oxygen vacancies are more strongly affected by the redox activity of the material.

Conclusions

9 Concluding Remarks

In this thesis, the electronic structure and defect chemistry of iron containing perovskites, in particular $Ba_xSr_{1-x}FeO_{3-\delta}$, were investigated. The investigation was divided into four consecutive parts in which the structural and compositional degrees of freedom were subsequently increased: starting with cubic defect-free $BaFeO_3$ to the Jahn-Teller distorted structure, to oxygen vacancies and finally proton containing $(Ba,Sr)FeO_{3-\delta}$. The controlled increase in complexity of the system - possible only in the field of simulation - provided valuable insights into these materials which typically remain obscured in experiments. The main aspects investigated were:

- **The electronic structure**, where oxygen ligand holes could be identified in $BaFeO_3$ which are partially delocalized in anti-bonding Fe-O states.
- **Structural instabilities**, where the ideal cubic perovskite structure of $BaFeO_3$ was found to be prone to Jahn-Teller type distortions.
- **The thermodynamics of oxygen non-stoichiometry**, where non-idealities in the vacancy formation energy in $Ba_xSr_{1-x}FeO_{3-\delta}$ could be traced to the effect of delocalized ligand holes.
- **The thermodynamics of proton uptake**, where electronic factors were shown to govern the proton uptake of solid oxides in general, and specifically in the system $Ba_xSr_{1-x}FeO_{3-\delta}$.

The electronic structure of cubic $BaFeO_3$ was calculated using DFT and analyzed in terms of local atomic orbitals, which allowed for a chemically intuitive discussion. The calculations confirmed previous experimental[1–3] and theoretical[4] studies that $BaFeO_3$ is a negative charge transfer material. Strong exchange interactions in the Fe $3d$ orbitals give rise to a large energetic separation of spin-up and spin-down d bands, with the spin-up d band falling below the O $2p$ valence band. The result is a charge transfer from oxygen to iron, which produces the characteristic $d^5\underline{L}$ ($\underline{L}$ = ligand hole) configuration of the material. A chemical bonding analysis showed that the Fe-O bond has a significant covalent contribution, and that the chemically active orbitals at the Fermi level (and ligand holes) have an anti-bonding $pd\sigma^*$ character. The presence and partially delocalized nature of these ligand holes forms the basis for the discussions in the subsequent chapters.

Having established a conceivable picture of the electronic structure, potential structural instabilities of the ideal cubic lattice were investigated. The phonon dispersion was

calculated revealing distinct dynamically unstable phonon modes which are isostructural to Jahn-Teller type distortions. Using a symmetry-mode displacement approach, the cubic structure was distorted along the unstable modes leading to a moderately Jahn-Teller distorted ground state. The structural instability inherent to the cubic phase could be traced to partly degenerate O $2p$ states at the Fermi level posing stresses in the electronic structure. The total energy changes associated with the Jahn-Teller distortion were found to be small. This may explain why experimentally a Jahn-Teller distortion has not been observed since small energy differences can easily be outweighed by external factors. However, when point defects are introduced in the lattice they may readily catalyze existing structural instabilities making the knowledge of unstable phonon modes imperative for an understanding of point-defect induced lattice distortions.

Based on these results, the defect chemistry of $Ba_xSr_{1-x}FeO_{3-\delta}$ was investigated with respect to the nature and formation of oxygen vacancies and proton interstitial defects. The presence of these point defects imparts a mixed ionic-electronic conductivity to the materials, which is considered to play a crucial role in technologies such as fuel- or electrolyzer cells. Using first-principles DFT calculations, this work has shown that many of the previously unresolved issues, especially regarding defect interactions, can be explained by taking into account the complex nature of the electronic structure, in particular the presence of delocalized ligand holes. The results presented in this thesis demonstrate that the electronic structure and defect chemistry of these materials are highly correlated, even for reactions such as the dissociative water incorporation which formally is an acid-base reaction.

The defect geometry and electronic properties of oxygen vacancies were investigated using DFT with the supercell approach. The formation of an oxygen vacancy involves the donation of two electrons of the former O^{2-} ion to the available ligand holes. Electron density distribution maps of $BaFeO_3$ thereby clearly revealed that these states are fairly delocalized, affecting both Fe and O ions beyond the directly adjacent [FeO_5] octahedra. The oxygen vacancy formation energy was calculated in $Ba_xSr_{1-x}FeO_{3-\delta}$ ($x = 0.0,\ 0.5,\ 1.0$), and for each of these compositions, as a function of oxygen vacancy concentration in the range $0 < \delta < 0.5$. It was shown that, with increasing Sr content and increasing oxygen vacancy concentration, the energy to form an oxygen vacancy increases. Both oxygen vacancy formation energies and the trend with δ are in agreement with experimental thermogravimetry data.[89,90] Taking this further, the dependence on δ could be traced to the position of the Fermi level which rises as more ligand holes become annihilated. This effect was found to effectively outweigh a concomitant decrease in Fe-O bond strength. While previous studies have proposed such a relation[91,95], here, this effect could be unambiguously quantified using electronic structure analyses of numerous

defective supercells.

The last chapter is devoted to the study of protonic defects and the factors determining the propensity for proton uptake in $Ba_xSr_{1-x}FeO_{3-\delta}$ and solid oxides in general. The proton uptake was studied via the hydration reaction: the dissociation of an ambient water molecule into a proton and a hydroxide ion with the proton being transferred to a lattice oxygen ion and the hydroxide ion filling an oxygen vacancy yielding two hydroxide ions on oxygen ion sites. Consequently, to get a high propensity for hydration, a material needs a favorable proton affinity of lattice oxygen ions and a favorable hydroxide affinity of oxygen vacancies.

Here, the defect geometry and bonding properties of protonic defects were investigated for the series $Ba_xSr_{1-x}FeO_{3-\delta}$ ($x = 0.0,\ 0.5,\ 1.0$) using DFT with the supercell approach. Within the O-H moiety, a strong covalent bond is established with distinct bonding and anti-bonding electronic states. The bonding-states are composed primarily of O $2p$ and O $2s$ orbitals which are energetically stabilized by the O-H bond formation. In addition to the covalent interaction, the O-H moiety is tilted towards a neighbouring oxygen ion forming a hydrogen bond; the degree of this tilt was shown to vary systematically with A-site composition, becoming more pronounced with increasing Ba-content. The hydration energy was calculated for the three different A-site compositions, and for each composition as a function of oxygen vacancies. With increasing Ba-content and increasing concentration of oxygen vacancies, the hydration energy becomes more negative. This is consistent with experimental thermogravimetry data.[14] It confirms that in $Ba_xSr_{1-x}FeO_{3-\delta}$ p-type electronic and proton conductivity are antagonistic properties. The concentrations of protons and holes are anti-correlated because they both appear as positive defects in the electroneutrality condition, but even more so, because the presence of holes energetically disfavors the dissociative water incorporation.

A new thermodynamic formalism was developed that allows quantifying the proton affinity of oxygen ions and the hydroxide affinity of oxygen vacancies by means of first-principles DFT calculations. The method was applied to a wide range of solid oxides ranging from binary oxides such as MgO to various perovskite oxides including $BaZrO_3$ and $BaFeO_3$. The study revealed an intriguing correlation between the affinities and the ionization potential of the materials across the various structure families investigated. The underlying origin is that oxygen $2p$ and $2s$ orbitals are stabilized more strongly upon O-H bond formation when they have a higher absolute band position in the unprotonated state, thus causing the proton affinity to become more negative. On the other hand, a higher absolute position of the O $2p$ and $2s$ orbitals makes the hydroxide affinity less negative. These relations have so far not been recognized in the literature, and constitute an important step in understanding the phenomena of proton uptake and con-

ductivity in solid oxides. They also help rationalize the trend in hydration energy in the $Ba_xSr_{1-x}FeO_{3-\delta}$ family of materials; with increasing concentration of vacancies the hydroxide affinity was found to become more negative. This was suggested to stem from an increased ionic charge of the oxygen and hydroxide ions as more ligand holes become occupied, which increases the electrostatic interaction with the cations.

As a closing remark, this thesis highlights the importance of the electronic structure in the study of defect chemical reactions. In particular, the negative charge transfer in the electronic structure of the studied oxides has far-reaching implications. The material becomes a p-type electronic conductor with ligand holes as charge carriers. These ligand holes are partially delocalized in $pd\sigma^*$ orbitals that are chemically active and cause redox reactions to affect charge and radii of both O and Fe ions. As a result, both the thermodynamics of oxygen vacancy formation and proton uptake critically depend on the concentration of ligand holes. Together, these effects unambiguously demonstrate how electronic structure and defect chemistry are closely intertwined in iron perovskites. From this knowledge, future strategies for the design of novel cathode materials can be derived that ultimately help to enhance the performance of fuel- and electrolyzer cells.

Appendix

A Computational details

This chapter provides computational details and numerical input parameters of the first-principles calculations that were carried out in this work.

A.1 VASP

The density functional theory (DFT) calculations in this thesis were carried out using the Vienna *ab-initio* simulation package (VASP, v.5.4.4)[22–24], in conjuncture with the projector-augmented wave method[138]. The wave functions were expanded in terms of plane waves with a constant energy cutoff of 500 eV and were optimized with a break condition for the self-consistent loop of 10^{-5} eV. The Brillouin zone of the 5-atom primitive unit cell was sampled with an $8 \times 8 \times 8$ Monkhorst–Pack k-point mesh. Exchange–correlation was treated with the Perdew–Burke– Ernzerhof (PBE) functional[139] with an additional on-site Hubbard-U interaction term[26] for the Fe $3d$ states of U_{eff} = 4 eV. Different values of U_{eff} were explored, ranging from 0 to 7 eV (figure A.1), with U_{eff} = 4 eV representing a good compromise between reproducing experimental values, e.g., of the magnetic moment, and falling in the range of U_{eff} values typically employed for Fe-containing perovskites (see, e.g., refs[4,140,141]). Structural optimizations were performed until residual forces fell below 10^{-4} eV/Å.

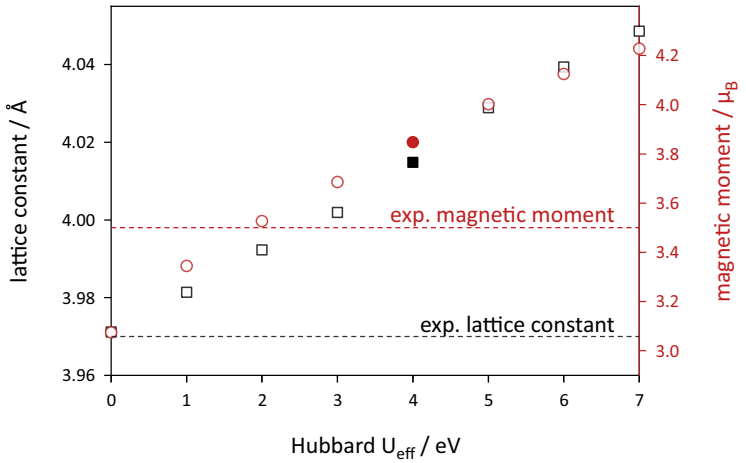

Figure A.1: Lattice constant and Fe magnetic moment as a function of the U_{eff} parameter for $BaFeO_3$. Filled symbols correspond to $U_{\text{eff}} = 4$ eV, which was used in this work.

A larger U-value increases the on-site repulsion of Fe $3d$ electrons of opposite spin, thus widening the gap between the Fe $3d$ spin-up and spin-down band. This leads to a reduced covalency between the O $2p$ states and the Fe $3d$ states and results in increasing Fe magnetic moments and an increasing lattice constant. Using U_{eff}=4 eV yields a Fe magnetic moment close to the experimental value while maintaining a reasonable lattice constant.

Point defects were modelled using a $2 \times 2 \times 2$ expansion of the primitive unit cell corresponding to a supercell of 40 atoms. The number of k-points in the supercells was reduced to a $4 \times 4 \times 4$ grid accordingly. All calculations were performed for neutral supercells (except for the proton and hydroxide affinity calculations, see § B.5) with a full relaxation of the supercell dimensions (allowing also for, e.g., monoclinic distortion) and of atomic coordinates. For the calculation of defect formation energies, defect-free $BaFeO_{3-\delta}$, $Ba_{0.5}Sr_{0.5}FeO_{3-\delta}$, and $SrFeO_{3-\delta}$ were also calculated in supercell form. In case of $Ba_{0.5}Sr_{0.5}FeO_{3-\delta}$, a strictly alternating distribution of Ba and Sr over the A-site of the perovskite lattice was imposed. Regarding the calculation of gas phase O_2, H_2, and H_2O, the molecules were placed into vacuum boxes of 12 Å edge lengths.

In cases of multiple point defects per supercell, different symmetry-independent defect arrangements are possible, which were generated with the "supercell" code.[43] More details on the different configurations are given in § B.4. Given the large number of supercells, which may contain several point defects and lack any symmetry elements, an efficient methodology for geometry and electronic structure optimization was required. A PBE+U approach was chosen consequently over the computationally much more demanding hybrid functionals.

A.2 LOBSTER

The optimized wave functions were projected onto an auxiliary basis set composed of local atomic orbitals using the LOBSTER code[27–31]. Specifically, the "pbeVASPFit2015" basis set[30] was used with the valence orbitals Ba $5s$ $6s$ $5p$, Sr $4s$ $5s$ $4p$, Fe $4s$ $3p$ $3d$, and O $2s$ $2p$. This ensured a low charge spilling (i.e. the percentage of electronic density lost during projection) of less than 2%. To obtain smooth DOS curves, a Gaussian smearing width of 0.2 eV was used in LOBSTER.

A.3 PHONOPY

The phonon dispersion and vibrational frequencies of $BaFeO_3$ were calculated with the Phonopy code[42]. The force constant matrix was evaluated within the harmonic approximation using finite ionic displacements of 0.01 Å in $2 \times 2 \times 2$ supercells. The electronic structure of the supercells containing the ionic displacements was converged to within 10^{-8} eV. The Gaussian smearing widths in these calculations was reduced to 0.05 eV (in contrast to the default value of 0.1 eV used in the VASP calculations in this work). From the displaced supercells, the forces acting on all ions were used to build the force constant matrices, based on which the vibrational frequencies and eigenvectors on a specified set of q-points are calcualted.

Importantly, the structural instabilities identified in $BaFeO_3$ are very sensitive with respect to the choice of the exchange-correlation functional, particularly, the U_{eff} value in the Hubbard-U correction scheme. As shown in figure A.2 , the frequencies of the Jahn-Teller modes R_3^+ and M_2^+ change significantly with U_{eff}. In fact, the cubic structure of $BaFeO_3$ becomes dynamically stable with respect to these modes at $U_{\text{eff}} > 6$ eV. This is in agreement with the theoretical study[142], where imaginary frequencies in $BaFeO_3$ were found to disappear for large U_{eff}-values of 6 and 8 eV. Similarly, in[79], the cubic structure of $BaFeO_3$ was found to be dynamically stable when calculated with the PBE functional revised for solids (PBEsol) in combination with a Hubbard-U correction term of $U_{\text{eff}} = 5.2$.

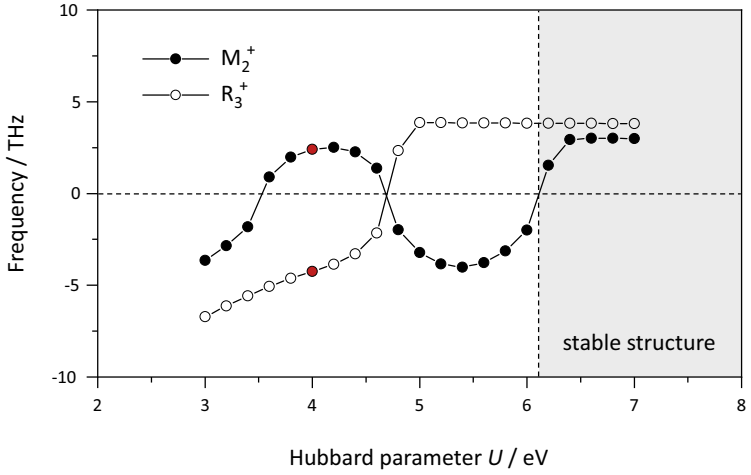

Figure A.2: Jahn-Teller type distortion modes R_3^+ and M_2^+ as a function of the U_{eff} parameter.

These results show that the structural stability in $BaFeO_3$ is extremely sensitive with respect to the calculation parameters and should be evaluated carefully. Nevertheless, with the settings employed here (PBE, $U_{\text{eff}} = 4$) the structure is found to be dynamically unstable with respect to the R_3^+ mode, and distortions along this mode can slightly reduce the total energy by 0.02 eV per formula unit.

B Supporting Material

This section provides additional information and computational details on the calculations of the $Ba_xSr_{1-x}FeO_{3-\delta}$ system. For details regarding the proton and hydroxide affinity calculations of other solid oxides (e.g. MgO or SiO_2) discussed in chapter § 8.4, the reader is referred to the supporting material of the corresponding publication[44].

B.1 First-principles thermodynamics at finite temperature

The defect formation energies calculated at $T = 0$ K can be converted to formation enthalpies or Gibbs energies following the procedure described in § 4.1 or[143]. This is shown here for the case of oxygen vacancy formation at the expense of electron holes in $BaFeO_3$ according to:

$$\mathrm{O_O^x} + 2\mathrm{h^\bullet} \rightleftharpoons \mathrm{v_O^{\bullet\bullet}} + \frac{1}{2}\,\mathrm{O_2(g)} \tag{B.1}$$

The defect formation energy of this reaction is given by,

$$\Delta_\mathrm{f} E_{\mathrm{v_O^{\bullet\bullet}}} = \Delta E^\mathrm{tot} + 0.5\; E^\mathrm{tot}(\mathrm{O_2}) \tag{B.2}$$

where ΔE^tot refers to the total energy difference between defective and defect-free supercells, and $E^\mathrm{tot}(\mathrm{O_2})$ is the total energy of an O_2 molecule in a vacuum box. Electron holes appearing in the reaction are included in the total energy of the defect-free supercell because $BaFeO_3$ is a p-type conductor. As temperature increases, the system's internal energy increases by virtue of electrons occupying excited states as well as occupied phonon modes. The defect formation enthalpy reads accordingly,

$$\begin{aligned}\Delta_\mathrm{f} H_{\mathrm{v_O^{\bullet\bullet}}}(T) = \Delta E^\mathrm{tot} + \Delta H^\mathrm{vib}(T) + \\ 0.5\left(E^\mathrm{tot}(\mathrm{O_2}) + H^\mathrm{o}(\mathrm{O_2}) + \int pdV\right)\end{aligned} \tag{B.3}$$

where $\Delta H^\mathrm{vib}(T)$ is the difference in internal energies between defective and defect-free supercells stemming from lattice vibrations, which can be obtained from phonon calculations, and $H^\mathrm{o}(\mathrm{O_2})$ is obtained from tabulated values[144] by integrating the heat capacity

to the temperature of interest. The pdV contribution of the O_2 molecule is evaluated within an ideal gas assumption, i.e. $pdV = dnRT$. Meanwhile, the pdV stemming from the volume change of defective and defect-free supercells is considered to be negligible at the dilute limit, such that $\Delta U^{\mathrm{vib}} = \Delta H^{\mathrm{vib}}$. The contribution from excited electronic states to the enthalpy of a system, $H^{\mathrm{el}}(T)$, could be estimated to be $\approx$ 0.05 eV at $T = 1500\ K$ by imposing a Fermi-Dirac distribution on the electronic density of states of $BaFeO_3$ and is neglected from hereon (see § 4.1). Finally, by including also entropic contributions, the Gibbs free energy of oxygen vacancy formation can be obtained via

$$\begin{aligned}\Delta_{\mathrm{f}} G_{\mathrm{v}_{\mathrm{O}}^{\bullet\bullet}}(T) = \Delta E^{\mathrm{tot}} + \Delta H^{\mathrm{vib}}(T) + T\Delta S^{\mathrm{vib}}(T) + \\ 0.5\left(E^{\mathrm{tot}}(\mathrm{O}_2) + H^{\mathrm{o}}(\mathrm{O}_2) + \int pdV + S^{\mathrm{o}}(\mathrm{O}_2)\right)\end{aligned} \tag{B.4}$$

where ΔS^{vib} is the difference in vibrational entropy between defective and defect-free supercells obtained from phonon calculations, and $S^{\mathrm{o}}(\mathrm{O}_2)$ is taken from tabulated values[144]. Figure B.1 shows the evolution of $\Delta_{\mathrm{f}} H_{\mathrm{v}_{\mathrm{O}}^{\bullet\bullet}}$, $T\Delta_{\mathrm{f}} S_{\mathrm{v}_{\mathrm{O}}^{\bullet\bullet}}$ and $\Delta_{\mathrm{f}} G_{\mathrm{v}_{\mathrm{O}}^{\bullet\bullet}}$. Examination of the data shows that the difference in oxygen vacancy formation energy at $T = 0$ K and the enthalpy at standard conditions ($T = 298$ K) is fairly small with $\approx$ 0.1 eV, justifying the comparison between experimental and theoretical data in tables 7.2 and 8.2, respectively.

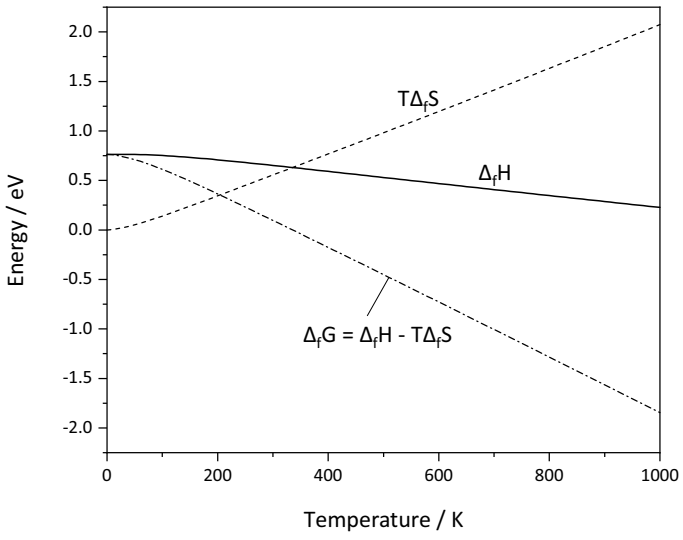

Figure B.1: Thermodynamic parameters of oxygen vacancy formation in $BaFeO_3$ at finite temperature.

B.2 BAND ALIGNMENT

Calculated band structures of periodic solids typically rely on system-dependent energy zero-points to which the energy levels (e.g. the Fermi level or band edges) are referenced. This precludes a direct comparison of calculated energy levels among different materials. The lack of a universal energy zero-point in periodic solids represents a long standing problem in solid state physics. Indeed, the average electrostatic potential in a periodic solid stemming from long-range Coulombic interactions cannot be calculated on an absolute scale (e.g. with respect to vacuum). The average electrostatic potential can be understood qualitatively as the potential well generated by a solid, the depth of which cannot be calculated when the bulk extends to infinity. This is different in molecular DFT calculations where the energy of an electron at vanishing electrostatic potential with zero kinetic energy (i.e. far away from the molecule in vacuum) is zero and serves as a meaningful universal energy reference of the calculated energy levels (e.g. HOMO, LUMO).

In more technical terms, the electrostatic potential at a given point in the unit cell depends on the Coulomb potential emanating from all other ions in the crystal (beyond the unit cell). An efficient method to calculate the electrostatic potential is the Ewald summation[145] which splits the total electrostatic potential into a short-range contribution calculated in real space and a long-range contribution calculated in reciprocal space. This ensures a high accuracy of the total potential while evaluating the two individual terms quickly. However, the long range term is not defined for very large distances ($G \rightarrow 0$, where G is a reciprocal space vector) causing the *average* electrostatic potential (depth of potential well) to remain unknown. In VASP, the average electrostatic potential is therefore conventionally set to zero, serving as a material-specific energy reference point for the energy levels.

However, in the study of extrinsic point defect formation involving the exchange of ionic or electronic species with surrounding reservoirs, knowledge of the absolute energy level positions in the crystal and the reservoirs is crucial. There exist different techniques to align DFT calculated band structures to a common reference level. A common technique, used in this work, is to align the energy levels with respect to the electrostatic potential at vacuum, which can be determined through separate surface slab calculations. The band alignment to vacuum enables the direct comparison of energy levels such as band edge positions and is needed for the calculation of the proton and hydroxide affinities.

In a surface slab calculation, several unit cells of the material are stacked along one of the crystallographic axes with a surface termination normal to the stacking direction that

is adjacent to a thick vacuum layer. In this work, the slabs are chosen to be symmetric to prevent the formation of electric dipoles across the slab (for perovskites this implies that the slabs become non-stoichiometric regarding the ratio of A- and B-site cations, but the slabs are sufficiently thick to ensure this has no effect on the band alignment). By introducing a vacuum layer, the electrostatic potential in vacuum can be calculated despite using periodic boundary conditions. The slab geometry of $BaFeO_3$ used in this work is shown in figure B.2 and is characterized by the following features:

- stacking direction [001]
- symmetric slab
- BO_2 terminated
- 7 unit cells (13 layers)
- ≈ 30 Å vacuum layer

The slabs were calculated with VASP[22–24] using both the PBE+U functional[26,139] with $U_{\text{eff}} = 4$ eV for Fe, and the HSE06 hybrid HF-DFT functional[146,147] intermixing 25 % of exact exchange. The PBE+U functional was used in conjuncture with figures 5.13, 7.3, 8.9, and the calculation of proton and hydroxide affinities. The HSE06 functional generally yields more accurate ionization potentials, however, at a massively increased computational cost. This was used only for correlating the calculated ion affinities to the ionization potentials in figures 8.4, 8.5, and 8.6. Regardless of the employed DFT functional, the slabs were calculated using high accuracy settings (energy cutoff of 500 eV, break condi-

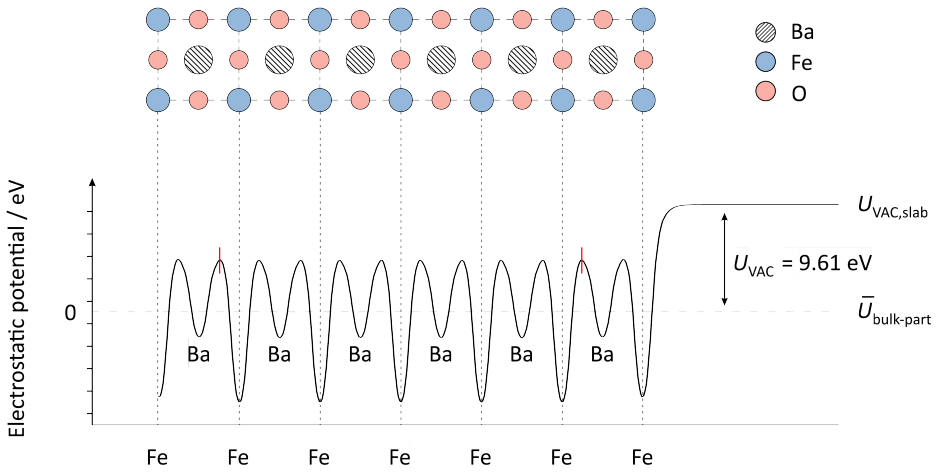

Figure B.2: Plane-averaged electrostatic potential along a 13-layer slab of $BaFeO_3$ with a ≈ 30 Å thick vacuum layer (potential of vacuum is cut off after ≈ 10 Å). The region used for determining $\overline{U}_{\text{bulk}-\text{part}}$ is indicated by the red markers.

tion for the electronic cycle of 10^{-6} eV, $8 \times 8 \times 1$ Monkhorst-Pack[148] k-point grid) and with the atomic positions fixed to those of the bulk geometry (i.e. static calculation). Figure B.2 shows the constructed slab with the calculated electrostatic potential. A list of the slab geometries used in the calculation of proton and hydroxide affinities for all other materials, e.g. MgO or SiO_2, can be found in the supporting material of the corresponding publication.[44]

The local electrostatic potential is obtained on a three-dimensional grid sampling the whole cell, including slab and vacuum layers. This three-dimensional potential is averaged along the slab direction using the script[149] to obtain a one-dimensional curve (figure B.2). From this curve, the vacuum potential can be determined as the difference between $U_{\mathrm{VAC,slab}}$ and $\overline{U}_{\mathrm{bulk-part}}$. The ionization potential (IP), i.e., the energy difference between vacuum and the valence band maximum, is then given by the relation

$$\mathrm{IP} = U_{\mathrm{vac}} - E_{\mathrm{VBM}} = 9.61\mathrm{eV} - 2.90\mathrm{eV} = 6.70\mathrm{eV} \tag{B.5}$$

where E_{VBM} is taken from a bulk calculation, to avoid electronic states at the surface influencing its position. The values in this example correspond to $BaFeO_3$ in the ideal cubic structure calculated with the HSE06 functional. By subtracting from the electronic eigenvalues of a bulk calculation first the value of E_{VBM} and then that of the IP, the energy levels are aligned to the vacuum potential. The band alignment method used in this work has been validated against literature data that includes both experimentally determined and calculated band edge positions (figure B.3).

Experimental data are scarce for most materials, but is available for some simple rock-salt structured oxides. Figure B.3 shows schematized band structures for the series MO (M=Mg, Ca, Sr, Ba) as obtained by HSE06 calculations of this work together with the literature data. Overall, the present methodology yields the same trend in ionization potential along the series compared to other data, i.e. a decrease in ionization potential from Mg to Ba. Smaller deviations in absolute band edge positions have been argued to stem from surface polarization effects influencing the calculated position of the vacuum potential. For a detailed discussion of surface polarization effects, and details of these calculations, the reader is referred to the supporting material of the corresponding publication, or[154].

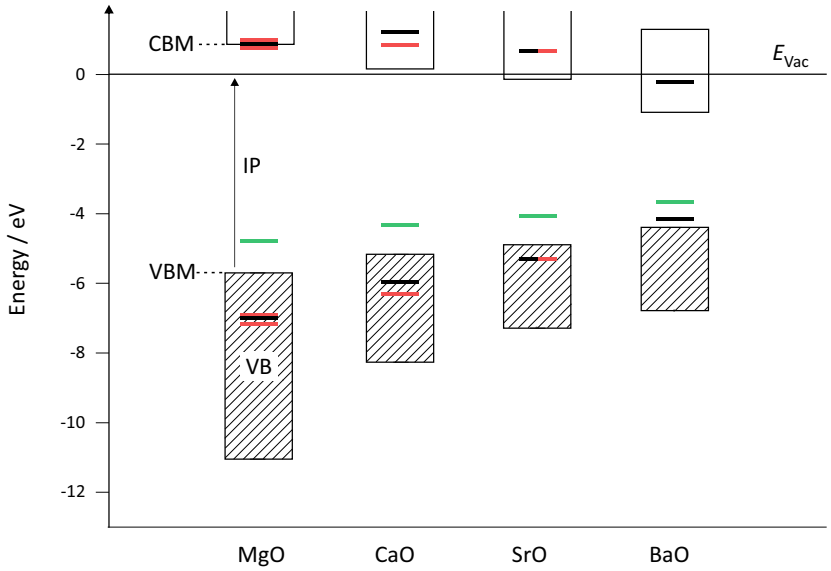

Figure B.3: Schematic illustration of HSE06 calculated band structures for alkaline earth oxides (hatched: valence band, empty: conduction band) compared to literature data. Red lines: experimental[150–152], green lines: theoretical data[152], black lines: theoretical data[153].

Surface slab calculations of systems with a low translational symmetry and an associated large unit cell tend to become prohibitively expensive, since their corresponding slabs easily reach up to several hundred atoms. In this work, this concerns the Jahn-Teller distorted phase of $BaFeO_3$ and oxygen non-stoichiometric supercells. To calculate the ionization potentials of these systems, an approach based on a constrained lattice expansion of the ideal cubic structure was chosen. In particular, the electrostatic potential of vacuum was calculated as a function of lattice constant of cubic $BaFeO_3$ (figure B.4). The ionization potentials of $Ba_8Fe_8O_{24-\delta}$ supercells were then calculated by interpolating the position of the vacuum potential from the data in figure B.4 with the pseudocubic lattice constant of the lower symmetric supercell. The Fermi level was taken from the supercells. Table B.1 summarizes the calculated ionization potentials of the different $BaFeO_{3-\delta}$ phases calculated in this work.

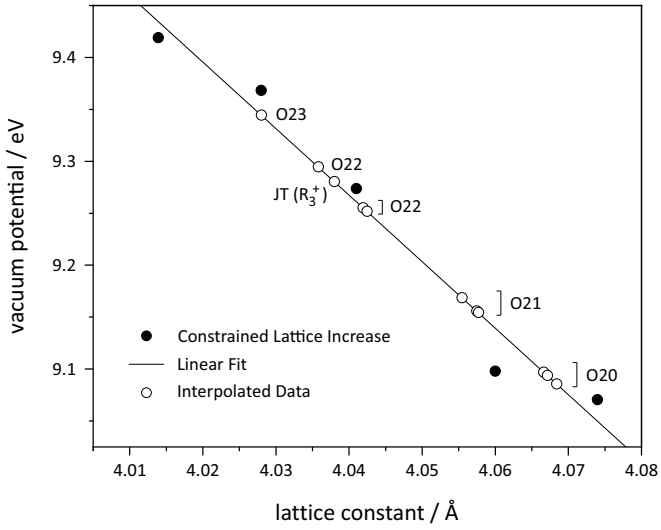

Figure B.4: Vacuum potential of constrained lattice increase of cubic $BaFeO_3$ (solid symbols) with interpolated data (empty symbols).

Table B.1: Ionization potentials (IP) of different $BaFeO_3$ phases. Same order for O-deficient supercells as in table B.2 where the positions of the vacancies in the supercell are specified.

system	add. info	DFT functional	$a^{\text{pseudo-cubic}}$ / Å	IP / eV
$BaFeo_3$	cubic	HSE	3.958	6.70
$BaFeo_3$	cubic	PBE+U	4.014	6.14
$Ba_8Fe_8o_{24}$	Jahn-Teller	PBE+U	4.038	6.20
$Ba_8Fe_8o_{23}$		PBE+U	4.028	5.99
$Ba_8Fe_8o_{22}$		PBE+U	4.042	5.82
$Ba_8Fe_8o_{22}$		PBE+U	4.042	5.83
$Ba_8Fe_8o_{22}$		PBE+U	4.036	5.84
$Ba_8Fe_8o_{21}$		PBE+U	4.056	5.61
$Ba_8Fe_8o_{21}$		PBE+U	4.057	5.64
$Ba_8Fe_8o_{20}$		PBE+U	4.058	5.52
$Ba_8Fe_8o_{20}$		PBE+U	4.067	5.12
$Ba_8Fe_8o_{20}$		PBE+U	4.067	4.99
$Ba_8Fe_8o_{20}$		PBE+U	4.068	5.03

B.3 DOS DIFFERENCE CURVES OF JAHN-TELLER DISTORTED $BaFeO_3$

Figure B.5 shows a comparison between the DOS of undistorted and Jahn-Teller distorted (R_3^+) $BaFeO_3$ on the left hand side. An increase in DOS relative to the undistorted cubic phase is highlighted in green, a depletion in red. The changes in total DOS are mirrored in the DOS difference curves of the $p_{\|}$ and e_g orbitals in the middle and on the right hand side of figure B.5. As clearly visible, the largest portion of changes in total DOS is related to changes in the $p_{\|}$ pDOS.

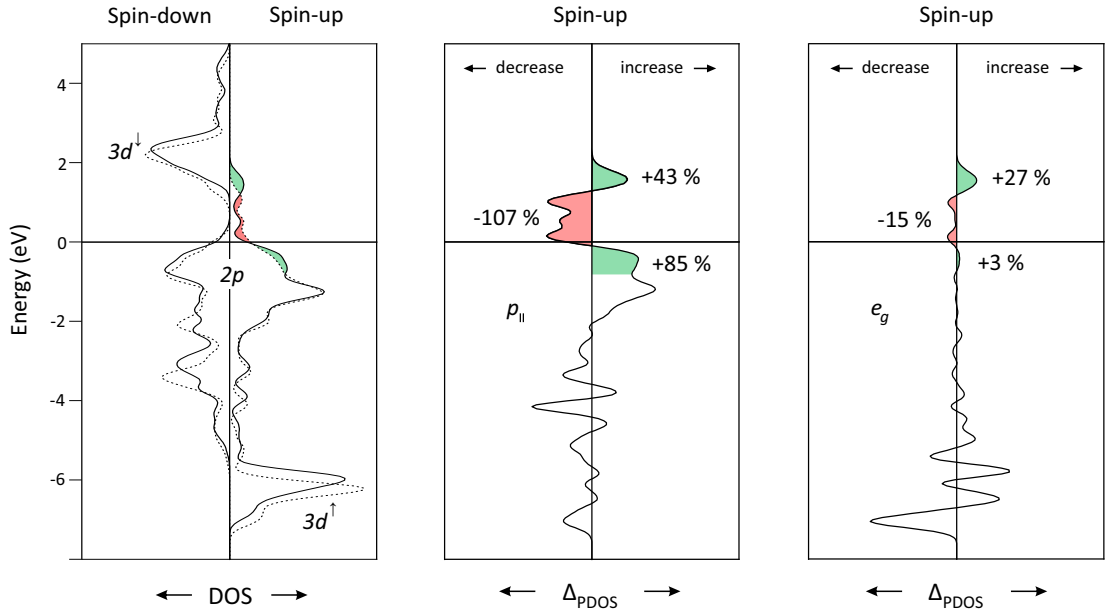

Figure B.5: Total DOS (left), pDOS difference curve of $p_{\|}$ orbitals (middle) and pDOS difference curve of e_g orbitals (right) of Jahn-Teller distorted $BaFeO_3$. The dashed line corresponds to the undistorted cubic phase.

B.4 SUPERCELL CONFIGURATIONS OF $Ba_xSr_{8-x}Fe_8O_{24-\delta}H$

In supercells containing multiple point defects, different symmetry-independent defect arrangements are possible. In order to screen all possible defect arrangements for the lowest total energy configurations, the *supercell* code was used.[43] The program yields, for a given number of point defects per supercell, all symmetry-independent defect arrangements. In order to document the different arrangements in the supercell, the oxygen lattice sites in a $Ba_8Fe_8O_{24}$ supercell have been labelled (figure B.6). The symmetry independent arrangements of $v_O^{\bullet\bullet}$ that yielded the three lowest total energies are summarized

in table B.2 along with the total energy and structural parameter after optimization. For the calculation of reaction energies and the discussion of electronic structure changes, the three lowest-energy configurations of a given oxygen stoichiometry are averaged.

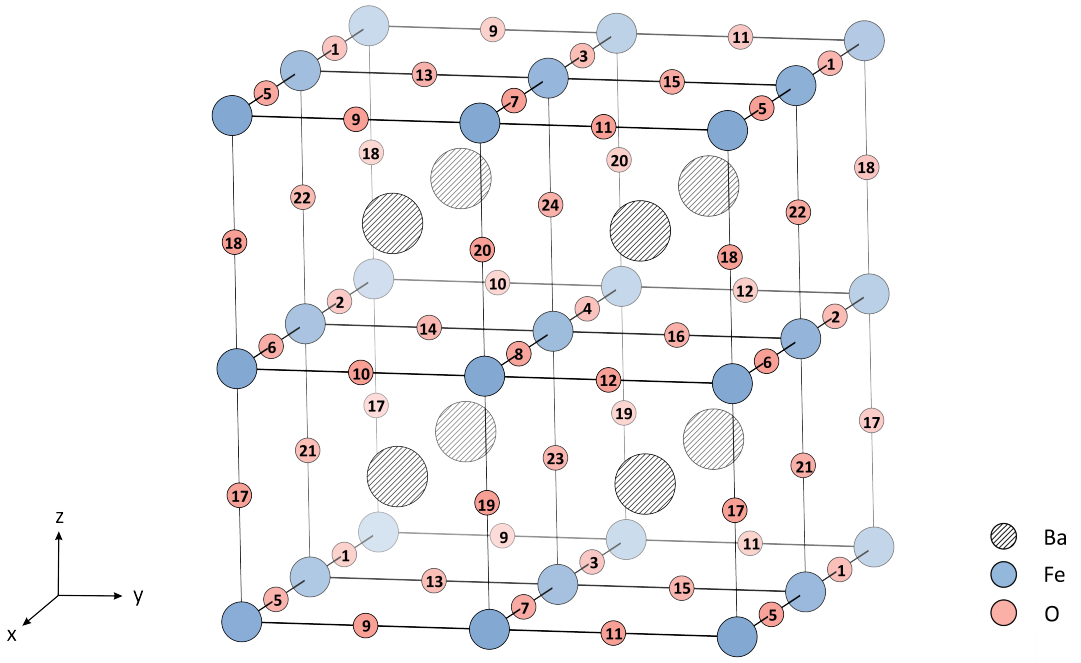

Figure B.6: Oxygen lattice sites in $Ba_8Fe_8O_{24}$ (red spheres: O, blue spheres: Fe, hatched spheres: Ba).

The configuration space becomes even more complicated when combining oxygen vacancies and protonic defects in one supercell. In this work, the approach taken was to distribute the protons only in those oxygen non-stoichiometric supercells which had yielded the three lowest total energies in the unprotonated state. Within a given oxygen non-stoichiometric supercell, the symmetry-independent proton positions were again screened using the *supercell* program. In table B.3, the configurations that yielded the lowest total energies are summarized along with the total energy and structural parameter after optimization. The defect arrangements are specified by the position of the lattice oxygen involved in the covalent OH bond and the lattice oxygen with the shorter of the two hydrogen bonds.

The configurations that yielded the three lowest total energies for both oxygen non-stoichiometric and proton-containing $BaFeO_3$ were taken to be the same for $Ba_{0.5}Sr_{0.5}FeO_3$ and $SrFeO_3$. A systematic screening of configurations with the lowest total energies was omitted for these compositions in order to keep the computational cost manageable.

Table B.2: Supercell configurations with different $v_O^{\bullet\bullet}$ arrangements.

	E_{tot}/eV	a/Å	b/Å	c/Å	Vol/Å^3	$v_O^{\bullet\bullet}$
$Ba_8Fe_8o_{24}$	-256.32	4.01	4.01	4.01	64.72	
$Ba_8Fe_8o_{24}$	-256.47	4.06	4.07	3.98	65.69	
$Ba_8Fe_8o_{23}$	-251.31	4.04	4.02	4.02	65.35	O1
$Ba_8Fe_8o_{22}$	-245.79	4.10	4.04	3.99	66.02	O1,O2
$Ba_8Fe_8o_{22}$	-245.74	4.07	4.07	3.99	66.05	O1,O10
$Ba_8Fe_8o_{22}$	-245.82	4.09	4.01	4.01	65.73	O1,O8
$Ba_8Fe_8o_{21}$	-239.68	4.13	4.02	4.02	66.68	O1,O2,O3
$Ba_8Fe_8o_{21}$	-239.73	4.12	4.01	4.04	66.79	O1,O2,O19
$Ba_8Fe_8o_{21}$	-239.72	4.15	4.05	3.98	66.78	O1,O2,O7
$Ba_8Fe_8o_{20}$	-232.95	4.13	4.04	4.04	67.24	O1,O2,O3,O4
$Ba_8Fe_8o_{20}$	-233.19	4.08	4.05	4.08	67.28	O1,O2,O19,O23
$Ba_8Fe_8o_{20}$	-233.09	4.16	4.12	3.92	67.27	O1,O2,O7,O8

Table B.3: Supercell configurations with different $v_O^{\bullet\bullet}$ and $OH_O^{\bullet}$ arrangements.

	E_{tot}/eV	a/Å	b/Å	c/Å	Vol/Å^3	$v_O^{\bullet\bullet}$	$OH_O^{\bullet}$	O$\cdots$H
$Ba_8Fe_8o_{24}H$	-261.00	4.06	4.08	4.00	66.38		O22H	O15
$Ba_8Fe_8o_{24}H$	-261.14	3.96	4.18	4.05	67.01		O24H	O8
$Ba_8Fe_8o_{24}H$	-261.16	4.19	4.02	3.98	66.98		O7H	O20
$Ba_8Fe_8o_{24}H_2$	-265.91	4.19	4.19	3.92	68.67		O7H,O16H	O24,O23
$Ba_8Fe_8o_{24}H_2$	-265.85	3.92	4.19	4.19	68.67		O24H,O12H	O8,O8
$Ba_8Fe_8o_{24}H_2$	-265.77	4.22	4.02	4.00	67.86		O7H,O23H	O20,O15
$Ba_8Fe_8o_{23}H$	-255.87	4.00	4.17	4.04	67.39	O1	O5H	O11
$Ba_8Fe_8o_{23}H$	-255.86	4.09	4.02	4.07	66.78	O1	O22H	O16
$Ba_8Fe_8o_{23}H$	-255.84	4.13	4.03	4.02	66.72	O1	O6H	O12
$Ba_8Fe_8o_{22}H$	-250.16	4.15	4.11	3.97	67.62	O1,O10	O9H	O20
$Ba_8Fe_8o_{22}H$	-250.16	4.14	4.12	3.98	67.78	O1,O10	O16H	O22
$Ba_8Fe_8o_{22}H$	-250.17	4.14	4.00	4.04	66.93	O1,O8	O6H	O16
$Ba_8Fe_8o_{21}H$	-243.99	4.18	4.06	4.02	68.27	O1,O2,O7	O22H	O15
$Ba_8Fe_8o_{21}H$	-243.96	4.16	4.02	4.09	68.27	O1,O2,O19	O18H	O11
$Ba_8Fe_8o_{21}H$	-244.00	4.18	4.06	4.02	68.13	O1,O2,O19	O12H	O17

B.5 Calculation of ion affinities of $BaFeO_3$

The proton and hydroxide affinities are defined as the energy changes of reactions B.6 and B.7, respectively.

$$\mathrm{H^+}(g) + \mathrm{O_O^x} \rightleftharpoons \mathrm{OH_O^\bullet} \tag{B.6}$$

$$\mathrm{OH^-}(g) + \mathrm{v_O^{\bullet\bullet}} \rightleftharpoons \mathrm{OH_O^\bullet} \tag{B.7}$$

The affinities are calculated indirectly by embedding reactions B.6 and B.7 into thermochemical cycles in which they represent the only unknown quantities. The two thermochemical cycles are shown in figures B.7 and B.8. The remaining energy contributions that appear in the thermochemical cycles and their determination by DFT are described below in § B.5.1 and § B.5.2. From the proton- and hydroxide affinities, the hydration energy can be calculated as

$$\Delta_\mathrm{r} E_{\mathrm{H_2O}} = E_\mathrm{PA} + E_\mathrm{HA} + E_{\mathrm{H-OH}} \tag{B.8}$$

where $E_{\mathrm{H-OH}}$ is the dissociation energy (16.9 eV) of the water molecule, taken as tabulated experimental value.[155] Equivalently, the hydration energy can be calculated from the defect formation energies.

$$\Delta_\mathrm{r} E_{\mathrm{H_2O}} = 2\Delta_\mathrm{f} E_{\mathrm{OH_O^\bullet}} - \Delta_\mathrm{f} E_{\mathrm{v_O^{\bullet\bullet}}} \tag{B.9}$$

where $\Delta_\mathrm{f} E_{\mathrm{OH_O^\bullet}}$ is the formation energy of a protonic defect and $\Delta_\mathrm{f} E_{\mathrm{v_O^{\bullet\bullet}}}$ the oxygen vacancy formation energy. However, these formation energies correspond to redox reactions (i.e. the incorporation of neutral H or O). The ion affinities, on the other hand, represent the purely ionic part of the hydration reaction without electron transfer. In addition to the proton- and hydroxide affinity, a hypothetical oxide ion affinity, E_OA, can be calculated according to

$$E_\mathrm{OA} = E_\mathrm{HA} - E_\mathrm{PA} \tag{B.10}$$

where E_OA is considered a hypothetical quantity since oxide ions are unstable in vacuum, i.e. the second electron affinity of the oxide ion is stabilized only in condensed phase by a

Madelung field (see supporting material of the corresponding publication[44]). The oxide affinity is used in § 8.6 to determine the standard chemical potential of an oxygen vacancy in the solid.

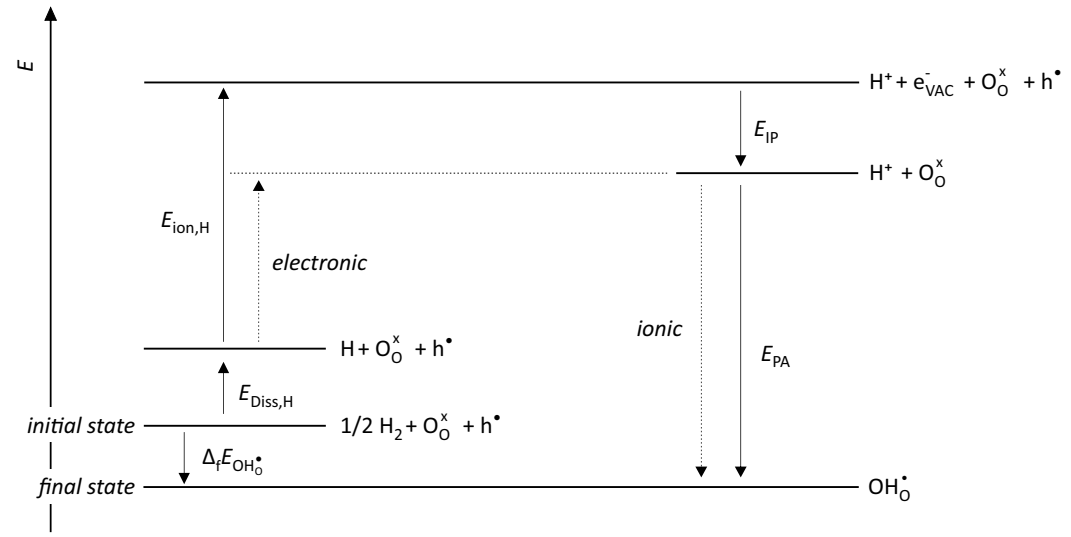

Figure B.7: Thermochemical cycle featuring the proton affinity of lattice oxygen ions.

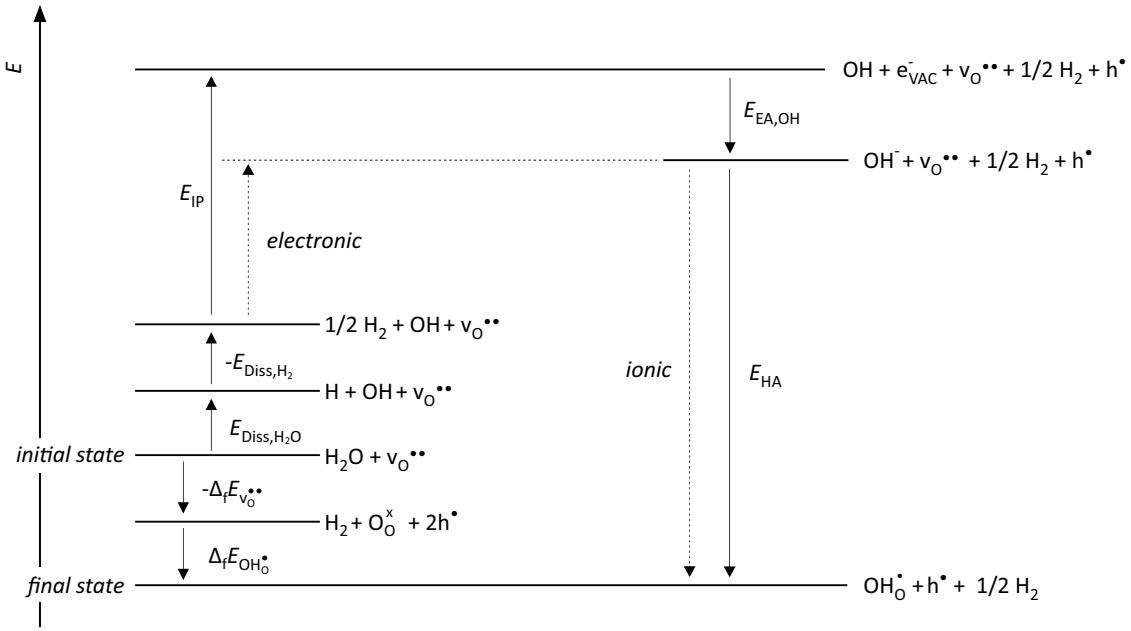

Figure B.8: Thermochemical cycle featuring the hydroxide affinity of oxygen vacancies.

B.5.1 PROTON AFFINITY

- $\Delta_f E_{OH_O^\bullet}$: The formation energy of the protonic defect in the solid is obtained from DFT supercell calculations (VASP[22–24], PBE+U functional[26,139] with $U_{\text{eff}} = 4$ eV for Fe), according to the reaction

$$O_O^x + \frac{1}{2}H_2 + h^\bullet \rightleftharpoons OH_O^\bullet \tag{B.11}$$

  where the charge state of the hydrogen is adjusted by removing an electron from the defect containing supercell, and placing it into a hypothetical electron reservoir of energy E_{VBM} (i.e. the defective supercell is charged). Structural optimizations were performed until residual forces fell below 10^{-4} eV/Å, allowing full relaxation of the supercell dimensions. The wave functions were optimized on $4 \times 4 \times 4$ Monkhorst-Pack[148] k-point mesh with an energy cutoff of 500 eV and a break condition for the electronic cycle of 10^{-6} eV. For the DFT calculation of H_2 (g), the molecule is placed in a vacuum box of 12 Å edge length and calculated using the PBE functional, giving $E_{H_2} = -6.77$ eV. In case of $BaFeO_3$, the calculated formation energy of a protonic defect according to reaction B.11 is -1.41 eV.

- $E_{\text{diss,H}}$: The dissociation energy of the H_2 molecule is taken as the tabulated experimental value of 4.52 eV.[156]

- $E_{\text{ion,H}}$: The ionization energy of the hydrogen atom is taken as the experimental value of 13.60 eV.

- E_{IP}: The ionization potential is calculated via surface slab calculations, see section § B.2. In case of $BaFeO_3$ (Jahn-Teller distorted phase), the ionization potential calculated with the PBE functional is 6.20 eV.

- E_{PA}: Finally the proton affinity is calculated from all other energy contributions via

$$\begin{aligned} E_{\text{PA}} &= E_{\text{H}} - 0.5E_{\text{diss,H}} - E_{\text{ion,H}} + E_{\text{IP}} \\ &= -1.41 - 4.52 - 13.60 + 6.20 \\ &= -11.07 \text{ eV} \end{aligned} \tag{B.12}$$

B.5.2 HYDROXIDE AFFINITY

- $\Delta_f E_{v_O^{\bullet\bullet}}$: The vacancy formation energy in the solid is obtained from DFT supercell calculations (VASP[22–24], PBE+U functional[26,139] with $U_{\text{eff}} = 4$ eV for Fe), according to the reaction

$$H_2 + O_O^x + 2h^\bullet \rightleftharpoons v_O^{\bullet\bullet} + H_2O \tag{B.13}$$

  where the charge state of the vacancy is adjusted by removing two electrons from the defect containing supercell, and placing them into a hypothetical electron reservoir of energy E_{VBM} (i.e. the defective supercell is charged). Structural optimizations were performed until residual forces fell below 10^{-4} eV/Å, allowing full relaxation of the supercell dimensions. The wave functions were optimized on $4 \times 4 \times 4$ Monkhorst-Pack[148] k-point mesh with an energy cutoff of 500 eV and a break condition for the electronic cycle of 10^{-6} eV. For the DFT calculation of H_2O (g), the molecule is placed in a vacuum box of 12 Å edge length and calculated using the PBE functional, giving $E_{O_2} = -14.22$ eV. In case of $BaFeO_3$, the vacancy formation energy according to reaction B.13 is -2.91 eV.

- E_{H}: The formation energy of the protonic defect in the solid is obtained from DFT supercell calculations using the PBE functional, see above. For $BaFeO_3$, a vale of -1.41 eV is calculated.

- E_{diss,H_2O}: The dissociation energy of the H_2O molecule is taken as the tabulated experimental value of 5.10 eV.[155]

- $E_{\text{diss,H}}$: The dissociation energy of the H_2 molecule is taken as the tabulated experimental value of =4.52 eV.[156]

- E_{IP}: The ionization potential is calculated via surface slab calculations, see section § B.2. In case of $BaFeO_3$ (Jahn-Teller distorted phase), the ionization potential calculated with the PBE functional is 6.20 eV.

- $E_{\text{EA,OH}}$: The electron affinity of the OH species is taken as the tabulated experimental value of -1.83 eV.[157]

- E_{HA}: Finally the hydroxide affinity is calculated from all other energy contributions via

$$\begin{aligned} E_{\mathrm{HA}} &= E_{\mathrm{H}} - E_{\mathrm{O}} - E_{\mathrm{IP}} - E_{\mathrm{EA,OH}} - E_{\mathrm{diss,H_2O}} + 0.5E_{\mathrm{H_2}} \\ &= -1.41 + 2.91 - 6.20 + 1.83 - 5.10 + 2.26 \\ &= -5.71 \text{ eV} \end{aligned} \tag{B.14}$$

B.6 Frenkel defect calculation in $BaFeO_3$ and $BaZrO_3$

The energy of the Frenkel disorder reaction B.15 was calculated for $BaZrO_3$ and $BaFeO_3$. Reaction B.15 describes the formation of an oxygen interstitial defect, O_i'', by displacing a lattice oxygen ion and leaving behind an oxygen vacancy, $v_O^{\bullet\bullet}$, at the original lattice site.

$$O_O^x + v_i \rightleftharpoons v_O^{\bullet\bullet} + O_i'' \tag{B.15}$$

The calculations were carried out with VASP[22–24] using the PBE+U functional[26,139] with $U_{\text{eff}} = 4$ eV for Fe and $2 \times 2 \times 2$ supercells, allowing full relaxation of the supercell dimensions. Structural optimizations were performed until residual forces fell below 10^{-4} eV/Å. The Brillouin-zone of the supercell was sampled with a $4 \times 4 \times 4$ Monkhorst-Pack k-point mesh.[148] In the input geometry, the interstitial oxygen ion is placed on the so-called hollow position[136] in case of $BaFeO_3$. For $BaZrO_3$, finding a configuration close to the global energy minimum required additional (symmetry-breaking) manual displacements of the oxygen interstitial. Figure B.9 shows the optimized geometries in the vicinity of the interstitial oxygen ions. The reaction energy of reaction B.15 is given by the difference in total energy between the defective and defect-free supercell. As such, reaction energies of 5.60 eV in case of $BaZrO_3$ and 2.33 eV in case of $BaFeO_3$ were determined.

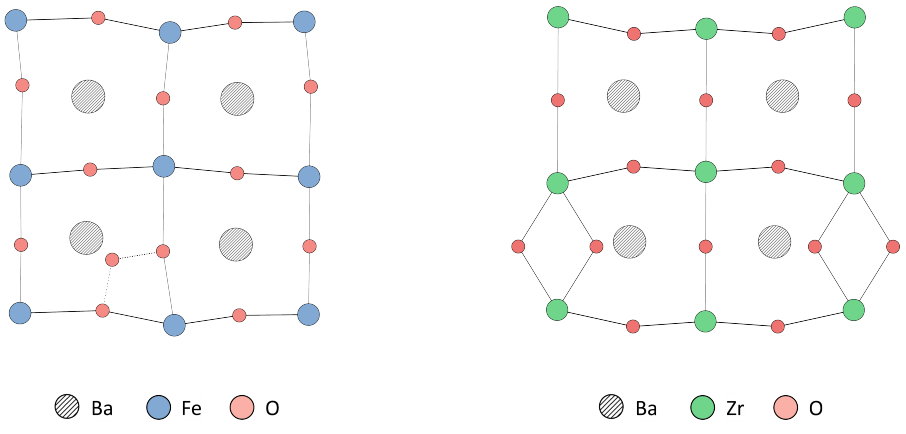

(a) $BaFeO_3$ **(b)** $BaZrO_3$

Figure B.9: Local lattice distortions in the vicinity of oxygen interstitial defects.

C Group theory applications

C.1 Symmetry-adapted linear combinations of p-orbitals

The symmetry-adapted linear combinations (SALCs) of the O 2p orbitals in the simple cubic perovskite lattice are generated using group theory for a set of high-symmetry k points and lines in the Brillouin zone. The generation of these SALCs is carried out in four consecutive steps, (*i*) define the basis sets, (*ii*) determine the groups of the wave vectors, (*iii*) find the irreducible representations (irreps) at the chosen k-vectors, (*iv*) construct the SALCs using a projection operator. The procedure employed here is based on chapter 10 in[68], and makes use of the online resources of the Bilbao Crystallographic Server[65,66]. In addition to[68], the understanding and chemical interpretation of the results is supported by refs.[56–58,67].

C.1.1 Step 1: Define basis sets

The cubic perovskite unit cell contains three oxygen ions with the coordinates, O1 = ($\frac{1}{2}$,0,0), O2 = (0,$\frac{1}{2}$,0), and O3 = (0,0,$\frac{1}{2}$). Each oxygen ion has three p-orbitals, p_{x}, p_{y}, p_{z}, giving rise to a total of nine p-orbitals. As discussed in § 5.4.1, based on the site symmetry group D_{4h} at each oxygen site, the total of nine p-orbitals can be immediately decomposed into the two independent basis sets, $p_{\parallel}$ and $p_{\perp}$. A basis functions of one of these basis sets cannot be transformed into a member of the other basis set by any of the space group's symmetry operations. The suffixes "$\parallel$" and "$\perp$" thereby specify whether the lobes of the p-orbitals are oriented parallel or perpendicular to the Fe-O bond axes.

$$\Gamma_{p_{\parallel}} = \begin{pmatrix} p_x,\ (1) \\ p_y,\ (2) \\ p_z,\ (3) \end{pmatrix}, \qquad \Gamma_{p_{\perp}} = \begin{pmatrix} p_y,\ (1) \\ p_z,\ (1) \\ p_x,\ (2) \\ p_z,\ (2) \\ p_x,\ (3) \\ p_y,\ (3) \end{pmatrix}$$

C.1.2 Step 2: The group of the k-vector

A list of the k-vectors used for the present analysis is given in table C.1. Each k vector, be it a k-point - or a line, is left invariant by some symmetry operations of the parent

point group O_h. The set of symmetry operations that leave a particular k-vector invariant constitute the group of the wave vector, given in table C.1. Consider, for example, the vector $k = (k, 0, 0)$ with $0 < k < \frac{\pi}{a}$, labeled Δ. This k-vector is left unchanged by rotations of 90° around the k_x axis, or reflections in planes including the k_x axis. The complete set of symmetry operations that leave Δ unchanged, forms the group C_{4v}. Wave functions with this k-vector are either left unchanged by the symmetry operations of that group, or transformed into a new wave function with the same energy.[58] When reaching the zone boundary at $k = (\frac{\pi}{a}, 0, 0)$, labeled X, a mirror plane perpendicular to the fourfold rotation around k_x is introduced, changing the group of the wave vector to D_{4h}.

The groups of the wave vectors can be found on the Bilbao Crystallographic Server under the tab "KVEC" of the section "Space group symmetry".[65,66]

Table C.1: Group of the wave vector for points and lines of high symmetry.

k-vector	label	group of wave vector
$(0, 0, 0)$	Γ	O_h
$(k, 0, 0)$	Δ	C_{4v}
$(\frac{\pi}{a}, 0, 0)$	X	D_{4h}
$(\frac{\pi}{a}, k, 0)$	Z	C_{2v}
$(\frac{\pi}{a}, \frac{\pi}{a}, 0)$	M	D_{4h}
$(\frac{\pi}{a}, \frac{\pi}{a}, k)$	T	C_{4v}
$(\frac{\pi}{a}, \frac{\pi}{a}, \frac{\pi}{a})$	R	O_h
(k, k, k)	Λ	C_{3v}

C.1.3 Step 3: Irreducible representations

The effect of site symmetry at the oxygen ion sites was to decompose the nine p orbitals into the irreps of the site symmetry group D_{4h}, which allowed two independent basis sets ,$p_{\parallel}$ and $p_{\perp}$, to be defined. The effect of the k-vector now leads to a further decomposition of the two basis sets into the irreps of the space group at the various points and lines in the Brillouin zone. The space groups irreps are thereby restricted to those irreps, which belong to the groups of the respective k-vectors. For example, at the point Γ, the basis sets can decompose into the irreps of the group O_h, whereas, at the point Δ, the basis sets can decompose into the irreps of the group C_{4v}.

For the present work, the irreps into which the two basis sets decompose are determined using the program BANDREP[67], which is part of the Bilbao Crystallographic

Server[65,66]. Alternatively, the space group irreps can be deduced by hand, which was done in[68]. Table C.2 shows the irreps at the different k-vectors using the solid state notation, where the capital letter specifies the position in the Brillouin zone, the subscript is a consecutive label of the different irreps with a given k, the superscript "+" or "-" indicates whether the irrep is *gerade* or *ungerade*, and the number in brackets gives the dimension of the irrep.

Table C.2: Space-group irreps of Bloch waves at different k-vectors.

	Γ	Δ	X	Z
e_{g}	$\Gamma_3^+(2)$	$\Delta_1(1)$, $\Delta_2(1)$	$\mathrm{X}_1^+(1)$, $\mathrm{X}_2^+(1)$	$2\mathrm{Z}_1(1)$
$t_{2\mathrm{g}}$	$\Gamma_5^+(3)$	$\Delta_3(1)$, $\Delta_5(2)$	$\mathrm{X}_4^+(1)$, $\mathrm{X}_5^+(2)$	$\mathrm{Z}_2(1)$, $\mathrm{Z}_3(1)$, $\mathrm{Z}_4(1)$
e_{u} ($p_\perp$)	$\Gamma_4^-(3)$, $\Gamma_5^-(3)$	$\Delta_1(1)$, $\Delta_2(1)$, $2\Delta_5(2)$	$\mathrm{X}_3^-(1)$, $\mathrm{X}_4^-(1)$, $\mathrm{X}_5^+(2)$, $\mathrm{X}_5^-(2)$	$\mathrm{Z}_1(1)$, $\mathrm{Z}_2(1)$, $\mathrm{Z}_3(1)$, $3\mathrm{Z}_4(1)$
$a_{2\mathrm{u}}$ ($p_\parallel$)	$\Gamma_4^-(3)$	$\Delta_1(1)$, $\Delta_5(2)$	$\mathrm{X}_1^+(1)$, $\mathrm{X}_5^-(2)$	$2\mathrm{Z}_1(1)$, $\mathrm{Z}_3(1)$

	M	T	R	Λ
e_{g}	$\mathrm{M}_1^+(1)$, $\mathrm{M}_2^+(1)$	$\mathrm{T}_1(1)$, $\mathrm{T}_2(1)$	$\mathrm{R}_3^+(2)$	$\Lambda_3(2)$
$t_{2\mathrm{g}}$	$\mathrm{M}_4^+(1)$, $\mathrm{M}_5^+(2)$	$\mathrm{T}_3(1)$, $\mathrm{T}_5(2)$	$\mathrm{R}_5^+(3)$	$\Lambda_1(1)$, $\Lambda_3(2)$
e_{u} ($p_\perp$)	$\mathrm{M}_3^+(1)$, $\mathrm{M}_4^+(1)$, $\mathrm{M}_5^+(2)$, $\mathrm{M}_5^-(2)$	$\mathrm{T}_3(1)$, $\mathrm{T}_4(1)$, $2\mathrm{T}_5(2)$	$\mathrm{R}_4^+(3)$, $\mathrm{R}_5^+(3)$	$\Lambda_1(1)$, $\Lambda_2(1)$, $2\Lambda_3(2)$
$a_{2\mathrm{u}}$ ($p_\parallel$)	$\mathrm{M}_1^+(1)$, $\mathrm{M}_2^+(1)$, $\mathrm{M}_3^-(1)$	$2\mathrm{T}_1(1)$, $\mathrm{T}_2(1)$	$\mathrm{R}_1^+(1)$, $\mathrm{R}_3^+(2)$	$\Lambda_1(1)$, $\Lambda_3(2)$

C.1.4 Step 4: Projection operator

The symmetry-adapted linear combinations (SALCs), $f(\Gamma_j)$, which transform as the jth irrep, Γ_j, are obtained by applying successively the symmetry operations of the group while taking into account the character of the irrep.

$$f(\Gamma_i) = \sum_A \chi_A\left(\Gamma_i\right) P_A\, f(\mathrm{r}) \tag{C.1}$$

Here, $f(\mathrm{r})$ is an original basis function to which the symmetry operations A of the group are applied with the projection operator P_A. The *projected* basis functions are then multiplied by the character χ_A of the given irrep Γ_i.[68]

By using equation C.1 to generate a new wave function from an original basis function, one forces the resulting wave function to have the same symmetry properties of the irrep itself that is used for the construction. That way, the resulting wave function is *adapted* to the symmetry of the irrep and, as such, to the symmetry of the crystal. E.g., the SALC

associated with the X_1^+ irrep with $k = (0, 0, \frac{\pi}{a})$ constructed from the $p_\parallel$ basis set, taking $p_z|3$ ("3" stands for the O3 ion in the unit cell) as the original basis function, is given as:

$$f(X_1^+) = \sum_A \chi_A\,(X_1^+)\; P_A\; p_z, \mathrm{O3} \propto p_z|3 \tag{C.2}$$

where the characters χ_A are taken from the Bilbao Crystallographic Server (under "Representations DSG" or "Representations DPG" in the section "Double point and space groups"). Since $p_z, |3$ is not an actual linear combination, the term "SALC" is not appropriate here, and the term "symmetry function" may be used for such cases, in which equation C.1 yields a single basis function. The choice of the original basis function to construct the symmetry function of X_1^+ is thereby arbitrary. If one would use $p_x|1$ as the original basis function, the projected functions cancel each other out and no meaningful result would be obtained with equation C.1.

$$f(X_1^+) = \sum_A \chi_A\,(X_1^+)\; P_A\; p_x|1 = 0 \tag{C.3}$$

The symmetry function of X_1^+ with $k = (0, 0, \frac{\pi}{a})$ generated from the $p_\parallel$ basis set is therefore given by $p_z|3$. The orientation of the k-vector with $k = (0, 0, \frac{\pi}{a})$ is chosen to be conform with the orientation on the Bilbao Crystallographic Server but the resulting symmetry function can easily be converted to $k = (\frac{\pi}{a}, 0, 0)$ which would be $p_x|1$. Equation C.1 is formulated for the case of one-dimensional irreps, such as X_1^+. In case of multi-dimensional irreps, the characters, χ_A, must be replaced by the diagonal matrix elements of the jth irrep, Γ_j.

$$f^i(\Gamma_j) = \sum_A D_{ii,A}\,(\Gamma_j)\; P_A\; f(\mathrm{r}) \tag{C.4}$$

where $D_{ii,A}(\Gamma_j)$ are the diagonal matrix elements of the jth irrep Γ_j and each symmetry operation A. For example, the SALC associated with the two-dimensional irrep X_5^- with $k = (0, 0, \frac{\pi}{a})$, generated from the $p_z|3$ basis function is given by.

$$f^{\mathrm{row1}}(X_5^-) = \sum_A D_{11,A}\,(X_5^-)\; P_A\; p_z|3 = 0 \tag{C.5}$$

$$f^{\mathrm{row2}}(X_5^-) = \sum_A D_{11,A}\,(X_5^-)\; P_A\; p_z|3 = 0 \tag{C.6}$$

The same procedure is repeated with the basis functions $p_{\mathrm{x}}|1$ and $p_{\mathrm{y}}|2$

$$f^{\mathrm{row1}}(\mathrm{X}_5^-) = \sum_A D_{11,A}\,(\mathrm{X}_5^-)\; P_A\; p_{\mathrm{x}}|1 = p_{\mathrm{x}}|1 + p_{\mathrm{y}}|2 \tag{C.7}$$

$$f^{\mathrm{row2}}(\mathrm{X}_5^-) = \sum_A D_{11,A}\,(\mathrm{X}_5^-)\; P_A\; p_{\mathrm{x}}|1 = p_{\mathrm{x}}|1 - p_{\mathrm{y}}|2 \tag{C.8}$$

$$f^{\mathrm{row1}}(\mathrm{X}_5^-) = \sum_A D_{11,A}\,(\mathrm{X}_5^-)\; P_A\; p_{\mathrm{y}}|2 = p_{\mathrm{y}}|2 + p_{\mathrm{x}}|1 \tag{C.9}$$

$$f^{\mathrm{row2}}(\mathrm{X}_5^-) = \sum_A D_{11,A}\,(\mathrm{X}_5^-)\; P_A\; p_{\mathrm{y}}|2 = p_{\mathrm{y}}|2 - p_{\mathrm{x}}|1 \tag{C.10}$$

As a result, the symmetry functions associated with X_5^- where $k = (0, 0, \frac{\pi}{a})$ are $p_{\mathrm{x}}|1$ and $p_{\mathrm{y}}|2$. These symmetry functions can easily be converted to a different orientation with $k = (\frac{\pi}{a}, 0, 0)$, giving $p_{\mathrm{y}}|2$ and $p_{\mathrm{z}}|3$.

The information on how the original basis functions behave under the symmetry operations of the different groups of the wave vectors was determined manually in this work and is provided in the tables C.3 - C.9. The orientation of the main rotation axes and order of symmetry operations in each table is chosen to be conform with the Bilbao Crystallographic Server. With this, the symmetry functions or SALCs at the different k-vectors projected from either the $p_{\parallel}$ or $p_{\perp}$ basis set, can be generated using equations C.1 and C.4.

Table C.3: Action table for the point group O.

	1	2_{001}	2_{010}	2_{100}	2_{110}	$2_{1\bar{1}0}$	4^-_{001}	4^+_{001}	4^-_{100}	2_{011}	$2_{01\bar{1}}$	4^+_{100}	4^+_{010}	2_{101}	4^-_{010}	2_{101}
1	1	1	1	1	2	2	2	2	1	1	1	1	3	3	3	3
2	2	2	2	2	1	1	1	1	3	3	3	3	2	2	2	2
3	3	3	3	3	3	3	3	3	2	2	2	2	1	1	1	1
$\mathbf{p}_{\mathrm{x}}$	p_{x}	$-p_{\mathrm{x}}$	$-p_{\mathrm{x}}$	p_{x}	p_{y}	$-p_{\mathrm{y}}$	p_{y}	$-p_{\mathrm{y}}$	p_{x}	$-p_{\mathrm{x}}$	$-p_{\mathrm{x}}$	p_{x}	p_{z}	$-p_{\mathrm{z}}$	$-p_{\mathrm{z}}$	p_{z}
$\mathbf{p}_{\mathrm{y}}$	p_{y}	$-p_{\mathrm{y}}$	p_{y}	$-p_{\mathrm{y}}$	p_{x}	$-p_{\mathrm{x}}$	$-p_{\mathrm{x}}$	p_{x}	p_{z}	p_{z}	$-p_{\mathrm{z}}$	$-p_{\mathrm{z}}$	p_{y}	$-p_{\mathrm{y}}$	p_{y}	$-p_{\mathrm{y}}$
$\mathbf{p}_{\mathrm{z}}$	p_{z}	p_{z}	$-p_{\mathrm{z}}$	$-p_{\mathrm{z}}$	$-p_{\mathrm{z}}$	$-p_{\mathrm{z}}$	p_{z}	p_{z}	$-p_{\mathrm{y}}$	p_{y}	$-p_{\mathrm{y}}$	p_{y}	$-p_{\mathrm{x}}$	p_{x}	p_{x}	$-p_{\mathrm{x}}$

Table C.4: Action table for the point group C_{4v} at the point Δ, where $k = (0, 0, k)$.

	1	2_{001}	4^+_{001}	4^-_{001}	m_{010}	m_{100}	m_{110}	$\mathrm{m}_{1\bar{1}0}$
1	1	1	2	2	1	1	2	2
2	2	2	1	1	2	2	1	1
3	3	3	3	3	3	3	3	3
$\mathbf{p}_\mathrm{x}$	p_x	$-p_\mathrm{x}$	$-p_\mathrm{y}$	p_y	p_x	$-p_\mathrm{x}$	$-p_\mathrm{y}$	p_y
$\mathbf{p}_\mathrm{y}$	p_y	$-p_\mathrm{y}$	p_x	$-p_\mathrm{x}$	$-p_\mathrm{y}$	p_y	$-p_\mathrm{x}$	p_x
$\mathbf{p}_\mathrm{z}$	p_z	p_z	p_z	p_z	p_z	p_z	p_z	p_z

Table C.5: Action table for the point group D_{4h} at the point X, where $k = (0, 0, \frac{\pi}{a})$.

	1	2_{001}	4^+_{001}	4^-_{001}	2_{010}	2_{100}	2_{110}	$2_{1\bar{1}0}$	-1	m_{001}	-4^+_{001}	-4^-_{001}	m_{010}	m_{100}	m_{110}	$\mathrm{m}_{1\bar{1}0}$
1	1	1	2	2	1	1	2	2	1	1	2	2	1	1	2	2
2	2	2	1	1	2	2	1	1	2	2	1	1	2	2	1	1
3	3	3	3	3	-3	-3	-3	-3	-3	-3	-3	-3	3	3	3	3
$\mathbf{p}_\mathrm{x}$	p_x	$-p_\mathrm{x}$	$-p_\mathrm{y}$	p_y	$-p_\mathrm{x}$	p_x	p_y	$-p_\mathrm{y}$	$-p_\mathrm{x}$	p_x	p_y	$-p_\mathrm{y}$	p_x	$-p_\mathrm{x}$	$-p_\mathrm{y}$	p_y
$\mathbf{p}_\mathrm{y}$	p_y	$-p_\mathrm{y}$	p_x	$-p_\mathrm{x}$	p_y	$-p_\mathrm{y}$	p_x	$-p_\mathrm{x}$	$-p_\mathrm{y}$	p_y	$-p_\mathrm{x}$	p_x	$-p_\mathrm{y}$	p_y	$-p_\mathrm{x}$	p_x
$\mathbf{p}_\mathrm{z}$	p_z	p_z	p_z	p_z	$-p_\mathrm{z}$	$-p_\mathrm{z}$	$-p_\mathrm{z}$	$-p_\mathrm{z}$	$-p_\mathrm{z}$	$-p_\mathrm{z}$	$-p_\mathrm{z}$	$-p_\mathrm{z}$	p_z	p_z	p_z	p_z

Table C.6: Action table for the point group C_{2v} at the point Z, where $k = (\frac{\pi}{a}, 0, k)$.

	1	2_{001}	m_{010}	m_{100}
1	1	-1	1	-1
2	2	2	2	2
3	3	3	3	3
$\mathbf{p}_\mathrm{x}$	p_x	$-p_\mathrm{x}$	p_x	$-p_\mathrm{x}$
$\mathbf{p}_\mathrm{y}$	p_y	$-p_\mathrm{y}$	p_y	$-p_\mathrm{y}$
$\mathbf{p}_\mathrm{z}$	p_z	p_z	p_z	p_z

Table C.7: Action table for the point group D_{4h} at the point M, where $k = (\frac{\pi}{a}, \frac{\pi}{a}, 0)$.

	1	2_{001}	4^+_{001}	4^-_{001}	2_{010}	2_{100}	2_{110}	$2_{1\bar{1}0}$	-1	m_{001}	-4^+_{001}	-4^-_{001}	m_{010}	m_{100}	m_{110}	$\mathrm{m}_{1\bar{1}0}$
1	1	-1	-2	2	-1	1	2	-2	-1	1	2	-2	1	-1	-2	2
2	2	-2	1	-1	2	-2	1	-1	-2	2	-1	1	-2	2	-1	1
3	3	3	3	3	3	3	3	3	3	3	3	3	3	3	3	3
$\mathbf{p}_\mathrm{x}$	p_x	$-p_\mathrm{x}$	$-p_\mathrm{y}$	p_y	$-p_\mathrm{x}$	p_x	p_y	$-p_\mathrm{y}$	$-p_\mathrm{x}$	p_x	p_y	$-p_\mathrm{y}$	p_x	$-p_\mathrm{x}$	$-p_\mathrm{y}$	p_y
$\mathbf{p}_\mathrm{y}$	p_y	$-p_\mathrm{y}$	p_x	$-p_\mathrm{x}$	p_y	$-p_\mathrm{y}$	p_x	$-p_\mathrm{x}$	$-p_\mathrm{y}$	p_y	$-p_\mathrm{x}$	p_x	$-p_\mathrm{y}$	p_y	$-p_\mathrm{x}$	p_x
$\mathbf{p}_\mathrm{z}$	p_z	p_z	p_z	p_z	$-p_\mathrm{z}$	$-p_\mathrm{z}$	$-p_\mathrm{z}$	$-p_\mathrm{z}$	$-p_\mathrm{z}$	$-p_\mathrm{z}$	$-p_\mathrm{z}$	$-p_\mathrm{z}$	p_z	p_z	p_z	p_z

Table C.8: Action table for the point group C_{4v} at the point T, where $k = (\frac{\pi}{a}, \frac{\pi}{a}, k)$.

	1	2_{001}	4^+_{001}	4^-_{001}	m_{010}	m_{100}	m_{110}	$\mathrm{m}_{1\bar{1}0}$
1	1	-1	-2	2	1	-1	-2	2
2	2	-2	1	-1	-2	2	-1	1
3	3	3	3	3	3	3	3	3
$\mathbf{p}_\mathrm{x}$	p_x	$-p_\mathrm{x}$	$-p_\mathrm{y}$	p_y	p_x	$-p_\mathrm{x}$	$-p_\mathrm{y}$	p_y
$\mathbf{p}_\mathrm{y}$	p_y	$-p_\mathrm{y}$	p_x	$-p_\mathrm{x}$	$-p_\mathrm{y}$	p_y	$-p_\mathrm{x}$	p_x
$\mathbf{p}_\mathrm{z}$	p_z	p_z	p_z	p_z	p_z	p_z	p_z	p_z

Table C.9: Action table for the point group C_{3v} at the point Λ, where $k = (k, k, k)$.

	1	3^+_{111}	3^-_{111}	$\mathrm{m}_{1\bar{1}1}$	$\mathrm{m}_{01\bar{1}}$	$\mathrm{m}_{\bar{1}01}$
1	1	3	2	2	1	3
2	2	1	3	1	3	2
3	3	2	1	3	2	1
$\mathbf{p}_\mathrm{x}$	p_x	p_z	p_y	p_y	p_x	p_z
$\mathbf{p}_\mathrm{y}$	p_y	p_x	p_z	p_x	p_z	p_y
$\mathbf{p}_\mathrm{z}$	p_z	p_y	p_x	p_z	p_y	p_x

C.1.5 List of Symmetry-Adapted Linear Combinations

A list of the resulting symmetry functions and SALCs is provided in tables C.10 - C.15. In certain cases, there are two different orientations of the k-vector, one which is conform with the Bilbao Crystallographic Server, and another one, which is conform with the k-vector path used in the band structure analysis in § 5.4.

Table C.10: Symmetry functions and SALCs at the point Γ.

Γ	$k = (0, 0, 0)$
$\Gamma_4^-(3)^{\,p_\parallel}$	$p_x, 1; p_y, 2; p_z, 3$
$\Gamma_4^-(3)^{\,p_\perp}$	$p_x, 2 + p_x, 3; p_y, 1 + p_y, 3; p_z, 1 + p_z, 2$
$\Gamma_5^-(3)^{\,p_\perp}$	$p_x, 2 - p_x, 3; p_y, 1 - p_y, 3; p_z, 1 - p_z, 2$

Table C.11: Symmetry functions and SALCs at the point Δ.

Δ	$k = (0, 0, k)$	$k = (k, 0, 0)$
$\Delta_1(1)^{\,p_\parallel}$	$p_z, 3$	$p_x, 1$
$\Delta_5(2)^{\,p_\parallel}$	$p_x, 1;\ p_y, 2$	$p_y, 2;\ p_z, 3$
$\Delta_1(1)^{\,p_\perp}$	$p_z, 1 + p_z, 2$	$p_x, 2 + p_x, 3$
$\Delta_1(1)^{\,p_\perp}$	$p_z, 1 - p_z, 2$	$p_x, 2 - p_x, 3$
$\Delta_5(2)^{\,p_\perp}$	$p_y, 1;\ p_x, 2$	$p_y, 3;\ p_z, 2$
$\Delta_5(2)^{\,p_\perp}$	$p_x, 3;\ p_y, 3$	$p_y, 1;\ p_z, 1$

Table C.12: Symmetry functions and SALCs at the point X.

X	$k = (0, 0, \frac{\pi}{a})$	$k = (\frac{\pi}{a}, 0, 0)$
$\mathrm{X}_1^+(1)^{\,p_\parallel}$	$p_z, 3$	$p_x, 1$
$\mathrm{X}_5^-(2)^{\,p_\parallel}$	$p_x, 1;\ p_y, 2$	$p_y, 2;\ p_z, 3$
$\mathrm{X}_3^-(1)^{\,p_\perp}$	$p_z, 1 + p_z, 2$	$p_x, 2 + p_x, 3$
$\mathrm{X}_4^-(1)^{\,p_\perp}$	$p_z, 1 - p_z, 2$	$p_x, 2 - p_x, 3$
$\mathrm{X}_5^+(2)^{\,p_\perp}$	$p_x, 3;\ p_y, 3$	$p_y, 1;\ p_z, 1$
$\mathrm{X}_5^-(2)^{\,p_\perp}$	$p_y, 1;\ p_x, 2$	$p_y, 3;\ p_z, 2$

Table C.13: Symmetry functions and SALCs at the point Z.

Z	$k = (\frac{\pi}{a}, 0, k)$	$k = (\frac{\pi}{a}, k, 0)$
$\mathrm{Z}_1(1)^{\,p_\parallel}$	$p_x, 1$	$p_x, 1$
$\mathrm{Z}_1(1)^{\,p_\parallel}$	$p_z, 3$	$p_y, 2$
$\mathrm{Z}_3(1)^{\,p_\parallel}$	$p_y, 2$	$p_z, 3$
$\mathrm{Z}_1(1)^{\,p_\perp}$	$p_z, 2$	$p_y, 3$
$\mathrm{Z}_2(1)^{\,p_\perp}$	$p_y, 1$	$p_z, 1$
$\mathrm{Z}_3(1)^{\,p_\perp}$	$p_y, 3$	$p_z, 2$
$\mathrm{Z}_4(1)^{\,p_\perp}$	$p_z, 1$	$p_y, 1$
$\mathrm{Z}_4(1)^{\,p_\perp}$	$p_x, 2$	$p_x, 3$
$\mathrm{Z}_4(1)^{\,p_\perp}$	$p_x, 3$	$p_x, 2$

Table C.14: Symmetry functions and SALCs at the point M.

M	$k = (\frac{\pi}{a}, \frac{\pi}{a}, 0)$
$\mathrm{M}_1^+(1)^{\,p_\parallel}$	$p_x, 1 + p_y, 2$
$\mathrm{M}_2^+(1)^{\,p_\parallel}$	$p_x, 1 - p_y, 2$
$\mathrm{M}_3^-(1)^{\,p_\parallel}$	$p_z, 3$
$\mathrm{M}_3^+(1)^{\,p_\perp}$	$p_y, 1 - p_x, 2$
$\mathrm{M}_4^+(1)^{\,p_\perp}$	$p_y, 1 + p_x, 2$
$\mathrm{M}_5^+(2)^{\,p_\perp}$	$p_z, 1;\ p_z, 2$
$\mathrm{M}_5^-(2)^{\,p_\perp}$	$p_x, 3;\ p_y, 3$

Table C.15: Symmetry functions and SALCs at the point T.

T	$k = (\frac{\pi}{a}, \frac{\pi}{a}, k)$
$\mathrm{T}_1(1)^{\,p_\parallel}$	$p_x, 1 + p_y, 2$
$\mathrm{T}_1(1)^{\,p_\parallel}$	$p_z, 3$
$\mathrm{T}_2(1)^{\,p_\parallel}$	$p_x, 1 - p_y, 2$
$\mathrm{T}_3(1)^{\,p_\perp}$	$p_y, 1 + p_x, 2$
$\mathrm{T}_4(1)^{\,p_\perp}$	$p_y, 1 - p_x, 2$
$\mathrm{T}_5(2)^{\,p_\perp}$	$p_z, 1;\ p_z, 2$
$\mathrm{T}_5(2)^{\,p_\perp}$	$p_x, 3;\ p_y, 3$

C.2 SYMMETRY-MODE DISPLACEMENT

Structural distortions are inherently related to an undistorted parent phase typically having a higher symmetry. In the symmetry-mode approach, group theory is used to describe structural distortions by the normal modes of the parent phase, i.e. periodic atomic displacements with specific symmetry properties that correspond to irreducible representations (irreps) of the space group of the parent phase.[158,159] Normal modes with negative imaginary frequencies indicate structural instabilities in the crystal, i.e. that the atomic displacement lowers the total energy of the crystal. The parent, high-symmetry phase in the present work is the ideal cubic perovskite structure with the space group $\mathrm{Pm\bar{3}m}$. To distort the cubic structure according to a normal mode, three pieces of information are required:

1. **Irreducible representations**: The irreps describing the distortion patterns to be imposed on the crystal structure. These are, in the present case, the irreps $R_3^+(2)$ and $M_2^+(1)$ (dimensionality given in brackets), which belong to the class of Jahn-Teller distortions and have been identified based on the phonon dispersion in chapter § 6.2.

2. **Order parameter**: The order parameter is a vector whose components specify the orientation of the distortion pattern. For example, if a distortion produces a unique high-symmetry axis, the order parameter specifies the crystallographic direction of that axis. A distortion pattern can also be applied in more than one crystallographic direction, in which case the final distortion is a superposition of the individual patterns as specified by the components in the order parameter. In case of multi-dimensional irreps, the order parameter specifies which distortion pattern is used. For more information, see[159]. The order parameter used in chapter § 6.3 are $(a, 0, 0)$ for the M_2^+- and $(a, 0)$ for the R_3^+-irrep.

3. **Amplitude**: The amplitude with which the distortion is applied, as defined in equation 6.5.

The distorted structures are generated with the program ISODISTORT[81,82], as part of the ISOTROPY suite[83]. The obtained structure files can be converted to the standard VASP format using the "Structure Data Converter and Editor" of the Bilbao Crystallographic Server[65,66].

Different order parameters of the irreps $R_3^+(2)$ and $M_2^+(1)$ with varying amplitude are shown in figure C.1. The order parameter $(a, 0, 0)$ for the M_2^+- and $(a, 0)$ for the R_3^+-irrep seemingly produce the largest energy gains upon distortion and are thus considered for

further discussion in chapter § 6.3. Note, that order parameters of type (a, b, c) for M_2^+- and (a, b) for the R_3^+-irrep are neglected in figure C.1. The different components a, b and c indicate that more than one polarization vector is applied, with the individual polarization vectors having different amplitudes. Since this represents a large number of possible combinations, these order parameters were not tested as part of this work.

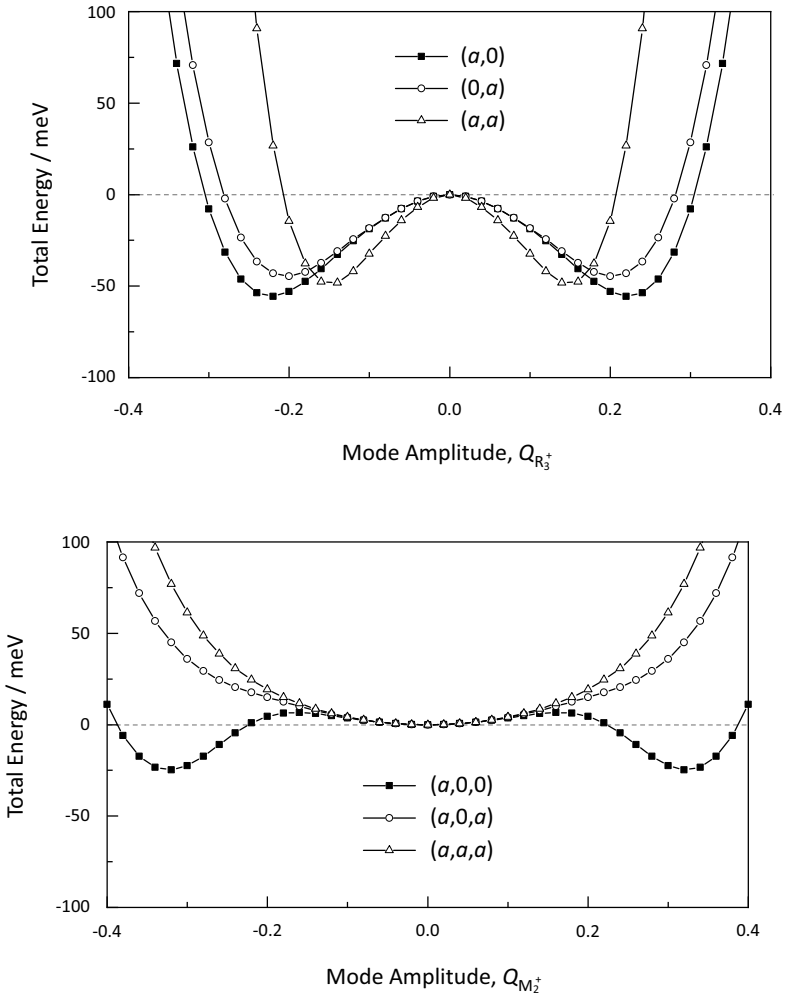

Figure C.1: Total energy evolution for distortions associated with the phonon modes R_3^+ and M_2^+, starting from the parent cubic structure of $BaFeO_3$ at fixed cell volume.

D Curriculum Vitae

MAXIMILIAN FELIX HOEDL

Werfmershalde 1, 70190 Stuttgart | +49 177 4959821 | maximilian.felix.hoedl@gmail.com

SCIENTIFIC EDUCATION

since 02/2017	Max-Planck Institute for Solid State Research, Stuttgart
	PhD Student in Chemistry
09/2014–02/2017	University of Augsburg, Augsburg
	M. Sc. Material Science (Grade 1.3)
09/2015–02/2016	University of Lisbon, Portugal
	Semester abroad (Erasmus scholarship)
02/2012–07/2012	Sao Paolo State University, Brazil
	Semester abroad (DAAD scholarship)
09/2010–08/2014	Ruprecht-Karls University, Heidelberg
	B. Sc. Geosciences (Grade 1.3)

WORKING EXPERIENCE

04/2014–07/2014	Plansee SE, Breitenwang, Austria
	Internship, Dpt. Solid Oxide Fuel Cells
09/2013–10/2013	Materials Research Center, Freiburg
	Internship, Characterization of materials
09/2009–09/2010	Diakonie Hospital, Stuttgart
	Voluntary, Internal Medicine

PERSONAL INFORMATION

Language	German (native), English (fluent),
	Portuguese (fluent), French (basics)
IT	Linux OS, Python, Scientific Illustration (CorelDraw),
	Microsoft Office, Latex
Interests	Piano (weekly lessons), Football (club member),
	Gardening, Cooking

E List of Publications

[1]: **Maximilian F. Hoedl**, Evgeniy Makagon, Igor Lubomirsky, Rotraut Merkle, Eugene A.Kotomin, and Joachim Maier. Impact of point defects on the elastic properties of $BaZrO_3$: Comprehensive insight from experiments and ab initio calculations. *Acta Materialia*(160):247-256, 2018.

[2]: Tor S. Bjørheim, **Maximilian F. Hoedl**, Rotraut Merkle, Eugene A. Kotomin, and Joachim Maier. Proton, hydroxide ion, and oxide ion affinities of closed-shell oxides: Importance for the hydration reaction and correlation to electronic structure. *The Journal of Physical Chemistry C*124(2):1277-1284, 2019.

[3]: **Maximilian F. Hoedl**, Denis Gryaznov, Rotraut Merkle, Eugene A. Kotomin, and Joachim Maier. Interdependence of oxygenation and hydration in mixed conducting $(Ba, Sr)FeO_{3-\delta}$ perovskites studied by density functional theory. *The Journal of Physical Chemistry C*124(22):11780-11789, 2020.

[4]: Giulia Raimondi, Francesco Giannici, Alessandro Longo, Rotraut Merkle, Alessandro Chiara, **Maximilian F. Hoedl**, Antonino Martorana, and Joachim Maier. X-ray spectroscopy of $(Ba, Sr, La)(Fe, Zn, Y)O_{3-\delta}$ identifies structural and electronic features favoring proton uptake. *Chemistry of Materials*32(19):8502-8511, 2020

[5]: Rotraut Merkle, **Maximilian F. Hoedl**, Giulia Raimondi, Reihaneh Zohourian, and Joachim Maier. Oxides with Mixed Protonic and Electronic Conductivity. *Annual Review of Materials Research*, in print, 2021.

Bibliography

[1] A.E. Bocquet, A. Fujimori, T. Mizokawa, T. Saitoh, H. Namatame, S. Suga, N. Kimizuka, Y. Takeda, and M. Takano. Electronic structure of $SrFe^{4+}O_3$ and related fe perovskite oxides. *Physical Review B*, 45(4):1561, 1992.

[2] M. Mizumaki, H. Fujii, K. Yoshii, N. Hayashi, T. Saito, Y. Shimakawa, T. Uozumi, and M. Takano. Electronic structure of $BaFeO_3$ studied by x-ray spectroscopy. *physica status solidi (c)*, 12(6):818–821, 2015.

[3] T. Tsuyama, T. Matsuda, S. Chakraverty, J. Okamoto, E. Ikenaga, A. Tanaka, T. Mizokawa, H.Y. Hwang, Y. Tokura, and H. Wadati. X-ray spectroscopic study of $BaFeO_3$ thin films: An Fe^{4+} ferromagnetic insulator. *Physical Review B*, 91(11):115101, 2015.

[4] B. Ribeiro, M. Godinho, C. Cardoso, R.P. Borges, and T.P. Gasche. Self-doping and the role of oxygen vacancies in the magnetic properties of cubic $BaFeO_{3-\delta}$. *Journal of Applied Physics*, 113(8):083906, 2013.

[5] S.D. Ebbesen, S.H. Jensen, A. Hauch, and M.B. Mogensen. High temperature electrolysis in alkaline cells, solid proton conducting cells, and solid oxide cells. *Chemical reviews*, 114(21):10697–10734, 2014.

[6] C. Duan, J. Tong, M. Shang, S. Nikodemski, M. Sanders, S. Ricote, A. Almansoori, and R. O'Hayre. Readily processed protonic ceramic fuel cells with high performance at low temperatures. *Science*, 349(6254):1321–1326, 2015.

[7] H. An, H.W. Lee, B.K. Kim, J.W. Son, K.J. Yoon, H. Kim, D. Shin, H.I. Ji, and J.H. Lee. A $5\times$ 5 cm^2 protonic ceramic fuel cell with a power density of 1.3 W cm^{-2} at 600° C. *Nature Energy*, 3(10):870–875, 2018.

[8] S. Choi, C.J. Kucharczyk, Y. Liang, X. Zhang, I. Takeuchi, H.I. Ji, and S.M. Haile. Exceptional power density and stability at intermediate temperatures in protonic ceramic fuel cells. *Nature Energy*, 3(3):202–210, 2018.

[9] C. Duan, R.J. Kee, H. Zhu, C. Karakaya, Y. Chen, S. Ricote, A. Jarry, E.J. Crumlin, D. Hook, R. Braun, N.P. Sullivan, and R. O'Hayre. Highly durable, coking and sulfur tolerant, fuel-flexible protonic ceramic fuel cells. *Nature*, 557(7704):217–222, 2018.

[10] J. Hou, L. Miao, J. Hui, L. Bi, W. Liu, and J.T.S. Irvine. A novel in situ diffusion strategy to fabricate high performance cathodes for low temperature proton-conducting solid oxide fuel cells. *Journal of Materials Chemistry A*, 6(22):10411–10420, 2018.

[11] J.M. Serra. Electrifying chemistry with protonic cells. *Nature Energy*, 4(3):178–179, 2019.

[12] A. Dubois, S. Ricote, and R.J. Braun. Benchmarking the expected stack manufacturing cost of next generation, intermediate-temperature protonic ceramic fuel cells with solid oxide fuel cell technology. *Journal of Power Sources*, 369:65–77, 2017.

[13] R.J. Braun, A. Dubois, K. Ferguson, C. Duan, C. Karakaya, R.J. Kee, H. Zhu, N.P. Sullivan, E. Tang, M. Pastula, A. Wood, T. Joia, and R. O'Hayre. Development of kw-scale protonic ceramic fuel cells and systems. *ECS Transactions*, 91(1):997, 2019.

[14] R. Zohourian, R. Merkle, G. Raimondi, and J. Maier. Mixed-conducting perovskites as cathode materials for protonic ceramic fuel cells: understanding the trends in proton uptake. *Advanced Functional Materials*, 28(35):1801241, 2018.

[15] R. Merkle, M.F. Hoedl, G. Raimondi, R. Zohourian, and J. Maier. Oxides with mixed protonic and electronic conductivity. *Annual Review of Materials Research*, 51, in press.

[16] R. Dronskowski. *Computational chemistry of solid state materials*, volume 300. Wiley Online Library, 2005.

[17] R.M. Martin. *Electronic structure: basic theory and practical methods*. Cambridge university press, 2020.

[18] P. Hohenberg and W. Kohn. Inhomogeneous electron gas. *Physical review*, 136(3B):B864, 1964.

[19] W. Kohn and L.J. Sham. Self-consistent equations including exchange and correlation effects. *Physical review*, 140(4A):A1133, 1965.

[20] W. Koch and M.C. Holthausen. *A chemist's guide to density functional theory*. John Wiley & Sons, 2015.

[21] M. Born and R. Oppenheimer. Zur quantentheorie der molekeln. *Annalen der physik*, 389(20):457–484, 1927.

[22] G. Kresse and J. Hafner. Ab-initio molecular dynamics for liquid metals. *Physical Review B*, 47(1):558–561, 1993.

[23] G. Kresse and J. Furthmüller. Efficiency of ab-initio total energy calculations for metals and semiconductors using a plane-wave basis set. *Computational Materials Science*, 6(1):15–50, 1996.

[24] G. Kresse and J. Furthmüller. Efficient iterative schemes for ab-initio total-energy calculations using a plane-wave basis set. *Physical Review B*, 54(16):11169–11186, 1996.

[25] C. Persson. *Brief Introduction to the Density Functional Theory - Lecture Notes*. University of Oslo, 2016.

[26] S.L. Dudarev, G.A. Botton, S.Y. Savrasov, C.J. Humphreys, and A.P. Sutton. Electron-energy-loss spectra and the structural stability of nickel oxide: An LSDA+U study. *Physical Review B*, 57(3):1505–1509, 1998.

[27] R. Dronskowski and P.E. Blöchl. Crystal orbital hamilton populations (COHP): energy-resolved visualization of chemical bonding in solids based on density-functional calculations. *The Journal of Physical Chemistry*, 97(33):8617–8624, 1993.

[28] V.L. Deringer, A.L. Tchougréeff, and R. Dronskowski. Crystal orbital hamilton population (COHP) analysis as projected from plane-wave basis sets. *The journal of physical chemistry A*, 115(21):5461–5466, 2011.

[29] S. Maintz, V.L. Deringer, A.L. Tchougréeff, and R. Dronskowski. Analytic projection from plane-wave and PAW wavefunctions and application to chemical-bonding analysis in solids. *Journal of computational chemistry*, 34(29):2557–2567, 2013.

[30] S. Maintz, V.L. Deringer, A.L. Tchougréeff, and R. Dronskowski. LOBSTER: A tool to extract chemical bonding from plane-wave based DFT. *Journal of computational chemistry*, 37(11):1030–1035, 2016.

[31] C. Ertural, S. Steinberg, and R. Dronskowski. Development of a robust tool to extract Mulliken and Löwdin charges from plane waves and its application to solid-state materials. *RSC advances*, 9(51):29821–29830, 2019.

[32] Robert S Mulliken. Electronic population analysis on LCAO-MO molecular wave functions. I. *The Journal of Chemical Physics*, 23(10):1833–1840, 1955.

[33] Richard FW Bader. A quantum theory of molecular structure and its applications. *Chemical Reviews*, 91(5):893–928, 1991.

[34] J. Maier. *Physical chemistry of ionic materials: ions and electrons in solids*. John Wiley & Sons, 2004.

[35] F.A. Kröger. The chemistry of imperfect crystals. Technical report, North-Holland Pub. Co., 1964.

[36] P. Debye and E. Hückel. The interionic attraction theory of deviations from ideal behavior in solution. *Z. Phys*, 24:185, 1923.

[37] N. Hainovsky and J. Maier. Simple phenomenological approach to premelting and sublattice melting in frenkel disordered ionic crystals. *Physical Review B*, 51(22):15789, 1995.

[38] J. Mizusaki, Y. Mima, S. Yamauchi, K. Fueki, and H. Tagawa. Nonstoichiometry of the perovskite-type oxides $La_{1-x}Sr_xCoO_{3-\delta}$. *Journal of Solid State Chemistry*, 80(1):102–111, 1989.

[39] F. Körmann, A. Dick, B. Grabowski, B. Hallstedt, T. Hickel, and J. Neugebauer. Free energy of bcc iron: Integrated ab initio derivation of vibrational, electronic, and magnetic contributions. *Physical Review B*, 78(3):033102, 2008.

[40] X. Zhang, B. Grabowski, F. Körmann, C. Freysoldt, and J. Neugebauer. Accurate electronic free energies of the 3*d*, 4*d*, and 5*d* transition metals at high temperatures. *Physical Review B*, 95(16):165126, 2017.

[41] N.W. Ashcroft and N.D. Mermin. *Solid state physics*. Saunders College Publishing, New York, 1976.

[42] A. Togo and I. Tanaka. First principles phonon calculations in materials science. *Scr. Mater.*, 108:1–5, Nov 2015.

[43] K. Okhotnikov, T. Charpentier, and S. Cadars. Supercell program: a combinatorial structure-generation approach for the local-level modeling of atomic substitutions and partial occupancies in crystals. *Journal of Cheminformatics*, 8(1):17, 2016.

[44] T.S. Bjørheim, M.F. Hoedl, R. Merkle, E.A. Kotomin, and J. Maier. Proton, hydroxide ion, and oxide ion affinities of closed-shell oxides: Importance for the hydration reaction and correlation to electronic structure. *The Journal of Physical Chemistry C*, 2019.

[45] C. Kittel. *Introduction to Solid State Physics*, volume 8. Wiley New York, 2005.

[46] D. Cahen and A. Kahn. Electron energetics at surfaces and interfaces: concepts and experiments. *Advanced Materials*, 15(4):271–277, 2003.

[47] A. Kahn. Fermi level, work function and vacuum level. *Materials Horizons*, 3(1):7–10, 2016.

[48] S.W. Saeed, T. Norby, and T.S. Bjørheim. Charge-carrier enrichment at $BaZrO_3/SrTiO_3$ interfaces. *The Journal of Physical Chemistry C*, 123(34):20808–20816, 2019.

[49] J. Maier. Acid–base centers and acid–base scales in ionic solids. *Chemistry–A European Journal*, 7(22):4762–4770, 2001.

[50] J. Maier. Point defects as acid—base active particles in ionic crystals. *Zeitschrift für anorganische und allgemeine Chemie*, 630(13-14):2562–2568, 2004.

[51] J. Maier. Defect chemistry and ion transport in nanostructured materials: Part II. aspects of nanoionics. *Solid State Ionics*, 157(1-4):327–334, 2003.

[52] S. Chakraverty, T. Matsuda, N. Ogawa, H. Wadati, E. Ikenaga, M. Kawasaki, Y. Tokura, and H.Y. Hwang. $BaFeO_3$ cubic single crystalline thin film: A ferromagnetic insulator. *Applied Physics Letters*, 103(14):142416, 2013.

[53] G. Raimondi, F. Giannici, A. Longo, R. Merkle, A. Chiara, M.F. Hoedl, A. Martorana, and J. Maier. X-ray spectroscopy of $(Ba, Sr, La)(Fe, Zn, Y)O_{3-\delta}$ identifies structural and electronic features favoring proton uptake. *Chemistry of Materials*, 2020.

[54] S. Mori. Magnetic properties of several phases of barium orthoferrate, $BaFeO_x$. *Journal of the Physical Society of Japan*, 28(1):44–50, 1970.

[55] N. Hayashi, T. Yamamoto, H. Kageyama, M. Nishi, Y. Watanabe, T. Kawakami, Y. Matsushita, A. Fujimori, and M. Takano. $BaFeO_3$: a ferromagnetic iron oxide. *Angewandte Chemie*, 123(52):12755–12758, 2011.

[56] F.A. Cotton. *Chemical applications of group theory*. John Wiley & Sons, 2003.

[57] T.A. Albright, J.K. Burdett, and M.H. Whangbo. *Orbital interactions in chemistry*. John Wiley & Sons, 2013.

[58] M. Tinkham. *Group theory and quantum mechanics*. Courier Corporation, 2003.

[59] G. A. Landrum and R. Dronskowski. The orbital origins of magnetism: from atoms to molecules to ferromagnetic alloys. *Angewandte Chemie International Edition*, 39(9):1560–1585, 2000.

[60] J. Zaanen, G.A. Sawatzky, and J.W. Allen. Band gaps and electronic structure of transition-metal compounds. *Physical review letters*, 55(4):418, 1985.

[61] V. Bisogni, S. Catalano, R.J. Green, M. Gibert, R. Scherwitzl, Y. Huang, V.N. Strocov, P. Zubko, S. Balandeh, J.M. Triscone, G. Sawatzky, and T. Schmitt. Ground-state oxygen holes and the metal–insulator transition in the negative charge-transfer rare-earth nickelates. *Nature Communications*, 7(1):1–8, 2016.

[62] A.R. West. *Solid state chemistry and its applications*. John Wiley & Sons, 2014.

[63] T. Wolfram and Ş. Ellialtıoğlu. *Electronic and optical properties of d-band perovskites*. Cambridge University Press, 2006.

[64] S.C. Miller and W.F. Love. *Tables of irreducible representations of space groups and co-representations of magnetic space groups*. Pruett Press, 1967.

[65] M. I. Aroyo, J. M. Perez-Mato, C. Capillas, E. Kroumova, S. Ivantchev, G. Madariaga, A. Kirov, and H. Wondratschek. Bilbao crystallographic server: I. databases and crystallographic computing programs. *Zeitschrift für Kristallographie-Crystalline Materials*, 221(1):15–27, 2006.

[66] M. I. Aroyo, A. Kirov, C. Capillas, J.M. Perez-Mato, and H. Wondratschek. Bilbao crystallographic server. ii. representations of crystallographic point groups and space groups. *Acta Crystallographica Section A: Foundations of Crystallography*, 62(2):115–128, 2006.

[67] B. Bradlyn, L. Elcoro, J. Cano, M.G. Vergniory, Z. Wang, C. Felser, M.I. Aroyo, and B.A. Bernevig. Topological quantum chemistry. *Nature*, 547(7663):298–305, 2017.

[68] T. Wolfram and Ş. Ellialtıoğlu. *Applications of group theory to atoms, molecules, and solids*. Cambridge University Press, 2014.

[69] Y. Liu, Z. Liu, Z. Li, S. Qin, X. Ye, X. Shen, B. Zhou, G. Zhou, S. Agrestini, M. Valvidares, H.B Vasili, Z. Hu, and Y. Long. Multiple magnetic transitions and electrical transport transformation of a $BaFeO_3$ cubic perovskite single crystal. *Physical Review B*, 101(14):144421, 2020.

[70] K. Mori, T. Kamiyama, H. Kobayashi, K. Oikawa, T. Otomo, and S. Ikeda. Structural evidence for the charge disproportionation of Fe^{4+} in $BaFeO_{3-\delta}$. *Journal of the Physical Society of Japan*, 72(8):2024–2028, 2003.

[71] J.B. MacChesney, J.F. Potter, R.C. Sherwood, and H.J. Williams. Oxygen stoichiometry in the barium ferrates; its effect on magnetization and resistivity. *The Journal of Chemical Physics*, 43(9):3317–3322, 1965.

[72] T. Ichida, Y. Bando, T. Shinjo, and T. Takada. Mössbauer study of some barium orthoferrates. *Bulletin of the Institute for Chemical Research, Kyoto University*, 1974.

[73] F. Iga, Y. Nishihara, T. Katayama, K. Murata, and Y. Takeda. Magnetic and transport properties of $BaFeO_{3-y}$. *Journal of Magnetism and Magnetic Materials*, 104:1973–1975, 1992.

[74] K. Mori, T. Kamiyama, H. Kobayashi, T. Otomo, K. Nishiyama, M. Sugiyama, K. Itoh, T. Fukunaga, and S. Ikeda. Mixed magnetic phase in 6H-type $BaFeO_{3-\delta}$. *Applied Crystallography*, 40(s1):s501–s505, 2007.

[75] P.K. Gallagher, J.B. MacChesney, and D.N.E. Buchanan. Mössbauer effect in the system $BaFeO_{2.5-3.0}$. *The Journal of Chemical Physics*, 43(2):516–520, 1965.

[76] H. Kobayashi, F. Iga, and Y. Nishihara. Study on the hexagonal $BaFeO_{3-y}$ system by the mössbauer effect. *Nuclear Instruments and Methods in Physics Research Section B: Beam Interactions with Materials and Atoms*, 76(1-4):258–259, 1993.

[77] S. Morimoto, K. Kuzushita, and S. Nasu. Mössbauer study of charge disproportionate $BaFeO_{3-y}$ and $Ba_{0.9}Sr_{0.1}FeO_{3-y}$ with 6H-perovskite structure. *Journal of magnetism and magnetic materials*, 272:127–129, 2004.

[78] A. Mercy, J. Bieder, J. Íñiguez, and P. Ghosez. Structurally triggered metal-insulator transition in rare-earth nickelates. *Nature communications*, 8(1):1–6, 2017.

[79] Y. Zhang, M.M. Schmitt, A. Mercy, J. Wang, and P. Ghosez. From charge-to orbital-ordered metal-insulator transition in alkaline-earth ferrites. *Physical Review B*, 98(8):081108, 2018.

[80] N.A. Benedek and C.J. Fennie. Why are there so few perovskite ferroelectrics? *The Journal of Physical Chemistry C*, 117(26):13339–13349, 2013.

[81] H. T. Stokes, D. M. Hatch, and B. J. Campbell. ISODISTORT, ISOTROPY software suite. `iso.byu.edu`, 2007.

[82] H.T. Stokes, D.M. Hatch, B.J. Campbell, and D.E. Tanner. ISODISPLACE: a web-based tool for exploring structural distortions. *Journal of Applied Crystallography*, 39(4):607–614, 2006.

[83] H. T. Stokes, D. M. Hatch, and B. J. Campbell. ISOTROPY. `stokes.byu.edu/isotropy.html`, 2007.

[84] C.J. Howard and M.A. Carpenter. Octahedral tilting in cation-ordered Jahn-Teller distorted perovskites-a group-theoretical analysis. *Acta Crystallographica Section B: Structural Science*, 66(1):40–50, 2010.

[85] M.F. Hoedl, D. Gryaznov, R. Merkle, E.A. Kotomin, and J. Maier. Interdependence of oxygenation and hydration in mixed-conducting $(Ba,Sr)FeO_{3-\delta}$ perovskites studied by density functional theory. *The Journal of Physical Chemistry C*, 124(22):11780–11789, 2020.

[86] I.E. Grey, C. Li, L.M.D. Cranswick, R.S. Roth, and T.A. Vanderah. Structure analysis of the 6H-$Ba(Ti,Fe^{3+},Fe^{4+})O_{3-\delta}$ solid solution. *Journal of Solid State Chemistry*, 135(2):312–321, 1998.

[87] J. Hombo, Y. Matsumoto, and T. Kawano. Electrical conductivities of $SrFeO_{3-\delta}$ and $BaFeO_{3-\delta}$ perovskites. *Journal of Solid State Chemistry*, 84(1):138–143, 1990.

[88] L. Wang, R. Merkle, and J. Maier. Surface kinetics and mechanism of oxygen incorporation into $Ba_{1-x}Sr_xCo_yFe_{1-y}O_{3-\delta}$ SOFC microelectrodes. *Journal of The Electrochemical Society*, 157(12):B1802, 2010.

[89] R. Zohourian. *Mixed-conducting perovskites as cathodes in protonic ceramic fuel cells: defect chemistry and transport properties*. PhD thesis, Stuttgart, 2018.

[90] J. Vieten, B. Bulfin, M. Senholdt, M. Roeb, C. Sattler, and M. Schmücker. Redox thermodynamics and phase composition in the system $SrFeO_{3-\delta}$—$SrMnO_{3-\delta}$. *Solid State Ionics*, 308:149–155, 2017.

[91] M.H.R. Lankhorst, H.J.M. Bouwmeester, and H. Verweij. High-temperature coulometric titration of $La_{1-x}Sr_xCoO_{3-\delta}$: evidence for the effect of electronic band structure on nonstoichiometry behavior. *Journal of solid state chemistry*, 133(2):555–567, 1997.

[92] E.A. Kotomin, Y.A. Mastrikov, M.M. Kuklja, R. Merkle, A. Roytburd, and J. Maier. First principles calculations of oxygen vacancy formation and migration in mixed conducting $Ba_{0.5}Sr_{0.5}Co_{1-y}Fe_yO_{3-\delta}$ perovskites. *Solid State Ionics*, 188(1):1–5, 2011.

[93] A.M Deml, V. Stevanovic, A.M. Holder, M. Sanders, R. O'Hayre, and C.B. Musgrave. Tunable oxygen vacancy formation energetics in the complex perovskite oxide $Sr_xLa_{1-x}Mn_yAl_{1-y}O_3$. *Chemistry of Materials*, 26(22):6595–6602, 2014.

[94] Y.L. Lee, J. Kleis, J. Rossmeisl, Y. Shao-Horn, and D. Morgan. Prediction of solid oxide fuel cell cathode activity with first-principles descriptors. *Energy & Environmental Science*, 4(10):3966–3970, 2011.

[95] M.H.R. Lankhorst and H.J.M. Bouwmeester. Determination of oxygen nonstoichiometry and diffusivity in mixed conducting oxides by oxygen coulometric titra-

tion: II. Oxygen nonstoichiometry and defect model for. *Journal of the Electrochemical Society*, 144(4):1268, 1997.

[96] S. Mori. Preparation of various phases of $BaFeO_{3-x}$. *Journal of the American Ceramic Society*, 48(3):165–165, 1965.

[97] S. Mori. Phase transformation in barium orthoferrate, $BaFeO_{3-x}$. *Journal of the American Ceramic Society*, 49(11):600–605, 1966.

[98] M. Parras, L. Fournes, J.C. Grenier, M. Pouchard, M. Vallet, J.M. Calbet, and P. Hagenmuller. Structural aspects and mössbauer resonance investigation of $Ba_2Fe_2O_5$. *Journal of Solid State Chemistry*, 88(1):261–268, 1990.

[99] X.D. Zou, S. Hovmöller, M. Parras, J.M. Gonzalez-Calbet, M. Vallet-Regi, and J.C. Grenier. The complex perovskite-related superstructure $Ba_2Fe_2O_5$ solved by HREM and CIP. *Acta Crystallographica Section A: Foundations of Crystallography*, 49(1):27–35, 1993.

[100] M. Parras, J.M. González-Calbet, M. Vallet-Regi, and J.C. Grenier. A high temperature study of the $BaFeO_{3-y}$ system. *Solid State Ionics*, 63:714–718, 1993.

[101] Victor Moritz Goldschmidt. Die gesetze der krystallochemie. *Naturwissenschaften*, 14(21):477–485, 1926.

[102] C. Chen, D. Chen, Y. Gao, Z. Shao, and F. Ciucci. Computational and experimental analysis of $Ba_{0.95}La_{0.05}FeO_{3-\delta}$ as a cathode material for solid oxide fuel cells. *Journal of Materials Chemistry A*, 2(34):14154–14163, 2014.

[103] X. Zhu, H. Wang, and W. Yang. Structural stability and oxygen permeability of cerium lightly doped $BaFeO_{3-\delta}$ ceramic membranes. *Solid State Ionics*, 177(33-34):2917–2921, 2006.

[104] R.A. Evarestov, E.A. Kotomin, and Y.F. Zhukovskii. Dft study of a single f center in cubic $SrTiO_3$ perovskite. *International journal of quantum chemistry*, 106(10):2173–2183, 2006.

[105] G. Raimondi. Unpublished data. 2021.

[106] R. Zohourian, R. Merkle, and J. Maier. Bulk defect chemistry of PCFC cathode materials: discussion of defect interactions. *ECS Transactions*, 77(10):133, 2017.

[107] E. Coulaud, G. Dezanneau, and G. Geneste. Hydration, oxidation, and reduction of $GdBaCo_2O_{5.5}$ from first-principles. *Journal of Materials Chemistry A*, 3(47):23917–23929, 2015.

[108] D. Gryaznov, R. Merkle, E.A. Kotomin, and J. Maier. Ab initio modelling of oxygen vacancies and protonic defects in $La_{1-x}Sr_xFeO_{3-\delta}$ perovskite solid solutions. *Journal of Materials Chemistry A*, 4(34):13093–13104, 2016.

[109] W. Tan, D. Huan, W. Yang, N. Shi, W. Wang, R. Peng, X. Wu, and Y. Lu. A first-principles study on divergent reactions of using a $Sr_3Fe_2O_7$ cathode in both oxygen ion conducting and proton conducting solid oxide fuel cells. *RSC Advances*, 8(47):26448–26460, 2018.

[110] Y. Xia, Z. Jin, H. Wang, Z. Gong, H. Lv, R. Peng, W. Liu, and L. Bi. A novel cobalt-free cathode with triple-conduction for proton-conducting solid oxide fuel cells with unprecedented performance. *Journal of Materials Chemistry A*, 7(27):16136–16148, 2019.

[111] Z. Wang, W. Yang, Z. Zhu, R. Peng, X. Wu, C. Xia, and Y. Lu. First-principles study of O_2 reduction on $BaZr_{1-x}Co_xO_3$ cathodes in protonic-solid oxide fuel cells. *Journal of Materials Chemistry A*, 2(39):16707–16714, 2014.

[112] N. Sata, K. Hiramoto, M. Ishigame, S. Hosoya, N. Niimura, and S. Shin. Site identification of protons in $SrTiO_3$: Mechanism for large protonic conduction. *Physical Review B*, 54(22):15795, 1996.

[113] K.S. Knight. Powder neutron diffraction studies of $BaCe_{0.9}Y_{0.1}O_{2.95}$ and $BaCeO_3$ at 4.2 K: a possible structural site for the proton. *Solid State Ionics*, 127(1-2):43–48, 2000.

[114] I. Sosnowska, R. Przeniosło, W. Schäfer, W. Kockelmann, R. Hempelmann, and K. Wysocki. Possible deuterium positions in the high-temperature deuterated proton conductor $Ba_3Ca_{1+y}Nb_{2-y}O_{9-\delta}$ studied by neutron and x-ray powder diffraction. *Journal of alloys and compounds*, 328(1-2):226–230, 2001.

[115] E. Kendrick, K.S. Knight, M.S. Islam, and P.R. Slater. Structural studies of the proton conducting perovskite $La_{0.6}Ba_{0.4}ScO_{2.8}$. *Solid State Ionics*, 178(13-14):943–949, 2007.

[116] I. Ahmed, C.S. Knee, M. Karlsson, S.G. Eriksson, P.F. Henry, A. Matic, D. Engberg, and L. Börjesson. Location of deuteron sites in the proton conducting perovskite $BaZr_{0.5}In_{0.5}O_{3-y}$. *Journal of Alloys and Compounds*, 450(1-2):103–110, 2008.

[117] A.K. Azad and J.T.S. Irvine. Location of deuterium positions in the proton-conducting perovskite $BaCe_{0.4}Zr_{0.4}Sc_{0.2}O_{2.90} \cdot x\ D_2O$ by neutron powder diffraction. *Chemistry of Materials*, 21(2):215–222, 2009.

[118] A.S. Farlenkov, L.P. Putilov, M.V. Ananyev, E.P. Antonova, V.A. Eremin, A.Y. Stroeva, E.A. Sherstobitova, V.I. Voronin, I.F. Berger, V.I. Tsidilkovski, and V.P. Gorelov. Water uptake, ionic and hole transport in $La_{0.9}Sr_{0.1}ScO_{3-\delta}$. *Solid State Ionics*, 306:126–136, 2017.

[119] R. Hempelmann, M. Soetratmo, O. Hartmann, and R. Wäppling. Muon diffusion and trapping in proton conducting oxides. *Solid State Ionics*, 107(3-4):269–280, 1998.

[120] M. Karlsson, M. E Björketun, P.G. Sundell, A. Matic, G. Wahnström, D. Engberg, L. Börjesson, I. Ahmed, S. Eriksson, and P. Berastegui. Vibrational properties of protons in hydrated $BaIn_xZr_{1-x}O_{3-x/2}$. *Physical Review B*, 72(9):094303, 2005.

[121] R.A. Davies, M.S. Islam, and J.D. Gale. Dopant and proton incorporation in perovskite-type zirconates. *Solid State Ionics*, 126(3-4):323–335, 1999.

[122] W. Münch, K.D. Kreuer, G. Seifert, and J. Maier. A quantum molecular dynamics study of proton diffusion in $SrTiO_3$ and $CaTiO_3$. *Solid State Ionics*, 125(1-4):39–45, 1999.

[123] M.S. Islam, R.A. Davies, and J.D. Gale. Proton migration and defect interactions in the $CaZrO_3$ orthorhombic perovskite: A quantum mechanical study. *Chemistry of materials*, 13(6):2049–2055, 2001.

[124] M.A. Gomez, M.A. Griffin, S. Jindal, K.D. Rule, and V.R. Cooper. The effect of octahedral tilting on proton binding sites and transition states in pseudo-cubic perovskite oxides. *The Journal of chemical physics*, 123(9):094703, 2005.

[125] C. Shi, M. Yoshino, and M. Morinaga. First-principles study of protonic conduction in In-doped $AZrO_3$ (A= Ca,Sr,Ba). *Solid State Ionics*, 176(11-12):1091–1096, 2005.

[126] M.E. Björketun, P.G. Sundell, and G. Wahnström. Structure and thermodynamic stability of hydrogen interstitials in $BaZrO_3$ perovskite oxide from density functional calculations. *Faraday Discussions*, 134:247–265, 2007.

[127] K. Nomura and H. Kageyama. Neutron diffraction study of $LaScO_3$-based proton conductor. *Solid State Ionics*, 262:841–844, 2014.

[128] K.D. Kreuer. Proton-conducting oxides. *Annual Review of Materials Research*, 33(1):333–359, 2003.

[129] D. Poetzsch, R. Merkle, and J. Maier. Proton uptake in the H^+-SOFC cathode material $Ba_{0.5}Sr_{0.5}Fe_{0.8}Zn_{0.2}O_{3-\delta}$: transition from hydration to hydrogenation with increasing oxygen partial pressure. *Faraday discussions*, 182:129–143, 2015.

[130] D. Poetzsch, R. Merkle, and J. Maier. Stoichiometry variation in materials with three mobile carriers—thermodynamics and transport kinetics exemplified for protons, oxygen vacancies, and holes. *Advanced Functional Materials*, 25(10):1542–1557, 2015.

[131] D. Poetzsch, R. Merkle, and J. Maier. Proton conductivity in mixed-conducting BSFZ perovskite from thermogravimetric relaxation. *Physical Chemistry Chemical Physics*, 16(31):16446–16453, 2014.

[132] T. Norby, M. Widerøe, R. Glöckner, and Y. Larring. Hydrogen in oxides. *Dalton transactions*, (19):3012–3018, 2004.

[133] T.S. Bjørheim, A. Kuwabara, I. Ahmed, R. Haugsrud, S. Stølen, and T. Norby. A combined conductivity and dft study of protons in $PbZrO_3$ and alkaline earth zirconate perovskites. *Solid State Ionics*, 181(3-4):130–137, 2010.

[134] A. Løken, T.S. Bjørheim, and R. Haugsrud. The pivotal role of the dopant choice on the thermodynamics of hydration and associations in proton conducting $BaCe_{0.9}X_{0.1}O_{3-\delta}$ (X= Sc,Ga,Y,In,Gd and Er). *Journal of Materials Chemistry A*, 3(46):23289–23298, 2015.

[135] K.D. Kreuer, W. Münch, A. Fuchs, U. Klock, and J. Maier. Proton conducting alkaline earth zirconates and titanates for high drain electrochemical applications. *Solid State Ionics*, 145(1-4):295–306, 2001.

[136] M.M. Kuklja, Y.A. Mastrikov, B. Jansang, and E.A. Kotomin. The intrinsic defects, disordering, and structural stability of $Ba_xSr_{1-x}Co_yFe_{1-y}O_{3-\delta}$ perovskite solid solutions. *The Journal of Physical Chemistry C*, 116(35):18605–18611, 2012.

[137] M. Shirpour, R. Merkle, and J. Maier. Evidence for space charge effects in Y-doped $BaZrO_3$ from reduction experiments. *Solid State Ionics*, 216:1–5, 2012.

[138] P. E. Blöchl. Projector augmented-wave method. *Physical Review B*, 50(24):17953–17979, 1994.

[139] J. P. Perdew, K. Burke, and M. Ernzerhof. Generalized gradient approximation made simple. *Physical Review Letters*, 77(18):3865–3868, 1996.

[140] Y.L. Lee, J. Kleis, J. Rossmeisl, and D. Morgan. Ab initio energetics of $LaBO_3$ (001)(B= Mn,Fe,Co, and Ni) for solid oxide fuel cell cathodes. *Physical Review B*, 80(22):224101, 2009.

[141] Z.M. Baiyee, C. Chen, and F. Ciucci. A DFT+U study of A-site and B-site substitution in $BaFeO_{3-\delta}$. *Physical Chemistry Chemical Physics*, 17(36):23511–23520, 2015.

[142] I. Cherair, E. Bousquet, M.M. Schmitt, N. Iles, and A. Kellou. First-principles study of strain-induced jahn–teller distortions in $BaFeO_3$. *Journal of Physics: Condensed Matter*, 30(25):255701, 2018.

[143] T.S. Bjørheim, M. Arrigoni, D. Gryaznov, E.A. Kotomin, and J. Maier. Thermodynamic properties of neutral and charged oxygen vacancies in $BaZrO_3$ based on first principles phonon calculations. *Physical Chemistry Chemical Physics*, 17(32):20765–20774, 2015.

[144] M.W. Chase. NIST-JANAF thermochemical tables for oxygen fluorides. *Journal of physical and chemical reference data*, 25(2):551–603, 1996.

[145] P.P. Ewald. Die Berechnung optischer und elektrostatischer Gitterpotentiale. *Annalen der Physik*, 369(3):253–287, 1921.

[146] J. Heyd, G. E Scuseria, and M. Ernzerhof. Hybrid functionals based on a screened coulomb potential. *The Journal of chemical physics*, 118(18):8207–8215, 2003.

[147] J. Heyd, G. E Scuseria, and M. Ernzerhof. Erratum:"hybrid functionals based on a screened coulomb potential"[j. chem. phys. 118, 8207 (2003)]. *J Chem Phys*, 124:219906, 2006.

[148] J.D. Pack and H.J. Monkhorst. " special points for brillouin-zone integrations"—a reply. *Physical Review B*, 16(4):1748, 1977.

[149] J. Bjoerk. vtotav.*. `https://github.com/compphys/ase_tools/blob/master/scripts/vtotav.py`, 2012.

[150] T. Jaouen, G. Jézéquel, G. Delhaye, B. Lépine, P. Turban, and P. Schieffer. Work function shifts, schottky barrier height, and ionization potential determination of thin MgO films on Ag (001). *Applied Physics Letters*, 97(23):232104, 2010.

[151] I.S. Choi, Y.J. Kim, and E.G. Heo. Characterization of negative electron affinity for MgO film by ultraviolet photoelectron spectroscopy. *SID Symposium Digest of Technical Papers*, 41(1):408–411, 2010.

[152] A.J. Logsdail, D.O. Scanlon, C.R.A. Catlow, and A.A. Sokol. Bulk ionization potentials and band alignments from three-dimensional periodic calculations as demonstrated on rocksalt oxides. *Physical Review B*, 90(15):155106, 2014.

[153] Y. Kumagai, K.T. Butler, A. Walsh, and F. Oba. Theory of ionization potentials of nonmetallic solids. *Physical Review B*, 95(12):125309, 2017.

[154] J. Goniakowski, F. Finocchi, and C. Noguera. Polarity of oxide surfaces and nanostructures. *Reports on Progress in Physics*, 71(1):016501, 2007.

[155] B. Ruscic, A.F. Wagner, L.B. Harding, R.L. Asher, D. Feller, D.A. Dixon, K.A. Peterson, Y. Song, X. Qian, C.Y. Ng, J. Liu, W. Chen, and D.W. Schwenke. On the enthalpy of formation of hydroxyl radical and gas-phase bond dissociation energies of water and hydroxyl. *The Journal of Physical Chemistry A*, 106(11):2727–2747, 2002.

[156] S.J. Blanksby and G.B. Ellison. Bond dissociation energies of organic molecules. *Accounts of chemical research*, 36(4):255–263, 2003.

[157] J.R. Smith, J.B. Kim, and W.C. Lineberger. High-resolution threshold photodetachment spectroscopy of OH^-. *Physical Review A*, 55(3):2036, 1997.

[158] C.J. Howard and H.T. Stokes. Structures and phase transitions in perovskites–a group-theoretical approach. *Acta Crystallographica Section A: Foundations of Crystallography*, 61(1):93–111, 2005.

[159] M.A. Carpenter and C.J. Howard. Symmetry rules and strain/order-parameter relationships for coupling between octahedral tilting and cooperative Jahn-Teller transitions in ABX_3 perovskites. I. theory. *Acta Crystallographica Section B: Structural Science*, 65(2):134–146, 2009.